UNIVERSITY OF PAVIA

PhD IN BIOMEDICAL SCIENCES

DEPARTMENT OF MOLECULAR MEDICINE
UNIT OF BIOCHEMISTRY

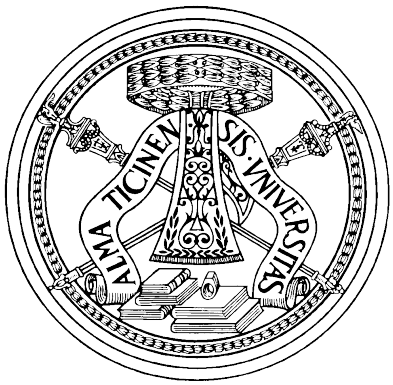

GENE THERAPY STRATEGY FOR CLASSICAL OSTEOGENESIS IMPERFECTA DUE TO MUTATIONS IN *COL1A2* GENE

Supervisor:
Prof. Antonella Forlino

PhD Experimental Thesis
by Silvia Maruelli

XXIX Cycle A. Y. 2015/2016

INDEX

Chapter I

Chapter I

INTRODUCTION

Collagen & collagen family

Collagen, an insoluble fibrous protein in the extracellular matrix, is one of the most abundant proteins in the animal kingdom. The extracellular organic matrix of some connective tissues, such as bone and cartilage, is composed for the major part (90 % and 60 %, respectively) of collagen[1,2]. The basic function of this protein in these tissues is to provide a structural scaffold for minerals, proteoglycans, glycoproteins and other non-collagenous proteins. Thus the collagen is responsible for the physiological and biomechanical properties of the bone and cartilage, such as resistance to pressure, torsion, and tension[3]. Collagens also work as biological substrates for cell adherence in all tissues, playing a major role in regulating essential cell functions as proliferation, migration, differentiation and apoptosis[4]. The term collagen normally refers to a family of proteins including at least 28 members identified in vertebrates **(Table 1)**[5].

Type	Class	Composition	Distribution	Pathology
I	Fibrillar	$\alpha1[I]_2\alpha2[I]$	Abundant and widespread: dermis, bone, tendon, ligament	Osteogenesis Imperfecta I, Ehlers–Danlos syndrome, osteoporosis
II	Fibrillar	$\alpha1[II]_3$	Cartilage, vitreous	Osteoarthrosis, chondrodysplasias
III	Fibrillar	$\alpha1[III]_3$	Skin, blood vessels, intestine	Ehlers–Danlos syndrome, arterial aneurysms
IV	Network	$\alpha1[IV]_2\alpha2[IV]$ $\alpha3[IV]\alpha4[IV]\alpha5[IV]$ $\alpha5[IV]_2\alpha6[IV]$	Basement membranes	Alport syndrome
V	Fibrillar	$\alpha1[V]3$ $\alpha1[V]_2\alpha2[V]$ $\alpha1[V]\alpha2[V]\alpha3[V]$	Widespread: bone, dermis, cornea, placenta	Ehlers–Danlos syndrome
VI	Network	$\alpha1[VI]\alpha2[VI]\alpha3[VI]$ $\alpha1[VI]\alpha2[VI]\alpha4[VI]$	Widespread: bone, cartilage, cornea, dermis	Bethlem myopathy
VII	Anchoring fibrils	$\alpha1[VII]_2\alpha2[VII]$	Dermis, bladder	Epidermolysis bullosa acquisita
VIII	Network	$\alpha1[VIII]_3$ $\alpha2[VIII]_3$ $\alpha1[VIII]_2\alpha2[VIII]$	Widespread: dermis, brain, heart, kidney	Fuchs endothelia corneal dystrophy
IX	FACIT	$\alpha1[IX]\alpha2[IX]\alpha3[IX]$	Cartilage, cornea, vitreous	Osteoarthrosis, multiple epiphyseal dysplasia
X	Network	$\alpha1[X]_3$	Cartilage	Chondrodysplasia
XI	Fibrillar	$\alpha1[XI]\alpha2[XI]\alpha3[XI]$	Cartilage, intervertebral disc	Chondrodysplasia, osteoarthosis
XII	FACIT	$\alpha1[XII]_3$	Dermis, tendon	—
XIII	MACIT	—	Endothelial cells, dermis, eye, heart	—
XIV	FACIT	$\alpha1[XIV]_3$	Widespread: bone, dermis, cartilage	—
XV	MULTIPLEXIN	—	Capillaries, testis, kidney, heart	—
XVI	FACIT	—	Dermis, kidney	—
XVII	MACIT	$\alpha1[XVII]_3$	Hemidesmosomes in epithelia	Generalized atrophic epidermolysis bullosa
XVIII	MULTIPLEXIN	—	Basement membrane, liver	Knobloch syndrome
XIX	FACIT	—	Basement membrane	—
XX	FACIT	—	Cornea (chick)	—
XXI	FACIT	—	Stomach, kidney	—
XXII	FACIT	—	Tissue junctions	—
XXIII	MACIT	—	Heart, retina	—
XXIV	Fibrillar	—	Bone, cornea	—
XXV	MACIT	—	Brain, heart, testis	Amyloid formation?
XXVI	FACIT	—	Testis, ovary	—
XXVII	Fibrillar	—	Cartilage	—
XXVIII	—	—	Dermis, sciatic nerve	Neurodegenerative disease?

Table 1. Types of collagen: tissue distribution and associated diseases.
Abbreviations: FACIT (fibril-associated collagen with interrupted triple helices); MACIT (membrane-associated collagen with interrupted triple helices); MULTIPLEXIN (multiple triple helix domains and interruptions)[5].

All members of the collagen family share the presence of at least a triple helix collagen domain characterized by the assembly of three left-handed helical molecules, called α helices, supercoiled to generate a right-handed helix of 1.5 nm diameter[6]. The supercoiled triple helix collagen model was independently proposed in 1955 on the basis of fiber diffraction analysis, amino acids composition data, molecular modeling and polypeptide structures by Ramachandran, by Rich and Crick, by Cowan and by McGavin and North[7]. Each of the three α-chains form an extended left-handed helix with a pitch of 18 amino acids per turn and supercoils around a central axis. A structural prerequisite for the assembly of the triple helix is a glycine residue present at every third position of the polypeptide chains. Thanks to its small size, the Gly residue is the only amino acid able to occupy the central position of the triple helix without causing chain distortions, while residues with bulkier side chains directed outward are located in second and third position[8] of the characteristic collagenous $(Gly\text{-}X\text{-}Y)_n$ repeated structure[9]. Residues in the X and Y position are often proline (28 %) and hydroxyproline (38 %) respectively, making the GlyProHyp the most common collagen triplet (10.5 %) **(Figure 1)**.

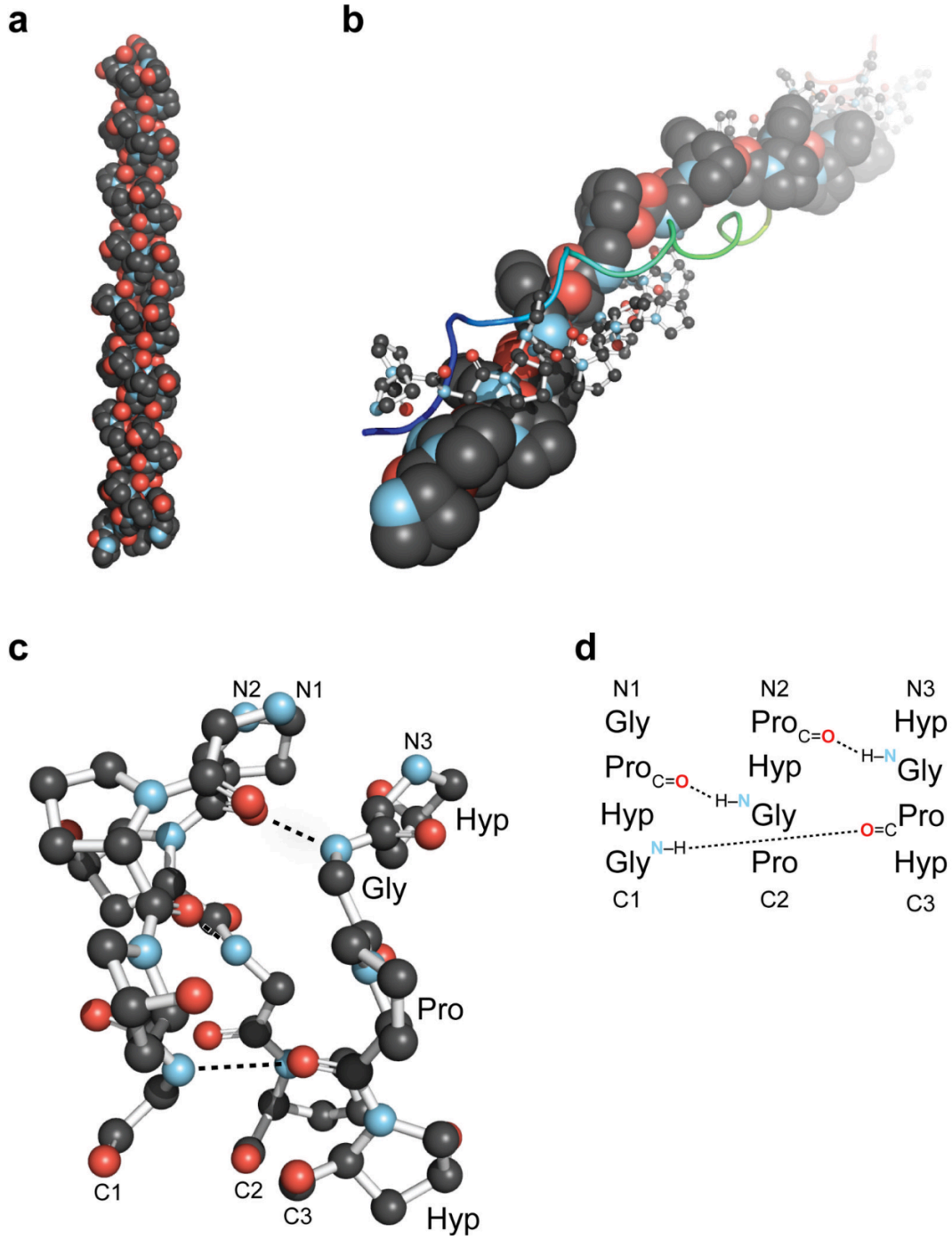

Figure 1. The collagen triple helix motif. **a** High-resolution crystal structure of a synthetic collagen triple helix $(ProHypGly)_4$–(ProHypAla)–$(ProHypGly)_5$[10]; **b** View down the axis of a $(ProProGly)_{10}$ triple helix with the three strands depicted in space-filling, ball-and-stick, and ribbon representation. **c** Ball-and-stick image of a segment of collagen triple helix, highlighting the ladder of inter-strand hydrogen bonds; **d** Stagger of the three strands in the segment in panel **c**.[5]

Depending on the collagen type, specific proline and lysine residues are modified by post-translation enzymatic hydroxylation[6], giving rise to the formation of accessory intramolecular hydrogen bonds that are fundamental for the formation and the stability of the triple helix[11–13]. Hydroxylysine residues are further modified by enzymatic glycosylation[4,5,14,15].

The 28 types of collagen, each having a specific function and present in specific tissues[5], can be divided in two main groups: non-fibrillar and fibrillar forming collagen. The fibrillar forming collagens present an uninterrupted triple helix domain, while non-fibrillar forming collagens have this domain interrupted.

On the basis of sequence homology and supramolecular organization the collagens can also be divided in: fibril-forming collagens (type I, II, III, V, XI, XXIV e XXVII), network-forming collagens (type IV, VI, VIII e XXI), fibril-associated collagens with interrupted triple helices (FACIT) (type IX, XII, XIV, XIX, XXI, XXII e XXVI), membrane-associated collagens with interrupted triple helices (MACIT) (type XII, XVII, XXIII e XXV), multiple triple helix domains and interruptions (multiplexins) (type XV e XVIII) and anchoring fibrils (VII)[5].

The collagen type XXVIII is outside of any of the category previously described because it is characterized by a triple helix domain flanked by an A domain typical of Von Willebrand factor **(Figure 2)**[13]. Mutations in the different collagen types lead to different rare pathologies **(Table 1)**[5,14,16].

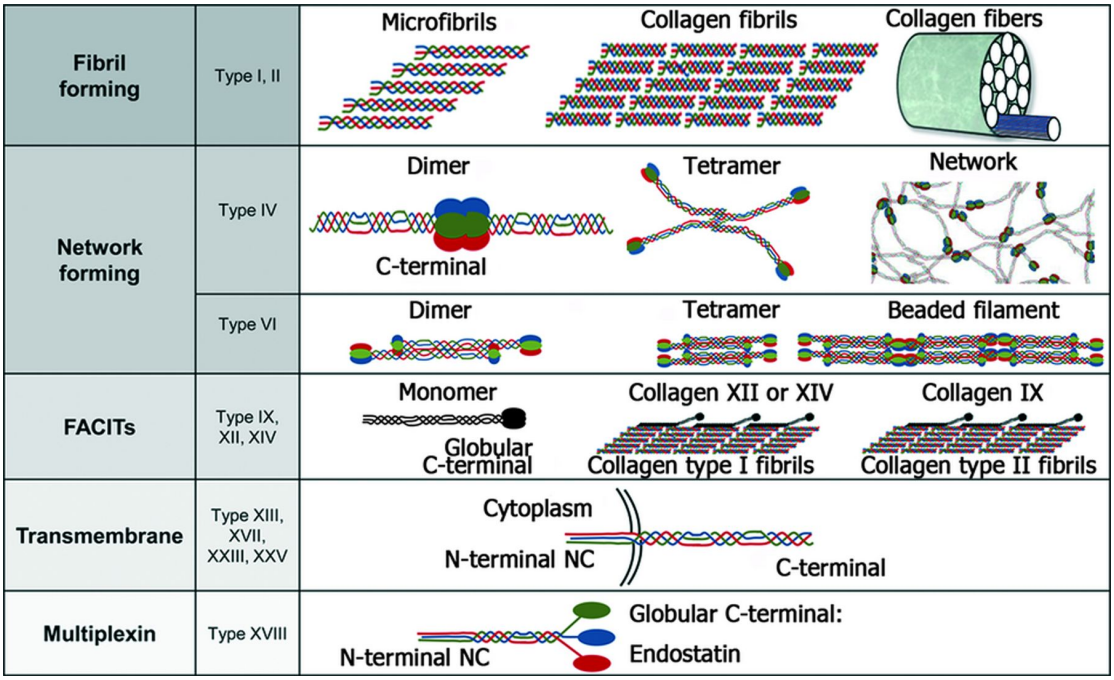

Figure 2. Supramolecular structures formed by some archetypal collagens[17]**.** The length of the triple helical motif varies considerably between different collagen types, reaching up to 300 nm in fibril-forming collagens, while other collagens may contain shorter and frequently interrupted helical domains[4].

The class of fibril-forming collagens includes the most abundant collagen types present in the human body, representing almost the 90 % of the total collagen. These collagens are characterized by their ability to assemble into highly ordered supramolecular aggregates made by quarter-staggered homofibrils or heterofibrils, with diameters between 25 and 400 nm[18]. A characteristic banded pattern with a periodicity of about 70 nm (called the D-period) is generated by the staggered arrangement of individual collagen monomers. Their major triple helical domain is at least 1000 amino acids long, corresponding to 300 nm (3000Å), and has a perfect uninterrupted $(Gly\text{-}X\text{-}Y)_n$ structure. The amino-terminal end usually contains at least one small triple helical domain, called the minor helix **(Figure 3)**[3,5,15].

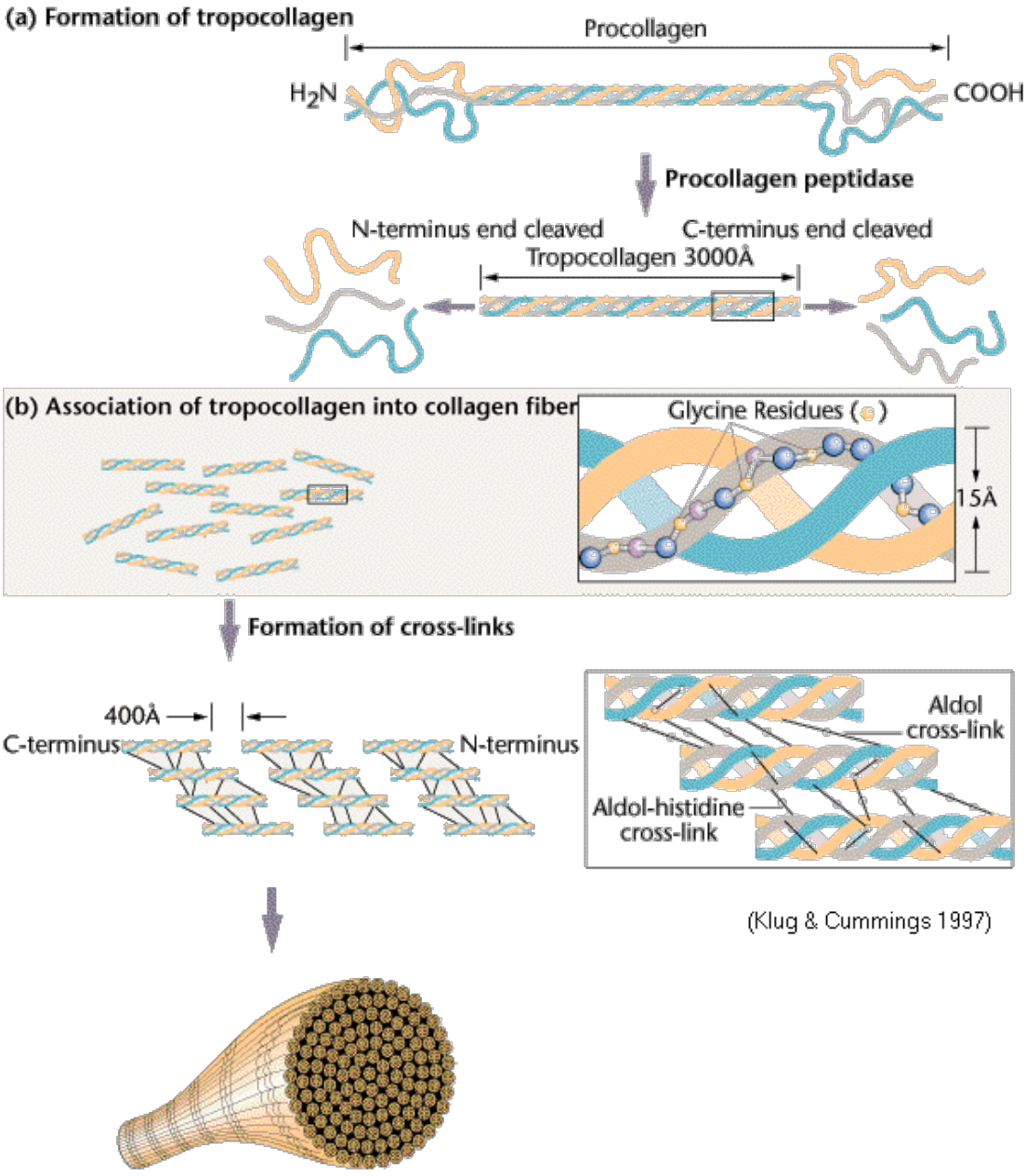

Figure 3. Molecular structure of fibril-forming collagen. The individual triple helices or tropocollagen molecules, are arranged to form fibrils which are of high tensile strength and flexibility and can be further assembled and cross-linked[19].

In cartilage and bone, fibril-forming collagens are the predominant collagen types: the bone matrix consists basically of two collagen types, 95 % type I and 5 % type V collagen, assembled in heterofibrils[1]. Similarly, the scaffold of all cartilages is made of type II and XI collagen heterofibrils, associated with FACIT collagen and minor amounts of other collagen types depending on the cartilage type and location[2,4].

Type I collagen

Structure

Type I collagen is the most abundant among the fibrillar collagens in bone, skin, ligaments, tendon and cornea, but it is also present in many interstitial connective tissues[20]. Due to its relevance, it is the most studied member of the collagen family.

It is synthesized in large quantity by fibroblasts, osteoblasts, odontoblasts and to a lesser extent by nearly all other tissue cells as a precursor molecule, named procollagen consisting of two pro-α1(I) and one pro-α2(I) chains that are assembled into a trimeric protein **(Figure 4)**. The α1(I) and α2(I) chains are composed by 1014 amino acids that are encoded by *COL1A1* and *COL1A2* genes, respectively[21,22]. In the procollagen molecule three domains can be identified: an amino-terminal non-collagenous domain (including N-propeptide and N-telopeptide), a long triple helical region (composed of 338 Gly-X-Y repeats) and a carboxyl-terminal non-collagenous domain (including C-telopeptide and C-propeptide). The single collagen molecule, once outside the cell, spontaneously assemble into fibrils that can include also, in a minor percentage, other types of collagen[23].

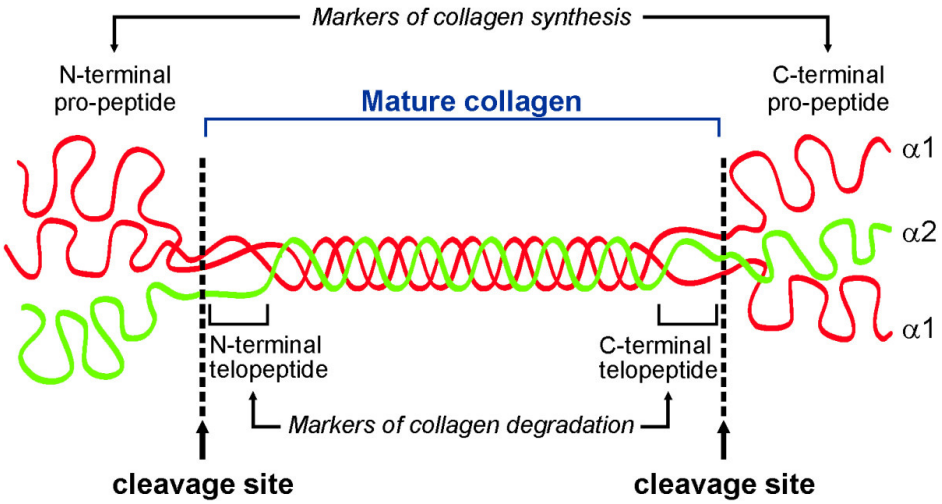

Figure 4. Molecular structure of type I procollagen. Central uninterrupted triple helical domain and the N- and C-random coil propeptides are shown. During the maturation process the two propeptides at both ends of the procollagen are cleaved by N- and C-procollagenases at the two specific cleavage sites (shown by the arrows) leaving two short non-helical telopeptides and the mature triple helix domain[24].

Biosynthesis

Type I collagen is the best characterized and most studied of fibrillar collagens, therefore its biosynthesis is used as a model for the synthesis of all other types of collagen. Collagen is a secreted protein and its biosynthesis and secretion is a complex process involving the rough endoplasmic reticulum (rER) and the Golgi compartment where the molecules undergo several post-translational modifications. A specific processing is also occurring following procollagen secretion in the extracellular environment **(Figure 5)**.

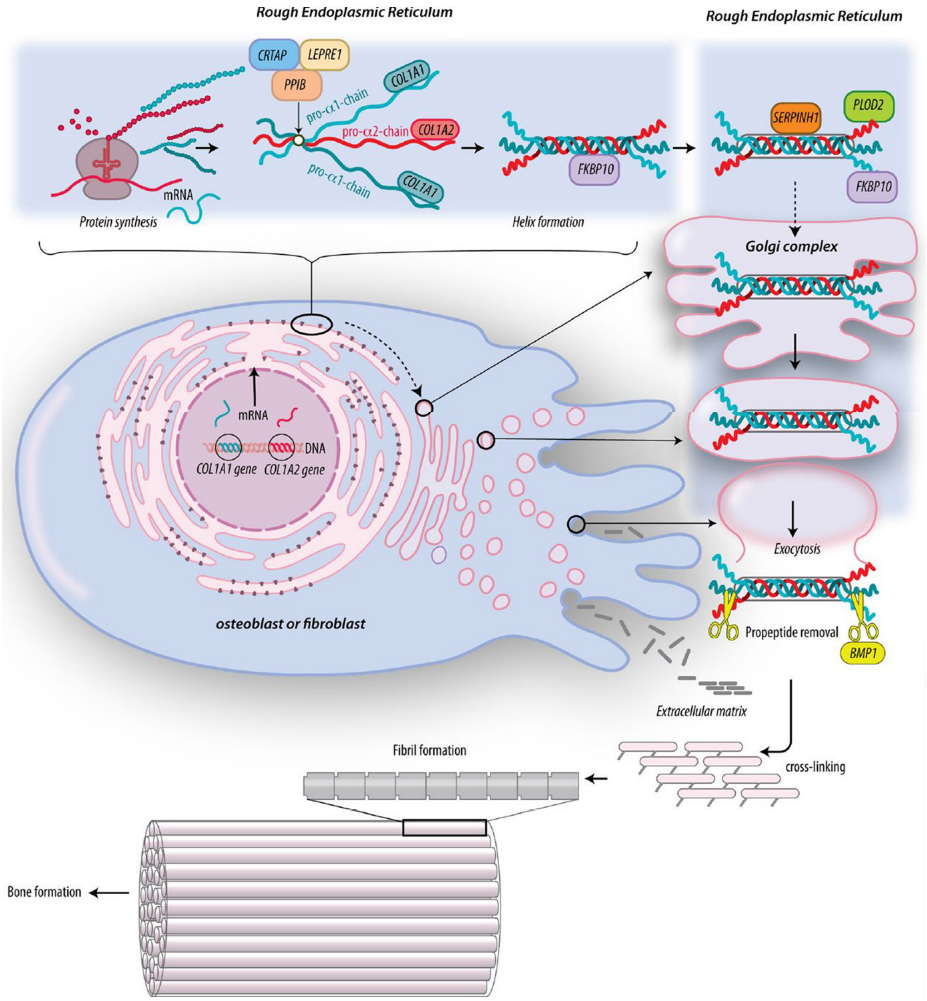

Figure 5. Overview of collagen type I biosynthesis. After translation, pro-α1 and pro-α2 chains are processed in the rough endoplasmic reticulum (rER). These chains have to align and interact at their C-terminal end in order to start the folding process of procollagen type I into a triple helix. During this folding process, post-translational modifications by specific enzymes take place. The pro-α chains give rise to the triple helix through the formation of disulphide bonds at the C-terminal end. After transport of procollagen type I to the Golgi complex and following exocytosis into the extracellular matrix, cleavage of the C- and N-propeptides results in formation of collagen type I. Subsequently, cross-linking involving lysine and hydroxylysine residues of collagen type I molecules leads to formation of fibrils. Multiple collagen type I fibrils generate collagen fibers[25].

The biosynthesis starts with the transcription of *COL1A1* and *COL1A2* genes (located on chromosomes 17 and 7 respectively) into the nucleus. The transcription level of collagen genes depends mainly on the cell type and it is influenced by a variety of growth factors and cytokines[26]. As the most part of genes, type I collagen-coding genes reveal a complex exon-intron pattern, whose transcription is characterized by differential polyadenilation at the 3'end[14].

Once the mRNA is processed, the precursors of the α chains called procollagens (pro-α1 and pro-α2) are independently synthesized in the rER and immediately undergo multiple steps of post-translational modifications.
Proline and lysine residues can be hydroxylated in different positions by different enzymes, according to the position they occupy in the Gly-X-Y triplet.

The enzyme prolyl 4-hydroxylase-1 (P4H1) catalyzes the addition of a hydroxyl group to C4 of proline residues located in the Y position of the collagenic triplet. This modification is essential for the intramolecular hydrogen bonds formation and therefore for the thermal stability of triple helix[27].

Two specific proline residues α1-Pro986 and α2-Pro707 undergo instead hydroxylation at C3 thanks to the activity of a complex formed by Cartilage Associated Protein (CRTAP), Prolyl 3-hydroxylase (P3H1) and Cyclophilin B (CyPB)[28].

The hydroxylation of specific lysine residues is performed by the lysyl 1-hydroxylase and lysyl 2-hydroxylase (LH1 and LH2). This modification is important for the formation of intramolecular link between the collagen molecules and the collagen fibrils[22] and provides sites for glycosylation[4,14].

The glycosylation is catalyzed by the enzymes hydroxylysyl-galactosyltransferase and galactosyl-hydroxylysyl-glucosyltransferase that transfer a galactose unit to hydroxylysine residues and a glucose unit to galactosyl-hydroxylysine residues, respectively[29].

All the above mentioned post translational modifications stop following the formation of the triple helix that impairs the protein access to the active site of the enzymes[25].
Assembly of the procollagen chains into triple helical molecules starts in the rER right after the synthesis of the C-terminal end. The pro-α chains give rise to the triple helix through to the formation of disulphide bonds between cysteine residues

at the C-terminal end of two pro-α1 and one pro-α2 chains. The triple helix formation proceeds from the carboxyl-terminal end toward the amino-terminal end in a zipper-like fashion[30,31]. The random coil procollagen N- and C-propeptides are important to increase the solubility of the molecule and avoid the formation of collagen fibril inside the cells[32].

The correct folding of the procollagen molecule requires specific rER chaperones such as protein disulphide isomerase (PDI) and peptidyl-prolyl *cis-trans* isomerase (PPI)[33]. The collagen-specific chaperon Heat Shock Protein 47 (HSP47) associates preferentially with folded collagen allowing its transfer to the Golgi compartment[32,34]. From the Golgi, where the last steps of glycosylation are completed, the procollagen is packed into transport vesicles and secreted into the pericellular space where fibrillar formation starts. N-propeptides and C-propeptides are cleaved off in the pericellular space by two specific zinc-proteases ADAMT2[35] and bone morphogenetic protein 1 (BMP-1), respectively[36], resulting in the formation of tropocollagen, the fundamental unit of collagen fibril. This step leads to a decrease in solubility of the molecules increasing their intrinsic property of self-assembling into higher ordered structure[37,38].

After the proteolytic cleavages, five collagen molecules arranged in a quarter-staggered manner form the minimal collagen fibril structure. This arrangement generates a characteristic banding pattern of 64-67 nm, called D-period[39]. The monomers are 300 nm long and 40 nm gaps separate consecutive monomers causing the characteristic birifrangent appearance of the collagen type I fibrils on the ultrastructural level **(Figure 6)**[4,38,40].

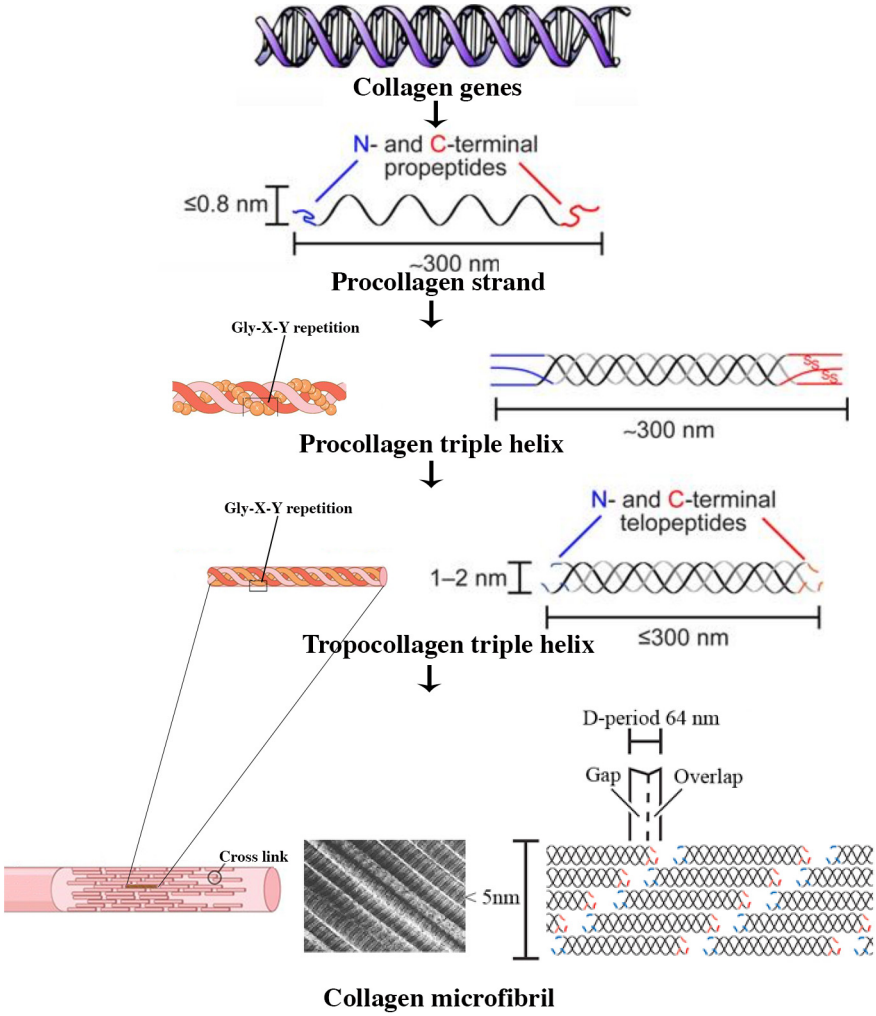

Figure 6. Assembly of collagen fibrils starting from gene transcription. The steps of the collagen microfibril assembly with the characteristic 64-67 nm pattern known as D-period observed at electron microscope, are represented. Adapted from Shoulders Annual Rev Biochem 2009 and Jones & Bartlett learning 2013.

The overlapping regions are fundamental for the formation of inter-chain cross links between lysine and hydroxylysine residues localized both in the triple helical domain and in the telopeptides and for the interactions of the collagen molecules with other non-collagenous proteins. The gap regions are important for the mineral nucleation[5]. The intermolecular cross-links are fundamental to determine the physical and mechanical properties of the fibril network.

Osteogenesis Imperfecta

The majority of the organic component in bone is type I collagen therefore defects in its structure, biosynthesis, assembly or turnover result in a variety of severe diseases, the most common and best described being Osteogenesis Imperfecta (OI)[4]. OI known as brittle bone disease, is a rare bone dysplasia with an incidence of 1:15,000-1:20,000 live births[41,42] and it was described for the first time in 1788[43]. OI patients can carry mutations in different genes and present a wide range of clinical outcomes, but the common phenotype is bone fragility and deformity. Other clinical manifestations include extra-skeletal alterations such as blue sclera, dentinogenesis imperfecta, hearing loss, decreasing pulmonary function, skin hyperlaxity and joint hypermobility[22,44]. For several years OI was considered to be caused only by mutations in the collagen type I encoding genes *COL1A1* and *COL1A2* and to have an autosomal dominant transmission [45]. During the last decade several mutations, mainly associated to a recessive transmission were identified in genes encoding for proteins involved in collagen biosynthesis, post translational modification, secretion, extracellular processing or involved in osteoblast differentiation and/or activity[46].

Classification

The first OI classification was based on clinical and radiographic features and genetics and was proposed in 1979 by Prof. Sillence before the molecular knowledge of the underlying collagen disorder was fully understood[44,47]. Based on this classification OI patients carrying collagen type I mutations, are divided into four groups, from type I to type IV. The OI type I is associated to quantitative deficiency of otherwise structurally normal collagen, whereas lethal type II, severe type III and moderate type IV forms have mutations that alter collagen structure. These forms accounts for over 85 % of OI cases all characterized by dominant transmission (AD). Up to date 15 more genetic causes of OI have been identified for the most linked to a recessive transmission of the disease (AR) and the Sillence classification has been updated.

The increased number of genes involved in the OI etiology led in 2016 Forlino and Marini to propose a new system based on the impaired metabolic pathways **(Table 2)**.

Inheritance	Gene symbol	OMIM number	Sillence type	Protein	Main location	Other typical features
Defects in collagen synthesis, structure, or processing (group A)						
AD	COL1A1	166200	I	Collagen type I, alpha 1	Extracellular matrix	Rare to sever bone deformity. Normal sclerae, gray to dark blue. Hearing loss and dentinogenesis imperfecta absent to common.
		166210	II			
		259420	III			
		166220	IV			Oter typica features: Type IV Oi/EDS is due to mutations at the first 85 aminoacid of α1(I); HBM/OI is caused by mutations blocking C-propeptide processing.
	COL1A2	166200	I	Collagen type I, alpha 2	Extracellular matrix	Rare to sever bone deformity. Normal sclerae, gray to dark blue. Hearing loss and dentinogenesis imperfecta absent to common.
		166210	II			
		259420	III			
		166220	IV			Oter typica features: Type IV Oi/EDS is due to mutations at the first 85 aminoacid of α2(I); HBM/OI is caused by mutations blocking C-propeptide processing.
AR	BMP1	614856	XIII	Bone morphogenic protein1/procollagen C proteinase	Pericellular environment	Mild to sever bone deformity. Normal sclerae, gray to dark blue. Hearing loss and dentinogenesis imperfecta absent. Other typical features: Umbelical hernia, HBM.
Defects in collagen modification (group B)						
AR	CRTAP	610682	VII	Cartilage-associated protein	Endoplasmic reticulum	Severe rhizomelia. Normal grey sclerae. Absent hearing loss and dentinogenesis imperfecta.
	LEPRE1/ P3H1	610915	VIII	Leucine proline-enriched proteoglycan1/prolyl 3-hydroxylase 1	Endoplasmic reticulum	
	PPIB	259440	IX	Peptidylprolyl isomerase B/cyclophilin B	Endoplasmic reticulum	Severe bone deformity. Grey sclerae. Absent hearing loss and dentinogenesis imperfecta.
	TMEM38B	615066	XIV	Transmembrane protein 38 B	Endoplasmic reticulum membrane	Severe bone deformity. Sclerae is from normal to blue. Absent hearing loss and dentinogenesis imperfecta.
Defects in collagen folding and cross-linking (group C)						
AR	SERPINH1	613848	X	Serpin peptidase inhibitor, clade H, member 1/heat shock protein 47	Endoplasmic reticulum	Severe bone deformity. Blue sclerae. Absent hearing loss. Present dentinogenesis imperfecta.Other typical features: skin blister and bullae at birth, inguinal hernia.
	FKBP10	610968	XI	FK506 binding protein 65	Endoplasmic reticulum	Mild to severe bone deformity. Normal grey sclerae. Absent hearing loss and dentinogensis imperfecta. Other typical features: variable congenital contractures, encompasses Bruck and Kuskokwim syndromes.
	PLOD2	609220	..	Procollagen-lysine, 2-oxoglutarate 5-dioxygenase 2	Endoplasmic reticulum	Moderate to severe bone deformity. Other typical features: progressive joint contractures.
Defects in bone mineralisation (group D)						
AD	IFITM5	610967	V	Interferon-induced transmembrane protein 5	Plasma membrane	Variable bone deformity. Normal to blue sclerae. Infrequent hearing loss. Absent dentinogenesis imperfecta. Other typical features: ossification of the forearm interosseous membrane, radia head dislocation, subephyphyseal metaphysel radiodence band.
AR	SERPINF1	613982	VI	Pigment epithelium-derived factor	Extracellular matrix	Moderate to severe bone deformity. Normal to blue sclerae. Absent hearing loss and absent dentinogenesis imperfecta. Other typical features: normal at birth, unmineralised osteoid, fish scale appearance of lamellar bone pattern, raised ALP, loss of serum PEDF.
	SPARC	182120	XVII	Secreted acid cysteine-rich protease, osteonectin	Extracellular matrix	White sclerae. Absence of dentinogenesis imperfecta. Occurence of bone fracture after the first year of life ad presence of mild joint hyperlaxity.
Defects in osteoblast development with collagen insufficiency (group E)						
AR	SP7	613849	XII	Transcription factor 7/osterix	Nucleus	Severe bone deformity. Normal sclerae. Absent hearing loss and absent dentnogenesis imperfecta. Other typical features: delay tooth eruption, midface hypoplasia.
	WNT1	615220	XV	Wingless-type MMTV integration site family, member 1	Extracellular matrix	Severe bone deformety. White sclerae. Absent hearing loss and absent dentinogenesis imperfecta. Other typical features: possible neurological defects.
	CREB3L1	616229	XVI	cAMP responsive element binding protein 3 like 1	Endoplasmic reticulum membrane	Severe bone deformity.

Table 2. OI functional classification of classical dominant and new recessive forms[48].

This novel OI classification identifies five groups: defects in collagen synthesis, structure or processing (group A); defects in collagen modification (group B); defects in collagen folding and cross-linking (group C); defects in bone mineralization (group D) and defects in osteoblast development with collagen insufficiency (group E).

Defects in collagen synthesis, structure or processing (group A)

The first group (group A) includes mutations that lead to defects in collagen synthesis, structure or processing. The mutated genes that belong to this group are: *COL1A1* (AD), *COL1A2* (AD) and *BMP1* (AR).

COL1A1 and *COL1A2* genes encode for the α1 and α2 collagen chains respectively. In normal type I collagen these two helical polypeptides assemble into a heterotrimeric triple helix made by two α1(I) chains and one α2(I) chain. 1489 unique DNA variants have been identified in *COL1A1* and *COL1A2* to be associated with OI [https://oi.gene.le.ac.uk/ accessed October 2016]. Different kinds of mutations in these genes were reported as causative of different forms of OI depending on the type of mutation. The position of the mutation seems to play a major role in influencing the severity of the outcome. As expected, the regions of the α-chains that play a key role in the network of protein interactions that regulates matrix physiology and those regions that are involved in chain assembly and folding are the ones causing major damage when altered. For this reason, mutations occurring in Major Ligand Binding Regions (MLBR) and in the C-terminal end result in more severe phenotypes, since they alter the protein-collagen interaction and the site where triple helical folding begins **(Figure 7)**.

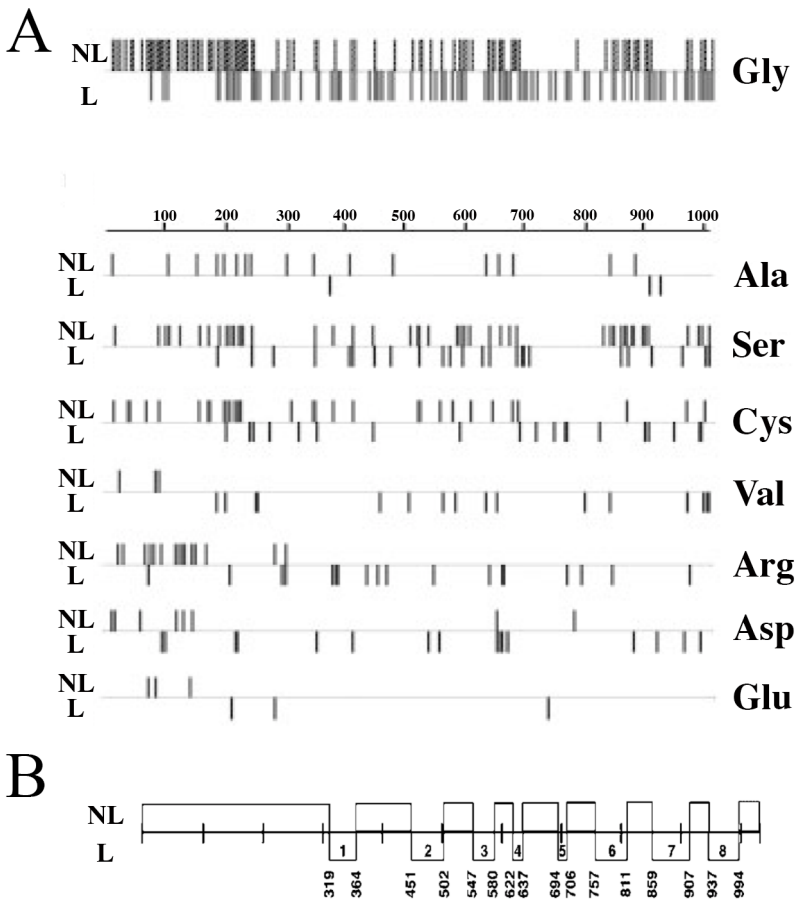

Figure 7. Distribution of the mutations along the pro-α collagen I chains. **A** Glycine substitutions in α1(I) chain caused by single-nucleotide changes shown for each substituting amino acid, indicated at the right end of each line. The top line indicates the scale used based on residue number in the triple-helical region. **B** Regional model for the distribution of mutations along the α2(I) chain. The lethal mutations are located in eight regularly spaced clusters. The vertical bars indicate the mutations. NL, nonlethal; L, lethal. Adaptation from Marini 2007[49].

Null mutations in *COL1A1* cause OI type I (OMIM # 166200) and lead to the reduced synthesis of normal collagen type I. The matrix insufficiency is responsible for increased bone fragility, associated with minimal deformity of long bone and spine and normal stature. Affected patients show bone fragility during childhood that decreases after puberty, increasing again following the fifth decade of life. Joint hypermobility and predisposition to develop scoliosis, kyphosis and chronic back pain are common[46,50,51]. The clinical manifestations characteristic of this OI form are blue sclera[52], and hearing loss (50 % of cases), that usually begins after the second decade of life[53].

Glycine substitutions with bulkier amino acid, exon skipping, insertions and deletions in *COL1A1* and *COL1A2* genes are dominant inherited and responsible for qualitative defect in collagen type I that lead to OI type II (OMIM # 166210), type III (OMIM # 259420) and type IV (OMIM # 166220). The type II is the perinatal lethal form of OI; it is the most severe form of OI and entails death *in utero*. Frequently infants affected by this OI form die in the immediate perinatal period: more than 60 % die in the first day, 80 % die in the first week and survival beyond one year is extremely rare. The first fractures are already detectable *in utero* and affected newborns have extremely fragile bones with marked deficiency of ossification, distinctive triangular face, bluish sclera, deformed extremities with multiple fractures and abnormal angulation of long bones, that leads to a typical "frog-like" position[45]. Death usually results from pulmonary failure probably due to small thorax and from multiple rib fractures[46,50,51].

The OI type III, the progressively deforming OI, is the most severe non-lethal form of the disease. Affected patients show intrauterine fractures, growth retardation and further progressive growth failure continues during childhood as a result of long bone deformation and multiple fractures (as many as 200 fractures in a lifetime). Pale blue or grey sclera is present at infancy, but they regain normal color after puberty. Bowing and angulation deformities appear over remodeling of the shafts of the long bones, and kyphoscoliosis starts during childhood and progresses into adolescence. Thoracic scoliosis has a severe negative influence on pulmonary function that can lead to early mortality. Over 80 % of patients have dental malocclusion and discoloration. The ambulation is impaired for the majority of them[46,50,51].

OI type IV severity shows a highly variable phenotype between the mild OI type I and the severe OI type III, even within families. Bone fractures occur at high frequency during childhood and their number decrease in older age. Osteoporosis and variable degrees of deformity of long bones and spine are present, but most of the patients achieve ambulation. In many affected patients there is a progressive kyphoscoliosis that may lead to severe cardiopulmonary and neurological complications[54]. Hearing impairment, dentinogenesis imperfecta, blue sclerae and malformation, such as basilar invagination, show variable occurrence[46,50,51].

Another gene present in the group A is *BMP1* codifying for the bone morphogenetic protein 1, the procollagen C-protease, essential to remove the C-propeptide after procollagen secretion allowing the self-assembly of the collagen monomers into fibrils. Mutations in *BMP1* lead to an unusual processing of the procollagen molecule that compromises the mineralization causing OI type XIII (OMIM # 614856). Both homozygous and heterozygous mutations are causative of this form of the disease that is mainly characterized by normal teeth, faint blue sclera, severe growth deficiency, severe bone deformity, borderline osteoporosis and an average of 10 to 15 fractures/year affecting both upper and lower limbs[55,56].

Defects in collagen modifications (group B)

The group B includes mutations in the genes: *LEPRE1* (AR)*, CRTAP* (AR)*, PPIB* (AR) *and TMEM38B* (AR).

LEPRE 1 (AR)*, CRTAP* (AR)*, PPIB* (AR) encode for three proteins that form a complex responsible for the post-translational 3-hydroxylation of the proline residue in position 986 of the pro-α1(I) and proline 707 on pro-α2(I) chain. These three proteins assemble into a trimeric complex in the rER in a 1:1:1 ratio[57]. Defects in members of the 3-hydroxylation complex result in the delay of type I collagen folding and its consequent over-glycosylation.

CRTAP encodes for Cartilage-associated protein, the helper protein of the complex expressed by chondrocytes and osteoblasts in the skeletal tissue. CRTAP, deficient patients[58,59] (type VII OI, OMIM # 610682) show moderate to lethal phenotype with growth deficiency and rhizomelia. Others features of patients affected by this OI form are severe osteoporosis with neonatal fractures and broad undertubulated long bones. Almost all CRTAP mutations identified result in nonsense-mediated decay (NMD) and absence of CRTAP protein with loss of α1(I) Pro-986 3-hydroxylation.

LEPRE1 encodes for Prolyl-3-hydroxylase 1 (P3H1), the enzymatic component of the complex. P3H1 contains a KDEL sequence for the endoplasmic reticulum retrieval and it is crucial for collagen modification. Patients with mutations in *LEPRE1* gene[60] (type VIII OI , OMIM # 610915), most of which lead to transcripts reduction, show a severe

to lethal phenotype with the same symptoms of type VII OI, making difficult to distinguish the two OI forms from a clinical point of view.

PPIB encodes for Peptidyl-prolyl Isomerase B/Cyclophilin B (PPIB), involved into *cis-trans* isomerization of proline residues present in the collagen chain. Mutations in *PPIB*[33] (type IX OI, OMIM # 259440) create premature stop codon or misfolded proteins that result in severe to lethal OI phenotype with white sclera, but without rhizomelia.

TMEM38B encodes for the transmembrane protein 38B, this protein forms a homotrimeric potassium channel in the endoplasmic reticulum membrane, affecting calcium release. Homozygous mutations in *TMEM38B* gene cause the autosomal recessive OI type XIV[61] (OMIM # 615066). This OI form is characterized by a variable degree of severity associated with multiple fractures and osteopenia. Dentinogenesis imperfecta, blue sclera and hearing defects not consistently present.

Defects in collagen folding and cross-linking (group C)

Defects in collagen folding and cross-linking are in the group C. The mutated genes belonging to this group are: *SERPINH1* (AR), *FKBP10* (AR) and *PLOD2* (AR).

SERPINH1 encodes for heat shock protein 47 (HSP47) a molecular chaperone that stabilizes and assists the correct transfer of collagen into the *cis*-Golgi. Recessive mutations in this gene were associated to OI type X[62] (OMIM # 613848) characterized by multiple bone deformities and fractures, generalized osteopenia, dentinogenesis imperfecta, and blue sclera.

FKBP10 encodes for the protein FKBP65, this protein is not a collagen specific chaperone but it seems to interact also with the enzyme responsible for the hydroxylation of lysine residues in the collagen C-telopeptides, namely lysyl hydroxylase 2 (LH2). Indeed dermal fibroblasts and bones with defects in *FKBP10* showed a reduction of the hydroxylation of the collagen C-telopeptide lysine residues[63]. Homozygous mutations in *FKBP10* are responsible for OI type XI[64] (OMIM # 610968), a very heterogeneous form with phenotype ranging from moderate to lethal.

PLOD2 (procollagen-lysine 2-oxoglutarate 5-dioxygenase) encodes for a bone-sprìecific collagen telopeptide lysil hydroxylase (TLH). Its deficiency results in underhydroxylation of the lysines of the collagen telopeptide, but not the triple helix, leading to abnormal collagen crosslinking. Patients with *PLOD2* mutations are characterized by progressive joint contractures[65].

Defects in bone mineralization (group D)

Defects in bone mineralization are in the group D, the mutated genes that belong to this group are: *IFITM5* (AD)*, SERPINF1* (AR) and *SPARC* (AR).

Interferon-induced transmembrane protein 5 (*IFITM5)* gene encodes for bone-restricted IFITM-like protein (BRIL), a transmembrane protein expressed by osteoblasts during early mineralization.

Dominant OI type V (OMIM # 610967) is due to mutations in *IFITM5* gene[66]. In particular, an overexpression of BRIL protein results in dose-dependent increase in mineralization while its knockdown results in reduced mineralization[67]. Patients affected by OI type V exhibit moderate to severe bone fragility. No blue sclera or dentinogenesis are present and the main features of this form are the presence of progressive calcification of the inter-osseous membranes in the forearms and legs which leads to movement restriction, the propensity to develop hyperplastic callus following a fracture or orthopedic surgery even of modest entity, and abnormal bone histomorphometry characterized by mesh-like lamellation[68].

Serpin peptidase inhibitor, clade F, member 1 (*SERPINF1)* gene encodes for the pigment epithelium derived factor (PEDF), a protein that upon binding to two distinct sites on type I collagen inhibits angiogenesis, thus blocking tumor growth and metastasis[69]. Furthermore, PEDF stimulates osteogenic gene expression and mineral deposition and inhibits osteoclasts maturation by enhancing osteoprotegerin expression[70]. Recessive mutations in *SERPINF1* are linked to OI types VI[55] (OMIM # 610968) clinically indistinguishable from type IV OI at its appearance, but it is characterized by progressive worsening of the phenotype. It was first described on the basis of histological analysis a distinctive “fish scales” pattern instead of a normal

lamellae orientation and a reduced osteoid mineralization[71]. These features lead to the conclusion that this form of OI is caused by defect in mineralization[22,46].

SPARC encodes for a glycoprotein called secreted acid, cysteine-rich proteins (SPARC), also known as osteonectin. This glycoprotein binds to collagen type I and to other extracellular proteins, elicits changes in cell shape, inhibits cell-cycle progression and influences the synthesis of extracellular matrix (ECM)[72]. A missense mutation in *SPARC* was associated to autosomal recessive OI XVII form[73] (OMIM # 182120) by Mendoza-Londono et al[73]. Two patients carrying a homozygous SPARC mutation were characterized by white sclerae, absence of dentinogenesis imperfecta, occurrence of bone fractures after the first year of life ad presence of mild joint hyperlaxity.

Defects in osteoblast development with collagen insufficiency (group E)

Defects in osteoblast development with collagen insufficiency are in the group E. The mutated genes that belong to this group are: *SP7* (AR), *WNT1* (AR), *CREB3L1* (AR).

SP7 encodes for an osteoblast-specific transcription factor of the SP gene family and it is a putative master regulator of bone cell differentiation[74]. An homozygous single base pair deletions in *SP7* gene was associated to the OI type XII[75] (OMIM # 613849) by Lapunzina et al.[75] in 2010. This OI form has an autosomal recessive inheritance and is characterized by recurrent fractures, mild bone deformations, generalized osteoporosis, delayed teeth eruption, no dentinogenesis imperfecta, normal hearing, and white sclera.

Wingless-type MMTV integration site family, member 1 (*WNT1)* gene is a mast regulator of osteoblasts function. Homozygous or compound heterozygous mutation in *WNT1* gene are associated to OI type XV[76] (OMIM # 615220), characterized by early-onset recurrent fractures, bone deformity, significant reduction of bone density, short stature, and, in some patients, blue sclera. Tooth development and hearing are normal. Learning and developmental delays and brain anomalies have been observed in some patients[77].

CREB3L1 gene encodes for c-AMP response element-binding protein 3-like 1 (OASIS), a trans-membrane protein present in the endoplasmic reticulum that is involved in the regulation of collagen type I expression in osteoblasts. Up to date only

one case has been reported[78] in which a mutation in CREB3L1 gene was responsible for OI type XVI (OMIM # 616229). The affected patient was a child who had fractures *in utero* and was small for gestational age. He continued to have fractures after birth, and X-rays showed beaded ribs, callus formation, and multiple fractured tubular bones with an accordion-like broadened appearance.

Most recently, a gene that is part of the regulated intramembrane proteolysis (RIP) pathway in osteoblasts has been reported to cause OI. In RIP, proteases in the Golgi membrane, site-1 protease (S1P) and site-2 protease (S2P), sequentially cleave regulatory proteins transported from the ER membrane in times of ER stress or sterol metabolite deficiency. Mutations causing single residue substitutions in or near the ion-coordination site of S2P (encoded by *MBTPS2,* the first X-linked gene for OI), and impairing its cleavage of substrate transcription factors, have been reported in two pedigrees with moderate to severe OI. Bone tissue with an MBTPS2 defect has reduced hydroxylation of α1(I) and α2(I) K87 and altered crosslinking of collagen, impairing bone strength[79].

Murine models

For the study of genetic diseases the use of animal models becomes fundamental. The animal models are an important source of information used to investigate the cause and the biochemical process behind the pathology development. Furthermore they represent the most efficient and safely way to test new therapies for the treatment of the disease before to move to human patients. These issues are of particular relevance in bone pathologies like OI, in which the retrieval of patient's bone samples is really difficult. Several animal models for OI, both for the dominant and recessive forms, have been developed during the years **(Table 3)**.

Mouse	Gene defect	Protein defect	Bone phenotype	Type
Autosomal dominant transmission				
Mov13/+	M-MuLV insertion in endogenous *Col1a1* intron 1	50% synthesis of normal pro-α1(I)	Reduced ductility and bone strength, increased tissue porosity, altered collagen organization	I
Transgenic	Exogenous mutant murine *Col1a1* cDNA	Gly859Cys	Deformed bones, poor mineralization, underdevelopment of the skeleton	II
Transgenic	Human *COL1A1* minigene	Human pro-α1(I) lacking 41 internal exons	Moderate to severe bone phenotype depending on transgene expression level, multiple fractures, short femurs, reduced mineral and collagen content	II–IV
Aga2/+	ENU-induced *Col1a1* c.4216–2T>A	Frameshift of last 48 amino acids and addition of 90 amino acids beyond stop codon	Severe bone phenotype: early lethality, multiple fractures, reduced bone mass, disturbed osteoblast function	III
Brtl/+	Knock-in *Col1a1* c.1546G>T	Gly349Cys	30% perinatal lethality, reduced body size, flared thorax, rib fractures, long bone deformity, bone fragility, reduced BMD, increased bone turnover due to increased osteoclast precursors and reduced osteoblast activity	IV
Gly610Cys/+ (*Amish*/+)	Knock-in *Col1a2* c.2098G>T	Gly610Cys	Moderately severe phenotype affected by genetic background, reduced body size, BMD and bone strength	IV
Jrt/+	ENU-induced *Col1a1 skipping exon 9*	18 amino acid deletion in the main triple helical domain	Low BMD, bone fragility, reduced bone strength, impaired mineralization	IV EDS
Autosomal recessive transmission				
Mov13/*Mov13*	M-MuLV insertion in endogenous *Col1a1* intron 1	Lack of pro-α1(I)	Lethal in mid-stage gestation due to rupture of major blood vessels	II
Oim/*Oim*	Naturally occurring *Col1a2* c.3983delG	Lack of pro-α2(I) in collagen I and synthesis of $[\alpha1(I)]_3$ homotrimers	Skeletal fractures, limb deformities, generalized osteopenia, small body size, reduced BMD Increased osteoclast activity	III-like
Brtl/*Brtl*	Knock-in *Col1a1* c.1546G>T	Gly349Cys	Absence of perinatal lethality, body size intermediate between *Brtl*/+ and wild type, no rib fractures, no flared thorax, normal BMD	Mild type IV (near normal)
Crtap/*Crtap*	Knockout of *Crtap* gene	Absence of CRTAP protein	Moderate phenotype: growth delay, skeletal deformity, kyphosis, reduced BMD	VII
Lepre1/*Lepre1*	Knockout of *Lepre1* gene	Absence of P3H1 protein	Moderate phenotype: reduced body size, reduced BMD	VIII
Ppib/*Ppib*	Knockout of *Ppib* gene	Absence of PPIB protein	Severe phenotype: premature death, reduced body size, bone deformity, reduced BMD	IX
Sp7/*Sp7*	Knockout of *Sp7* gene	Absence of SP7 protein	Lethal phenotype: severe bone deformity, absence of bone mineralization	OI-like

Table 3. Murine model of dominant and recessive forms of Osteogenesis Imperfecta. Abbreviations: EDS Ehlers-Danlos syndrome, ENU, N-ethyl-N-nitrosourea; M-MuLV, Moloney murine leukemia virus[50].

The most used murine models for the dominant forms of OI are the *Brtl/+* mouse and the *Amish/+* mouse.

The Brtl/+ mouse model

This mouse was the first knock-in murine model developed for the study of non lethal OI and it was demonstrated to be a valid model of the disease [80].

In *Brtl/+* mouse, by gene targeting in embryonic stem cells (ES), a mutant allele carrying a G>T transvertion in the exon 23 of *Col1a1* gene was introduced under the control of the endogenous *Col1a1* promoter. The mutation is present in single copy in the genome and has a dominant transmission. The point mutation causes a G349C substitution in the α1(I), a defect previously described in a child affected by OI type IV. At birth, *Brtl/+* mice have size and weight similar to those of the normal littermates. 40-60 % of the mutant mice die within few hours after birth for respiratory distress, while the surviving pups show a 50 % reduction in size until 6 weeks of age, after which their size increases to about 80 % of the normal[80]. Mice have a general undermineralization of the skeleton, especially of the skull, deformed rib cage, long bones thinner than normal and bowed and flared thorax. *Brtl/+* mouse reflects the clinical course of the disorder during growth, with a drastic reduction of fracture frequency after puberty. The femurs of prepubertal 1-month-old and pubertal 2-month-old *Brtl*/+ mice have lower bone mineral density (BMD) than femurs from age-matched wild type mice, while at the postpubertal age of 6 months the BMD is comparable between mutant and WT mice. Similar results were obtained with microCT analysis, that showed reduced cortical thickness at 1 and 2 months of age in *Brtl*/+ mice, but similar to control at 6 months. Also mechanical tests showed an initial reduction of yield and maximum load, followed by an improvement in adulthood. Since no improvement in the geometrical organization of bone has been found, these observations suggested a strengthening mechanism at the level of extracellular matrix rather than an alteration in whole bone structural background[81].

Light microscopy analysis showed a thinner and poorly mineralized calvarium, disorganized and osteoporotic vertebral bodies and the presence of osteoid proliferation and tissue composed of fibroblasts rather than mature bone in nasal

turbinates. The pulp cavity of the teeth was necrotic and infected with bacteria, common features associated with dentinogenesis imperfecta[80].

Transcriptomic and proteomic analysis performed on skin and bone tissues of *Brtl*/+ mice with lethal or non-lethal outcome highlighted in both models retention of the mutated collagen at the level of the rER. But interestingly the ability to cope with cellular stress was different in mice with the same mutation and different outcomes. The data suggested that the intracellular stress, due to mutant collagen retention, could have a role in modulating the OI outcome[82,83].

The Amish/+ mouse model

The *Amish*/+ knock in mouse model for dominant non lethal OI was obtained by gene targeting in ES cells, as described above for the generation of the *Brtl*/+ mouse. A G>T transversion at nucleotide 2098 of *Col1a2* was introduced in the murine genome causing the substitution of the glycine 610 with a cysteine in the α2 chain of collagen type I[84]. This mutation reproduced the molecular defect first identified in a large pedigree of Old Order Amish affected by a moderately severe form of OI[84].

A reduced BMD hallmark for OI, was described in the *Amish*/+ mice further validating the mouse as model for the disease also from a phenotypic point of view[84]. Interestingly this mutation seemed to cause slightly different outcome depending on the genetic background of the mice. For example changing the mouse strain the growth curve of the Amish mice was different[84]. This is particularly relevant since it further supports the role of the genome in the phenotypic variability that is a feature described in OI patients and for which the mechanism is still under investigation.

Further studies of the mineral and matrix properties of the long bone of this mouse model revealed a reduced, thinner and more spaced secondary trabeculae. The vertebrae showed reduced bone volume, trabecular number and connectivity density[85].

One of the further characteristic of children affected by OI is their decreased exercise capacity and muscle strength but it is still not clear if this phenotype is correlated to the physical activity or to a muscle pathology. No gross muscle morphological differences and muscle functional alteration were reported in the *Amish/+* model[86].

Interestingly a similar study was performed on another OI model the *Oim/Oim*[87] mouse, carrying a mutation in homozygosis in the α2 chain of type I collagen. In the *Oim/Oim,* in contrast respect to the *Amish/+* findings, the relative muscle weight and function were compromised. Furthermore in *Amish/+* exercise on treadmill improved skeletal property without increment on the fracture number[86]. These observations suggested that the muscular phenotype in OI could be dependent on the mutation type and also the bone strength of OI patients can respond in a different way to the exercise stimuli[86].

Recently the intracellular retention of mutated collagen and the presence of cellular stress was demonstrated also in this mouse model, similarly to what described for the *Brtl/+* mouse, a modulating effect of intracellular pathways on OI phenotype [88]. Thus low protein (LP) diet was attended to reduce cellular stress by stimulating autophagic degradation of misfolded collagen. Unexpectedly the administration of this diet to 8 weeks old mice led to an increase of fragility in the bone[89]. As postulated the diet improved osteoblast differentiation and bone matrix mineralization but bone modeling and animal growth were compromised.

Despite this the increase in the mineralization process due to the diet suggested the possibility to use such approach as treatment to increase the bone quality in OI patients[89].

Osteogenesis Imperfecta therapy

Nowadays no definitive cure is available for OI patients and mainly palliative treatments aiming to ameliorate the patient's quality of life are available.

Physiotherapy approach

One of the main problems for the patients affected by OI is the achievement and maintenance of gross motor skills, thus physiotherapy may play a relevant role both in infant and in adult patients. The use of physiotherapy and hydrotherapy focused on muscle strength and joint range of motion are the most important contribution to improve the life of patients[22,90,91].

Orthopedic surgery

At the moment orthopedic surgery is the most used approach for the management of the disease. The correction of body deformity and the recurrent fractures are treated with osteotomy and the insertion of rods in the medullary canal of long bones[92].

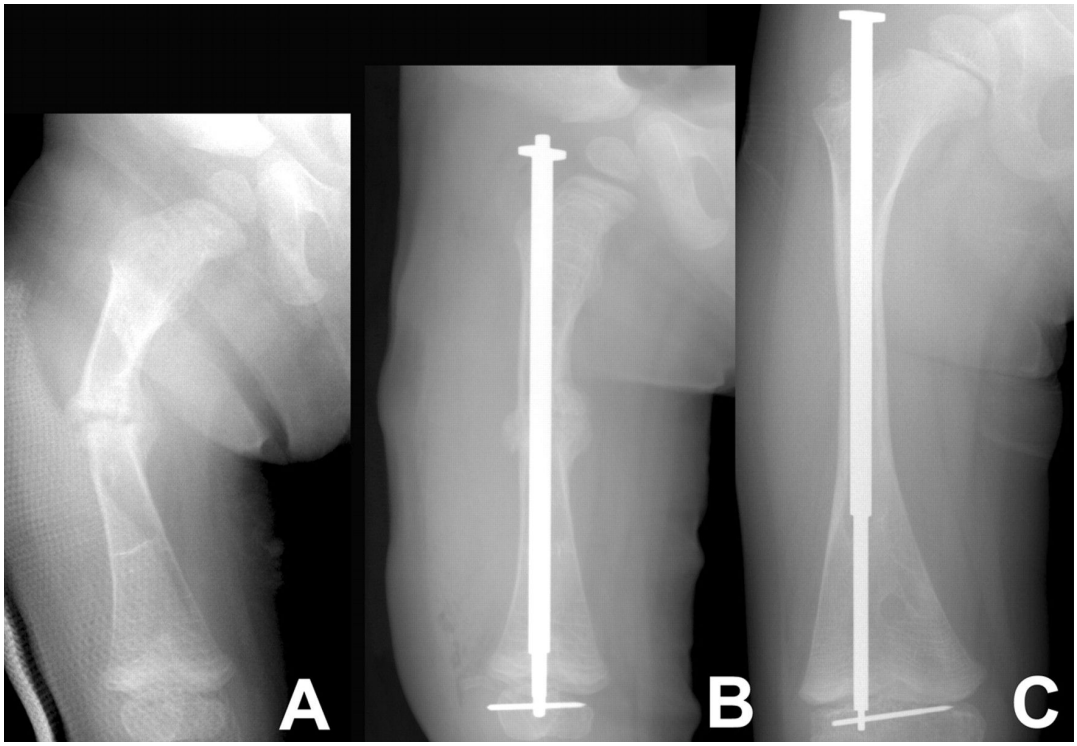

Figure 8. Radiographic follow up of a patient after telescopic rodding in intramedullary canal[93].

The use of this procedure is also useful to reduce the incidence of fractures and to avoid the bowing of the bone. Specific secondary interventions can be necessary for example for the treatment of scoliosis, to reduce spine curve, pain, and to improve respiratory function[94,95].

Pharmacological therapy

Pharmacological therapy in the last twenty years was mainly based on the use of bisphosphonates (BPs). Originally used for the treatment of late-onset osteoporosis bisphosphonates are analogues of the pyrophosphate that deposit on the bone surface.

BPs adsorption to mineral surface of the bone brings these molecules into close extracellular contact with osteoclasts (OC). OC are the only cells able to acidify the bone surface to release the BP molecules thus these cells appear to be the only cell type capable of internalizing substantial amounts of these dugs.

BPs accumulates intracellularly and acts by inhibiting osteoclast activity. Once the precursor or mature osteoclasts incorporate bisphosphonates by endocytosis, BPs can act trough different mechanisms based on their nature; typically they act as non-hydrolysable analogues of adenosine triphosphate, inducing OC apoptosis, or inhibit farnesyl pyrophosphate (FPP) synthase consequently disrupting subcellular localization of signaling proteins[96]. Thereby their function impaired cells viability and bone reabsorption is reduced[97]. The treatment with bisphosponate causes an increase in BMD, decreases bone turnover and ameliorates the vertebral geometry by counteracting the high turnover cellular status of bone (**Figure 9**)[98,99]. One of the problems related to this therapy is that even if there is an increase in the BMD, since the mutated collagen molecules remain, a decreasing in bone quality is present causing bone brittleness. Anyway the application of these drugs is still under evaluation because studies on humans and mice have raised concerns about the effect of high cumulative doses, on bone remodeling and healing**,** especially in pediatric age[100,101].

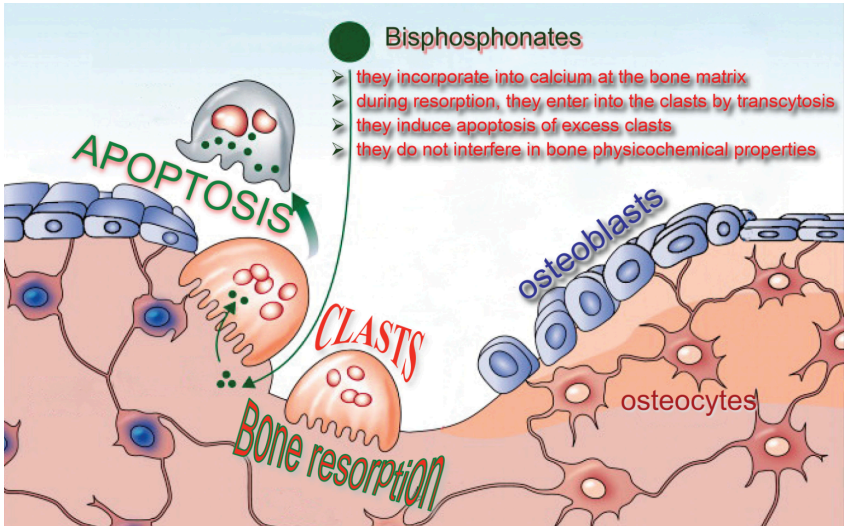

Figure 9. One of the mechanisms of action of bisphosphonates in controlling bone remodeling. Bisphosphonates are easily bounded to calcium and, as a result, incorporated by osteoclasts inducing their apoptosis[102].

The teriparatide (TPD) is another agent adopted for OI therapy, currently used for the treatment of osteoporosis and approved by the Food and Drug Administration (FDA). In postmenopausal women, this anabolic agent increases BMD and reduces vertebral and non-vertebral fractures by stimulating osteoblasts over osteoclasts function. Increased bone mass density was reported in mild OI, but no differences in the number of fractures were recorded[103].

A different pharmacological approach consists in the administration of recombinant human growth hormone (rGH). This treatment is based on the fact that rGH stimulates the collagen synthesis and longitudinal bone growth, especially when combined with bisphosphonates treatment[104]. It seems to be effective in OI patients with quantitative defects in collagen type I in increasing growth rate, bone turnover, bone formation, but no effect on fracture risk was reported[105].

Antibodies approach

Denosumab is a full-humanized antibody FDA-approved targeting the NF-kB ligand (RANKL), a stimulator of osteoclast formation secreted by osteoblasts and osteocytes. Inhibition of this pathway was proven to be effective in murine models increasing femur bone density, periosteal and endosteal diameters, cortical thickness and bone

stiffness **(Figure 10)**[106]. Clinical trials ongoing in children with a recessive OI type VI showed promising results[107].

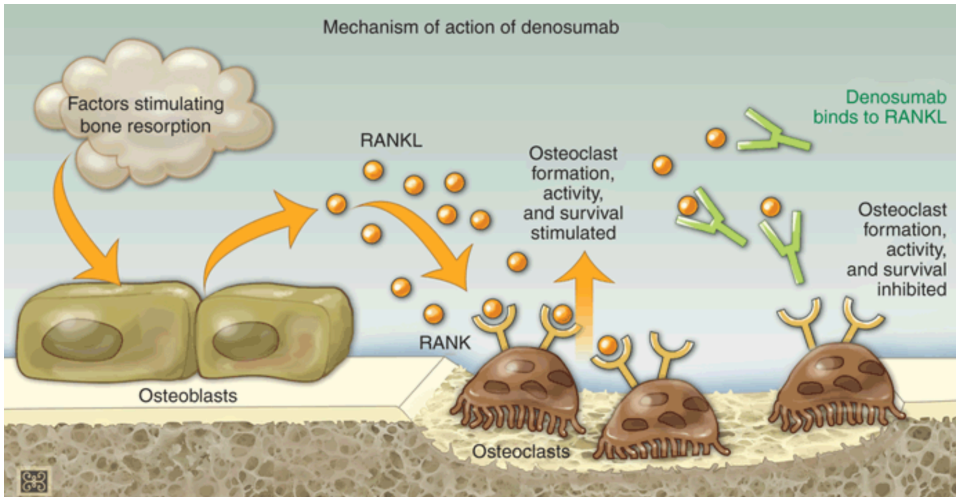

Figure 10. Mechanism of action of Denosumab.

The presence of Denosumab impairs the capability of RANK to bind its receptor on osteoclast thus their differentiation, activity and vitality are compromised[108].

Anti-sclerostin antibody (Scl-Ab) seems to be also a promising agent to treat OI patients. Sclerostin is a negative regulator of bone formation produced by osteocytes that acts inhibiting anabolic WNT signaling in osteoblasts. Sclerostin antibody therapy will have an anabolic effect on the skeleton by stimulating osteoblast via the canonical WNT signaling pathway[109]. The use of this antibody has been proven effective ameliorating the phenotype of an OI murine model[110].

TGF-β is a key coordinator of bone remodeling and the pathway in which is involved is one of major contributor to low bone mass in OI. Theoretically the inhibition of TGF-β will be capable of ameliorating the bone phenotype, thus antibody against TGF-β have been test and seems to be useful in the treatment of dominant and recessive OI in murine models[111]. A human clinical trial in phase I with the use of an antibody against the three isoforms of TGF- β is ongoing[112].

All the therapies described above improve OI patient's life quality but they do not cure the disease since they do not eliminate the genetic cause of the pathology. To be able to really treat the molecular defect in OI, a cell therapy or gene therapy should be developed. The aim of such approaches should either be to correct the genetic mutation or to reduce the amount of abnormal type I collagen produced and accumulated in bone matrix in order, at least, to mimic the milder form of OI.

Cell therapy

The rational behind the use of cell therapy is that in mosaic patients no clinical skeletal phenotype has been reported even in presence of a high number of mutant osteoblasts. Thus the introduction of normal cells in an OI patient will resemble this mosaicism status[113,114]. Cell therapy had been mainly focused on the use of mesenchymal stem cells (MSCs), the progenitor of many cells in the connective-tissue lineage, included osteoblasts[115]. Transplantation experiments in murine models using wild type MSCs showed a slight amelioration in bone matrix properties, even if the yield of engraftment was very low (around 2-5 %)[116,117]. The same results were also reported in OI children[118–120]. This treatment gave promising results but it is still necessary to improve the bone engraftment efficiency, clarify the long-term effects of transplantation and evaluate the best source of stem cells with higher osteoblast differentiation ability[121].

Gene therapy

The resolutive cure for dominant OI would be the correction of the DNA mutation, but for the more severe forms the silencing of the mutant allele may represent an interesting and probably more feasible option. The ability to suppress the mutant allele will convert a severe phenotype characterized by collagen structural defects, to a mild OI, associated to collagen insufficiency. Several attempts in this direction were made with different rate of success by using various antisense technologies such as antisense oligodeoxyribonucleotides (ODNs), ribozymes, short interfering RNA (siRNA) and short hairpin RNA (shRNA) (**Figure 11)**[122].

The majority of the published reports come from studies using either *in vitro* or *ex vivo* approaches, only few data are available from *in vivo* studies in OI murine models[123–126].

A silencing approach using allele specific shRNA has been recently used to efficiently suppress the mutant *Col1a1* allele in primary fibroblasts from the *Brtl*/+ mouse[127]. In this work the authors were able to specifically suppress the expression of the mutant allele (52 %) not affecting the expression of the normal one (14 %). The suppression of the gene led to the down-regulation of 40 % of the mutated protein without compromising cells proliferation[127]. The limiting factor of this strategy is the requirement of specific silencing molecules for the hundreds of different mutations known to cause dominant OI. To overcame this limitation, a mutation-independent approach in human bone derived cells using siRNA/shRNA targeting heterozygous single nucleotide polymorphisms (SNPs) in *COL1A2*[128] or insertion/ deletion polymorphisms (indels) in both the *COL1A1* and *COL1A2* genes[129] were attempted. The authors reported a 71 % reduction in *COL1A2* transcript when targeting SNPs, a 65-78 % reduction in *COL1A1* and 26-49 % *COL1A2* when indels were targeted.

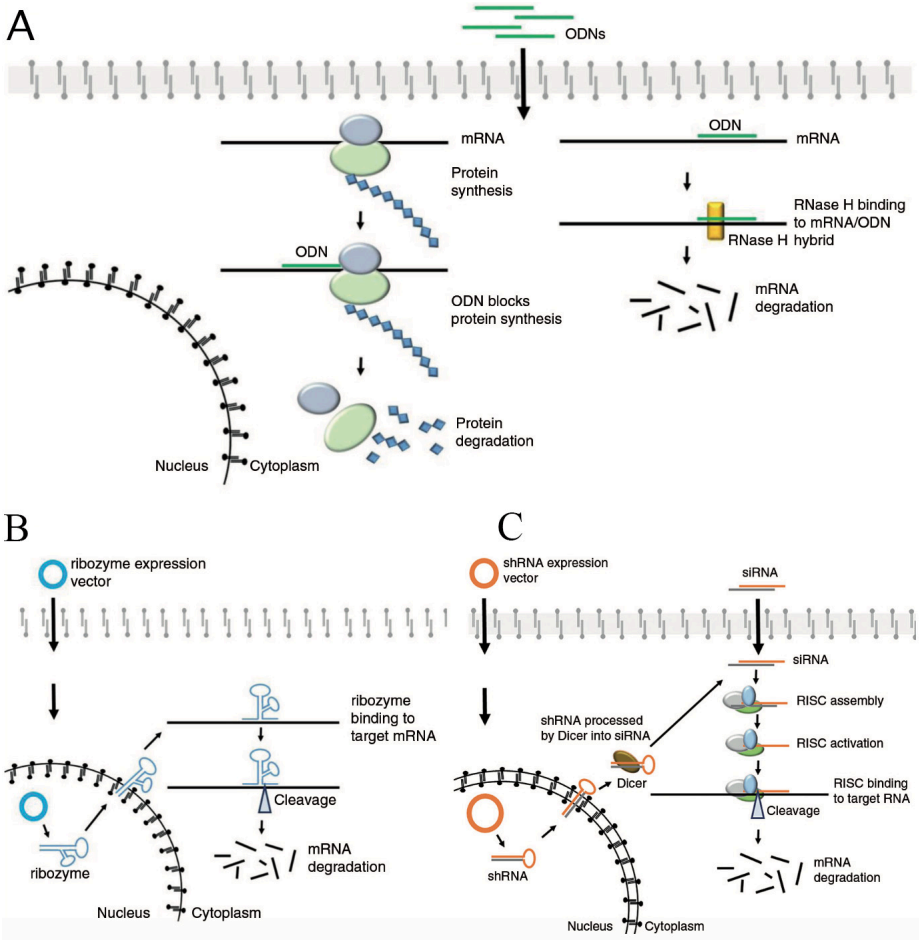

Figure 11. Gene therapy strategies to target mutant collagen transcripts.

A Antisense oligodeoxyribonucleotides (ODNs) able to hybridize their target RNA leading to its degradation through RNAase H or to directly inhibit protein translation. **B** Hammerhead ribozymes, synthetic RNA molecules containing a catalytic core and binding arms complementary to the mutant mRNA, specifically bind to the target mRNA leading to its degradation **C** Short interfering RNA (siRNA) can either be transfected into the target cells as synthetic double-stranded RNA (siRNA) or produced by plasmids coding for small hairpin RNA (shRNA) and stably incorporated into the endogenous genomic DNA. shRNA is processed by the cell's machinery leading to siRNA molecule. siRNAs are incorporated into the nuclease-containing multiprotein complex RISC (RNA-induced silencing complex) and one of the two siRNA strands, the guide strand, guides the RISC to its complementary target mRNA, which is then cleaved and degraded[130].

Effective targeting of the mutant gene in MSCs and in induced pluripotent stem cells (iPS) using OI patients cells had been also demonstrated[128,131,132] but how to transfer the correct cells *in vivo* is still an open question.

RNA interference (RNAi)

The concept of post-transcriptional regulation of gene expression by RNA-RNA interaction was introduced for the first time in the 1993 when in the *C. elegans* was found a small RNA transcribed by *lin-4* complementary to the transcript for *lin-14*[133], a gene encoding for a protein necessary for timing cell division.

Only after a couple of years the scientific society coined the term RNA interference (RNAi)[134], now used to delineate all the biological processes in which RNA molecules lead to the inhibition of gene expression. The concept was so important, and the consequences of the discovery so useful for the advancement in the research field, that Professor Andrew Z. Fire and Professor Craig C. Mello won the Nobel Prize in 2006 in physiology or medicine for their findings. Since then many discoveries were achieved regarding the RNAi mechanism of action.

The RNAi is driven by small non-codify double strand RNA (dsRNA) able to regulate chromatin structure, chromosome segregation, RNA transcription, processing stability and translation[135]. The RNAi is relevant not only in biogenesis of several tissue[136–138] but also in the development of several pathology, including cancer[139].

Three classes of RNAi have been recognized over the years: piwi-interacting RNAs (piRNAs), short interfering RNAs (siRNAs), and micro RNAs (miRNAs)[140].

The piRNAs are one of the most expressed small RNAs found in animals and they regulate germ line cells. In comparison to the members of the other two classes they are bigger in size (26-31 bp), their sequence is less conserved and their structure is more complex. The piRNAs act through the interaction with the piwi protein family and even if their precursor is still poorly understood it seems to be a single strand RNA on the contrary respect to the other two RNAi molecules[141].

The siRNAs derive from double strand RNA of 21-23 bp and their main role appears to be a defensive mechanism against foreign or invasive nucleic acids[142], but they are also known to be able to silence the gene from which they derive[143]. The miRNAs have size similar to siRNAs, but they differ in their role. The miRNAs are the regulator of the endogenous genes, and normally do not regulate the one from which they are synthetized[144].

Even though the synthesis of siRNAs and miRNAs is complex and in part different many are the common steps occurring in the cytoplasm of the cells.

One of them is the interaction with the Dicer complex. Dicer is responsible for the excision of both natural siRNA and miRNA from their precursors.

The Dicer enzyme is characterized by the presence of different domain: a DEXD/H ATPase domain, a DUF283 domain, a PAZ domain, two tandem RNase III domains, and a dsRNA-binding domain (dsRBD)[145].

The PAZ and RNase III domains occupy a central role in the cleavage of the double strand RNA. The PAZ specifically binds RNA duplex with short (2 bp) 3' overhangs. The dsRNA extends for approximately two helical turns along the surface of the protein and is cleaved by the two RNase III domains. Each active site is responsible for the cutting of one strand of the RNA molecule leading to the formation of a new end with 2 bp 3' overhangs[145,146].

After the double strand processing, through the Dicer enzyme, all the 20-30 bp RNAs enter in the RISC assembly pathway. This assembly process involves the unwinding of the double strand, probably mediated by an helicase, and the association of only one of the two strands with the Argonaute (Ago) protein[147,148] present in the RISC complex. The selection of the strand that enter in the complex is led by the thermodynamic stability of the two duplex ends, only the strand with the 5' end less stable base-pair, named guide strand, will be associate with the Ago protein. This association is possible thanks to the PAZ domain present in the Ago protein, shared with Dicer protein, that will bind with the 3' terminus of the RNA guide strand[147].

Finally both siRNAs and miRNAs single strand recognize the target sequence through a Watson-Crick base pair interaction[149].

Small interfering RNA (siRNA)

For what concern siRNA normally they derive from long linear perfectly base-paired dsRNA introduced directly in the cytoplasm or taken from the environment[142]. They are processed by Dicer, enter in the RISC complex and silence directly the RNA target as described above. Recently endogenous siRNA have been identified and in this case

a nuclear phase is obligate. The canonical pathway with which siRNAs lead to RNAi is the degradation of the RNA target.

siRNA binding to the Ago protein of the RISC leads to the localization of the complex in a subcellular foci called P bodies rich in mRNA degradation factors[150].

Once the complex has bound the RNA target the degradation is carried out through the PIWI domain of the Ago protein. The PIWI domain leads to the cleavage of the phosphodieter bond between the 10^{th} and 11^{th} nucleotide counting from the 5' end of the siRNA[147]. siRNA mismatches at, or near, the cleavage site lead to the suppression of the endonucleotic effect. Once cleaved the cellular exonucleases degrade completely the fragments.

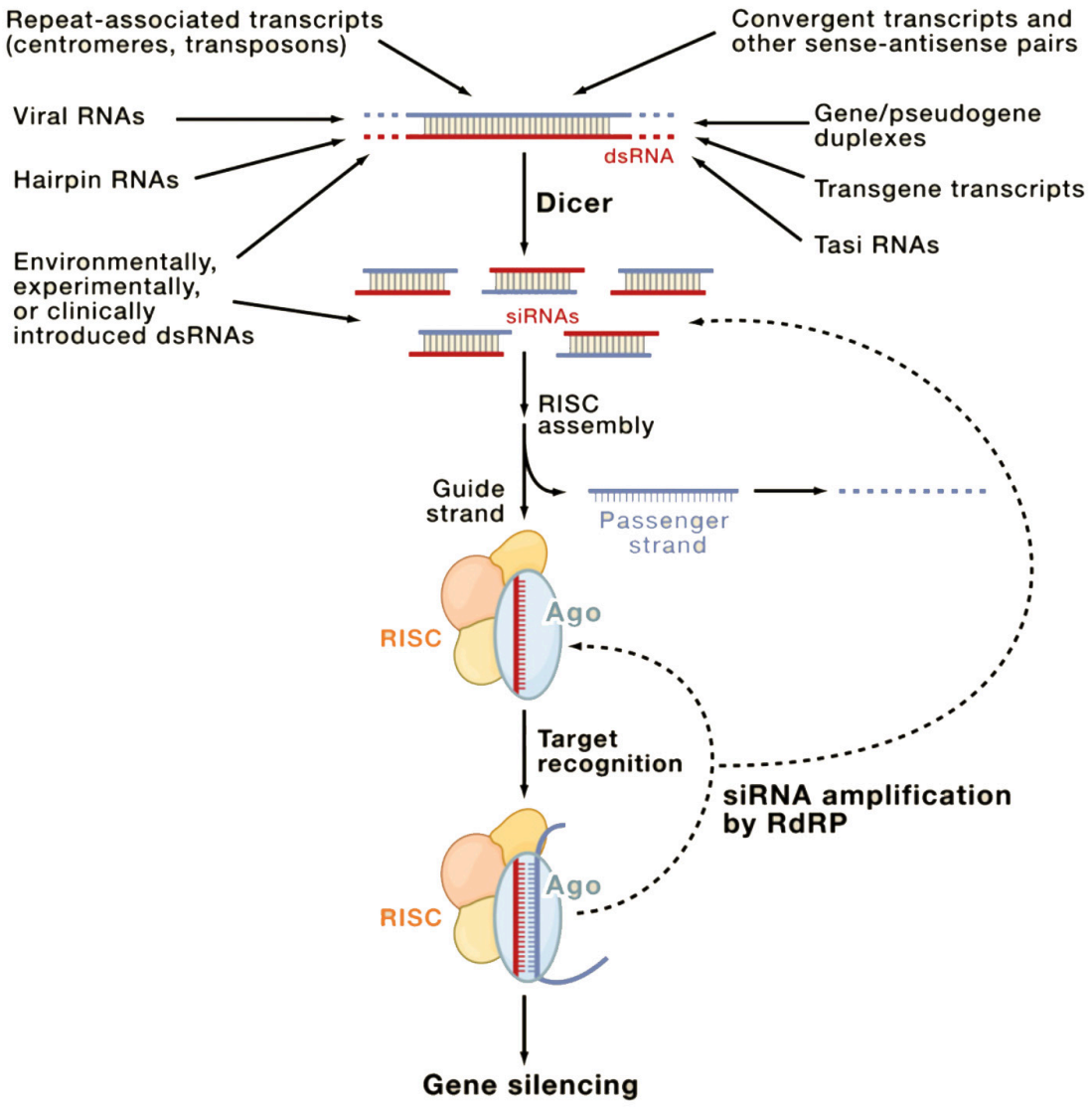

Figure 12. siRNA Sources and maturation.

Several different categories of transcripts can adopt dsRNA structures that can be processed by Dicer into siRNAs. A siRNA consists of a guide strand (red), which assembles into functional siRISC, and a passenger strand (blue), which is ejected and degraded. All forms of siRISC contain the siRNA bound to an Ago protein. Target RNAs are then recognized by base pairing leading to their cleavage[135].

Micro RNA (miRNA)

MicroRNAs are encoded by endogenous genes and are responsible for their regulation. Normally are produced by a single transcription unit that leads to the formation of more than one miRNA, but in some cases they can be individually produced. Their transcription is performed by RNA polymerase II and the product is 5' capped and 3' polyadenylated[151].

The resulting primary or pri-miRNAs needs to be processed and transformed in the functional miRNA. For this maturation is essential the formation of a stem-loop structure. In mammals this structure is typically formed by imperfectly paired stem of 33 bp with a terminal loop and a 5' and 3' flanking segments[144].

The next phase is carried out in the nucleus and leads to the formation of the pre-miRNA. The Drosha enzyme, an RNase III family member, catalyzes the process and, in mammal, its function is dependent on the cofactor DGCR8. This cofactor contains two dsRBD domains and is able to stably associates the pri-miRNA with the Drosha enzyme forming the processor complex[152]. Drosha use the stable link between the cofactor and the dsRNA as an anchor to position its catalytic site at the correct distance from the stem flank junction[151,153]. Once the complex has successfully bound the pri-miRNA the two flanking segments are cut and the pre-miRNA is formed. Pre-miRNAs is then exported by exportin-5/RAN GTP into the cytoplasm where Dicer cleaves the pre-miRNA near its stem–loop releasing the mature miRNA.

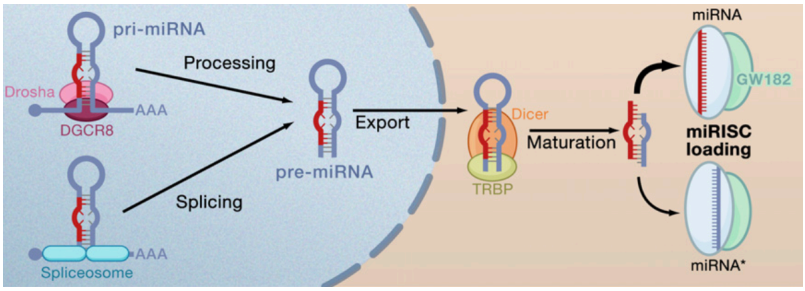

Figure 13. Biogenesis of miRNAs and their assembly into miRISC.

Transcription leads to capped and polyadenylated pri-miRNAs. In animals, Drosha processes the pri-miRNA with the aid of DGCR8 to generate a pre-miRNA. This is exported from the nucleus and processed by Dicer to form the mature miRNA/miRNA* duplex. After processing, miRNAs are assembled into miRISC. Only one strand of the duplex is stably associated with a miRISC complex, * is used to indicate the guide miRNA[135].

Differently from the siRNA, the miRISC complex can lead to gene silencing not only through the cleavage of the mRNA target, but using several different mechanisms. Most miRNAs present some mismatches with their mRNA target, but the core region is composed by the recognition of at least 2-8 bp. If the miRNAs have a perfect complementary interaction with its target the Ago protein is stimulated to cleave the mRNA strand[154], otherwise if mismatches are present in the central region the miRISC leads to the repression of mRNA translation. On this topic several issues are still unsolved and the debate of whether repression occurs at translation initiation or after that is not fully understood. Several studies were performed to solve the question, but the inconsistent results led to believe that both mechanisms are possible. Some studies show that the miRISC complex represses the elongation trough the premature dissociation of the ribosome from the mRNAs[155]. For what concern the repression of the initiation of the translation at the moment three different models are proposed.

As known the translation begins with the recognition of the mRNA 5' terminal cap by the eIF4E complex that recruits the 40S ribosomal subunit. The 40s subunit in turn recruits the 60s ribosomal subunit at the AUG codon and the translation can start. Moreover the eIF4G can interact with the polyA-binding protein (PABP1) that is present at the 3' term of the mRNA circularizing it. This possibility enhances strongly the translational process.

One of the model suggest to explain the repression of the translation initiation process is the competition between the miRISC and the eIF4E for the mRNA 5' terminus[156,157]. A second model hypothesizes the stimulation by the miRISC complex of the deadenylatation of the mRNA tail. In this model the initiation is repressed because without its intact tail the mRNA is unable to circularize[158,159]. The last model proposes the miRISC as a blocking mechanism for the binding of the 60S ribosomal subunit[160]. The Ago protein of the RISC complex is able to recruit the eIF6. eIF6 protein is involved in the maturation and biogenesis of the 60S ribosomal subunit so the association between Ago protein and eIF6 will lead to a depletion of 60S subunit from the start codon[160].

Moreover some studies suggest that the miRNAs are able to decrease the mRNAs translation process not only through the mRNA destabilization via the mechanism

described above but also incrementing the mRNA degradation[158,159]. Even if the mechanisms is not well defined this process require the interaction with Ago protein and the decapping and deadenylation of the mRNA through the cellular machinery[159].

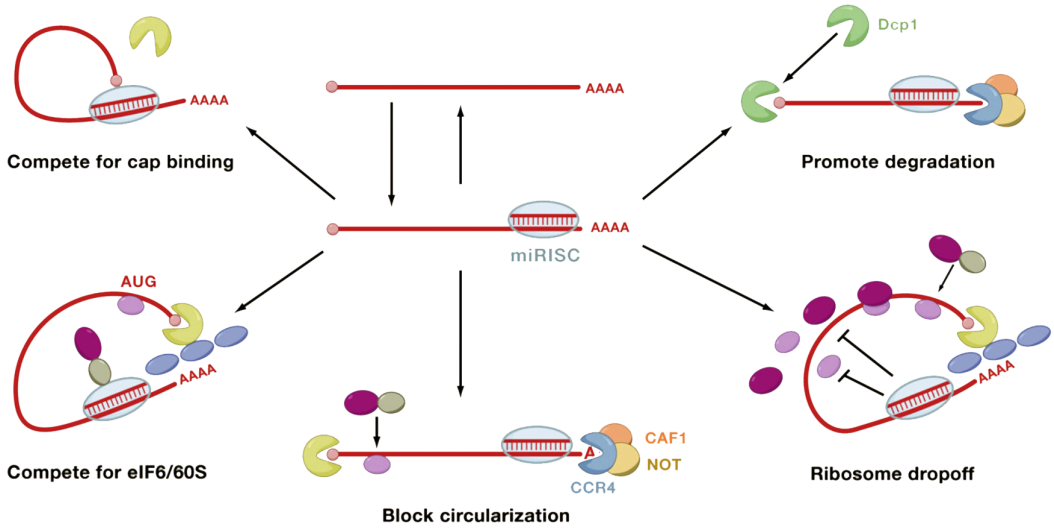

Figure 14. Possible Mechanisms of miRISC-Mediated Repression.

When miRISCs bind to mRNAs, they can repress initiation at the cap recognition stage (upper left) or the 60S recruitment stage (lower left). Alternatively, they can induce deadenylation of the mRNA and thereby inhibit circularization of the mRNA (bottom). They can also repress a post-initiation stage of translation by inducing ribosomes to drop off prematurely (lower right). Finally, they can promote mRNA degradation by inducing deadenylation followed by decapping[135].

RNAi based therapeutic approach

The RNAi in gene therapy using siRNA and shRNA has been largely explored to suppress the expression of mutant causative alleles in several diseases.

Small interfering RNA (siRNA)

siRNAs specific for a particular gene of interest can be easily design and chemically synthesized at low cost. The siRNAs delivery into the cells can be quickly achieved and once in the cells they are able to directly interact with the endogenous *RNA-interfering silencing complex* (RISC) thus favoring a rapid degradation of the target mRNA **(Figure 15)**.

Short hairpin RNA (shRNA)

The shRNA are 19-22 bp long RNA molecules with a hairpin structure composed by 4-11 nucleotide[161]. Similarly to the siRNA the shRNA function is to down-regulate the expression of a specific gene by complementary binding to the mRNA target. The shRNAs take advantage of the cellular machinery to generate pre-miRNA formation and lead to gene suppression, as a normal miRNA would do. The main difference is that shRNAs are introduced in the cell via vectors as plasmid or virus often integrated into the host genome and opportunely transcribed by the cellular machinery. Once they have been transcribed they enter in the cellular maturation process typical for the pri-miRNA synthetized by the cells **(Figure 15)**.

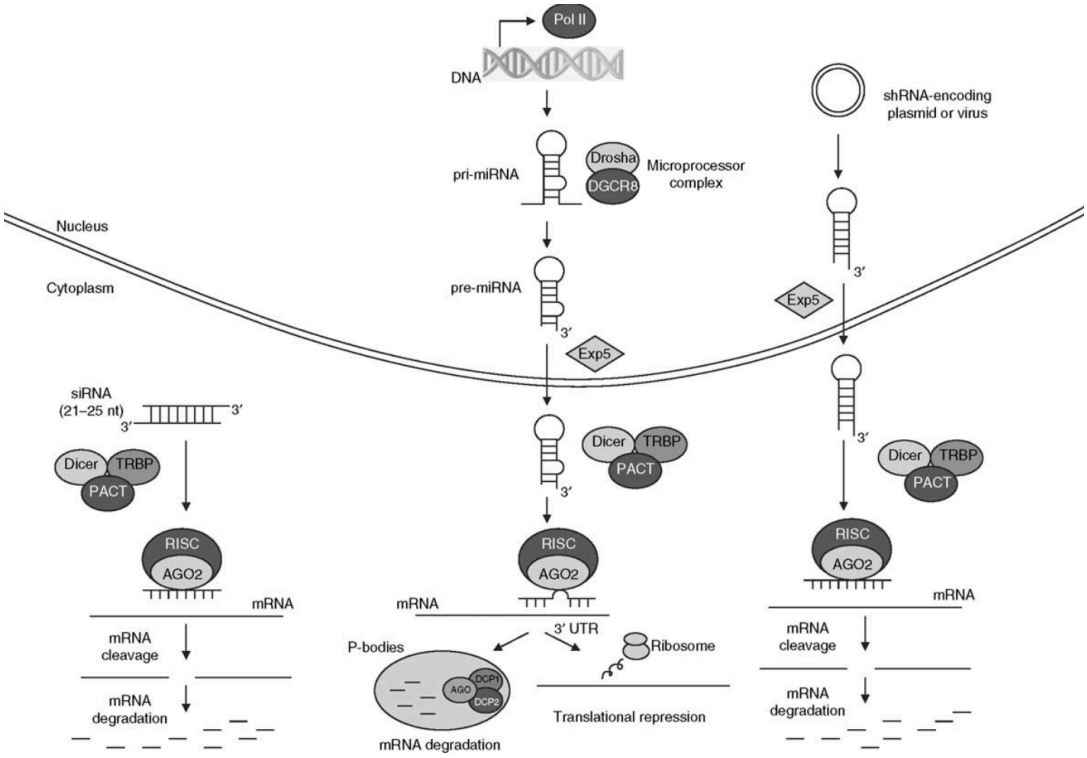

Figure 15. Model for post-transcriptional suppression of siRNAs and shRNAs.

Dicer processes long pri-miRNA molecules into small interfering RNA duplexes. The mature siRNA assembled into the RNA-induced silencing complex (RISC), which subsequently acts on its target by translational repression or mRNA cleavage, depending, at least in part, on the level of complementarity between the small RNA and its target. The picture shows both the mechanism of siRNA and shRNA once they are inside the cell[162].

Several antisense technologies can be used to suppress the gene expression. One of the main advantages in the use of siRNAs and shRNAs instead of ribozymes or ODNs is their higher stability once they enter in the cytoplasm. In fact double strand RNA is less prone to be degraded by the nucleases[163]. Their stability leads to a higher efficiency in the silencing in respect to others antisense technologies[164].

siRNA and shRNA mechanism of action

To suppress gene expression, both small interfering RNA (siRNA) and short hairpin RNA (shRNA) can be adopted. But even if they have similar function their different origin leads to different off-target effects and thus possible different applications. siRNA due to their small nature and processing are really fast in their effect[161], they reach the nucleus in only 15 minutes after transfection and disseminate in the cytoplasm within the following 4h[165]. Among the disadvantages, due to their RNA

nature, they have a rather fast turnover and only 1 % of the siRNAs is present in the cells after 48h[166–168]. On the contrary shRNAs have to be synthetize through the cells machinery and one single copy can give rise to a lot of functioning shRNA thus the effect will last more.

It has been demonstrated that for shRNA 5 copies are sufficient to reach a stable knockdown effect[161,169,170] while to obtain a strong down regulation with siRNA a nM concentration need to be used.

Even if the siRNAs are less effective in comparison to the shRNAs their nature allows a faster and cheaper synthesis and modifications can be done in relatively easy way in comparison to the shRNAs to allow their localization[161].

In conclusion the choice between the use of siRNAs or shRNAs have to be made depending on the goal of the study. siRNAs, thanks to their easy manufacturing and transient nature effect, are more suitable for medical disorders such as viral infection or proof of principle studies. shRNAs, due to their high and sustainable effect and the low dose necessary, are more indicated for long term treatments. This is implemented thanks to the fact that shRNAs may be integrated in the genome[163].

Despite its promising feature the use of synthetic siRNAs or shRNAs delivery bring many challenges. For instance one of the main concern with this technology is their short half-life, the high dosage require for the *in vivo* experiment, cell type dependent transfection efficiency the difficulty to reach the tissue of interest and the cytotoxicity associated with the transfection[171,172].

In the last years the improved knowledge on delivery systems allowed a higher knock down of the target genes using these technologies with lower toxicity effect *in vivo* leading to very promising outcome for the therapeutic use of these molecules. Different conditions ranging from Hepatitis C virus[173], Transthyretin Amyloidosis[174] to Glaucoma[175] have been addressed with success in patients.

RNAi-based lead NCs under clinical trials (as in September 2015: https://clinicaltrials.gov/)						
Products	**RNAi m.**	**Company**	**Condition**	**Phase**	**Stage**	**Trial number**
SPC 3649 (locked nucleic and lna-miR122)	miRNA	Santaris	Hepatitis C virus	II	Complete	NCT 01200420
ALN-TTR02 (SNALP) Patisiran	siRNA	Alnylan	Transthyretin (TTR)-mediated amyloidosis	III	Recruiting	NCT 01960348
ALN-TTRsc (galNAc-conjugated siRNA) Revusiran	siRNA	Alnylan	TTR mediate Familial Amyloidotic Cardiomyopathy	III	Recruiting	NCT 02319005
ND L02-s0201	siRNA	Nitto Denko Corporation	Extensive hepatic fibrosis	Ib/II	Active	NCT 02227459
Atu027 (PKN3)	siRNA	Silence therapeutics	Advanced or metastatic pancreatic adenocarcinoma	I/II	Active	NCT 01808638
DCR-MYC (LPN)	siRNA	Dicerna pharmaceuticals	Hepatocellular carcinoma	Ib/II	Recruiting	NCT 02314052
ALNPCS02 (SNALP)	siRNA	Alnylan	Hypercholesteremia therapy	I (i.v.)	Complete	NCT 01437059
				i (s.c.)	Complete	NCT 02314442
ALN-VSP02 (SNALP)	siRNA	Alnylan	Solid tumor with liver metastasis	I	Complete	NCT 00882180
TKM-080301 (TKM-PLK1) (SNALP)	siRNA	Takmira	Solid tumo with liver metstasis	I	Complete	NCT 01437007
			Neuroendocrin and Adrenocortical tumor	I/II	Complete	NCT01262235
			Hepatocellular carcinoma, Hepatoma	I/II	Active	NCT 02191878

Table 4 State of clinical trials of different RNAi therapeutics[176].

Delivery systems

One of the most critical factors in the delivery of siRNAs and shRNAs is the fact that they are strongly negative charged molecules, thus they generally cannot cross the membrane by simple diffusion as many small molecules do[177], furthermore their endocytosis and lysosomes degradation[178,179] can compromise their therapeutic activity. shRNAs can also lead to cellular toxicity due to the perturbation of miRNA pathway in a dose dependent manner[180].

For what concern the systemic barrier faced in the *in vivo* delivery many are the problems that need to be overcome. In their naked form siRNA and shRNA are easily degraded by endonuclease[181], furthermore some tissue, can be poorly vascularized and with a dense matrix that could compromise the delivery, for example bone. Moreover the delivery system used to carry the dsRNA to the cell target could stimulate immune response[182,183].

To overcome as much as possible these limitation new RNAi delivery systems specific for the specific target cells, tissues or organs of interest are and will still need to be developed.

Viral delivery methods

Viral vectors that allow achieving high transfection efficiency represent one of most used delivery system. This kind of delivery was use in chronic disease such as neurodegenerative disorder, cancer, heart failure and HIV infection. This method was used, with success, both *in vitro* and *in vivo* to down-regulate gene expression[162].

Moreover, depending on the type of viruses used, the viral system can provide a transient or long-term expression of the RNAi molecules. In the majority of the case the most used are the adeno-associate virus. They allow to introduce transiently the DNA or RNA codifying for the shRNA avoiding exogenous modification of the host genome[184].

On the other hand the use of retrovirus, by ensuring a stable integration of the exogenous DNA codifying for the shRNA in the host genome, will lead to a stable down-regulation of the gene of interest.

But, if from a point of view their nature seems to be an advantage, more and more concern have been raised on their actual safety[185,186]. Difficulty in controlling the timing and dose, and the potential inflammatory and immunogenic effect have furthermore limited their use[187–190].

Non-viral delivery methods

Since stable integrated viral vectors may be dangerous due to their random integration in the endogenous genome non-viral systems have taken a major role in the gene therapy development. Typically these vehicles are cationic preparations able to complex the RNAi molecules, thanks to their positive charge and the ability to bind on the external cell membranes. There are several classes of different promising vectors based on peptides, polymers, and cationic lipids.

Peptide

One of the first non-viral methods used is based on cell-penetrating peptides (CPPs). CPPs are a class of short amino acid able to penetrate the plasma membrane[191].

This ability is due to the high presence of positive charged amino acids and to their amphipathic nature that allow these molecules to interact with the negative charged head of the plasma membrane and to enter in the cells through a receptor and energy independent mechanism[172]. These molecules are known to be able to efficiently and rapidly enter in the cytoplasm[192].

Hydrophilic cationic peptides penetrate in the cells thanks to transient pore that close really quickly after the peptides have cross the plasma membrane. Amphiphilic CPPs enter in the cells because they insert into the lipid bilayer and cross the cell membrane by the formation of lipid raft or transient channel. Some amphiphilic peptides enter in the cells trough endocytosis[191]. A plethora of molecules have been delivered intracellularly thanks to their association with CPPs[193] and siRNA is one of them.

If CPPs enter through the endocytosis pathways the siRNA will need to be transfer to the cytoplasm to perform its action, whereas if CPPs create punched holes siRNA will be already in the correct cellular compartment to be effective[191].

Moreover siRNA can be transported both through covalent and non covalent complex with CPPs, but the use of non covalent methods have several advantage such as the absence of chemical modification of the siRNA and the simplification of the purification process[194].

Polymers

Another transfection agent is represented by the use of linear or branched cationic polymers (polyplex).

The RNA molecules interact with the polyplex thanks to the positive charges on the polyplex that protects the RNA molecule from the nuclease enzyme present in plasma[195]. The properties of this compound can be modified depending on different factor for instance the ratio between the positive charges of the polyplex compound

and the negative groups of the siRNA can alter the size, surface charge, and structure of the compound[196]. Moreover more branched structure seems to have an higher transfection efficiency while an higher molecular weight correlate with a greater toxicity[196].

A high number of polymers have been investigated and the more common used are the poly-ethyleneimine (PEI) and the poly-D,L-lactide-co-glycolide (PLGA).

The most investigated both *in vivo* and *in vitro* for siRNAs delivery is the PEI[197]. These particles give also the advantage to be modifiable to stabilize the nanoparticle for systemic injection. In fact they can be conjugated with polyethylene glycol (PEG)[198]. The conjugation implements the stability of the siRNA in serum and allows the functionalization of the particle with a ligand that can lead the transfection toward a specific target[199,200].

PLGA is important for its biodegradable and biocompatible property known from decades and used for pharmaceutical applications[201]. Also in this case modifications to the polymer composition can be done. For example to implement the cellular uptake of the carriers PLGA was coated with chitosan[202].

Liposomes

Due to their well-known nature, simplicity, biocompatibility and biodegradability liposomes are the most used approach to deliver both *in vitro* and *in vivo* siRNAs and shRNAs inside the cells[196].

Liposomes are spherical vesicles of at least one lipid bilayer that were described for the first time by Bangham et al in the 1964[203]. The combination of a lipid outer surface and aqueous core allows targeting and stability requirements to be decoupled from drug loading. The aqueous core can be loaded with different types of drugs, DNAs, siRNAs, and/or contrast agents[204]. Even though neutral liposomes have been successfully used to deliver siRNAs *in vitro* and *in vivo*[205], cationic lipids are the most used lipid-based siRNAs delivery systems. Three different parts compose the cationic lipids: the cationic head group, the carbon chain length of the tail group, and a linker. This last component guarantees the possibility to modify their surface with molecules of interest

to target specific cells.

The use of these vehicles opened a new era in the cell specific targeting strategy especially for tissues, such as bone, really difficult to be reached by systemic delivery.

Among liposome particularly promising for bone delivery seems to be the recently developed liposome synthetized by the group of Prof Xhang at the Hong Kong University[206]. The cationic liposomes were specifically linked to a small peptide $(AspSerSer)_6$ or $(DSS)_6$ able to bind randomly orientated crystals of hydroxyapatite rather then more mature elongated ones[207]. The ability of such liposomes to be directed toward osteoblast-mediated mineralizing nodules and amorphous calcium phosphate was demonstrated both *in vitro* and *in vivo*[206,207]. Thus this system is particularly promising since it will facilitate the delivery of siRNAs to the osteogenic-lineage cells present in the bone-formatting surface establishing the foundation for the use of siRNAs in clinical application.

AIM OF THE WORK

Classical Osteogenesis Imperfecta (OI) is a rare brittle bone disease caused mainly by dominant mutations in the *COL1A1* or *COL1A2* genes encoding for the two α chains of collagen type I. A large number of different mutations have been identified along the collagen chains; the majority of them represented by glycine substitution impairing collagen triple helix folding. Patients affected by OI are characterized by bone deformity, frequent fractures and growth delay.

No definitive treatment is so far available for OI and the therapeutic options, based either on surgical interventions or drug administration, are for the most focused on ameliorating patient's life quality. Since OI is a genetic disorder, only a gene therapy approach, aimed to correct or suppress the expression of the mutant allele, could be effective to cure patients.

The main purpose of my PhD project was to develop a new gene therapy treatment for classical Osteogenesis Imperfecta.

In particular, I focused my attention on the OI forms caused by mutations in the *COL1A2* gene. It is known that in absence of α2(I) chain, a collagen $\alpha 1(I)_3$ homotrimer is synthesized and that patients carrying null *COL1A2* alleles are affected by a specific form of Enhler Danlos Syndrome (EDS), characterized by vascular defect but without bone phenotype. Based on this observation, the total suppression of *COL1A2* expression only in the bone tissue should rescue the main phenotypic outcome of OI patients. This strategy will also have the advantage to be mutation independent, since it allows the treatment of many patients carrying different molecular defects with a single silencing molecule.

Thus a silencing approach using a specific siRNA able to target both mutant and wild type *COL1A2* alleles has been developed.

Murine cells and mice were used to test this strategy both *in vitro* and *in vivo*.

The specific aims of my project were the following:

- to identify by *in silico* analysis potential siRNAs specific for the murine *Col1a2* transcript;
- to test *in vitro* the efficiency and specificity of the selected siRNAs in primary murine embryonic fibroblasts and osteoblasts;
- to demonstrate *in vivo* the efficiency and specificity of the siRNA found to be the most effective by the *in vitro* analysis;
- to identify a siRNA bone specific delivery system.

RESULTS

Design of siRNAs targeting the *Col1a2* gene and analysis of their efficiency and specificity *in vitro*

Three siRNAs targeting the murine *Col1a2* gene, encoding for the α2 chain of collagen type I, were selected *in silico* as described in the material and method section and their efficiency was evaluated on primary murine embryonic fibroblasts (MEFs). Since the *Col1a2* gene is highly repetitive and rich in GC in the region coding for the triple helix domain, the siRNAs target sites were chosen at the 3'-end, encoding for the C-propeptide domain. To evaluate the siRNAs ability to suppress the expression of *Col1a2,* primary MEFs were isolated from E13.5-14.5 embryos and used for transfection experiments. A cell density of 1×10^4 in 24 well plate was used and two different siRNA concentrations were tested, 10 nM and 50 nM. RNA was extracted 48 hours after the transfection. qPCR analysis showed that the siRNA-3554 and the siRNA-3825 were particularly efficient, siRNA-3554 suppressed 92 % of the *Col1a2* expression at 10 nM and 86.3 % at 50 nM, siRNA-3825 63 % and 81 % at 10 and 50 nM respectively **(Figure 16 A)**. On the contrary siRNA-4215 did not significantly change *Col1a2* expression (26 % at 10 nM and 49 % at 50 nM), also siRNA-LacZ (negative control) didn't affect *Col1a2* expression, as predicted.

To evaluate the temporal efficiency of the 2 most effective siRNAs a time course experiment was performed using siRNA-3554 and siRNA-3825. MEFs were transfected using two different cell densities, 1×10^4 and 2×10^4 and two different siRNAs concentrations, 10 and 50 nM. The RNA was collected at 24, 48 and 72 hours after the transfection. Using the lowest cell density (1×10^4 cells/well) and 10 nM of siRNA, after 24 hours both siRNAs suppressed about 85 % of the *Col1a2* expression. 48 hours after the transfection the siRNA-3554 caused a *Col1a2* down-regulation of 85 % while siRNA-3825 of 75 % and 72 hours post transfection both siRNAs suppressed the gene expression of 78 % **(Figure 16 B)**.

The use of the higher siRNAs concentration at the lowest cell density increased the *Col1a2* suppression, 24 hours post transfection both siRNA caused 84 % *Col1a2* down

regulation, 48 hours post transfection 91 % and 72 hours post transfection 86 % for siRNA-3554 and 83 % for siRNA-3825. But this siRNAs concentration compromised the cell health. A large number of cells were detaching from the well and indeed the amount of RNA extracted from each well was very low.

At the highest cell density tested (2×10^4 cells/well) only the 50 nM siRNAs concentration showed good efficiency for both siRNA molecules tested. At 10 nM after 24 hours siRNA-3554 suppressed about 66 % of the *Col1a2* expression while siRNA-3825 65 %. 48 hours after the transfection the siRNA-3554 caused a *Col1a2* down-regulation of 70 % while siRNA-3825 of the 73 % and 72 hours post transfection both siRNA suppressed the gene expression of 71 % for siRNA-3554 and of 64 % for siRNA-3825.

Using the higher siRNAs concentration (50 nM) an increased suppression was obtained at all time points analyzed. At 24 hours post transfection siRNA-3554 caused 72 % of *Col1a2* down regulation while siRNA-3825 80 %, 48 h post transfection a 83 % and 85 % suppression obtained for siRNA-3554 and siRNA-3825 respectively and 72 h post transfection a suppression of 78 % for siRNA-3554 and 83 % for siRNA-3825 achieved **(Figure 16 C)**.

Since again high cell death was detected when 50 nM siRNA was used, all the following experiments were performed using 10 nM siRNA and 1×10^4 cell density.

The siRNA-3554 was selected for all the other experiments given its higher efficacy at the 10 nM concentration.

The genes encoding for the α chains of type I collagen, *Col1a1* and *Col1a2*, share high similarity and thus the specificity of the siRNA-3554 against *Col1a2* was tested. 48 hours post transfection RNA was extracted and qPCR was performed to evaluate the expression level of both *Col1a1* and *Col1a2* genes. The siRNA-3554 suppressed 81 % of *Col1a2* expression leaving the *Col1a1* expression unchanged **(Figure 16 D).**

Since to monitor siRNA *in vivo,* a siRNA-3554 labeled with the FAM fluorochrome was planned to be used, the efficiency and specificity of the FAM labeled siRNA-3554 was also tested in order to determine possible negative effect of the labeling. The FAM siRNA-3554 revealed 89 % *Col1a2* down regulation leaving the *Col1a1* expression unchanged **(Figure 16 D)**. siRNA-LacZ and FAM siRNA-LucF (negative controls) didn't affect *Col1a*2 expression as predicted.

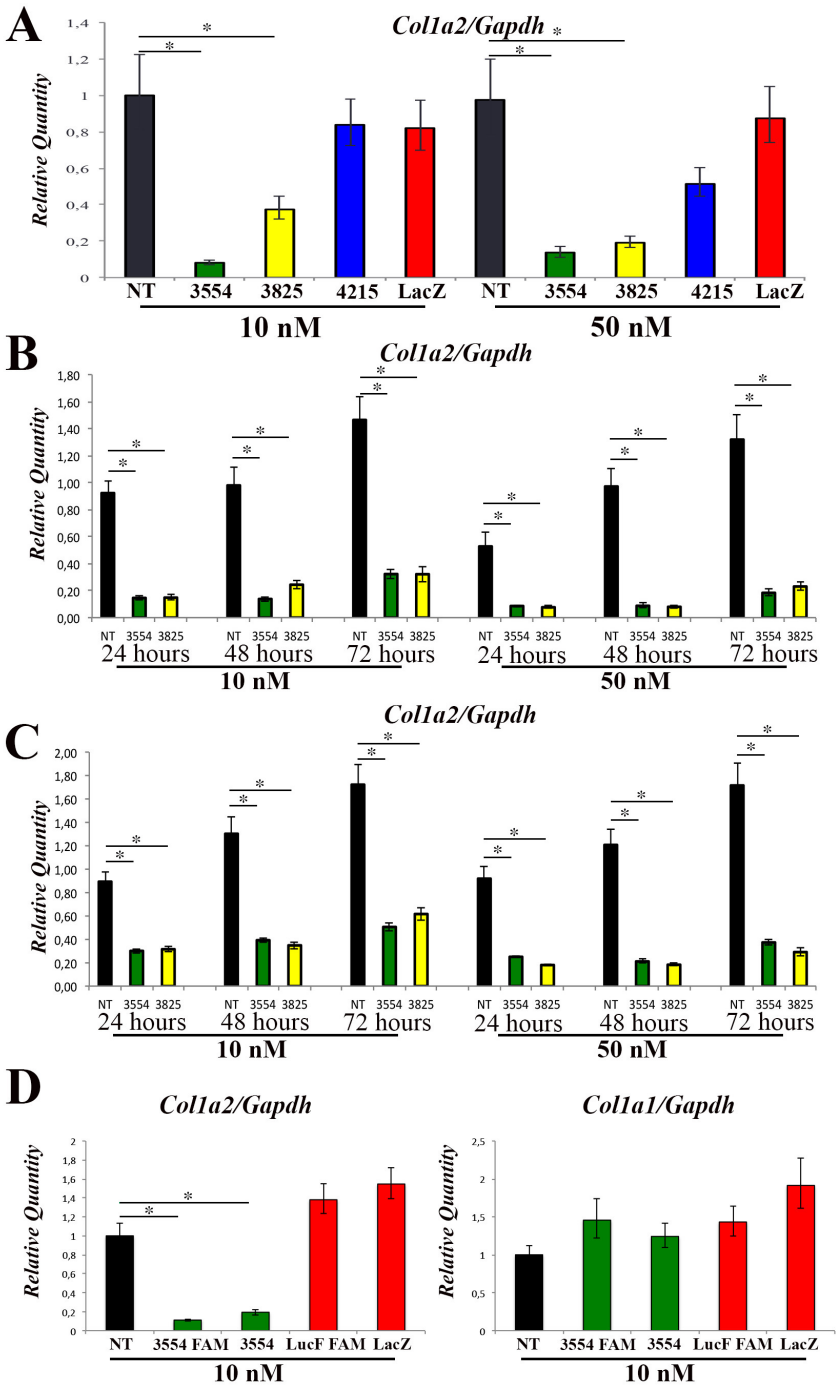

Figure 16. *Col1a2* and *Col1a1* qPCR analysis to evaluate siRNAs efficiency and specificity in transfected MEF cells. A *Col1a2* qPCR revealed a strong gene suppression upon MEFs transfection using siRNA-3554 and siRNA-3825, the siRNA-4215 minimally affect *Col1a2* expression; **B** *Col1a2* qPCR showed siRNA-3554 and siRNA-3285 efficiency plating 1×10^4 cell/well at all tested time points: 24, 48 and 72 hours after transfection and at both siRNAs concentrations used, 10 and 50 nM. A better suppression was evident at the higher siRNAs concentration used; **C** *Col1a2* qPCR showed siRNA-3554 and siRNA-3285 efficiency plating 2×10^4 cell/well at all tested time points: 24, 48 and 72 hours after transfection. A better suppression was evident at the higher siRNAs concentration used; **D** *Col1a1* and *Col1a2* qPCR revealed siRNA-3554 specificity against *Col1a2* expression. A strong down-regulation of *Col1a2* expression upon siRNA-3554 and FAM siRNA-3554 transfection was evident in presence of unchanged *Col1a1* expression level. All the values are expressed as mean±sd. NT= Not Transfected, LacZ and LucF FAM= siRNA negative controls. * p value < 0.05.

siRNA-3554 effect on the α2(I) chain expression

To assess if the suppression of the *Col1a2* gene determined by siRNA-3554 leads to the α2 chain down-regulation, 48 hours after the transfection the collagen was labelled *in vitro* by incubating the MEFs in presence of tritiated proline. Since collagen is particularly rich in this amino acid the amount of 3H-Pro incorporated is sufficient for its detection following purification from medium and cell layer fractions. The SDS-PAGE analysis of the pepsin labeled purified collagen from both medium and cell layer demonstrated a strong reduction of the α2 chain of collagen type I in cells transfected with the siRNA-3554 **(Figure 17 A)**.

The densitometric analysis of the α1 and α2 bands intensity revealed that both in medium and cell layer the ratio between α1 and α2 chains was about 10:1 compared to 2:1 in cells not transfected or transfected with the siRNA-LacZ negative control **(Figure 17 B)**.

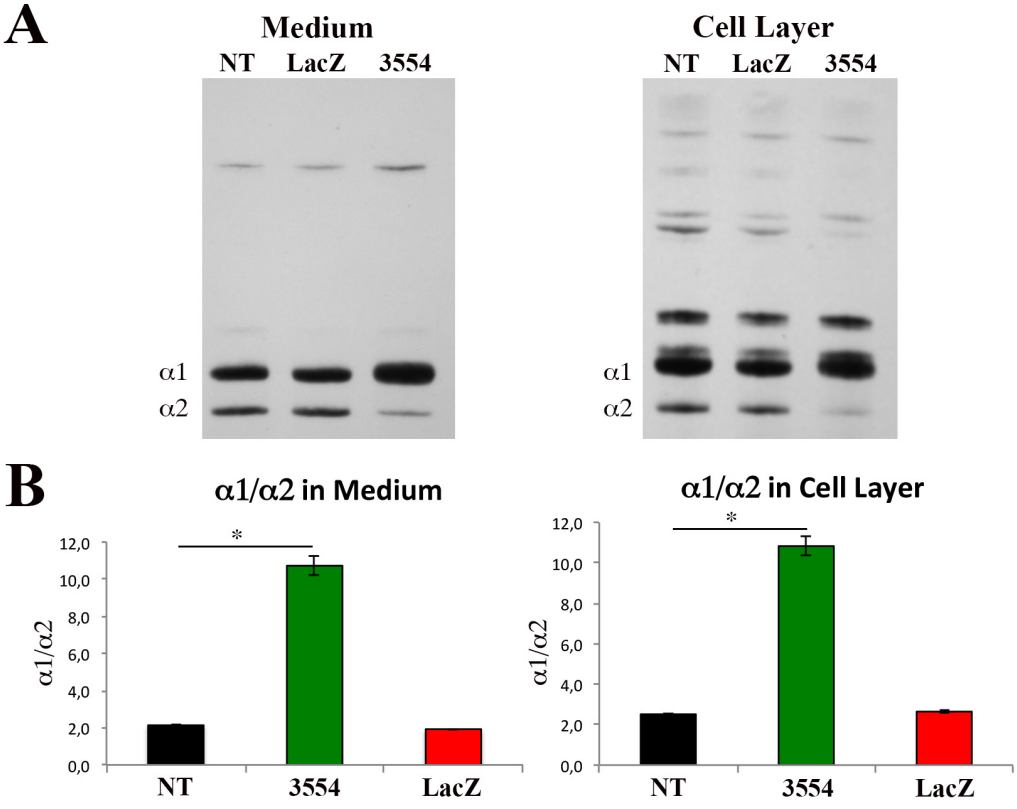

Figure 17. siRNA-3554 suppression of α2(I) expression in MEFs.

A SDS-PAGE of collagen type I extracted from medium and cell layer of transfected MEFs; **B** Quantification of the ratio between α1 and α2 chains of collagen type I. The siRNA-3554 is really specific and efficient also at protein level. The parameters are expressed as mean±sd. NT= Not transfected, LacZ= negative control siRNA. * p value <0.05

Efficiency and specificity of siRNA-3554 in osteoblast cells

Osteoblasts are the target cells to treat Osteogenesis Imperfecta and thus the efficiency and specificity of the siRNA-3554 were also tested in primary murine osteoblasts. Cells were transfected in 24 well plates at cell density of 2×10^4 cells/well using 10 mM siRNA. The cell density was chosen based on the lower growth rate of osteoblasts compared to MEFs. The RNA was collected 48 hours after the transfection and *Col1a1* and *Col1a2* qPCR analysis was performed. Only the cells transfected with the siRNA-3554, and not the one not transfected or transfected with the siRNA-LacZ negative control, showed a specific 82 % down-regulation of the *Col1a2* expression, without any change in the *Col1a1* expression level **(Figure 18 A)**.

A silencing time course experiment with the siRNA-3554 was also performed and RNA was collected 1, 2, 8 and 12 days after transfection. A down-regulation of *Col1a2* expression of 84 %, 78 %, 63 % and 40 % was obtained at 1, 2, 8, 12 days after the transfection respectively **(Figure 18 B)**. No effect on the expression of *Col1a1* was detected confirming specificity of siRNA-3554 for *Col1a*2.

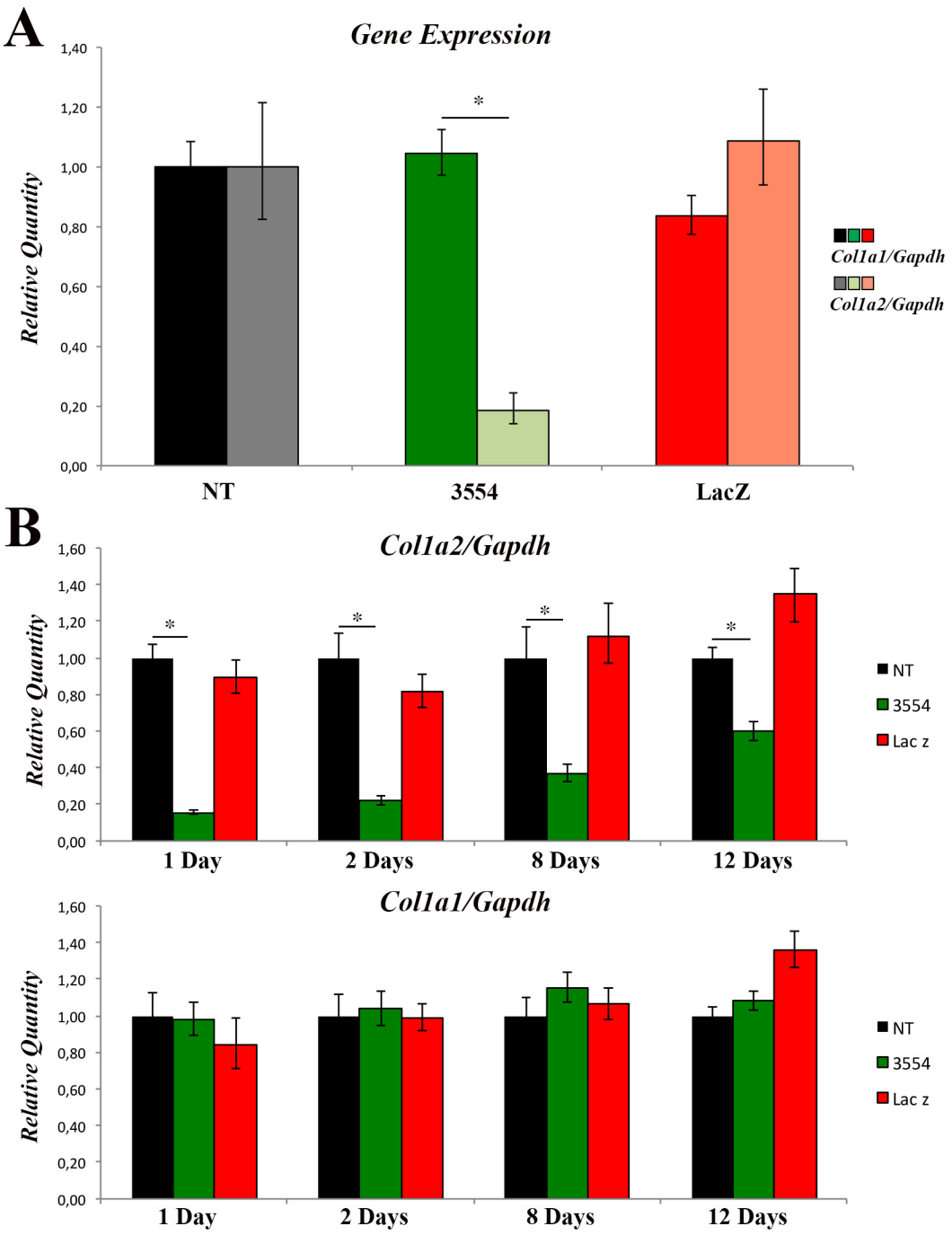

Figure 18. Efficiency and specificity of siRNA-3554 in osteoblasts cells.

A *Col1a1* and *Col1a2* qPCR cofirmed siRNA-3554 specificity against *Col1a2* expression following transfection with 10 nM siRNA. A strong down-regulation of *Col1a2* expression upon siRNA-3554 transfection was evident in presence of unchanged *Col1a1* expression level; **B** *Col1a1* and *Col1a2* qPCR revealed siRNA-3554 specificity against *Col1a2* expression also 12 days following transfection with 10 nM siRNA. A strong down-regulation of *Col1a2* expression upon siRNA-3554 transfection was evident in presence of unchanged *Col1a1* expression level. All the values are expressed as mean±sd. NT= Not Transfected, LacZ= siRNA negative control. * p value <0.05.

Evaluation of the effect of siRNA-3554 on osteoblasts mineralization

To assess if the down-regulation of *Col1a2* gene and consequent suppression of α2(I) protein, determined by siRNA-3554, would compromise bone mineralization, the mineralization of primary osteoblasts transfected with siRNA-3554 was evaluated. Osteoblasts mineralization was induced 24h after transfection supplementing the culture medium with dexamethasone, ascorbic acid and β-glycerophosphate, as described in materials and methods section. After 19 days Von Kossa staining was performed to visualize the mineral nodules **(Figure 19 A)**.

The mineralized area was measured and expressed as percentage over total well area. Values obtained were normalized to the total amount of DNA per well **(Figure 19 B)**.

Interestingly, transfected (n=9) and control cells (n=12) produced the same amount of mineralized area (0.014 ±0.004 % siRNA-3554; 0.017 ±0.005 % control), suggesting that the suppression of α2 chain of collagen type I is not affecting mineralization.

It should anyway be considered that the siRNA efficiency after 12 days is reduced to 50%.

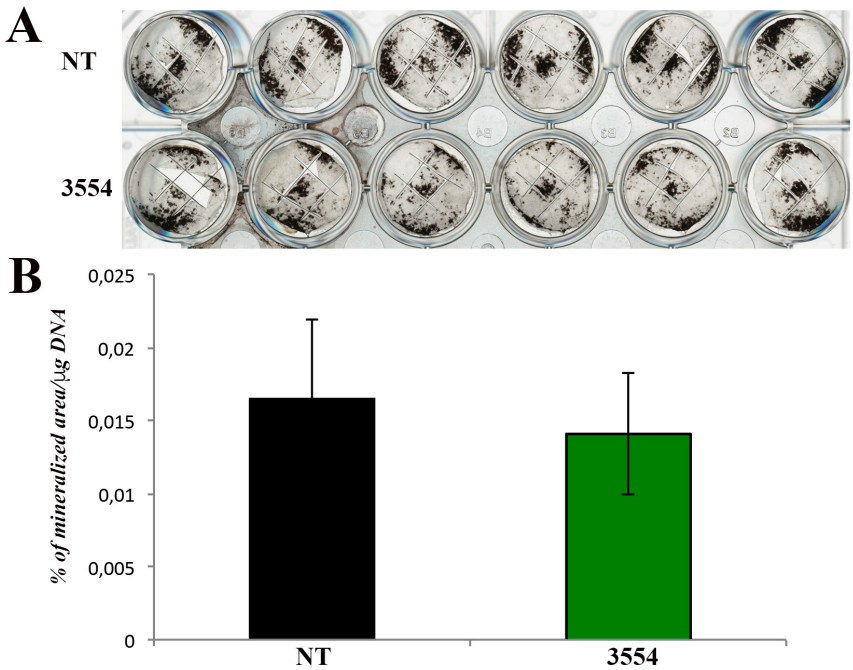

Figure 19. siRNA-3554 did not impair osteoblast mineralization.

A Not transfected (NT) control and siRNA-3554 transfected WT osteoblasts stained by Von Kossa following induction of mineralization; **B** Quantitation of mineralized nodules in osteoblasts not transfected (NT) or transfected using siRNA-3554. The osteoblasts transfection with siRNA-3554 did not affect the mineralization level. The values are expressed as mean±SEM.

Evaluation of siRNA-3554 efficiency and specificity *in vivo* using biphasic calcium phosphate muscular implant in nude mice

Molecular and protein evaluation

To have a proof-of-principle of the *in vivo* efficiency of siRNA-3554, biphasic calcium phosphate (BCP) implant loaded with murine mesenchymal stem cells (MSCs) expressing the Luciferase F (*LucF*) and the green fluorescent protein (*EGFP*) genes was prepared and transplanted intramuscularly in Rj:NMRI-nude mice. This implant was chosen since it was reported to favor bone formation[208,209]. Following implantation, siRNA-3554, siRNA-LucF or saline solutions were injected at the implant site three times a week for three weeks. At the sacrifice the implants appeared as a compact mass of cells and particles **(Figure 20 A)**.

The qPCR analysis performed using the RNA extracted from the samples revealed that the *Col1a2* expression was significantly down-regulated (48 %) only in the implants injected with the siRNA-3554, and this suppression was specific since no effect on *Col1a1* level was detected **(Figure 20 B)**.

The collagen type I from the implants was also extracted and analysed by SDS-PAGE and the α1 and α2 bands of collagen type I were quantified. The ratio between α1 and α2 chains was used as index of collagen α2 suppression and indeed the ratio was increased only following injection with siRNA-3554 and not upon either PBS or siRNA-LucF administration **(Figure 20 C)**.

Thus the data showed that the suppression was present in our *in vivo* model both at molecular and protein level, even if the effect was less strong that what detected in the *in vitro* assays.

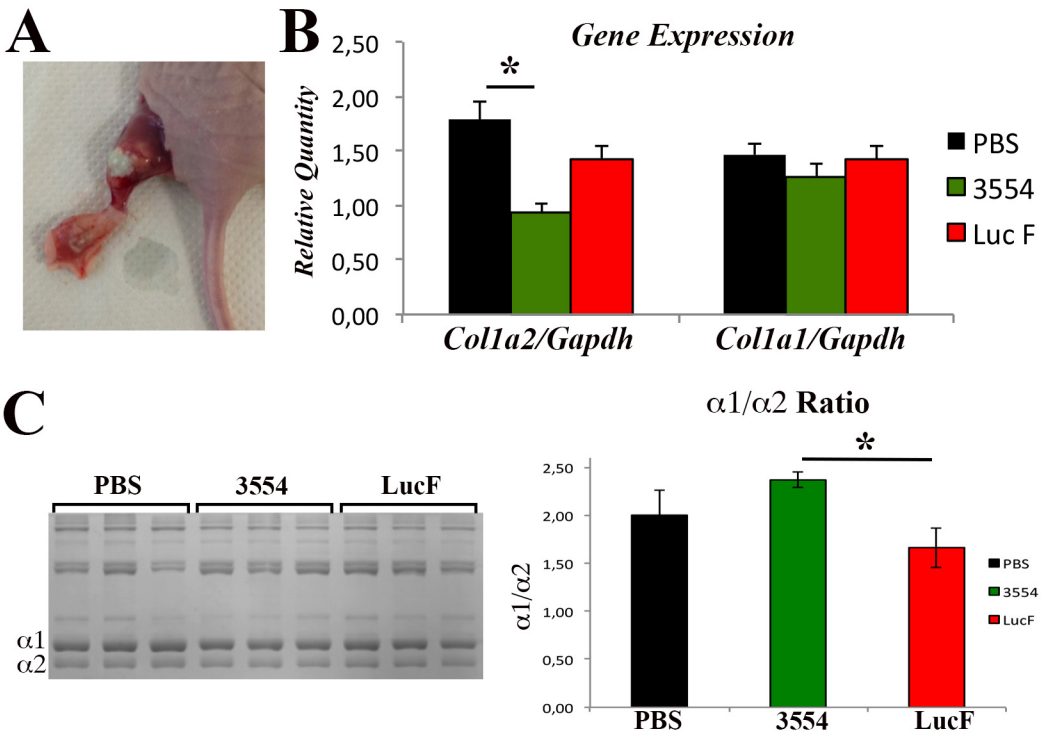

Figure 20. *In vivo* efficiency and specificity of siRNA-3554.

A Intramuscular BCP implants at the end of the experiment following mice sacrifice; **B** *Col1a1* and *Col1a2* qPCR analysis using RNA extracted from BCP implants injected with saline solution (PBS), siRNA-3554 or siRNA-LucF revealed a specific down-regulation of *Col1a2* only in the samples injected with siRNA-3554; **C** SDS-PAGE of pepsin isolated collagen from BCP implants and quantification of the ratio between α1 and α2 chains of collagen type I. The increase α1/α2 ratio in samples injected with siRNA-3554 demonstrated its efficiency also at the protein level. LucF = siRNA negative control. * p value <0.05. The values are expressed as mean±sd.

Histological evaluation

To evaluate the effect of the siRNAs injection on the tissue properties of the implants different histological staining were performed. The Masson's Trichrome confirmed the presence of newly formed bone (red asterisks) in all samples, demonstrating that the inhibition of *Col1a2* did not impair bone formation **(Figure 21 A)**.

The immunohistochemistry using antibody against CD68, specifically labelling the macrophages, revealed that the siRNAs did not affect the number of macrophages, suggesting the absence of inflammation reaction **(Figure 21 B)**.

Interestingly even if the EGFP positive cells implanted with the BCP were present in all the samples the most part of the cells in the implants were of host origin **(Figure 21 C)**.

Of note areas of picnotic nuclei were detectable (dashed circles) in siRNAs injected samples stained with Massom's Trichrome, suggesting a necrotic effect of lipoplex injections.

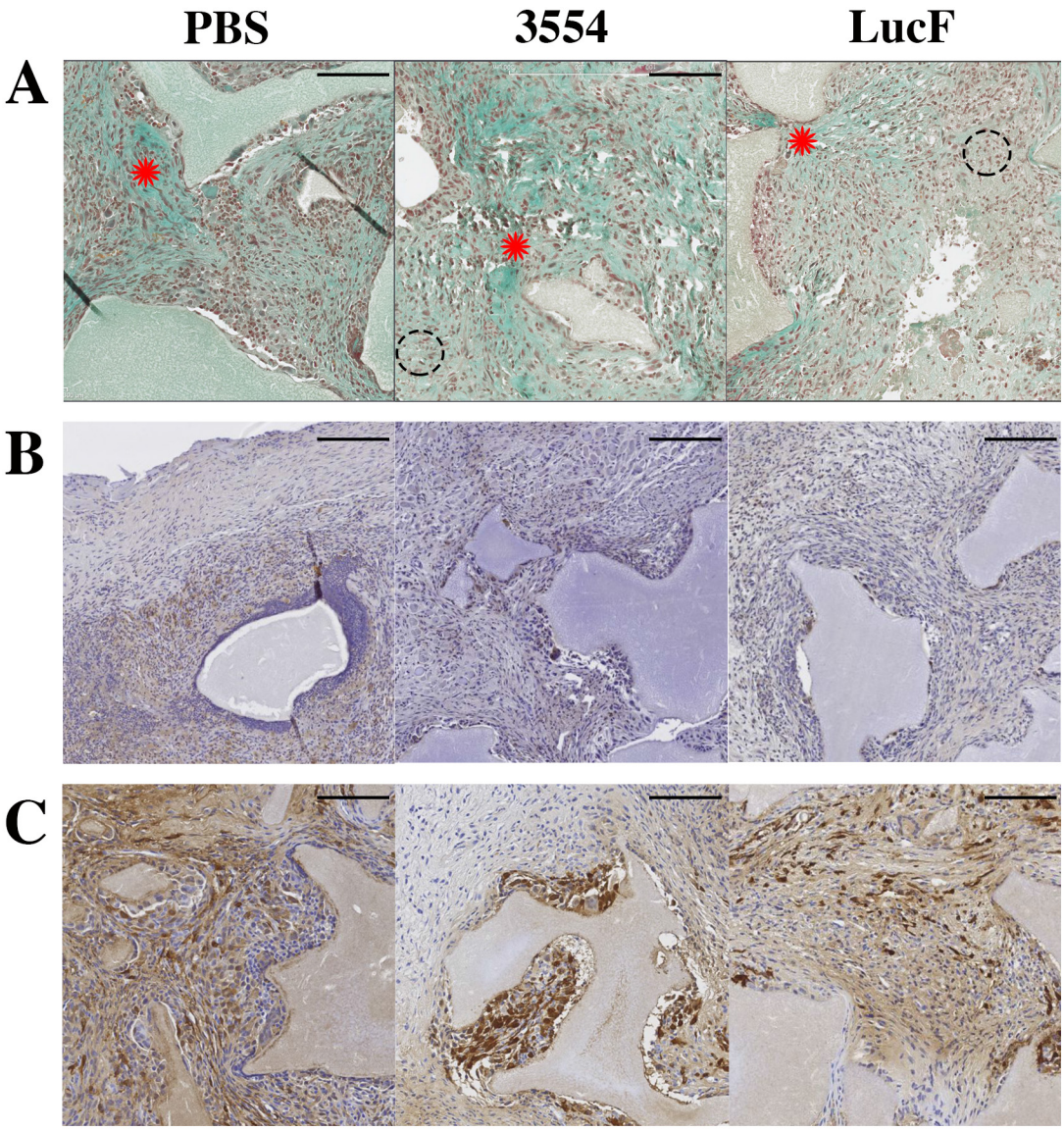

Figure 21. Histological analysis of BCP implants injected with siRNAs.

Sections obtained from BCP implants injected with saline (PBS), siRNA-3554 or siRNA-LucF, respectively and stained with: **A** Masson's Trichrome where bone formation is indicated by red asterisks and picnotic nuclei by dasher circles; **B** Immunohistochemistry for CD68 showed that the macrophage (brown) number was not altered in the siRNA samples; **C** Immunohistochemistry for EGFP, showed EGFP-MSCs (brown) implanted with the BCP still present in all the samples. Bar scale = 100µm.

In vivo intramedullary injection of siRNA-3554 in mice tibia

To test the effect of siRNA-3554 directly on bone, a siRNA-lipoplex complex was injected in the medullary canal of the tibia of C57Bl/6 mice. siRNAs were labeled with the FAM fluorochrome to be able to follow their distribution *in vivo*. The labeled siRNA-3554 and the negative control FAM siRNA-LucF were injected every other day for a week as described in the methods section.

Following mice sacrifice tibias were collected to evaluate the *in vivo* siRNA distribution by confocal microscopy analysis. The images show a predominant medullary localization of the siRNAs suggesting that this type of delivery will not be able to suppress *Col1a2* in bone cells **(Figure 22)**.

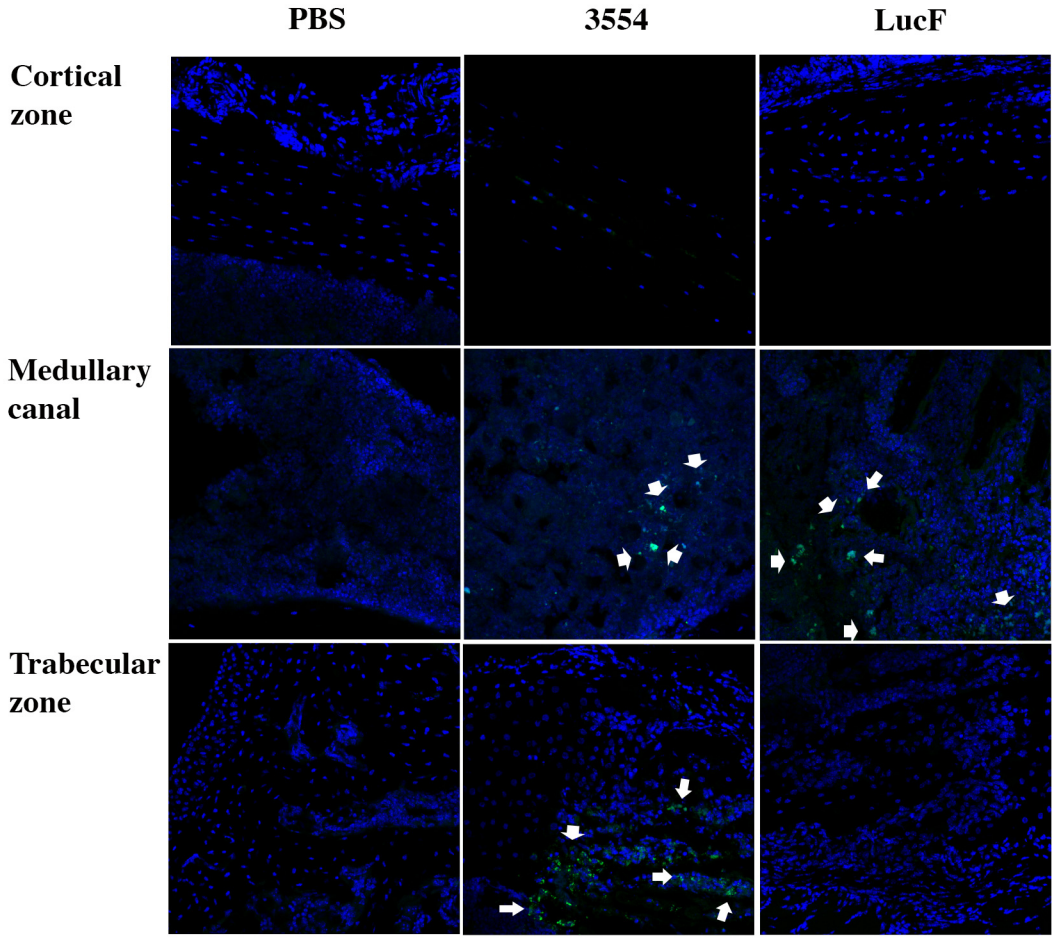

Figure 22. Confocal analysis of tibiae injected with siRNA.

siRNA-FAM localization (green signal) in tibia sections from mice injected with FAM-siRNAs (siRNA-3554 or siRNA-LucF) or PBS; nuclei were counterstained with DAPI. The siRNA molecules were localized in the medullary canal (white arrow). Magnification 40X.

In vivo callus injection of siRNAs in mice

In order to attempt a better osteoblasts targeting *in vivo* a fracture model was developed. The idea was that since fracture healing is recapitulating all the steps of bone formation in a bit over a month time frame, a fracture system could allow to mimic the effect of siRNA delivery during bone formation. For this purpose siRNAs were injected at fracture site as described in the material and method section. The RNA was collected and the expression of the *Co1a1* and *Col1a2* genes was analyzed.

An extremely high variability for both genes expression was evident and no specific down-regulation of *Col1a2* was found **(Figure 23)**.

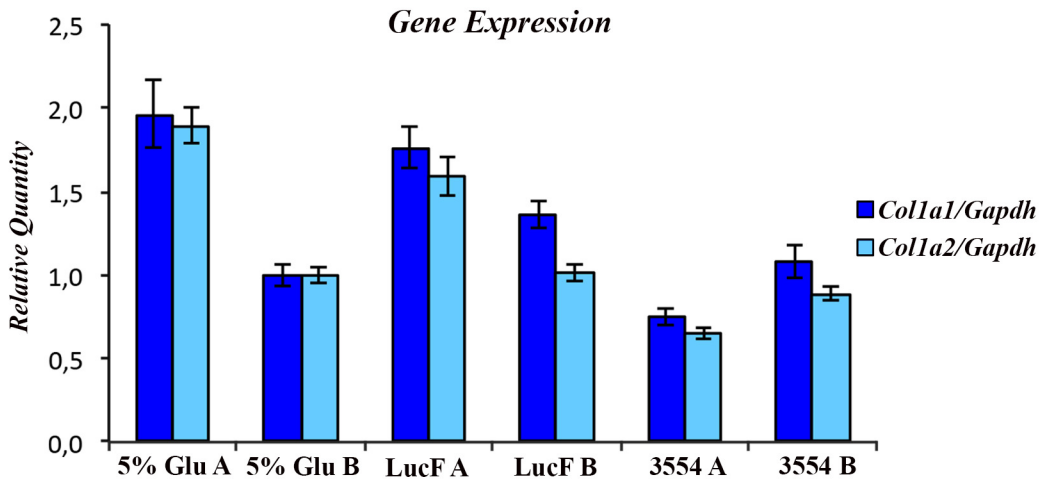

Figure 23. Gene expression analysis of collagen type I at callus site.

Gene expression analysis on the RNA extracted from callus injected with siRNAs. Variability in the expression of both *Col1a1* and *Col1a2* genes was present and no specific down-regulation of *Col1a2* was found. The values are expressed as mean±sd.

In vitro test of siRNA-liposome $(DSS)_6$ complex as delivery system specifically targeting bone surface

To overcome the problems encountered in the *in vivo* delivery of siRNAs specifically to bone, a new method was adopted and a liposome $(DSS)_6$, reported to specifically targeting bone surface, was selected[206]. The stability of siRNA-liposome $(DSS)_6$ complex was evaluated in presence of blood serum since the siRNA-Liposome$(DSS)_6$-complex will be administrated systemically. Aliquot of free siRNA or siRNA-liposome $(DSS)_6$-complex were incubated for different time at 37°C in presence of 50 % murine serum and RNA quality was evaluated following extraction from the mixture by gel electrophoresis. The siRNA-liposome $(DSS)_6$ complex was able to improve the siRNA stability, in fact after 24 hours of incubation the siRNA was detectable only if encapsulated in the liposome complex **(Figure 24)**.

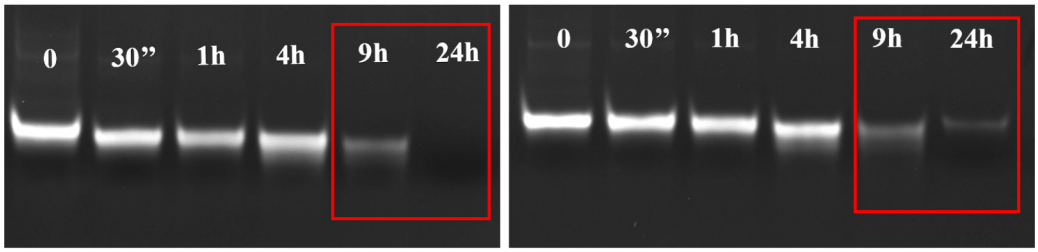

Figure 24. Evaluation of siRNA liposome $(DSS)_6$ complex stability *in vitro*.

Stability in 50 % serum of siRNA-liposome $(DSS)_6$ complex. The presence of the lipoplex was able to increase the siRNA stability.

DISCUSSION

The present research describes the successful identification of an efficient and specific silencing RNA (siRNA) molecule able to target the murine *Col1a2* transcript both *in vitro* and *in vivo* and the identification of a possible delivery system targeting specifically the bone surface.

Gene therapy for Osteogenesis Imperfecta: a challenging and promising tool to treat an incurable disease

The aim of the study was the development of a novel gene therapeutic approach for the dominant form of Osteogenesis Imperfecta, a bone disease for which no definitive cure exist. Currently, physiotherapy, rehabilitation and orthopedic surgery are the treatments of choice for OI[210]. Regarding drug based therapy, multiple clinical trials are ongoing to evaluate the effect of bisphosphonates, which inhibit osteoclast functions, thus increasing bone volume[211]. Recently, clinical trials using anti-RANKL, anti sclerostin and anti-TGF-β antibodies are under investigation[106,212,213]. But even if all these approaches improve OI patient's lifestyle, they do not cure the disease, since they do not eliminate the genetic cause of OI. In order to accomplish this ultimate goal it is necessary to develop a gene therapy treatment. Classical OI is a dominant negative genetic disorder and the only real cure for the disease will be to correct the molecular defect present in the mutant allele. But, although the gene editing tools improved over the last years[214], the repair of endogenous mutations is still challenging. To this purpose nature teaches us an important lesson that could indeed allow the optimization of more feasible gene therapy approaches. A mild form of the disease affects OI patients carrying a null *COL1A1* allele, thus, by inactivating the mutant allele or its transcript, it will be possible to transform a severe into a milder phenotype. The disease will not be solved, but the patients outcome will ameliorate significantly[113,114]. For glycine substitutions in α2(I) chain a more straight forward silencing approach against both normal and mutant alleles could be effective and improve patients phenotype since the synthesis of α1(I) homotrimers in absence of α2 synthesis is reported to be associated to a form of Enhler Danlos Syndrome characterized by vascular phenotype,

but not associated to skeletal outcome.

Thus an allele specific silencing approach, focused on targeting mutant transcript for *COL1A1* mutation or both alleles for mutation in *COL1A2*, seems particularly appealing.

Silencing both *Col1a2* alleles to treat dominant Osteogenesis Imperfecta

In my research I was interested in demonstrating the goodness of a mutation independent *COL1A2* suppression to treat the OI patients carrying mutations in this gene. Among the various silencing techniques available we chose for our study the small interfering RNA (siRNA). siRNAs are chemical synthesized double strand RNA that, to be effective, need to be introduced in nM amount inside the target cells. They have a short half life and after 48h only 1 % of siRNAs was reported to be still active[161]. Furthermore siRNAs were demonstrated to effectively and preferentially down regulate the expression of defective collagen allele in OI cells[127,215,216].
Indeed effective targeting of mutant gene in mesenchymal stem cells (MSCs) and in induced pluripotent stem cells (iPS) using OI patient's cells had been demonstrated both for *COL1A1* and *COL1A2*.

For the study primary murine cells and a mouse model was used. The availability of *in vitro* and *in vivo* animal models is particularly relevant in studies aimed to identify novel therapeutic approaches. The *in vitro* is an important tool that allows to dissect and analyze specific cellular pathways without the interference of the whole tissue/organ environment, on the other hand the use of *in vivo* models is a mandatory step before clinical trials. To suppress the expression of murine *Col1a2* alleles, three specific siRNAs were designed targeting the non repetitive sequence of the *Col1a2* mRNA. The collagen genes are highly repetitive and reach in GC dinucleotide in the region encoding for the triple helical domain, thus targeting this sequence was not recommended since the risk of poor specificity would have been very high. The efficiency and specificity of the selected *Col1a2*-siRNAs were tested *in vitro* in primary murine fibroblasts and osteoblasts and one of them was able to suppress over

80 % of the target *Col1a2* even at low concentration, without affecting the expression of the highly similar *Col1a1* gene.

A strong reduction of the α2(I) chain was also confirmed by metabolic collagen labeling with tritium proline.

Homozygous null mutations in *COL1A2* lead to a range of phenotypes. Those associated with non sense mediated decay (NMD) lead to assembly of α1(I) homotrimers. Clinically, formation of homotrimers causes mild Ehlers–Danlos syndrome, with hypermobility in childhood and cardiac valve disease in adulthood, rather than Osteogenesis Imperfecta. By contrast, the homozygous *Oim/Oim* mouse, which harbors a naturally occurring homozygous *Col1a2* mutation, a patient with Osteogenesis Imperfecta due to a deletion in the α2(I) C-propeptide, not show activation of NMD and produce normal levels of *COL1A2* transcript translated into α2(I) chains that could not be incorporated into collagen molecules. The resulting outcome a very severe form of OI. Thus given that α1(I) homotrimer formation alone does not lead to Osteogenesis Imperfecta, the intracellular accumulation of α2(I) may cause the skeletal outcome.

Of note mutant *Oim/Oim* osteoblasts have impaired differentiation ability[217]. In order to evaluate if the suppression of both *Col1a2* alleles was compromising osteoblasts mineralization thus worsening the cell phenotype instead to ameliorate it, we performed a mineralization assay *in vitro* using murine primary calvarial osteoblasts following siRNA transfection. Interestingly no delay or reduced mineralization was noticed, supporting the idea that a bone specific targeting of *Col1a2* will not compromise osteoblasts function. The same experiment will be done using osteoblasts from the OI murine model *Amish*/+ in order to clarify the effect of the targeting on the mineralization of cells carrying a *Col1a2* mutation.

Silencing *Col1a2* alleles by siRNA is effective also *in vivo*

To date, silencing approaches have been tested mainly *in vitro*, and further *in vivo* studies are needed in appropriate animal models before moving on to clinical trials. Thus to demonstrate the efficacy of the proposed *Col1a2* silencing approach *in vivo,* experiments were performed by means of a local delivery of the selected siRNA-3554.

We took advantages of the ability of BCP beads loaded with mesenchymal stem cells to stimulate bone formation in relative short time following intramuscular implantation in nude mice[218]. This strategy allowed us, by directly injecting the siRNA at the BCP implant site, to evaluate its effect in term of efficiency and specificity *in vivo* after three weeks.

The suppression of the *Col1a2* expression, although specific, was less than in the *in vitro* assays, and similarly the reduction of the α2(I) chain was lower. The reason for this could be linked to some intrinsic limitations of the system such as the difficulty to reach the cells inside the implant and the formation of a connective tissue capsule around the implant that could impair siRNAs entering into the target cells. Nevertheless bone formation in the implant was not compromised by the *Col1a2* siRNA injection.

Since the efficiency and specificity of the selected siRNA were proven, both *in vitro* and *in vivo*, we decided to attempt a different delivery system to evaluate the siRNA efficiency *in vivo.*

The long bone intramedullary injection of siRNAs was demonstrated to be an effective system to target them to bone cells[219].

Thus we injected the *Col1a2* siRNA-3554 FAM labeled in the medullary canal of the murine tibia in WT mice, but confocal analysis revealed that the siRNA was localized for the most part in the bone marrow suggesting that this type of delivery was not able to suppress *Col1a2* in bone forming cells.

Fractures are a “physiological” condition in which the bone is not completely calcified and osteoblast are highly active[220] and it reproduces the various step on bone development. Thus we administrated the *Col1a2* siRNA-3554 mixed to Jet-PEI complex after the induction of a standardized tibia fracture in mice. Analyzing the callus at the fracture site we found that the expression of collagen genes has a high variability and no suppression of *Col1a2* was detected. The reason for this could be once again linked to some limits of the used system. In particular the presence of a high number of different cell types could account for the variable level of collagen type I genes expression and the inflammation, detected 2 weeks after fracture, could have compromised siRNA entering in osteoblasts cells.

Bone specific siRNA delivery: a challenging of the field

To overcome the limits encountered in siRNA local delivery *in vivo* we decided to exploit a systemic delivery, but we needed to consider the necessity of addressing our silencing molecules preferentially if not exclusively to bone tissue. For systemic delivery of therapeutic nucleic acids, viral vectors have been used because of their high transfection efficacy, but the severe safety risks due to their oncogenic potential and their inflammatory and immunogenic effects prevent them from repeated administration[187,189]. siRNA delivery systems made in the last years a rapid progress, but bone remains a difficult target tissue to be reached[221]. Atelocollagen-mediated systemic administration of siRNAs successfully inhibited bone metastasis[222]. The complexation of siRNAs with polyethylenimine also was demonstrated to be effective following systemic administration to deliver the siRNAs into different organs, but no data on specific bone targeting are available jet[197,223].

Systemic delivery of siRNA is a quite promising therapeutic approach but it should be taken into consideration that in clinical trial a high number of repeated siRNA injections could result in a decreased patient compliance and consequent impediment to patient treatment[224].

Moreover one of the major concerns in the use of systemic injection is that the large therapeutic doses administered of siRNA, that would be needed to stimulate sufficient bone formation, may carry a high risk for adverse effects in non-skeletal tissues[225].

Recently, a bone targeting system involving dioleoyl trimethylammonium propane-based cationic liposomes covalently attached to six repetitive sequences of the tripeptide Asp-Ser-Ser has been successful in delivering siRNAs specifically to bone-formation surfaces[206]. The $(DSS)_6$-liposomes were used by Zhang et al to target the siRNA specific for the casein kinase-2 interacting protein-1 (*Plekhol1*) coding gene to osteoblasts. The authors showed that with this vehicle the systemically injected siRNAs were specifically delivered to the bone formation surface[206].

Prof Zhang shared with us a $(DSS)_6$-liposomes preparation and indeed the encapsulation of our *Col2a1* siRNA-3554 increased the siRNA stability in 50 % serum, condition mimicking the *in vivo* siRNA circulation in the blood stream. The analysis of bone *Col1a2* suppression *in vivo* following $(DSS)_6$-liposomes-siRNA-3554

complex systemic injection will be necessary to prove the goodness of this delivery system for OI treatment.

In conclusion, following the *in silico* design of three siRNAs molecules targeting the murine *Col1a2* we successfully identify a siRNA that efficiently and specifically suppresses *in vitro* and *in vivo* the *Col1a2* expression. The optimization of a bone specific delivery system will open a new era in the treatment of OI, at least for those forms with dominant mutations in the *COL1A2* gene.

MATERIALS AND METHODS

Animals

C57Bl/6 control mice were purchased from Harlan Laboratories and maintained in the animal facility at the Department of Molecular Medicine of the University of Pavia according to the current laws on the animal care. All the experiments were approved by the OPBA (Office for the Animals Welfare) of the University of Pavia and by the Italian Ministry of Health.

Rj:NMRI-nude mice were purchased from the Elevages Janvier SAS and maintained in the animal facility at the research group U957 of the INSERM located in the faculty of Medicine of the University of Nantes.

All animal handling and surgical procedures were conducted according to European Community Guidelines (2010/63/EU) for the care and use of laboratory animals. The local Ethic Committee (CEEA.2012.27) approved the animal experimentation protocol for the research.

In silico siRNA selection and synthesis

The Basic Local Alignment Search Tool (BLAST) was used to identify three siRNAs 19-21 nucleotides long specifically targeting the 3'-end of the murine *Col1a2* (NM_007743.3) gene encoding for the C-propeptide domain of the α2 chain of type I collagen: siRNA-3554 (5'-GGACUAUGAAGUUGAUGCA-3') targeting exon 49 (NM_007743.3, 3633-3652), siRNA-3825 (5'-GCCAACAAGCATGTCTGGTTA-3') targeting exon 50 (NM_007743.3, 3904-3925), and siRNA-4215 (5'-GAATTCCGTGTGGAGGTTG-3') targeting exon 52 (NM_007743.3, 4303-4322). The sequences of all three siRNAs differed by at least 6 nucleotides from the sequence of any other gene of the murine genome. Their efficiency and specificity were first tested *in vitro* using Murine Embryonic Fibroblasts (MEF) as detailed below. The three siRNAs targeting murine *Col1a2* and two negative controls for *in vitro* and *in vivo* experiments: siRNA-LacZ (5'-GUGACCAGCGAAUACCUGU-3') and siRNA-LucF

(5'-CUUACGCUGAGUACUUCGA-3') respectively, were purchased from Eurogentec with the addition of a dTdT nucleotide at their 3'-end. siRNA-LacZ was designed against the bacterial β-galattosidase gene and siRNA-LucF was specific for the transcript of lucifesase *firefly* gene, both genes are absent from the murine genome. siRNA-LucF was also labeled with the fluorochrome molecule FAM at the 5'-end for some experiments as detailed below.

Isolation and culture of primary Murine Embryonic Fibroblasts (MEFs)

Murine Embryonic Fibroblasts (MEFs) were obtained from E13.5-14.5 day post fertilization embryos. Wild type (WT) C57Bl/6 females were mated with WT males and plug was checked daily. After 13.5-14.5 days the plugged pregnant females were euthanized by cervical dislocation and both uterine horns containing embryos were removed and transferred in a petri dish containing Phosphate Buffered Saline (PBS, Sigma) under sterile hood. The head and the internal organs of each embryo were removed and the remainder of the body was used for MEFs isolation. Briefly the body was transferred in a sterile tube, minced and sequentially digested with 2X trypsin (1 g/l trypsin, 0.4 g/l EDTA, 1.7 g/l NaCl) for 5 minutes at 37°C. Cells obtained from four successive digestions were passed through a 40 μm polypropylene mesh (Millipore), added with Dulbecco Modified Eagle's Medium (D-MEM, Lonza) supplemented with 10 % Fetal Bovine Serum (FBS), 4 mM glutamine, 100 μg/ml penicillin and 0.1 mg/ml streptomycin and pooled.

The cells were than centrifuged for 5 min at 120 g, the supernatant was removed and the MEFs were resuspended in 10 ml of complete D-MEM. The cells obtained from each embryo were plated in a 10 cm petri dish and incubated at 37°C. Cells at passages P3-P6 were used for all the experiments.

Isolation and culture of primary murine calvarial osteoblasts

Murine calvarial osteoblasts were isolated from 1-2 day old mice. Pups were euthanized by decapitation, the cranium from each mouse was dissected, cleaned from

the surrounding connective tissue, cut in half and collected in a 24 well plate in presence of α-Minimal Essential Medium (α –MEM, Sigma) supplemented with 10 % Fetal Bovine Serum (FBS), 4 mM glutamine, 100 μg/ml penicillin and 0.1 mg/ml streptomycin and 25 μg/ml sodium ascorbate (Fluka). Calvaria were then pooled and sequentially digested with collagenase type II 200 U/ml (GIBCO) at 37°C in an oscillating water bath for 20 minutes. Cells obtained from the first two digestions were discharged, while cells from the following three digestions were passed through a 70 μm polypropylene mesh, added with α -MEM containing 10 % FBS to inhibit collagenase and pooled. The cells were centrifuged for 5 min at 150 g, the supernatant was removed and the cells were resuspended in 5 ml complete α -MEM. Cells were counted using the vital dye Trypan blue and plated in a petri dish at a density of 2×10^5 cells/dish. The medium was changed twice a week and cells were used at Passage 1.

Transfection

For MEFs transfection experiments cells were plated in 24 well plated at a density of $1x10^4$ or 2×10^4 cells/well. After 24 h the cells were transfected using Interferin (PolyPlus transfection) following manufacturer's recommendation.

For each siRNA two concentrations were tested 10 and 50 mM respectively and the RNA was collected 48 hours after the transfection.

For the two more efficient and specific siRNAs, siRNA-3554, and siRNA-3825 and the negative control siRNA-LacZ a time course was performed. Briefly following transfection at the above detailed concentrations the RNA was collected 24, 48 and 72 hours after the transfection. Each experiment was performed in duplicate.

For primary osteoblasts transfection, cells were plated in 24 well plate at a density of $2x10^4$ cells/well. After 24h the cells were transfected using Interferin (PolyPlus transfection) as recommended by the manufacturer. siRNA-3554 was used at a concentration of 10 nM and the RNA was collected 1, 2, 8, 12 day after the transfection and used for qPCR.

Biphasic calcium phosphate (BCP) implants

Twelve Rj:NMRI-nude female 5 week old mice were used. The mice were anesthetized by inhalation of 2 % isoflurane at a flow rate of 1 L/min and injected with 10 ul of Buprécare 1 μg/ml intramuscularly and disinfected with betadine solution. The leg was incised at the level of the tibia and a pocket in the muscle tissue was created. The implant was then inserted in both legs of the mice, and the cut was sutured with a non-resorbable suture thread.

Each implant was composed by 40 mg of MBCP 0.5-1 mm granules (Biomatlante) incubated for 1 hour at RT with $1.4X10^6$ murine Mesenchymal Stem Cells (GIBCO) modified to express luciferase and EGFP genes (Luc/eGFP MSCs) in 60 μl of PBS.

After one week three injections of a siRNA lipoplex complex were performed for three weeks, in the last week fluorescently labelled siRNAs were used. The lipoplex complex was obtained as following: a solution containing 0.67 μg/μl of siRNA and 0.67 μg/μl of DNA plasmid pSL301 was mixed with a solution containing 8 mM Liposome (209120DOPE) and incubated 20 minutes at RT to allow the siRNA encapsulation. The mice were divided in 3 groups composed of 4 mice each. The mice belonging to the different groups were injected with 10 μg of siRNA-3554 or siRNA-LucF or PBS, respectively. The animals were then sacrificed 28 days after the implant. The implants were used to evaluate collagen type I gene expression and protein levels and for histological analysis.

Intramedullary siRNA tibia injection

For siRNA intratibial injection 6 C57Bl/6 WT male 1 month old were used. The mice were divided in 3 groups composed of 2 mice each. A hole at the level of the proximal tibiae was performed using a 29 G needle in mice under anesthesia. The hole was used to deliver the siRNA in the intramedullary canal; the different groups were injected with lipoplex complex containing 10 μg of fluorescent siRNA-3554 or siRNA-LucF or PBS, respectively. For lipoplex complex formation a solution containing 0.67 μg/μl of siRNA and 0.67 μg/μl of DNA plasmid pSL301 was mixed with a solution containing 8 mM Liposome (209120DOPE) and incubated 20 minutes at RT to allow the siRNA

encapsulation. Three injections of the lipoplex complex were performed in one week and the mice were sacrificed 3 days after the last injection. The samples were used for confocal analysis as detailed below.

Tibia fractures

For siRNA injections at fracture site 6 C57Bl/6 WT male 1 month old were used. The mice were divided in 3 groups composed of 2 mice each. Mice were anesthetized and on both tibias a pin was inserted in the intramedullary canal to stabilize the fracture; the cut made to insert the pin was sutured with a resorbable suture thread. Using a device, which exploits a three-point force theory, a composed fracture approximately at ¼ of distance from the distal proximity of the tibiae of the mice was performed. After the surgery X-ray were made using the Faxitron Mx-20 (Faxitron) set at 25 kV for 19 second, the radiographic cassette were acquired using the Kodak DirectView elite CR System K-Pacs software (KodaK).

Four day after fracture the different groups were injected with 10 μg of siRNA-3554, or siRNA-LucF or 5 % glucose, respectively. The siRNA was complexed with 1.4 μl of *in vivo* Jet-PEI solution (Polyplus) following the manufacturer instruction. The injections were performed at fracture site every other day for 5 times and the mice were sacrificed the day after the last injection. The samples were used to evaluate the expression level of collagen type I genes, as detailed below.

Gene expression analysis

The RNA from not transfected and transfected MEFs and osteoblasts was collected at the different time points detailed above using the RNeasy Plus Mini Kit (Quiagen) according manufacturer instruction.

The RNA from BCP implants was extracted, following removal of the surrounding connective tissue, using Tri-Reagent (Sigma). Briefly the implants were crushed with the use of a pestle in 1.5 ml tube (Argos EW-44468-19) in a final volume of 1 ml of Tri-Reagent and the extraction proceeded following the manufacturer instruction.

The RNA from the callus was also extracted using Tri-Reagent (Sigma). Each callus was dissected and minced in a glass vials using 1 mL of Tri-Reagent for sample.

The RNA from the long bone was extracted using Tri-Reagent (Sigma). The bone marrow was flushed with PBS and tibia and femur were minced in a glass vials using 1 mL of Tri-Reagent for sample.

cDNA was synthesized from 100 ng of RNA using the High Capacity cDNA Reverse Transcription kit (Applied Biosistem) in a final volume of 20 µl. qPCR analysis was performed using TaqMan commercially available probes from Applied Biosystems, and the TaqMan Universal PCR Master Mix (Applied Biosystems) in a final volume of 25 ul using the MX3000P qPCR (Stratagene).

All samples were run in triplicate. Expression levels for *Col1a1* (probe Mm00801666_g1) and *Col1a2* (probe Mm00483888_m1) were evaluated.

Gapdh (Mm99999915_g1) was used as normalizer. Relative expression levels were calculated using the ΔΔCt method.

Collagen type I analysis

MEFs were plated in 6 well plate at a density of $1.2x10^5$ cells/well. After 24 hours the cells were transfected with 10 nM siRNA-3554 or siRNA-LacZ using Interferin (PolyPlus transfection) as described above. The day after transfection the cells were pre-labelled with D-MEM, 1 % FBS containing 0.1 mg/ml ascorbic acid for 2 hours to stimulate collagen production. The labelling was performed for 18 hours in D-MEM pre-labelling medium using 20 µCi of ^{3}H-Pro/well.

Protease inhibitors (1.52 mg/mL EDTA, 1.57 mg/mL benzamidine, 0.25 mg/mL N-ethylmaleimide) were added to the medium before collection. Medium was transferred into tubes containing 20 µg of cold bovine collagen used as carrier for collagen precipitation. The cell layer was washed with PBS and the cells were lysed in PBS supplemented with protease inhibitors, by freezing thawing at -80°C. Cells were finally scraped and collected into a tube containing 20 µg bovine collagen as carrier. Collagen from both medium and cell layer fractions was precipitated with half volume of 96 % ethanol for 1 hour at 4°C and centrifuged at 13000 g for 20 min. The surnatant was

removed and the pellet was incubated overnight with 100 µg/ml pepsin dissolved in 0.5 M acetic acid at 4°C. Then the collagen was precipitated with 2 M NaCl, 0.5 M acetic acid for 30 min on ice, centrifuged at 13000 g for 20 min and washed with ethanol 70 % for one hour on ice. The sample was centrifuged at 13000 g for 20 min, dried in vacuum and resuspended in 50 µl of 1 X Laemmli buffer (62.5 mM Tris HCl, pH 6.8, 10 % glycerol, 2 % sodium dodecyl sulphate (SDS), 0.02 % bromophenol blue). The radioactivity (counts for minute, CPM) of the collagen samples was measured using a liquid scintillation analyzer (TRI-CARB 2300 TR). The same amount of ^{3}H-labeled collagen (10.000 CPM for medium and 15.000 CPM for cell layer) was denaturated at 80°C for 5 min and separated on 6 % polyacrylamide-urea-SDS gels. The gels were run at 80 Volt using the running buffer 19 mM Tris HCl, 0.1 % (w/v) SDS and 192 mM glycine. Then they were incubated 30 min in 30 % methanol, 5 % acetic acid and 1 hour in enhancer solution (EN^{3}HANCE PerkinElmen) with gentle agitation. After 30 min of washing in tap water the gels were dried for 2 hours. The gels were placed in contact with a radiography film at -80°C for 1 week. Films were developed and acquired by VersaDoc 3000 (BioRad).

Osteoblasts mineralization assay

Mineralization was induced on non-transfected and transfected osteoblast. For this purpose cells were transfected 24h after plating. The following day mineralization media containing (α-MEM, 10 % FBS, 100 µg/ml penicillin, 0.1 mg/ml streptomycin and 100 µg/ml ascorbic acid 5×10^{-8} M dexamethasone (Sigma Aldrich)), 0.2 mM ascorbic acid (Fluka) and 10 mM β-glycerophosphate (Sigma-Aldrich) was added for 19 days, changing the media three times a week. The cells were then fixed in 10 % Formalin Solution Neutral Buffer (Sigma) for 30 min at room temperature (RT) and Von Kossa staining was performed. Briefly, cells were incubated for 1 hour with 5 % silver nitrate exposed to direct light and then washed with deionized water and incubated with 5 % sodium thiosulfate for 5 min. The calcified extracellular matrix appeared as black nodules. Images were acquired with a digital scanner at 2400 dpi resolution and analyzed with the Leica application suite V4.5 software. Mineralized

spots were manually delimited and the percentage of mineralized area was calculated on the total well area. Normalization was performed on the total DNA per well.

Collagen analysis from biphasic calcium phosphate (BCP) implants

The dissected implants were washed in PBS and decalcified in 0.5 M EDTA pH 7.1 for 7 days changing the solution every other day. Collagen was extracted by pepsin digestion. The decalcified implants were washed with PBS and incubated with 0.1 mg/ml pepsin in 0.5 M acetic acid at 4°C for three days. The collagen was then precipitate with 0.9 M NaCl in 0.5 M acetic acid, washed in EtOH 70 % and lyophilized.

The pellet was resuspended in 0.5 M acetic acid and 5 µl of it was lyophilized, resuspended in 10µl of 1 X Laemmli buffer[226] (62.5 mM Tris HCl, pH 6.8, 10 % glycerol, 2 % sodium dodecyl sulphate (SDS), 0.02 % bromophenol blue), denatured at 80°C for 5 minutes and separated on 6 % polyacrylamide-urea-SDS gels in presence of 0.5 M urea. The gels were stained with Coomassie Picric Staining[227], and digitalized by Versadoc (Biorad). The bands intensity was measured using Quantity one software (Biorad).

Histological analysis

The BCP implants were removed from the mice following euthanasia by cervical dislocation. The implants from 2 mice from each group underwent to histological analysis. The tissue was fixed for 24 hours in 4 % PFA, decalcified in 4.13 % Ethylenediaminetetraacetic acid (EDTA-Alfa Aesar) dehydrate and included in paraffin. Sections of 3 µm of thickness were obtained using microtomo RM2265 (Leica) on to Sperfrost Plus (Menzel-Glaser) glass and stained with Trichrome Masson's staining. Immunohistochemistry was also performed to evaluate the level of LucF expressing cells and the presence of Macrophage (CD68).

The different staining and immunohistochemistry were performed on deparaffinised and rehydrated sections in according to the staining procedure.

Trichrome Masson's staining

Masson's Trichrome Commercial staining kit (Sigma) was used. Briefly the sections were fixed again with pre-warmed Bauin solution (Sigma). Sequentially the nuclei were stained with ferric hematoxylin of Weigert (Sigma), bathed in an Ecarlate Biebrich-Fucsin acid solution, differentiated with fosfotungstic acid/fosfomolibdic acid and finally stained with an anilin blue solution (Sigma). Masson's trichrome technique combines light green solution for collagen (green), fuchsine for cytoplasm, muscle and erythrocytes (red) and hematoxylin for cell nuclei (blue/ black).

Immunohistochemistry

After the rehydratation step the section were washed with Tris buffered saline (TBS) tween 0.05 % pH 7.6 three times for 5 min each under gently agitation. Slides were treated with 3 % H_2O_2 for 15 min at room temperature (RT) to block endogenous peroxidase activity, followed by three washes with TBS tween 0.05 %.

The cross reaction was minimize with a blocking step using 10 % normal serum with 1 % BSA in TBS for 2 h at room temperature. Primary antibody was then applied over night at 4°C.

The primary antibody CD68 (MCA1815T, mouse anti- human, 1:100, Abd Serotex) was used to detect macrophages M0. CD68 is a member of the lysosome-associated membrane protein (LAMP)-1 family. It is a transmembrane glycoprotein highly expressed by monocytes and tissue macrophages[228,229].

The primary antibody used to detect the presence of mMSCs implanted with the BCP particles modified to express luciferase and EGFP genes (Luc/eGFP MSCs) was an anti-luciferase rabbit polyclonal (1:100, Abcam, Cambridge, UK).

Finally, the hybridized probe was detected by immunohistochemistry using biotin-SP-conjugated IgG. Sections were counterstained with Gill-2 hematoxylin (Thermo Shandon Ltd, Runcorn, UK) dehydrated and mounted using Pertex (HistoLab Products AB, Sweden).

Tissue staining was viewed using Nanozoomer 2.0 Hamamatsu slide scanner. Qualitative histological evaluations were then performed.

Confocal microscopy

Tibia from siRNAs and placebo injected mice were dissected, cleaned from soft tissues and fixed for 24 hours in 4 % PFA. Bones were decalcified in 0.5 M EDTA pH 7.1 at 4°C, embedded in optimal cutting temperature compound (OCT; Tissue-Tek, Sakura Finetek), and 10 µm cryosections (cryostat Leica CM1850 UV, Leica) were cut onto superfrost Plus Gold Slides (Thermo Fisher Scientific). The nuclei were counterstained by 0.5 µg/mL 4,6-diamidino-2-phenylindole (DAPI). The sections were examined by TCS SP2-Leica confocal microscope (Leica).

siRNA-liposome(DSS_6) stability

To evaluate the stability of siRNA-3554 after encapsulation with liposome(DSS)6 in a physiological environment, the complex was incubated with blood serum. In detail, 100 µg of siRNA-3554 in 100 µl of RNAse free water were complexed with 20 mg of liposome in 100 µl of RNAse free water for 20 minutes at RT. For each time point analysed 2 µg of complex or non encapsulated siRNA were incubated with 50 % murine serum at 37°C and collected after 0, 0.5, 1, 4, 9 and 24 hours.

The siRNA was extracted using the NucleoZOL (Marchery-Nagel) solution following the manufacturer instruction. The samples were resuspended in 10 µl of RNAse free water and loaded in a 20 % acrylamide-TBE-SDS gel.

Statistical analysis

All results were expressed as mean ± standard deviation or SEM as specified in figure legends. Statistical comparisons were based on Student's t-test. A $p<0.05$ was considered significant.

Chapter II

INTRODUCTION

Bone fracture healing

The major clinical outcome of Osteogenesis Imperfecta patients is bone fragility causing multiple fractures even in absence of minimal trauma.

The bone healing process is a really well characterized process and its peculiarity is that the correct healing of the bone lead to the production of new bone without scar[230]. This ability is due to the fact that fracture healing recapitulates the ontological processes taking place during embryonic development. Thus fracture healing is considered one of the few postnatal processes truly regenerative[231].

The healing process of the bone involves two phases: an anabolic phase and a catabolic phase, although these two processes are almost contemporary. Indeed even if the anabolic and catabolic processes take place consecutively, they overlap substantially and are a continuum of changing cell populations and signaling processes within the regenerating tissue **(Figure 25)**.

The initial anabolic phase is characterized by an increase in tissue volume related to the *de novo* recruitment and differentiation of stem cells from skeletal and vascular tissues. The anabolic phase is followed by a prolonged phase in which catabolic activities predominate, and is characterized by a reduction in the volume of the callus tissue. Basically the tissues will undergo a swelling process in which cartilaginous tissue and blood vessels will be formed followed by the calcification leading to primary bone formation[232,233]. The increase in the number of blood vessels lead to the cartilaginous tissue development and to the differentiation in the surrounding muscle sheath[234,235] of the soft callus. As the chondrocyte undergo toward differentiation the cartilage extracellular matrix begins to mineralize and the anabolic phase of fracture repair terminates with chondrocyte apoptosis[42,236].

At the same time in some areas of the callus the catabolic phase has already begun. This prolonged catabolic activity, such as cartilage resorption and specific anabolic process, is liable of the callus remodeling and reduction. In this phase the secondary

bone formation is initiated, the cartilage is resorbed and primary angiogenesis continues as the nascent bone tissue replaces the cartilage.

The resorption of the cartilage is carried out by the osteoclasts that resorb also the secondary bone synthetized during the period of cartilage resorption. The long catabolic phase is characterized by coupled cycles of osteoblasts and osteoclasts activity in which the callus tissues are remodeled until the original normal condition restored.

During this period, the marrow space is re-established and the original marrow structure of hematopoietic tissue and bone is regenerated. The extensive vascular bed regresses and the high vascular flow rate returns to its pre-injury status[237,238].

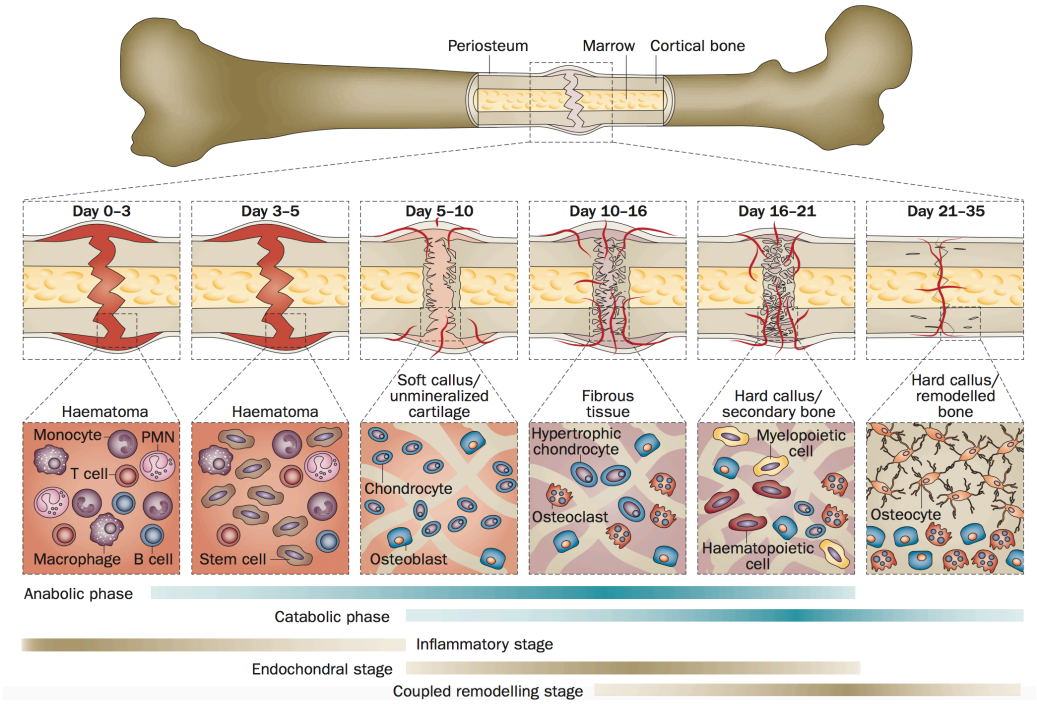

Figure 25. Temporal overview of the biological events during fracture healing in mice. The major metabolic phases (blue bars) of fracture healing overlap with biological stages (brown bars). Both anabolic and catabolic phases of fracture healing are presented in the context of three major biological stages (inflammatory, endochondral bone formation and coupled remodeling). The primary cell types that are found at each stage and the time span of their prevalence in each stage are shown. The time scale of healing is equivalent to a mouse closed femur fracture fixed with an intramedullary rod. Abbreviations: BMP, bone morphogenetic protein; BMPR, bone morphogenetic protein receptor; DKK1, Dickkopf-related protein 1; LRP, LDL-receptor-related protein; MSC, mesenchymal stem cell; PMN, polymorphonuclear leukocyte; PTH, parathyroid hormone; PTHrP, parathyroid-hormone-related protein; RANKL, receptor on nuclear factor κB ligand[220].

During bone fracture healing the final outcome is the recovery of both the original geometry and biomechanical properties of the damaged tissue structure. This process is defined by specific morphogenetic genes and thus is dependent on instructive interactions between various proximate tissues[239]. The healing process recapitulates several stages of endochondral bone development. In bone, undifferentiated mesenchymal cells deriving from the periosteum, the surrounding soft tissues, and the marrow space initiate this process at the site of the damage[240–248].

During the endochondral bone development, undifferentiated mesenchymal cells differentiate into chondrocytes, that proliferate, undergo the process of hypertrophy, ossification, death, vasculogenesis, and finally, are replaced with bone forming osteoblasts[249]. After a fracture, signals that initiate the repair process originate from the bone marrow, injured bone matrix and inflammatory cells that infiltrate the site of injury. The initial injury leads to mesenchymal stem cell recruitment and differentiation[250–252].

The understanding of the basic stages of fracture repair has been well established. A crucial role is unrolling by soluble factors pro-inflammatory cytokines, the TGF-β superfamily, and angiogenic factors **(Figure 26)**[239].

Even if the role of inflammatory cytokines in initiating the repair response has long been known[253,253,254,255], the role of these molecules is only now becoming fully appreciated.

The first type of resorption, in bone healing, take place during the endochondral period in which mineralized cartilage is removed and primary bone formation takes place. Macrophage colony-stimulating factor (M-CSF), receptor activator of nuclear factor kappa-B ligand (RANKL), and osteoprotegerin (OPG) are elevated, yet most of the cytokines that have been associated with bone remodeling, including interleukin (IL) 1a, IL1b, and IL-6, are absent during this period[254,256].

During the secondary bone formation a second type of resorption occurs and is driven solely through the coupled process of remodeling. IL-1 and IL-6 begin to show increased levels of expression while OPG, M-CSF, and RANKL show diminished expression levels. The mechanisms that regulate calcified cartilage resorption and bone are different[257].

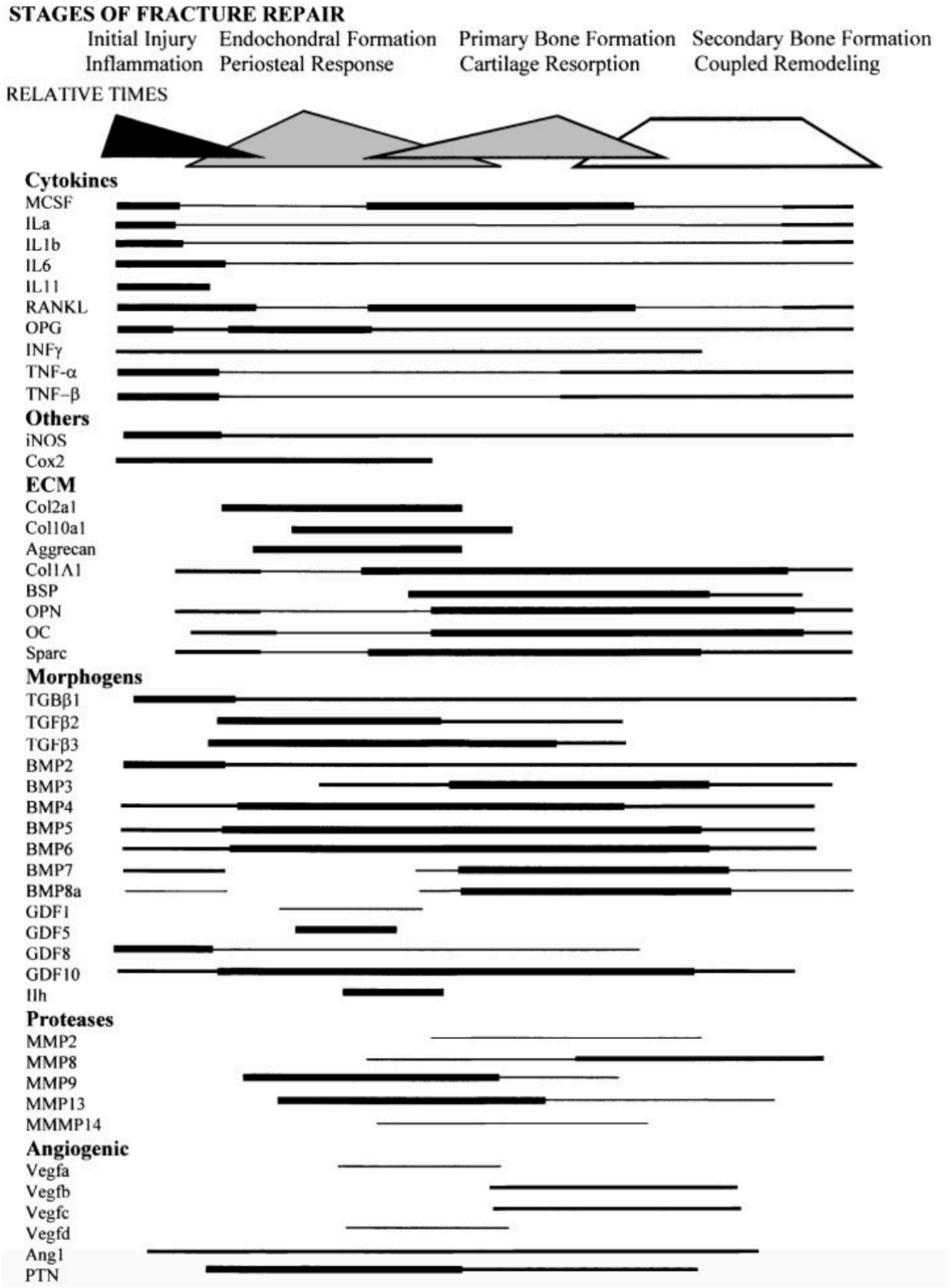

Figure 26. Schematic summary of the stages of fracture repair and their associated molecular processes. Relative levels of mRNAs expression of molecules involved in the healing process. Line thickness indicates low, medium and high expression level, denoted by three line widths[259].

Since 1965 when Urist et al. discovered the connection between demineralized bone and the induction of *de novo* of cartilage and bone at extra skeletal sites[242] the bone morphogenetic proteins (BMPs)[258,259] and the TGF-β superfamily of morphogenetic proteins has been perhaps the most intensively studied group of factors in skeletogenesis and fracture repair[260,261].

The role of endogenous BMPs was defined studding the temporal and spatial distribution of BMP-4 mRNA expression[262]. Specific members of the transforming growth factor-β superfamily was found to act in combinations to promote the various stages of intramembranous and endochondral bone formation observed during fracture healing[263].

Fracture healing creates a demand on the surrounding tissues to increase blood flow so that induction of bone regeneration can occur within the callus. Such dependency of optimal bone healing on the development of an adequate blood flow has been well established in a number of studies of fracture repair and extensively reviewed[264–267]. Furthermore, endochondral ossification in normal fracture healing also requires the coordination of both the molecular mechanisms that regulate the extracellular matrix remodeling and the vascular penetration of new blood vessels into the resorbing matrix[268]. Thus, matrix degradation and angiogenesis are either correlated or concurrent processes during endochondral bone formation. The final stages of endochondral ossification and bone remodeling are dependent on the action of specific matrix metalloproteinases to degrade the cartilage and bone, allowing the invasion of the blood vessels.

Although fracture repair usually restores the damaged skeletal to its pre-injury cellular composition, structure and biomechanical function, the process of regeneration of the bone can depend on the angle of dislocation of fracture and about 10 % of them will not heal normally[220].

Fracture healing in OI

Very limited information is available on the bone healing process of OI patients. For the most a normal healing[269] was reported although cases of hyperplastic callus formation associated to healing delay were described[270–272]. Anyway due to the complexity of obtaining proper tissue samples at different healing stages no data are available on the progression of the different steps of fracture repair in OI. What is known so far comes from few studies performed on OI models. Indeed a better knowledge of bone healing will have an important impact on the understanding the true capability of the different drugs, so far in use for OI treatment to improve the bone quality after the frequent fractures characteristic of the disease.

Bone fracture repair in OI murine models: *Brtl/+* and *Oim/Oim*

The only OI murine model for dominant classical OI deeply used to evaluate the fracture healing process is the *Brtl/+* mouse, carrying in heterozygosis a typical G349C substitution in the α1(I) chain and reproducing the moderate severe outcome of OI type IV patients. The studies were focused on the effect of bisphosphonate administration on the fracture repair[273,274], but some information could be extrapolated from the placebo mutant and WT groups. The analyses were mainly focused on the geometrical and biomechanical properties of the bones at 2, 3 and 5 weeks from fracture performed in 2 months old mice. No difference on callus mineralization was detected between mutant and WT littermates at all time points considered. Tissue Mineral Density (TMD) increased in callus from 2 weeks to 3 weeks and again from 3 to 5 weeks in both mutant and WT animals. Reduced stiffness was reported in *Brtl*/+ at 3 weeks, but no difference was found at 5 weeks. Histological analysis on callus sections after 2 weeks from fracture did not reveal any difference in the amount of cartilage between mutant and WT animals. In both intact and fractured tibia *Brtl*/+ bones showed a decreased crystallinity compared to WT and the callus site revealed an increased carbonate-to-phosphate ratio[273].

The other OI model used to investigate fracture healing process in OI was the *Oim/Oim*[275,276] mouse carrying in homozygosis a mutation in the C-propeptide of the α2 chain of type I collagen. This mouse is an unusual model of recessive OI caused by collagen mutations, but it was widely used as model for severe OI type III due to the high incidence of spontaneous fractures.

The *Oim/Oim* mice were fractured at 6 weeks of age and the healing was evaluated after 2, 3, 4 and 6 weeks. The fracture site was more comminuted in mutant with respect to WT due to extreme bone brittleness of this OI model. Bony union occurred in all mice regardless the genotype by 6 weeks post fracture. Although the number of mice used for the study was quite low, a smaller callus area was detected in mutant mice compared to WT as well as a reduced intensity on X-ray film at 3 and 4 weeks from fracture. No difference in quantity of callus cartilage was found between WT and mutant by histological evaluation.

AIM OF THE WORK

The main clinical outcome in Osteogenesis Imperfecta patients is the occurrence of fractures even in absence of minimal trauma. Very limited information is available on the healing process in OI patients, but detailed knowledge of the repair process is mandatory to evaluate the effect of the drugs used to treat the disease, such as bisphosphonates, anti-RANK antibody or anti-TGFβ antibody. In literature information on the bone healing process in two murine models for OI, the *Oim/Oim* and the *Brtl*/+ mice, is available. The *Oim/Oim* mouse, carrying in homozygosis a mutation in the C-propeptide of the α2 chain of type I collagen, a molecular defect impairing the α2 incorporation in the collagen type I triple helix molecule, is a model for rare form of recessive OI. The *Brtl*/+ mouse, that carries in heterozygosis a typical glycine substitution (G349C) in the α1(I) chain, is a well validate model for classical dominant OI.

A third Osteogenesis Imperfecta mouse model is available in my laboratory, the *Amish*/+ mouse, carrying in heterozygosis a G610C substitution in the α2(I) chain, thus reproducing classical dominant OI caused by mutations in *Col1a2* gene. At the moment no information is available on the bone healing of this mouse and the aim of my project was indeed to investigate this process to contribute to a better understanding of the bone repair in OI.

RESULTS

Bilateral fracture of tibiae in *Amish*/+ and WT mice

Tibiae from *Amish*/+ and control mice (n=21) were fractured and collected at different time points to evaluate the healing process.

The *Amish*/+ mice carry in heterozygosis a G610C substitution in the α2 chain of type I collagen and they were deeply characterized as a valid model for the dominant OI type IV form[84].

A steel pin was inserted in the medullary canal before surgery to generate a composed fracture associated to endochondral ossification.

X-ray analysis of fractured tibiae at different time points in the healing process

The healing process was analysed 2 weeks (WT n=8, *Amish*/+ n=7), 3 weeks (n=6 for both and *Amish*/+), and 5 weeks (n=8 for both WT and *Amish*/+) after surgery.

First X-rays were performed on both legs and the images were used to measure the callus perimeter and area **(Figure 27 A)**.

At 2 weeks no significant difference was detected regarding the perimeter. The callus perimeter of WT mice measured 1.23±0.21 cm and 1.32±0.10 cm for the right and left leg respectively, the *Amish*/+ callus showed a perimeter of 1.08±0.26 cm and 1.25±0.08 cm for the right and left leg, respectively. At 3 weeks after fracture the perimeter of the WT callus was 1.21±0.1 cm and 1.1±0.12 cm for the right and left leg, respectively, and the *Amish*/+ callus showed a perimeter of 1.18±0.16 cm and 1.22±0.14 cm for the right and left leg, respectively and no significant difference was again detected. Finally at 5 weeks after fracture the perimeter of the WT callus was 1.22±0.15 cm and 1.26±0.11 cm for the right and left leg, respectively while for the *Amish*/+ callus was 1.14±0.10 cm and 1.13±0.04 cm for the right and left leg,

respectively. A significant decrease of callus perimeter in the *Amish/+* was detected only for the left leg at 5 weeks after fracture ($p<0.05$) **(Figure 27 B)**.

The callus area was assessed at 2 and 5 weeks after fracture by the calculation of the mean value of sagittal and lateral X-ray performed as described in material and methods section (n=8). A significant decrease in callus area was evident in *Amish/+* mice with respect to WT littermates at 2 weeks 0.065±0.024 mm^2 and 0.097±0.025 mm^2, respectively $p<0.05$. At 5 weeks the callus area of *Amish/+* was still smaller than WT, but the difference was not significant (0,084±0,018 mm^2 and 0.110±0.033 mm^2, respectively, $p=0.078$) **(Figure 27 C)**.

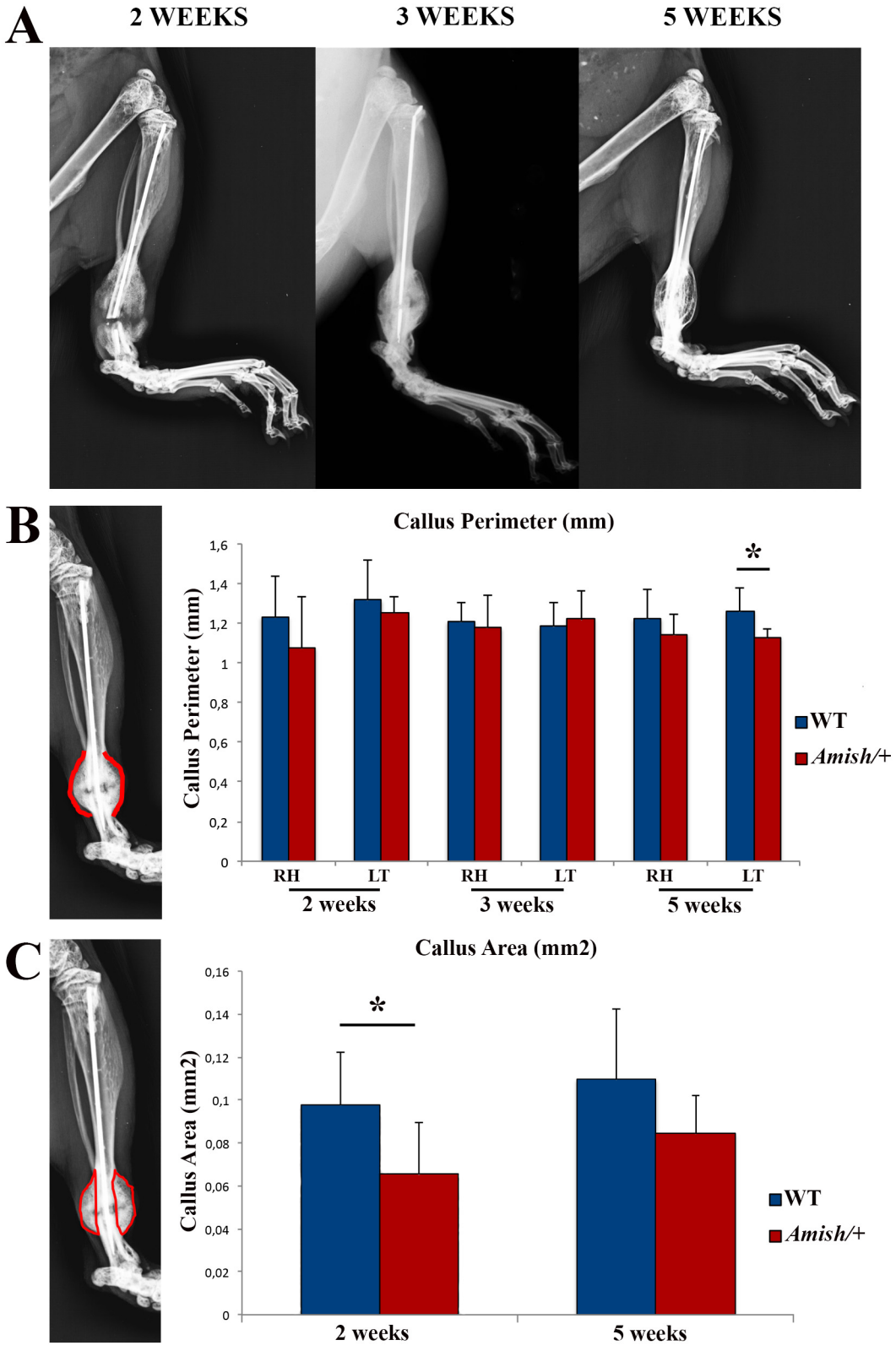

Figure 27. X-ray analysis at different time points during healing of tibiae fracture.

A Representative images of X-ray acquired 2, 3 and 5 weeks after fracture; **B** Callus perimeter analysis of left and right legs for each genotype and time point; **C** Area of the callus of WT and *Amish/+* mice at 2 and 5 weeks after fracture, *=$p<0.05$. The values are expressed as mean±sd.

µCT analysis of fractured tibiae at different time points in the healing process

The geometrical properties of the callus were evaluated by micro Computer Tomography (µCT) as described in material and method section (n=8). One tibia from each fractured mouse was used. Bone Volume (BV), Total Volume (TV), BV/TV, Total Surface (TS), Bone Surface (BS), Intersection Surface, BS/BV, BS/TV, Trabecular Bone Pattern (Tb.Pf.) and Bone Mineral Density (BMD) were evaluated. A significant decrease in *Amish/+* calli compared to WT littermates was detected for the BV (6.65±2.92 mm^3 and 11.81±4.73 mm^3 respectively, $p<0.05$) and for BS (231.44±92.81 mm^3 and 343.34±99.21 mm^3 respectively, $p<0.05$) 2 weeks after fracture **(Figure 28)**.

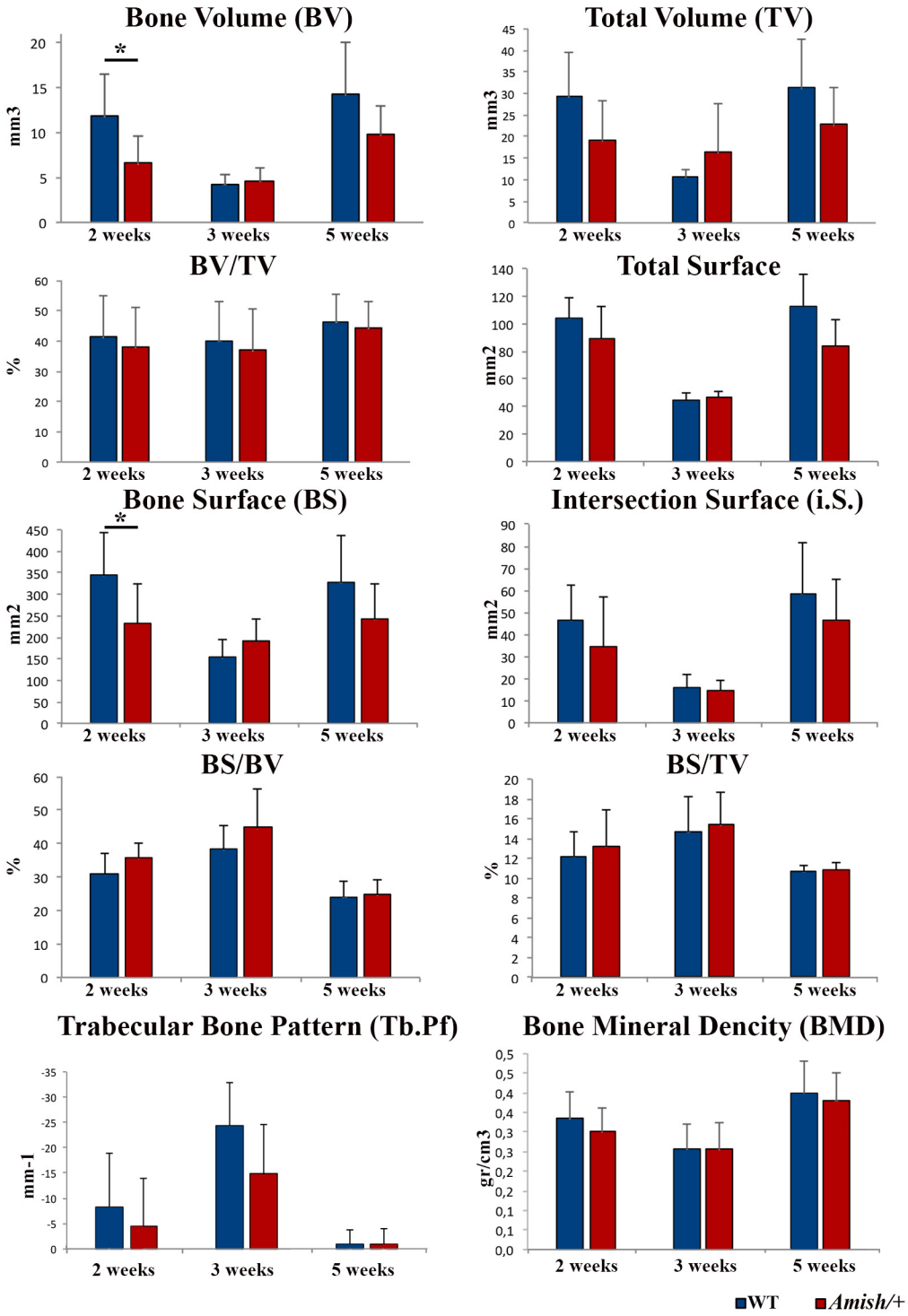

Figure 28. µCT analysis at different time points during healing of tibiae fracture.

µCT callus parameters measured 2, 3 and 5 weeks after fracture (n=8). Bone volume and bone surface in the *Amish*/+ samples, 2 weeks after fracture, were significantly reduced in comparison to the WT littermates (*=$p<0.05$). The values are expressed as mean±sd.

Collagen type I and CNBr collagen peptides analysis

To evaluate the bone healing process from a biochemical point of view, collagen type I analysis was performed. Collagen was extracted by means of pepsin digestion from callus 2 and 3 weeks after fracture and analysed by SDS-PAGE. A first polyacrylamide-urea-SDS gel was used to separate the monomer α chains of the collagen type I **(Figure 29 A)**. The densitometric analysis of the α1 and α2 bands, that in collagen type I has a ratio α1/α2=2:1 given the collagen chain stoichiometry, revealed a higher ratio α1/α2=2.75:1 in callus samples. In callus the cartilage tissue is present before bone formation and collagen type II, whose α1 chains have the same electrophoretic migration of the α1 chain of type I collagen, is its main component. Thus we hypothesized that the higher α1/α2 ratio in the collagen extracted from callus was due to the presence of a certain amount of collagen type II.

The quantitation of collagen type II versus collagen type I could be used to evaluate the repair phase of the fracture since a persistence of cartilage will indicate a delay in the bone formation. To this aim the comigrating α1(I) and α1(II) bands were cut and digested with cyanogen bromide (CNBr). A peculiar feature of collagen α chains is to have a certain number of methionine residues in the triple helical domain that, following digestion using CNBr, will generate CNBr peptides of specific size. These peptides are different in the α1(I) and α1(II) chains giving rise to specific CB maps **(Figure 29 B)**. Following in gel-digestion the α1 band was loaded in a second polyacrylamide-urea-SDS gel to discriminate the different CB peptides **(Figure 29 C)**. To evaluate the amount of cartilaginous tissue in the callus the intensity analysis of the peptide bands corresponding to the cianobromide peptide 10 (CB10) of α1(II) and CB6 belonging to α1(I) were evaluated and their ratio calculated. The CB10/CB6 ratio was 2.45±1.27 in WT samples and 5.34±3.68 in *Amish/+* callus 2 weeks after fracture, and 0.82±0.46 in WT and 1.71±0.78 in mutant 3 weeks after fracture. The ratio CB10/CB6 was significantly higher in mutant mice 2 weeks after fracture ($p<0.03$) suggesting a delay in the bone formation **(Figure 29 D)**. The ratio remained higher in mutant mice compared to WT also after 3 weeks from fracture, but the difference was not significant ($p=0.12$).

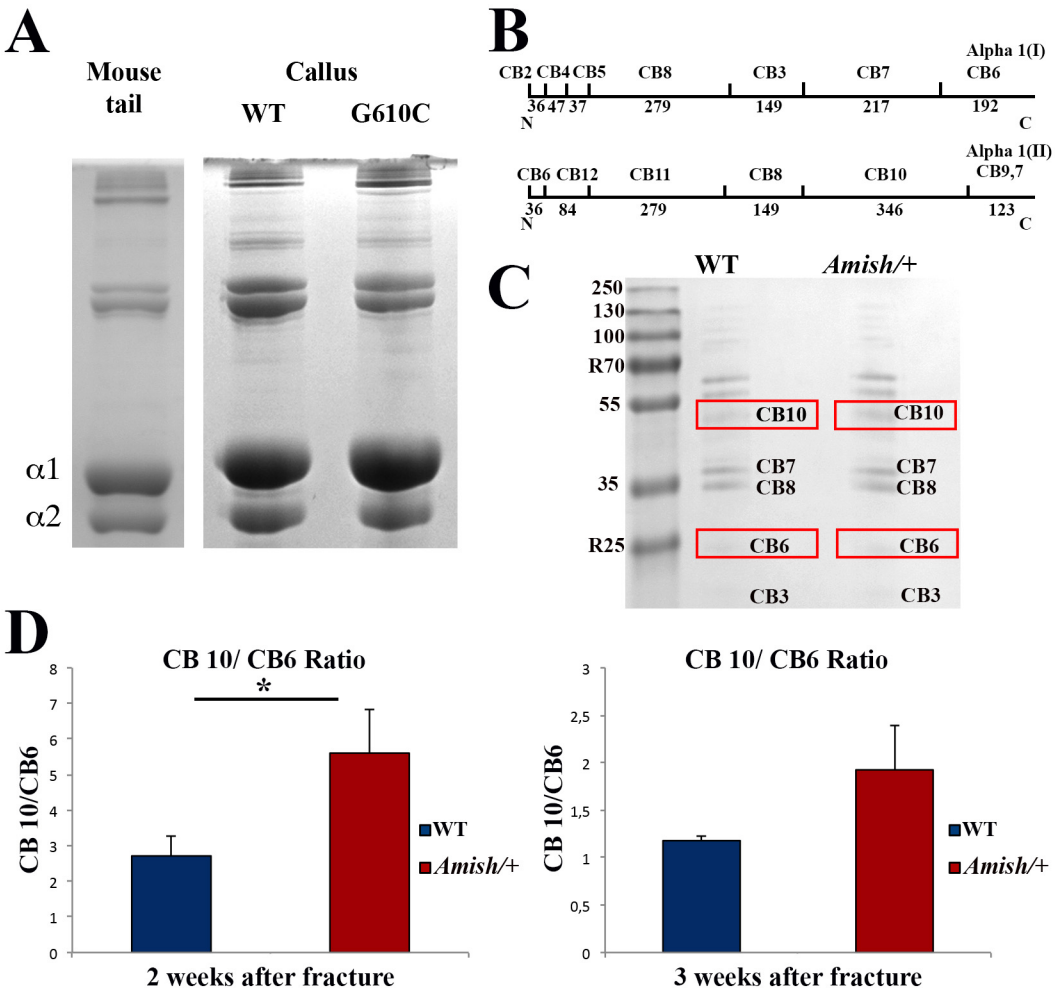

Figure 29. Collagen type I analysis at different time points during healing of tibiae fracture.

A Representative polyacrylamide-urea-SDS gels of collagen type I extracted from mouse tail and from callus; **B** Maps of Methionine residues position along the α1 chains of collagen type I and II and their specific cyanogen bromide (CNBr) peptides (CB) with proper size (number of amino acids); **C** Representative SDS-Urea-PAGE separation of collagen peptides obtained from CNBr digestion of α1 band; **D** Ratio between α1(II) CB10 and α1(I) CB6 quantified on cianobromide peptide gels. The ratio CB10/CB6 was significantly increased in *Amish/+* mice in comparison to the WT 2 weeks after fractures (*=p<0,03) (n=11 and 7 for WT and *Amish/+* respectively). The values are expressed as mean±SEM.

DISCUSSION

Fracture healing in Osteogenesis Imperfecta patients:

a difficult field to study

Osteogenesis Imperfecta is a phenotypically and molecularly heterogeneous group of connective tissue disorders that share a common phenotype: bone fragility in absence of minimal trauma. Given the fragility, bones are susceptible to fractures and the management of multiple fractures is one of the main problem affecting OI patients[277].

Even if fractures are very common in OI, fracture healing, the physiologic process that restores the functional and biomechanical competency of the injured bone, has been very poorly investigated. Few cases of hyperplastic callus formation associated to healing delay were described in patients together with the presence of an higher frequency of non-union fractures[270–272]. No information is available on the progression of fracture repair in OI patients due to the complexity of obtaining tissue samples at different healing stages from patients, and controls.

Mutation in *Col1a2* lead to the delay in the healing process

The knowledge of the pathophysiological mechanism of the osteogenetic healing process is anyway mandatory both to develop treatments and to evaluate the effects of different treatments since the fracture healing is commonly used as a model system.

What is known so far comes from very few studies performed on OI mouse models, the unique tools available to dissect this biological process.

For what concern the *Brtl/+* murine model[80] for dominant classical OI, carrying a mutation in the *Col1a1* gene, the analyses were mainly focused on the geometrical and biomechanical properties of the bones at 2, 3 and 5 weeks after fracture in 2 months old mice. No differences on callus size, mineralization and amount of cartilage between mutant and WT littermates were detected[81]. A reduced stiffness together with a decreased crystallinity and an increased carbonate-to-phosphate ratio at callus site

were detected in *Brtl*/+ mice 3 weeks after fracture. These data suggested that even if the turn over of the bone is lower in the *Brtl*/+ mice, there is no evidence of a delay in the healing process[273].

Interestingly, the study on the bone healing process in the *Oim/Oim* mouse[278], an unusual model of recessive OI carrying a mutation in the *Col1a2* gene, revealed the presence of more comminuted fractures, a decreased callus area together with a reduced X-ray callus density at 3 and 4 weeks after fracture that was normalized at 6 weeks, suggesting a possible impairment in the initial repair phases[275].

To clarify whether the OI healing process was truly dependent on the type of gene involved, *COL1A1* versus *COL1A2*, or on the transmission of the disease, dominant versus recessive, we evaluated the healing process in a third OI model, the *Amish/*+ mouse[84], model of dominant OI carrying in heterozygosis a G610C substitution in the α2 chain of type I collagen. Our experiment demonstrated in *Amish/*+ mice 2 weeks after fracture a reduced callus size and lower bone volume and bone surface together with a higher presence of cartilaginous tissue indicating a delay of the healing process.

Since a compromised bone healing was suggested in the *Oim/Oim* and we found a delay in the *Amish/*+ model, but in the *Brtl/*+ mouse the healing process was reported to be similar to WT, it seems that mutations in the *Col1a2* gene are particular harmful for the healing process. This is surprising given collagen stoichiometry, mutations in the *COL1A1* gene produce 75 % of mutated collagen, while cells with mutations in the *COL1A2* gene only 50 %, thus is seems unlikely that a more disruptive effect will be associated to *COL1A2* defects. Indeed higher level of mutant collagen is supposed to negatively affect more the new bone formation.

The differences among the OI mouse models could be correlated to the different positions of the mutations, feature that play a major role in influencing the severity of the phenotype[49]. Studies using OI murine models and human patients cells revealed that mutations in collagen genes delay the triple helix formation, thus prolonging for the single α chains the ER exposure time to the action of enzymes responsible for post-translational modifications[279]. Since the three collagen α chains are folding in a zipper like fashion from C- to N- terminal end, mutations at the C-terminal end cause higher degree of post-translational hydroxylation and glycosylation. Thus collagen over-

modification level is strictly dependent on the position of the mutation along the chains. In the *Amish*/+ model a more C-terminal mutation (G610C) is present and this can account for the more severe phenotype compared to *Brtl*/+ mouse (G349C). In addition, in both models the presence as substitutive amino acid of a cysteine residue that can form disulphide bounds with other extracellular molecules complicates the interpretation.

Furthermore it is important to take in consideration that in the *Amish*/+ model we performed a biochemical assay to quantify the presence of cartilage at the callus site, assay that was not performed either in the *Brtl*/+ mouse or in *Amish*/+. Direct comparison of histological and biochemical data should be performed to achieve proper conclusions. Indeed histological examination of the callus at the different time points after fracture is ongoing in the lab.

In the *Amish*/+ model the delay in healing was detected only in the first step of the process, 2 weeks after fracture, the anabolic phase begins, suggesting a delay in the differentiation/recruitment of the bone cells.

Very interestingly, mice deficient in the collagen receptor integrin α1β1, that mediates cell adhesion to extracellular matrix components, developed significantly less callus tissue than the wild type mice, and showed defects in cartilage formation until two weeks after fracture, demonstrating the importance of proper collagen-integrin interaction in fracture healing[280]. In particular, the collagen-integrin interaction was shown to play an essential role in the regulation of MSC proliferation.

The understanding of the healing process will permit both a more conscious and targeted administration of drug treatments and a more precise screening of OI therapies.

MATERIALS AND METHODS

Animals

The *Amish*/+ mice (C57Bl/6) carrying in heterozygosis the G610C substitution in the α2 chain of collagen type I were kindly provided by Prof Charlotte Phillips, University of Missouri-Colombia, USA[84]. C57BL/6 littermates were used as controls. The animals were maintained in the animal facility at the Department of Molecular Medicine of the University of Pavia according to the current laws on the animal care. All the experiments were approved by the OPBA (Office for the Animals Welfare) of the University of Pavia and by the Italian Ministry of Health.

Genotyping

DNA isolated from tail biopsies of 21-day-old mice was genotyped by PCR using the following primers: forward primer

5'-TCCCTGCTTGCCCTAGTCCCAAAGATCCTT-3' (4530303-4530332 bp NC_000072.6); and reverse

5'-AGGGTATAGATCAGACAGCTGGCACATCCA-3' (4530468-4530439 bp NC_000072.6). The PCR cycle consisted of e a predenaturation step at 94°C for 10 min followed by 94°C for 30 sec, 68°C for 30 sec, and 72°C for 30 sec for 40 cycles then a final extension step at 72°C for 10 minutes. The amplicons of 165 bp for the wild type allele and 337 bp for the mutant allele were separated on 1 % agarose gel.

Tibia fracture

24 G610C (C57BL/6) and 24 WT littermate mice 2 month old were used for the study of the bone healing process. The mice were divided in 3 groups with 8 mice for each genotype. Mice were anesthetized and on both tibias a pin was inserted in the intramedullary canal; the cut made to insert the pin was sutured with a resorbable suture thread. Using a device, which exploits a three-point force theory, a bilateral

composed fracture approximately at ¼ of distance from the distal proximity of the tibiae of the mice was performed.

X-ray analysis

The mice were sacrificed at three different time points: 2, 3, 5 weeks after fracture in groups of 8 mice for each time point and genotype. Immediately after the euthanasia X-ray was performed using the Faxitron Mx-20 (Faxitron) set at 25kV for 19 second, the radiographic cassettes were acquired using the Kodak DirectView elite CR System K-Pacs software (KodaK). Callus perimeter and callus area were evaluated using Leica application suite V 4.5. For the area the mean value of sagittal and lateral X-ray were considered.

µCT analysis

One fractured tibia from each mouse was dissected, cleaned from soft tissues, fixed with 4 % PFA for 24 hours, washed with PBS and stored at 4°C until analysis. The tibias were scanned at a pixel size of 9 µm with using the SkyScan1076 *in-vivo* micro-CT (Bruker) a high-resolution cone-beam micro-CT scanner.

Each tibia was scanned in air, an aluminum filter was used to remove image noise. Average scan duration was 21 minutes with 360° of rotation and the X-ray tube voltage was set at 49kV and the X-ray intensity was 200 µA. The ring artifact correction was 6, and the beam hardening correction was 10 %.

Bone parameters were calculated using the Skyscan CT Analyzer (CTAn) software. Using this software, the volume of interest was manually defined as callus formation.

Binarized images were performed: an upper threshold of 255 and a lower threshold of 35 were used to delineate each pixel as “bone” or “non-bone”.

A set of 2 hydroxyapatite (HA) phantoms were scanned and used for calibration to BMD. Bone Volume (BV), Total Volume (TV), BV/TV, Total Surface, Bone Surface (BS), Intersection Surface, BS/BV, BS/TV, Trabecular Bone Pattern (Tb.Pf.) and Bone Mineral Density (BMD) were evaluated.

Collagen analysis

The contralateral fractured tibia was used for collagen analysis. The callus, cleaned from surrounding soft tissue, was washed in PBS and minced. The sample was then decalcified in 0.5 M EDTA pH 7.1 at 4°C for 7 days, changing the solution every other day. Collagen was extracted by means of pepsin digestion. Briefly after wash with PBS the bone chips were digested with 0.1 mg/ml pepsin in 0.5 M acetic acid at 4°C for seven days. The collagen was precipitated with 0.9 M NaCl in 0.5 M acetic acid, washed in 70 % EtOH and lyophilized. The pellet was resuspended in 0.5 M acetic acid and 5 µl were lyophilized and resuspended in 10µl of 1 X Laemmli buffer[226] (62.5 mM Tris HCl, pH 6.8, 10 % glycerol, 2 % sodium dodecyl sulphate (SDS), 0.02 % bromophenol blue), denatured at 80°C for 5 minutes and separated on 6 % polyacrylamide-urea-SDS gels. The gel was stained with Coomasie Picric Staining[227] and acquired by Versadoc (Biorad). The bands intensity was measured using Quantity one software (Biorad). Based on the results obtained from the 1D SDS-PAGE an equal amount of each sample was loaded to obtain an equal loading for all the samples. The gel was then stained with Coomassie Blue[281]. The α1(I) band was cut and digested for 2 hours with a solution 25 % cyanogen bromide, 75 % Formic acid under steering. The band was than washed with deionized water, incubated with 1 X Laemmli buffer for 10 min at 90°C and loaded on 12 % polyacrylamide-urea-SDS gels. The gel was stained with Coomassie Picric Staining and acquired by Versadoc (Biorad). The intensity of the bands corresponding to the collagen CB peptides CB10 (II) and CB6 (I) was determined using Quantity one software (Biorad). For the identification of the CB10 peptide of type II collagen a purified type II collagen extracted from calf cartilage was used as standard. For the identification of the CB6 peptide of type I collagen a purified type I collagen extracted from tails tendon was used as standard.

Statistical analysis

All results were expressed as mean ± standard deviation or SEM as specified in figure legends. Statistical comparisons were based on Student's t-test. A $p<0.05$ was considered significant.

BIBLIOGRAPHY

1. Birk, D. E., Fitch, J. M., Babiarz, J. P. & Linsenmayer, T. F. Collagen type I and type V are present in the same fibril in the avian corneal stroma. *J. Cell Biol.* **106,** 999–1008 (1988).
2. Sandberg, M. M., Hirvonen, H. E., Elima, K. J. & Vuorio, E. I. Co-expression of collagens II and XI and alternative splicing of exon 2 of collagen II in several developing human tissues. *Biochem. J.* 595–602 (1993).
3. Kadler, K. Extracellular matrix 1: Fibril-forming collagens. *Protein Profile* **2,** 491–619 (1995).
4. Seibel, M. J., Robins, S. P. & Bilezikian, J. P. *Dynamics of bone and cartilage metabolism*. (Academic Press, 2006).
5. Shoulders, M. D. & Raines, R. T. Collagen Structure and Stability. *Annu Rev Biochem* **78,** 929–958 (2010).
6. Gelse, K. Collagens—structure, function, and biosynthesis. *Adv. Drug Deliv. Rev.* **55,** 1531–1546 (2003).
7. Ramachandran, G. N. & Kartha, G. Structure of Collagen. 1954, 1955. *Natl. Med. J. India* **19,** 348–52
8. Beck, K. *et al.* Destabilization of osteogenesis imperfecta collagen-like model peptides correlates with the identity of the residue replacing glycine. *Proc. Natl. Acad. Sci. U. S. A.* **97,** 4273–8 (2000).
9. Brazel, D. *et al.* Completion of the amino acid sequence of the alpha 1 chain of human basement membrane collagen (type IV) reveals 21 non-triplet interruptions located within the collagenous domain. *Eur. J. Biochem.* **168,** 529–36 (1987).
10. Bella, J., Eaton, M., Brodsky, B. & Berman, H. M. Crystal and molecular structure of a collagen-like peptide at 1.9 A resolution. *Science* **266,** 75–81 (1994).
11. Berg, R. A. & Prockop, D. J. The thermal transition of a non-hydroxylated form of collagen. Evidence for a role for hydroxyproline in stabilizing the triple-helix of collagen. *Biochem. Biophys. Res. Commun.* **52,** 115–20 (1973).
12. Brodsky, B. & Persikov, A. V. Molecular structure of the collagen triple helix. *Advances in Protein Chemistry* **70,** 301–339 (2005).
13. Brinckmann, J. Collagens at a glance. *Topics in Current Chemistry* **247,** 1–6 (2005).
14. Gelse, K., Pöschl, E. & Aigner, T. Collagens--structure, function, and biosynthesis. *Adv. Drug Deliv. Rev.* **55,** 1531–46 (2003).
15. Yamauchi, M. & Sricholpech, M. Lysine post-translational modifications of collagen. *Essays Biochem.* **52,** 113–33 (2012).
16. Gordon, M. K. & Hahn, R. A. Collagens. *Cell Tissue Res.* **339,** 247–57 (2010).
17. Singh, B., Fleury, C., Jalalvand, F. & Riesbeck, K. Human pathogens utilize host extracellular matrix proteins laminin and collagen for adhesion and invasion of the host. *FEMS Microbiol. Rev.* **36,** (2012).
18. Ottani, V., Raspanti, M. & Ruggeri, A. Collagen structure and functional implications. *Micron* **32,** 251–60 (2001).
19. Deshmukh, S. N., Dive, A. M., Moharil, R. & Munde, P. Enigmatic insight into

collagen. *J. Oral Maxillofac. Pathol.* **20,** 276–83 (2016).
20. Kuznetsova, N. V, Forlino, A., Cabral, W. A., Marini, J. C. & Leikin, S. Structure, stability and interactions of type I collagen with GLY349-CYS substitution in α1(I) chain in a murine Osteogenesis Imperfecta model. *Matrix Biol.* **23,** 101–112 (2004).
21. Symoens, S. *et al.* Type I Procollagen C-Propeptide Defects: Study of Genotype-Phenotype Correlation and Predictive Role of Crystal Structure. *Hum. Mutat.* **35,** n/a-n/a (2014).
22. Forlino, A., Cabral, W. a, Barnes, A. M. & Marini, J. C. New perspectives on osteogenesis imperfecta. *Nat. Rev. Endocrinol.* **7,** 540–557 (2011).
23. Wenstrup, R. J. *et al.* Type V collagen controls the initiation of collagen fibril assembly. *J. Biol. Chem.* **279,** 53331–7 (2004).
24. Fan, D., Takawale, A., Lee, J. & Kassiri, Z. Cardiac fibroblasts, fibrosis and extracellular matrix remodeling in heart disease. *Fibrogenesis Tissue Repair* **5,** 15 (2012).
25. van Dijk, F. S. *et al.* Osteogenesis Imperfecta: A Review with Clinical Examples. *Mol. Syndromol.* **2,** 1–20 (2011).
26. Rossert, J., Terraz, C. & Dupont, S. Regulation of type I collagen genes expression. *Nephrol. Dial. Transplant* **15 Suppl 6,** 66–8 (2000).
27. Shoulders, M. D. & Raines, R. T. Collagen structure and stability. *Annu. Rev. Biochem.* **78,** 929–58 (2009).
28. Hudson, D. M., Kim, L. S., Weis, M., Cohn, D. H. & Eyre, D. R. Peptidyl 3-hydroxyproline binding properties of type I collagen suggest a function in fibril supramolecular assembly. *Biochemistry* **51,** 2417–24 (2012).
29. Ishikawa, Y. & Bächinger, H. P. A molecular ensemble in the rER for procollagen maturation. *Biochim. Biophys. Acta* **1833,** 2479–91 (2013).
30. Dai, N. & Etzkorn, F. A. Cis-trans proline isomerization effects on collagen triple-helix stability are limited. *J. Am. Chem. Soc.* **131,** 13728–13732 (2009).
31. Engel, J. & Prockop, D. J. The zipper-like folding of collagen triple helices and the effects of mutations that disrupt the zipper. *Annu. Rev. Biophys. Biophys. Chem.* **20,** 137–52 (1991).
32. Lamandé, S. R. & Bateman, J. F. Procollagen folding and assembly: the role of endoplasmic reticulum enzymes and molecular chaperones. *Semin. Cell Dev. Biol.* **10,** 455–64 (1999).
33. van Dijk, F. S. *et al.* PPIB Mutations Cause Severe Osteogenesis Imperfecta. *Am. J. Hum. Genet.* **85,** 521–527 (2009).
34. Tasab, M., Batten, M. R. & Bulleid, N. J. Hsp47: a molecular chaperone that interacts with and stabilizes correctly-folded procollagen. *EMBO J.* **19,** 2204–2211 (2000).
35. Bekhouche, M. & Colige, A. The procollagen N-proteinases ADAMTS2, 3 and 14 in pathophysiology. *Matrix Biol.* **44,** 46–53 (2015).
36. Canty, E. G. & Kadler, K. E. Procollagen trafficking, processing and fibrillogenesis. *J. Cell Sci.* **118,** 1341–1353 (2005).
37. Charles, P., Mosekilde, L., Risteli, L., Risteli, J. & Eriksen, E. F. Assessment of bone remodeling using biochemical indicators of type I collagen synthesis and degradation: relation to calcium kinetics. *Bone Min.* **24,** 81–94 (1994).
38. Hulmes, D. J. S. Building Collagen Molecules, Fibrils, and Suprafibrillar Structures. *J. Struct. Biol.* **137,** 2–10 (2002).

39. Bruckner, P. Suprastructures of extracellular matrices: paradigms of functions controlled by aggregates rather than molecules. *Cell Tissue Res.* **339,** 7–18 (2010).
40. Jastrzebska, M. *et al.* New insight into the shortening of the collagen fibril D-period in human cornea. *J. Biomol. Struct. Dyn.* 1–13 (2016). doi:10.1080/07391102.2016.1153520
41. Primorac, D., Anti, D., Bari, I., Hudetz, D. & Ivkovi, A. Osteogenesis Imperfecta – Multi-Systemic and Life-Long Disease that Affects Whole Family. **38,** 767–772 (2014).
42. Steiner, R. D., Adsit, J. & Basel, D. *COL1A1/2-Related Osteogenesis Imperfecta*. *GeneReviews(®)* (1993).
43. Lowenstein, E. J. Osteogenesis imperfecta in a 3,000-year-old mummy. *Childs. Nerv. Syst.* **25,** 515–6 (2009).
44. Sillence, D. O., Senn, A. & Danks, D. M. Genetic heterogeneity in osteogenesis imperfecta. *J. Med. Genet.* **16,** 101–116 (1979).
45. Byers, P. H., Tsipouras, P., Bonadio, J. F., Starman, B. J. & Schwartz, R. C. Perinatal lethal osteogenesis imperfecta (OI type II): a biochemically heterogeneous disorder usually due to new mutations in the genes for type I collagen. *Am. J. Hum. Genet.* **42,** 237–248 (1988).
46. Marini, J. C. & Blissett, A. R. New genes in bone development: what's new in osteogenesis imperfecta. *J. Clin. Endocrinol. Metab.* **98,** 3095–103 (2013).
47. Sillence, D. O. & Rimoin, D. L. Classification of osteogenesis imperfect. *Lancet (London, England)* **1,** 1041–2 (1978).
48. Forlino, A. & Marini, J. C. Osteogenesis imperfecta. *Lancet (London, England)* **387,** 1657–71 (2016).
49. Marini, J. C. *et al.* Consortium for osteogenesis imperfecta mutations in the helical domain of type I collagen: regions rich in lethal mutations align with collagen binding sites for integrins and proteoglycans. *Hum. Mutat.* **28,** 209–21 (2007).
50. Forlino, A., Cabral, W. A., Barnes, A. M. & Marini, J. C. New perspectives on osteogenesis imperfecta. *Nat. Rev. Endocrinol.* **7,** 540–57 (2011).
51. Basel, D. & Steiner, R. D. Osteogenesis imperfecta: recent findings shed new light on this once well-understood condition. *Genet. Med.* **11,** 375–85 (2009).
52. Sillence, D. Osteogenesis imperfecta: an expanding panorama of variants. *Clin Orthop Relat Res* 11–25 (1981).
53. Primorac, D. *et al.* Osteogenesis imperfecta at the beginning of bone and joint decade. *Croat. Med. J.* **42,** 393–415 (2001).
54. Vetter, U., Pontz, B., Zauner, E., Brenner, R. E. & Spranger, J. Osteogenesis imperfecta: a clinical study of the first ten years of life. *Calcif. Tissue Int.* **50,** 36–41 (1992).
55. Martínez-Glez, V. *et al.* Identification of a mutation causing deficient BMP1/mTLD proteolytic activity in autosomal recessive osteogenesis imperfecta. *Hum. Mutat.* **33,** 343–50 (2012).
56. Asharani, P. V *et al.* Attenuated BMP1 function compromises osteogenesis, leading to bone fragility in humans and zebrafish. *Am. J. Hum. Genet.* **90,** 661–74 (2012).
57. Ishikawa, Y., Wirz, J., Vranka, J. A., Nagata, K. & Bächinger, H. P. Biochemical characterization of the prolyl 3-hydroxylase 1.cartilage-associated

protein.cyclophilin B complex. *J. Biol. Chem.* **284,** 17641–7 (2009).
58. Morello, R. *et al.* CRTAP Is Required for Prolyl 3- Hydroxylation and Mutations Cause Recessive Osteogenesis Imperfecta. *Cell* **127,** 291–304 (2006).
59. Baldridge, D. *et al.* CRTAP and LEPRE1 mutations in recessive osteogenesis imperfecta. *Hum. Mutat.* **29,** 1435–42 (2008).
60. Cabral, W. a *et al.* Prolyl 3-hydroxylase 1 deficiency causes a recessive metabolic bone disorder resembling lethal/severe osteogenesis imperfecta. *Nat. Genet.* **39,** 359–365 (2007).
61. Shaheen, R. *et al.* Study of autosomal recessive osteogenesis imperfecta in Arabia reveals a novel locus defined by TMEM38B mutation. *J. Med. Genet.* **49,** 630–635 (2012).
62. Lindert, U. *et al.* Molecular Consequences of the SERPINH1/HSP47 Mutation in the Dachshund Natural Model of Osteogenesis Imperfecta. *J. Biol. Chem.* **290,** 17679–89 (2015).
63. Barnes, A. M. *et al.* Absence of FKBP10 in recessive type XI osteogenesis imperfecta leads to diminished collagen cross-linking and reduced collagen deposition in extracellular matrix. *Hum. Mutat.* **33,** 1589–98 (2012).
64. Kelley, B. P. *et al.* Mutations in FKBP10 cause recessive osteogenesis imperfecta and bruck syndrome. *J. Bone Miner. Res.* **26,** 666–672 (2011).
65. Ha-Vinh, R. *et al.* Phenotypic and molecular characterization of Bruck syndrome (osteogenesis imperfecta with contractures of the large joints) caused by a recessive mutation in *PLOD2*. *Am. J. Med. Genet. Part A* **131A,** 115–120 (2004).
66. Semler, O. *et al.* A mutation in the 5′-UTR of IFITM5 creates an in-frame start codon and causes autosomal-dominant osteogenesis imperfecta type v with hyperplastic callus. *Am. J. Hum. Genet.* **91,** 349–357 (2012).
67. Moffatt, P. *et al.* Bril: a novel bone-specific modulator of mineralization. *J. bone Miner. Res. Off. J. Am. Soc. Bone Miner. Res.* **23,** 1497–1508 (2008).
68. Glorieux, F. H. *et al.* Type V osteogenesis imperfecta: a new form of brittle bone disease. *J. Bone Miner. Res.* **15,** 1650–8 (2000).
69. Li, F., Song, N., Tombran-Tink, J. & Niyibizi, C. Pigment epithelium-derived factor enhances differentiation and mineral deposition of human mesenchymal stem cells. *Stem Cells* **31,** 2714–23 (2013).
70. Vranka, J. A., Sakai, L. Y. & Bächinger, H. P. Prolyl 3-hydroxylase 1, enzyme characterization and identification of a novel family of enzymes. *J. Biol. Chem.* **279,** 23615–21 (2004).
71. Glorieux, F. H. *et al.* Osteogenesis imperfecta type VI: a form of brittle bone disease with a mineralization defect. *J. Bone Miner. Res.* **17,** 30–8 (2002).
72. Bradshaw, A. D., Graves, D. C., Motamed, K. & Sage, E. H. SPARC-null mice exhibit increased adiposity without significant differences in overall body weight. *Proc. Natl. Acad. Sci. U. S. A.* **100,** 6045–50 (2003).
73. Mendoza-Londono, R. *et al.* Recessive Osteogenesis Imperfecta Caused by Missense Mutations in SPARC. *American Journal of Human Genetics* (2015). doi:10.1016/j.ajhg.2015.04.021
74. Nakashima, K. *et al.* The novel zinc finger-containing transcription factor Osterix is required for osteoblast differentiation and bone formation. *Cell* **108,** 17–29 (2002).
75. Lapunzina, P. *et al.* Identification of a frameshift mutation in osterix in a patient

with recessive osteogenesis imperfecta. *Am. J. Hum. Genet.* **87,** 110–114 (2010).
76. Laine, C. M. *et al.* WNT1 mutations in early-onset osteoporosis and osteogenesis imperfecta. *N. Engl. J. Med.* **368,** 1809–16 (2013).
77. Pyott, S. M. *et al.* WNT1 mutations in families affected by moderately severe and progressive recessive osteogenesis imperfecta. *Am. J. Hum. Genet.* **92,** 590–7 (2013).
78. Symoens, S. *et al.* Deficiency for the ER-stress transducer OASIS causes severe recessive osteogenesis imperfecta in humans. *Orphanet J. Rare Dis.* **8,** 154 (2013).
79. Lindert, U. *et al.* MBTPS2 mutations cause defective regulated intramembrane proteolysis in X-linked osteogenesis imperfecta. *Nat. Commun.* **7,** 11920 (2016).
80. Forlino, A., Porter, F. D., Lee, E. J., Westphal, H. & Marini, J. C. Use of the Cre/lox recombination system to develop a non-lethal knock-in murine model for osteogenesis imperfecta with an alpha1(I) G349C substitution. Variability in phenotype in BrtlIV mice. *J. Biol. Chem.* **274,** 37923–31 (1999).
81. Kozloff, K. M. *et al.* Brittle IV mouse model for osteogenesis imperfecta IV demonstrates postpubertal adaptations to improve whole bone strength. *J. Bone Miner. Res.* **19,** 614–22 (2004).
82. Forlino, A. *et al.* Differential expression of both extracellular and intracellular proteins is involved in the lethal or nonlethal phenotypic variation of BrtlIV, a murine model for osteogenesis imperfecta. *Proteomics* **7,** 1877–91 (2007).
83. Bianchi, L. *et al.* Altered cytoskeletal organization characterized lethal but not surviving Brtl+/- mice: insight on phenotypic variability in osteogenesis imperfecta. *Hum. Mol. Genet.* **24,** 6118–33 (2015).
84. Daley, E. *et al.* Variable bone fragility associated with an Amish COL1A2 variant and a knock-in mouse model. *J. Bone Miner. Res.* **25,** 247–61 (2010).
85. Masci, M. *et al.* Bone mineral properties in growing Col1a2(+/G610C) mice, an animal model of osteogenesis imperfecta. *Bone* **87,** 120–9 (2016).
86. Jeong, Y. *et al.* Hindlimb Skeletal Muscle Function and Skeletal Quality and Strength in +/ *G610C* Mice With and Without Weight-Bearing Exercise. *J. Bone Miner. Res.* **30,** 1874–1886 (2015).
87. Gentry, B. A., Ferreira, J. A., McCambridge, A. J., Brown, M. & Phillips, C. L. Skeletal muscle weakness in osteogeneis imperfecta mice. *Matrix Biol.* **29,** 638–644 (2010).
88. Mirigian, L. S. *et al.* Osteoblast Malfunction Caused by Cell Stress Response to Procollagen Misfolding in α2(I)-G610C Mouse Model of Osteogenesis Imperfecta. *J. Bone Miner. Res.* **31,** 1608–16 (2016).
89. Mertz, E. L. *et al.* Makings of a brittle bone: Unexpected lessons from a low protein diet study of a mouse OI model. *Matrix Biol.* **52–54,** 29–42 (2016).
90. Engelbert, R. H. *et al.* Osteogenesis imperfecta in childhood: Impairment and disability. A prospective study with 4-year follow-up. *Arch. Phys. Med. Rehabil.* **85,** 772–778 (2004).
91. Van Brussel, M. *et al.* Physical Training in Children with Osteogenesis Imperfecta. *J. Pediatr.* **152,** 111–116.e1 (2008).
92. Esposito, P. & Plotkin, H. Surgical treatment of osteogenesis imperfecta: current concepts. *Curr. Opin. Pediatr.* **20,** 52–57 (2008).
93. Cho, T.-J. *et al.* Interlocking Telescopic Rod for Patients with Osteogenesis Imperfecta. *J. Bone Jt. Surg.* **89,** (2007).

94. Huang, M. J. & Lenke, L. G. Scoliosis and severe pelvic obliquity in a patient with cerebral palsy: surgical treatment utilizing halo-femoral traction. *Spine (Phila. Pa. 1976).* **26,** 2168–70 (2001).
95. Sawin, P. D. & Menezes, a H. Basilar invagination in osteogenesis imperfecta and related osteochondrodysplasias: medical and surgical management. *J. Neurosurg.* **86,** 950–960 (1997).
96. Rogers, M. J., Crockett, J. C., Coxon, F. P. & Mönkkönen, J. Biochemical and molecular mechanisms of action of bisphosphonates. *Bone* **49,** 34–41 (2011).
97. Papapoulos, S. E. Bisphosphonates: how do they work? *Best Practice and Research: Clinical Endocrinology and Metabolism* **22,** 831–847 (2008).
98. Devogelaer, J. P., Malghem, J., Maldague, B. & Nagant de Deuxchaisnes, C. Radiological manifestations of bisphosphonate treatment with APD in a child suffering from osteogenesis imperfecta. *Skeletal Radiol.* **16,** 360–3 (1987).
99. Bachrach, L. K. & Ward, L. M. Clinical review 1: Bisphosphonate use in childhood osteoporosis. *J. Clin. Endocrinol. Metab.* **94,** 400–9 (2009).
100. E., A. & S., S. Beneficial effect of bisphosphonate during five years of treatment of severe osteogenesis imperfecta. *Acta Paediatr. Int. J. Paediatr.* **87,** 64–68 (1998).
101. Marini, J. C. Bone: Use of bisphosphonates in children—proceed with caution. *Nat. Rev. Endocrinol.* **5,** 241–243 (2009).
102. Consolaro, A. & Consolaro, A. The use of bisphosphonates does not contraindicate orthodontic and other types of treatment! *Dental Press J. Orthod.* **19,** 18–26 (2014).
103. Orwoll, E. S. *et al.* Evaluation of teriparatide treatment in adults with osteogenesis imperfecta. *J. Clin. Invest.* **124,** 491–498 (2014).
104. Antoniazzi, F. *et al.* GH in combination with bisphosphonate treatment in osteogenesis imperfecta. *Eur. J. Endocrinol.* **163,** 479–87 (2010).
105. Antoniazzi, F. *et al.* Growth hormone treatment in osteogenesis imperfecta with quantitative defect of type I collagen synthesis. *J. Pediatr.* **129,** 432–439 (1996).
106. Bargman, R., Huang, A., Boskey, A. L., Raggio, C. & Pleshko, N. RANKL inhibition improves bone properties in a mouse model of osteogenesis imperfecta. *Connect. Tissue Res.* **51,** 123–131 (2010).
107. Semler, O. *et al.* First use of the RANKL antibody denosumab in osteogenesis imperfecta type VI. *J. Musculoskelet. Neuronal Interact.* **12,** 183–8 (2012).
108. Lewiecki, E. M. & Bilezikian, J. P. Denosumab for the treatment of osteoporosis and cancer-related conditions. *Clin. Pharmacol. Ther.* **91,** 123–33 (2012).
109. Li, X. *et al.* Sclerostin antibody treatment increases bone formation, bone mass, and bone strength in a rat model of postmenopausal osteoporosis. *J. Bone Miner. Res.* **24,** 578–588 (2009).
110. Sinder, B. P. *et al.* Rapidly growing Brtl/+ mouse model of osteogenesis imperfecta improves bone mass and strength with sclerostin antibody treatment. *Bone* **71,** 115–23 (2015).
111. Grafe, I. *et al.* Excessive transforming growth factor-β signaling is a common mechanism in osteogenesis imperfecta. *Nat. Med.* **20,** 670–5 (2014).
112. Trachtman, H. *et al.* A phase 1, single-dose study of fresolimumab, an anti-TGF-β antibody, in treatment-resistant primary focal segmental glomerulosclerosis. *Kidney Int.* **79,** 1236–1243 (2011).
113. Cabral, W. A. & Marini, J. C. High proportion of mutant osteoblasts is

compatible with normal skeletal function in mosaic carriers of osteogenesis imperfecta. *Am. J. Hum. Genet.* **74,** 752–60 (2004).
114. Raghunath, M., Mackay, K., Dalgleish, R. & Steinmann, B. Genetic counselling on brittle grounds: Recurring osteogenesis imperfecta due to parental mosaicism for a dominant mutation. *Eur. J. Pediatr.* **154,** 123–129 (1995).
115. Baksh, D., Song, L. & Tuan, R. S. Adult mesenchymal stem cells: characterization, differentiation, and application in cell and gene therapy. *J. Cell. Mol. Med.* **8,** 301–16
116. Panaroni, C. *et al.* In utero transplantation of adult bone marrow decreases perinatal lethality and rescues the bone phenotype in the knockin murine model for classical, dominant osteogenesis imperfecta. *Blood* **114,** 459–68 (2009).
117. Pereira, R. F. *et al.* Marrow stromal cells as a source of progenitor cells for nonhematopoietic tissues in transgenic mice with a phenotype of osteogenesis imperfecta. *Proc. Natl. Acad. Sci. U. S. A.* **95,** 1142–7 (1998).
118. Horwitz, E. M. *et al.* Isolated allogeneic bone marrow-derived mesenchymal cells engraft and stimulate growth in children with osteogenesis imperfecta: Implications for cell therapy of bone. *Proc. Natl. Acad. Sci. U. S. A.* **99,** 8932–7 (2002).
119. Horwitz, E. M. *et al.* Clinical responses to bone marrow transplantation in children with severe osteogenesis imperfecta. *Blood* **97,** (2001).
120. Horwitz, E. M. *et al.* Transplantability and therapeutic effects of bone marrow-derived mesenchymal cells in children with osteogenesis imperfecta. *Nat. Med.* **5,** 309–313 (1999).
121. R., B. & A., F. Treatment options for osteogenesis imperfecta. *Expert Opin. Orphan Drugs* **3,** 165–181 (2015).
122. Shapiro, J. R., Byers, P. H., Glorieux, F. H. & Sponseller, P. D. *Osteogenesis imperfecta : a translational approach to brittle bone disease*.
123. Khillan, J. S., Li, S. W. & Prockop, D. J. Partial rescue of a lethal phenotype of fragile bones in transgenic mice with a chimeric antisense gene directed against a mutated collagen gene. *Proc. Natl. Acad. Sci. U. S. A.* **91,** 6298–302 (1994).
124. Dawson, P. A. & Marini, J. C. Hammerhead ribozymes selectively suppress mutant type I collagen mRNA in osteogenesis imperfecta fibroblasts. *Nucleic Acids Res.* **28,** 4013–20 (2000).
125. Grassi, G., Forlino, A. & Marini, J. C. Cleavage of collagen RNA transcripts by hammerhead ribozymes in vitro is mutation-specific and shows competitive binding effects. *Nucleic Acids Res.* **25,** 3451–8 (1997).
126. Toudjarska, I., Kilpatrick, M. W., Niu, J., Wenstrup, R. J. & Tsipouras, P. Delivery of a hammerhead ribozyme specifically downregulates mutant type I collagen mRNA in a murine model of osteogenesis imperfecta. *Antisense Nucleic Acid Drug Dev.* **11,** 341–6 (2001).
127. Rousseau, J. *et al.* Allele-specific Col1a1 silencing reduces mutant collagen in fibroblasts from Brtl mouse, a model for classical osteogenesis imperfecta. *Eur. J. Hum. Genet.* **22,** 667–74 (2014).
128. Lindahl, K., Rubin, C.-J., Kindmark, A. & Ljunggren, O. Allele dependent silencing of COL1A2 using small interfering RNAs. *Int. J. Med. Sci.* **5,** 361–5 (2008).
129. Lindahl, K. *et al.* Allele Dependent Silencing of Collagen Type I Using Small Interfering RNAs Targeting 3'UTR Indels - a Novel Therapeutic Approach in

Osteogenesis Imperfecta. *Int. J. Med. Sci.* **10,** 1333–1343 (2013).
130. Besio, R. & Forlino, A. New frontiers for dominant osteogenesis imperfecta treatment: gene/cellular therapy approaches. *Adv. Regen. Biol.* **1,** (2015).
131. Deyle, D. R. *et al.* Normal collagen and bone production by gene-targeted human osteogenesis imperfecta iPSCs. *Mol. Ther.* **20,** 204–13 (2012).
132. Millington-Ward, S. *et al.* RNAi of COL1A1 in mesenchymal progenitor cells. *Eur. J. Hum. Genet.* **12,** 864–6 (2004).
133. Lee, R. C., Feinbaum, R. L. & Ambros, V. The C. elegans heterochronic gene lin-4 encodes small RNAs with antisense complementarity to lin-14. *Cell* **75,** 843–54 (1993).
134. Fire, A. *et al.* Potent and specific genetic interference by double-stranded RNA in Caenorhabditis elegans. *Nature* **391,** 806–11 (1998).
135. Carthew, R. W. & Sontheimer, E. J. Origins and Mechanisms of miRNAs and siRNAs. *Cell* **136,** 642–55 (2009).
136. Kim, D. Y. & Sung, J.-H. Regulatory role of microRNAs in the proliferation and differentiation of adipose-derived stem cells. *Histol. Histopathol.* **32,** 1–10 (2017).
137. Simionescu-Bankston, A. & Kumar, A. Noncoding RNAs in the regulation of skeletal muscle biology in health and disease. *J. Mol. Med. (Berl).* **94,** 853–66 (2016).
138. Chen, J.-F. *et al.* The role of microRNA-1 and microRNA-133 in skeletal muscle proliferation and differentiation. *Nat. Genet.* **38,** 228–233 (2006).
139. Friedman, J. M. & Jones, P. A. MicroRNAs: critical mediators of differentiation, development and disease. *Swiss Med. Wkly.* **139,** 466–72 (2009).
140. Malone, C. D. & Hannon, G. J. Small RNAs as Guardians of the Genome. doi:10.1016/j.cell.2009.01.045
141. Siomi, M. C., Sato, K., Pezic, D. & Aravin, A. A. PIWI-interacting small RNAs: the vanguard of genome defence. *Nat. Rev. Mol. Cell Biol.* **12,** 246–258 (2011).
142. Mello, C. C. & Conte, D. Revealing the world of RNA interference. *Nature* **431,** 338–342 (2004).
143. Golden, D. E., Gerbasi, V. R. & Sontheimer, E. J. An Inside Job for siRNAs. *Mol. Cell* **31,** 309–312 (2008).
144. Bartel, D. P. MicroRNAs: genomics, biogenesis, mechanism, and function. *Cell* **116,** 281–97 (2004).
145. MacRAE, I. J., LI, F., ZHOU, K., CANDE, W. Z. & DOUDNA, J. A. Structure of Dicer and Mechanistic Implications for RNAi. *Cold Spring Harb. Symp. Quant. Biol.* **71,** 73–80 (2006).
146. Zhang, H., Kolb, F. A., Jaskiewicz, L., Westhof, E. & Filipowicz, W. Single Processing Center Models for Human Dicer and Bacterial RNase III. *Cell* **118,** 57–68 (2004).
147. Tomari, Y. & Zamore, P. D. Perspective: machines for RNAi. *Genes Dev.* **19,** 517–29 (2005).
148. Meister, G. & Tuschl, T. Mechanisms of gene silencing by double-stranded RNA. *Nature* **431,** 343–349 (2004).
149. Fabian, M. R., Sonenberg, N. & Filipowicz, W. Regulation of mRNA translation and stability by microRNAs. *Annu. Rev. Biochem.* **79,** 351–79 (2010).
150. Liu, J., Valencia-Sanchez, M. A., Hannon, G. J. & Parker, R. MicroRNA-

dependent localization of targeted mRNAs to mammalian P-bodies. *Nat. Cell Biol.* **7,** 719–723 (2005).
151. Kim, V. N. MicroRNA biogenesis: coordinated cropping and dicing. *Nat. Rev. Mol. Cell Biol.* **6,** 376–385 (2005).
152. Denli, A. M., Tops, B. B. J., Plasterk, R. H. A., Ketting, R. F. & Hannon, G. J. Processing of primary microRNAs by the Microprocessor complex. *Nature* **432,** 231–235 (2004).
153. Han, J. *et al.* Molecular Basis for the Recognition of Primary microRNAs by the Drosha-DGCR8 Complex. *Cell* **125,** 887–901 (2006).
154. Brodersen, P. *et al.* Widespread Translational Inhibition by Plant miRNAs and siRNAs. *Science (80-.).* **320,** 1185–1190 (2008).
155. Petersen, C. P., Bordeleau, M.-E., Pelletier, J. & Sharp, P. A. Short RNAs Repress Translation after Initiation in Mammalian Cells. *Mol. Cell* **21,** 533–542 (2006).
156. Thermann, R. & Hentze, M. W. Drosophila miR2 induces pseudo-polysomes and inhibits translation initiation. *Nature* **447,** 875–878 (2007).
157. Mathonnet, G. *et al.* MicroRNA Inhibition of Translation Initiation in Vitro by Targeting the Cap-Binding Complex eIF4F. *Science (80-.).* **317,** 1764–1767 (2007).
158. Wu, L., Fan, J. & Belasco, J. G. MicroRNAs direct rapid deadenylation of mRNA. *Proc. Natl. Acad. Sci.* **103,** 4034–4039 (2006).
159. Behm-Ansmant, I. mRNA degradation by miRNAs and GW182 requires both CCR4:NOT deadenylase and DCP1:DCP2 decapping complexes. *Genes Dev.* **20,** 1885–1898 (2006).
160. Chendrimada, T. P. *et al.* MicroRNA silencing through RISC recruitment of eIF6. *Nature* **447,** 823–828 (2007).
161. Rao, D. D., Vorhies, J. S., Senzer, N. & Nemunaitis, J. siRNA vs. shRNA: similarities and differences. *Adv. Drug Deliv. Rev.* **61,** 746–59 (2009).
162. López-Fraga, M., Martínez, T. & Jiménez, A. RNA Interference Technologies and Therapeutics. *BioDrugs* **23,** 305–332 (2009).
163. Miyagishi, M., Hayashi, M. & Taira, K. Comparison of the Suppressive Effects of Antisense Oligonucleotides and siRNAs Directed Against the Same Targets in Mammalian Cells. *Antisense Nucleic Acid Drug Dev.* **13,** 1–7 (2003).
164. Robb, G. B., Brown, K. M., Khurana, J. & Rana, T. M. Specific and potent RNAi in the nucleus of human cells. *Nat. Struct. Mol. Biol.* **12,** 133–137 (2005).
165. Jarve, A. *et al.* Surveillance of siRNA integrity by FRET imaging. *Nucleic Acids Res.* **35,** e124–e124 (2007).
166. Grünweller, A., Gillen, C., Erdmann, V. A. & Kurreck, J. Cellular Uptake and Localization of a Cy3-Labeled siRNA Specific for the Serine/Threonine Kinase Pim-1. *Oligonucleotides* **13,** 345–352 (2003).
167. Ohrt, T. In situ fluorescence analysis demonstrates active siRNA exclusion from the nucleus by Exportin 5. *Nucleic Acids Res.* **34,** 1369–1380 (2006).
168. Chiu, Y.-L., Ali, A., Chu, C.-Y., Cao, H. & Rana, T. M. Visualizing a correlation between siRNA localization, cellular uptake, and RNAi in living cells. *Chem. Biol.* **11,** 1165–75 (2004).
169. McAnuff, M. A., Rettig, G. R. & Rice, K. G. Potency of siRNA versus shRNA mediated knockdown in vivo. *J. Pharm. Sci.* **96,** 2922–2930 (2007).
170. Cullen, B. R. RNAi the natural way. *Nat. Genet.* **37,** 1163–5 (2005).

171. BEHLKE, M. Progress towards in Vivo Use of siRNAs. *Mol. Ther.* **13,** 644–670 (2006).
172. López-Fraga, M., Martínez, T. & Jiménez, A. RNA interference technologies and therapeutics: from basic research to products. *BioDrugs* **23,** 305–32 (2009).
173. Janssen, H. L. A. *et al.* Treatment of HCV Infection by Targeting MicroRNA. *N. Engl. J. Med.* **368,** 1685–1694 (2013).
174. Coelho, T. *et al.* Safety and Efficacy of RNAi Therapy for Transthyretin Amyloidosis. *N. Engl. J. Med.* **369,** 819–829 (2013).
175. Martínez, T. *et al.* In Vitro and In Vivo Efficacy of SYL040012, a Novel siRNA Compound for Treatment of Glaucoma. *Mol. Ther.* **22,** 81–91 (2014).
176. Singh, M. S. & Peer, D. RNA nanomedicines: the next generation drugs? *Curr. Opin. Biotechnol.* **39,** 28–34 (2016).
177. Wang, J., Lu, Z., Wientjes, M. G. & Au, J. L.-S. Delivery of siRNA therapeutics: barriers and carriers. *AAPS J.* **12,** 492–503 (2010).
178. Dominska, M. & Dykxhoorn, D. M. Breaking down the barriers: siRNA delivery and endosome escape. *J. Cell Sci.* **123,** 1183–1189 (2010).
179. Tseng, Y.-C., Mozumdar, S. & Huang, L. Lipid-based systemic delivery of siRNA. *Adv. Drug Deliv. Rev.* **61,** 721–731 (2009).
180. Khan, A. A. *et al.* Transfection of small RNAs globally perturbs gene regulation by endogenous microRNAs. *Nat. Biotechnol.* (2009). doi:10.1038/nbt.1543
181. van de Water, F. M. INTRAVENOUSLY ADMINISTERED SHORT INTERFERING RNA ACCUMULATES IN THE KIDNEY AND SELECTIVELY SUPPRESSES GENE FUNCTION IN RENAL PROXIMAL TUBULES. *Drug Metab. Dispos.* **34,** 1393–1397 (2006).
182. Kedmi, R., Ben-Arie, N. & Peer, D. The systemic toxicity of positively charged lipid nanoparticles and the role of Toll-like receptor 4 in immune activation. *Biomaterials* **31,** 6867–6875 (2010).
183. Landesman-Milo, D. & Peer, D. Toxicity profiling of several common RNAi-based nanomedicines: a comparative study. *Drug Deliv. Transl. Res.* **4,** 96–103 (2014).
184. Couto, L. B. & High, K. A. Viral vector-mediated RNA interference. *Curr. Opin. Pharmacol.* **10,** 534–542 (2010).
185. Check, E. Gene therapy: A tragic setback. *Nature* **420,** 116–118 (2002).
186. Nguyen, T., Menocal, E. M., Harborth, J. & Fruehauf, J. H. RNAi therapeutics: an update on delivery. *Curr. Opin. Mol. Ther.* **10,** 158–167 (2008).
187. Lehrman, S. Virus treatment questioned after gene therapy death. *Nature* **401,** 517–8 (1999).
188. Liu, Q. & Muruve, D. A. Molecular basis of the inflammatory response to adenovirus vectors. *Gene Ther.* **10,** 935–940 (2003).
189. Sun, J. Y., Anand-Jawa, V., Chatterjee, S. & Wong, K. K. Immune responses to adeno-associated virus and its recombinant vectors. *Gene Ther.* **10,** 964–76 (2003).
190. Donahue, R. E. *et al.* Helper virus induced T cell lymphoma in nonhuman primates after retroviral mediated gene transfer. *J. Exp. Med.* **176,** 1125–35 (1992).
191. Tai, W. & Gao, X. Functional peptides for siRNA delivery. *Adv. Drug Deliv. Rev.* (2016). doi:10.1016/j.addr.2016.08.004
192. Derossi, D., Chassaing, G. & Prochiantz, A. Trojan peptides: the penetratin

system for intracellular delivery. *Trends Cell Biol.* **8,** 84–7 (1998).
193. Meade, B. R. & Dowdy, S. F. Exogenous siRNA delivery using peptide transduction domains/cell penetrating peptides. *Adv. Drug Deliv. Rev.* **59,** 134–140 (2007).
194. Simeoni, F., Morris, M. C., Heitz, F. & Divita, G. Insight into the mechanism of the peptide-based gene delivery system MPG: implications for delivery of siRNA into mammalian cells. *Nucleic Acids Res.* **31,** 2717–24 (2003).
195. Agarwal, A., Unfer, R. & Mallapragada, S. K. Novel cationic pentablock copolymers as non-viral vectors for gene therapy. *J. Control. Release* **103,** 245–258 (2005).
196. Wang, J., Lu, Z., Wientjes, M. G. & Au, J. L.-S. Delivery of siRNA Therapeutics: Barriers and Carriers. *AAPS J.* **12,** 492–503 (2010).
197. Urban-Klein, B., Werth, S., Abuharbeid, S., Czubayko, F. & Aigner, A. RNAi-mediated gene-targeting through systemic application of polyethylenimine (PEI)-complexed siRNA in vivo. *Gene Ther.* **12,** 461–466 (2005).
198. Jeong, J. H., Mok, H., Oh, Y.-K. & Park, T. G. siRNA Conjugate Delivery Systems. *Bioconjug. Chem.* **20,** 5–14 (2009).
199. Schiffelers, R. M. Cancer siRNA therapy by tumor selective delivery with ligand-targeted sterically stabilized nanoparticle. *Nucleic Acids Res.* **32,** e149–e149 (2004).
200. Kim, S. H., Jeong, J. H., Lee, S. H., Kim, S. W. & Park, T. G. PEG conjugated VEGF siRNA for anti-angiogenic gene therapy. *J. Control. Release* **116,** 123–9 (2006).
201. Khan, A. *et al.* Sustained Polymeric Delivery of Gene Silencing Antisense ODNs, siRNA, DNAzymes and Ribozymes: *In Vitro* and *In Vivo* Studies. *J. Drug Target.* **12,** 393–404 (2004).
202. Nafee, N., Taetz, S., Schneider, M., Schaefer, U. F. & Lehr, C.-M. Chitosan-coated PLGA nanoparticles for DNA/RNA delivery: effect of the formulation parameters on complexation and transfection of antisense oligonucleotides. *Nanomedicine Nanotechnology, Biol. Med.* **3,** 173–183 (2007).
203. Bangham, A. D. & Horne, R. W. Negative staining of phospholipids and their structural modification by surface-active agents as observed in the electron microscope. *J. Mol. Biol.* **8,** 660–IN10 (1964).
204. Torchilin, V. P. Recent advances with liposomes as pharmaceutical carriers. *Nat. Rev. Drug Discov.* **4,** 145–60 (2005).
205. Halder, J. *et al.* Focal adhesion kinase targeting using in vivo short interfering RNA delivery in neutral liposomes for ovarian carcinoma therapy. *Clin. Cancer Res.* **12,** 4916–24 (2006).
206. Zhang, G. *et al.* A delivery system targeting bone formation surfaces to facilitate RNAi-based anabolic therapy. *Nat. Med.* **18,** 307–14 (2012).
207. Yarbrough, D. K. *et al.* Specific binding and mineralization of calcified surfaces by small peptides. *Calcif. Tissue Int.* **86,** 58–66 (2010).
208. Kim, B.-S., Choi, M.-K., Yoon, J.-H. & Lee, J. Evaluation of bone regeneration with biphasic calcium phosphate substitute implanted with bone morphogenetic protein 2 and mesenchymal stem cells in a rabbit calvarial defect model. *Oral Surg. Oral Med. Oral Pathol. Oral Radiol.* **120,** 2–9 (2015).
209. Gamblin, A.-L. *et al.* Bone tissue formation with human mesenchymal stem cells and biphasic calcium phosphate ceramics: the local implication of

osteoclasts and macrophages. *Biomaterials* **35,** 9660–7 (2014).
210. Monti, E. *et al.* Current and emerging treatments for the management of osteogenesis imperfecta. *Ther. Clin. Risk Manag.* **6,** 367–81 (2010).
211. Ward, L. M. *et al.* Alendronate for the treatment of pediatric osteogenesis imperfecta: a randomized placebo-controlled study. *J. Clin. Endocrinol. Metab.* **96,** 355–64 (2011).
212. Bargman, R. Comparable outcomes in fracture reduction and bone properties with RANKL inhibition and alendronate treatment in a mouse model of osteogenesis imperfecta. *Osteoporos Int* **vi,** 1141–1150 (2012).
213. Bi, X. *et al.* Correlations Between Bone Mechanical Properties and Bone Composition Parameters in Mouse Models of Dominant and Recessive Osteogenesis Imperfecta and the Response to Anti-TGF-β Treatment. *J. Bone Miner. Res.* (2016). doi:10.1002/jbmr.2997
214. Wijshake, T., Baker, D. J. & van de Sluis, B. Endonucleases: new tools to edit the mouse genome. *Biochim. Biophys. Acta - Mol. Basis Dis.* **1842,** 1942–1950 (2014).
215. Lindahl, K., Rubin, C.-J., Kindmark, A. & Ljunggren, Ö. Allele dependent silencing of COL1A2 using small interfering RNAs. *Int. J. Med. Sci* **5,** 361–365 (2008).
216. Ljunggren, O., Lindahl, K., Rubin, C.-J. & Kindmark, A. Allele-specific gene silencing in osteogenesis imperfecta. *Endocr. Dev.* **21,** 85–90 (2011).
217. Li, H. *et al.* Immature osteoblast lineage cells increase osteoclastogenesis in osteogenesis imperfecta murine. *Am. J. Pathol.* **176,** 2405–13 (2010).
218. Brennan, M. Á. *et al.* Pre-clinical studies of bone regeneration with human bone marrow stromal cells and biphasic calcium phosphate. *Stem Cell Res. Ther.* **5,** 114 (2014).
219. Zheng, L.-Z. *et al.* Src siRNA prevents corticosteroid-associated osteoporosis in a rabbit model. *Bone* **83,** 190–196 (2016).
220. Einhorn, T. A. & Gerstenfeld, L. C. Fracture healing: mechanisms and interventions. *Nat. Rev. Rheumatol.* **11,** 45–54 (2014).
221. Oliveira, S., Storm, G. & Schiffelers, R. M. Targeted delivery of siRNA. *J. Biomed. Biotechnol.* **2006,** 63675 (2006).
222. Takeshita, F. *et al.* Efficient delivery of small interfering RNA to bone-metastatic tumors by using atelocollagen in vivo. *Proc. Natl. Acad. Sci. U. S. A.* **102,** 12177–82 (2005).
223. Aigner, A. Delivery systems for the direct application of siRNAs to induce RNA interference (RNAi) in vivo. *J. Biomed. Biotechnol.* **2006,** 71659 (2006).
224. Tanaka, T. *et al.* Sustained small interfering RNA delivery by mesoporous silicon particles. *Cancer Res.* **70,** 3687–96 (2010).
225. Itaka, K. *et al.* Bone regeneration by regulated in vivo gene transfer using biocompatible polyplex nanomicelles. *Mol. Ther.* **15,** 1655–62 (2007).
226. Laemmli, U. K. Cleavage of structural proteins during the assembly of the head of bacteriophage T4. *Nature* **227,** 680–5 (1970).
227. Stephano, J. L., Gould, M. & Rojas-Galicia, L. Advantages of picrate fixation for staining polypeptides in polyacrylamide gels. *Anal. Biochem.* **152,** 308–13 (1986).
228. Becquart, P. *et al.* Ischemia is the prime but not the only cause of human multipotent stromal cell death in tissue-engineered constructs in vivo. *Tissue*

Eng. Part A **18,** 2084–94 (2012).
229. Deschepper, M. *et al.* Proangiogenic and prosurvival functions of glucose in human mesenchymal stem cells upon transplantation. *Stem Cells* **31,** 526–35 (2013).
230. Gómez-Barrena, E. *et al.* Bone fracture healing: cell therapy in delayed unions and nonunions. *Bone* **70,** 93–101 (2015).
231. Vortkamp, A. *et al.* Recapitulation of signals regulating embryonic bone formation during postnatal growth and in fracture repair. *Mech. Dev.* **71,** 65–76 (1998).
232. Phillips, A. M. Overview of the fracture healing cascade. *Injury* **36 Suppl 3,** S5-7 (2005).
233. Moreau, P. G. Book review: Rockwood and Green's fractures in adults. *Ann. Saudi Med.* **14,** 75 (1994).
234. Hausman, M. R., Schaffler, M. B. & Majeska, R. J. Prevention of fracture healing in rats by an inhibitor of angiogenesis. *Bone* **29,** 560–4 (2001).
235. Kurdy, N. M., Weiss, J. B. & Bate, A. Endothelial stimulating angiogenic factor in early fracture healing. *Injury* **27,** 143–5 (1996).
236. Lee, F. Y., Choi, Y. W., Behrens, F. F., DeFouw, D. O. & Einhorn, T. A. Programmed removal of chondrocytes during endochondral fracture healing. *J. Orthop. Res.* **16,** 144–50 (1998).
237. Melnyk, M., Henke, T., Claes, L. & Augat, P. Revascularisation during fracture healing with soft tissue injury. *Arch. Orthop. Trauma Surg.* **128,** 1159–1165 (2008).
238. Holstein, J. H. *et al.* Endostatin Inhibits Callus Remodeling during Fracture Healing in Mice. *J. Orthop. Res.* **31,** 1579–1584 (2013).
239. Gerstenfeld, L. C., Cullinane, D. M., Barnes, G. L., Graves, D. T. & Einhorn, T. A. Fracture healing as a post-natal developmental process: Molecular, spatial, and temporal aspects of its regulation. *J. Cell. Biochem.* **88,** 873–884 (2003).
240. Nakahara, H. *et al.* Bone and cartilage formation in diffusion chambers by subcultured cells derived from the periosteum. *Bone* **11,** 181–8 (1990).
241. Bostrom, M. P. *et al.* Immunolocalization and expression of bone morphogenetic proteins 2 and 4 in fracture healing. *J. Orthop. Res.* **13,** 357–67 (1995).
242. Urist, M. R. Bone: formation by autoinduction. *Science* **150,** 893–9 (1965).
243. Iwata, H., Sakano, S., Itoh, T. & Bauer, T. W. Demineralized bone matrix and native bone morphogenetic protein in orthopaedic surgery. *Clin. Orthop. Relat. Res.* 99–109 (2002).
244. Jingushi, S. *et al.* Intramuscular bone induction by human recombinant bone morphogenetic protein-2 with beta-tricalcium phosphate as a carrier: in vivo bone banking for muscle-pedicle autograft. *J. Orthop. Sci.* **7,** 490–4 (2002).
245. Kinner, B., Gerstenfeld, L. C., Einhorn, T. A. & Spector, M. Expression of smooth muscle actin in connective tissue cells participating in fracture healing in a murine model. *Bone* **30,** 738–45 (2002).
246. Jaiswal, N., Haynesworth, S. E., Caplan, A. I. & Bruder, S. P. Osteogenic differentiation of purified, culture-expanded human mesenchymal stem cells in vitro. *J. Cell. Biochem.* **64,** 295–312 (1997).
247. Bianco, P., Riminucci, M., Gronthos, S. & Robey, P. G. Bone marrow stromal stem cells: nature, biology, and potential applications. *Stem Cells* **19,** 180–92

(2001).
248. Sekiya, I., Vuoristo, J. T., Larson, B. L. & Prockop, D. J. In vitro cartilage formation by human adult stem cells from bone marrow stroma defines the sequence of cellular and molecular events during chondrogenesis. *Proc. Natl. Acad. Sci. U. S. A.* **99,** 4397–402 (2002).
249. Provot, S. & Schipani, E. Molecular mechanisms of endochondral bone development. *Biochem. Biophys. Res. Commun.* **328,** 658–65 (2005).
250. Gerstenfeld, L. C. *et al.* Three-dimensional reconstruction of fracture callus morphogenesis. *J. Histochem. Cytochem.* **54,** 1215–28 (2006).
251. Gerstenfeld, L. C., Cullinane, D. M., Barnes, G. L., Graves, D. T. & Einhorn, T. A. Fracture healing as a post-natal developmental process: molecular, spatial, and temporal aspects of its regulation. *J. Cell. Biochem.* **88,** 873–84 (2003).
252. Shapiro, F. Bone development and its relation to fracture repair. The role of mesenchymal osteoblasts and surface osteoblasts. *Eur. Cell. Mater.* **15,** 53–76 (2008).
253. Kimble, R. B. *et al.* Interleukin-1 receptor antagonist decreases bone loss and bone resorption in ovariectomized rats. *J. Clin. Invest.* **93,** 1959–67 (1994).
254. Kimble, R. B., Bain, S. & Pacifici, R. The functional block of TNF but not of IL-6 prevents bone loss in ovariectomized mice. *J. Bone Miner. Res.* **12,** 935–41 (1997).
255. Barnes, G. L., Kostenuik, P. J., Gerstenfeld, L. C. & Einhorn, T. A. Growth factor regulation of fracture repair. *J. Bone Miner. Res.* **14,** 1805–15 (1999).
256. Kon, T. *et al.* Expression of osteoprotegerin, receptor activator of NF-kappaB ligand (osteoprotegerin ligand) and related proinflammatory cytokines during fracture healing. *J. Bone Miner. Res.* **16,** 1004–14 (2001).
257. Kim, N., Odgren, P. R., Kim, D. K., Marks, S. C. & Choi, Y. Diverse roles of the tumor necrosis factor family member TRANCE in skeletal physiology revealed by TRANCE deficiency and partial rescue by a lymphocyte-expressed TRANCE transgene. *Proc. Natl. Acad. Sci. U. S. A.* **97,** 10905–10 (2000).
258. Wozney, J. M. *et al.* Novel regulators of bone formation: molecular clones and activities. *Science* **242,** 1528–34 (1988).
259. Celeste, A. J. *et al.* Identification of transforming growth factor beta family members present in bone-inductive protein purified from bovine bone. *Proc. Natl. Acad. Sci. U. S. A.* **87,** 9843–7 (1990).
260. Joyce, M. E., Jingushi, S. & Bolander, M. E. Transforming growth factor-beta in the regulation of fracture repair. *Orthop. Clin. North Am.* **21,** 199–209 (1990).
261. Rosier, R. N., O'Keefe, R. J. & Hicks, D. G. The potential role of transforming growth factor beta in fracture healing. *Clin. Orthop. Relat. Res.* S294-300 (1998).
262. Nakase, T. *et al.* Transient and localized expression of bone morphogenetic protein 4 messenger RNA during fracture healing. *J. Bone Miner. Res.* **9,** 651–9 (1994).
263. Cho, T.-J., Gerstenfeld, L. C. & Einhorn, T. A. Differential temporal expression of members of the transforming growth factor beta superfamily during murine fracture healing. *J. Bone Miner. Res.* **17,** 513–20 (2002).
264. Glowacki, J. Angiogenesis in fracture repair. *Clin. Orthop. Relat. Res.* S82-9 (1998).
265. Rowe, N. M. *et al.* Angiogenesis during mandibular distraction osteogenesis.

Ann. Plast. Surg. **42,** 470–5 (1999).
266. Gerber, H. P. & Ferrara, N. Angiogenesis and bone growth. *Trends Cardiovasc. Med.* **10,** 223–8 (2000).
267. Einhorn, T. A. & Lee, C. A. Bone regeneration: new findings and potential clinical applications. *J. Am. Acad. Orthop. Surg.* **9,** 157–65
268. Vu, T. H. *et al.* MMP-9/gelatinase B is a key regulator of growth plate angiogenesis and apoptosis of hypertrophic chondrocytes. *Cell* **93,** 411–22 (1998).
269. JA, H. *Tachdjian's Pedriatic Orthopeadics*. (Saunders, 2002).
270. Cheung, M. S., Glorieux, F. H. & Rauch, F. Natural history of hyperplastic callus formation in osteogenesis imperfecta type V. *J. Bone Miner. Res.* **22,** 1181–6 (2007).
271. Ramírez, N., Vilella, F. E., Colón, M. & Flynn, J. M. Osteogenesis imperfecta and hyperplastic callus formation in a family: a report of three cases and a review of the literature. *J. Pediatr. Orthop. B* **12,** 88–96 (2003).
272. Alharbi, M. *et al.* Pamidronate treatment of children with moderate-to-severe osteogenesis imperfecta: a note of caution. *Horm. Res.* **71,** 38–44 (2009).
273. Meganck, J. A. *et al.* Fracture healing with alendronate treatment in the Brtl/+ mouse model of osteogenesis imperfecta. *Bone* **56,** 204–12 (2013).
274. Uveges, T. E. *et al.* Alendronate treatment of the brtl osteogenesis imperfecta mouse improves femoral geometry and load response before fracture but decreases predicted material properties and has detrimental effects on osteoblasts and bone formation. *J. Bone Miner. Res.* **24,** 849–59 (2009).
275. Delos, D. *et al.* The effects of RANKL inhibition on fracture healing and bone strength in a mouse model of osteogenesis imperfecta. *J. Orthop. Res.* **26,** 153–64 (2008).
276. Bargman, R. *et al.* Comparable outcomes in fracture reduction and bone properties with RANKL inhibition and alendronate treatment in a mouse model of osteogenesis imperfecta. *Osteoporos. Int.* **23,** 1141–50 (2012).
277. Dahan-Oliel, N. *et al.* Quality of life in osteogenesis imperfecta: A mixed-methods systematic review. *Am. J. Med. Genet. Part A* **170,** 62–76 (2016).
278. Chipman, S. D. *et al.* Defective pro alpha 2(I) collagen synthesis in a recessive mutation in mice: a model of human osteogenesis imperfecta. *Proc. Natl. Acad. Sci. U. S. A.* **90,** 1701–5 (1993).
279. Taga, Y., Kusubata, M., Ogawa-Goto, K. & Hattori, S. Site-specific Quantitative Analysis of Overglycosylation of Collagen in Osteogenesis Imperfecta Using Hydrazide Chemistry and SILAC. *J. Proteome Res.* **12,** 2225–2232 (2013).
280. Ekholm, E. *et al.* Diminished callus size and cartilage synthesis in alpha 1 beta 1 integrin-deficient mice during bone fracture healing. *Am. J. Pathol.* **160,** 1779–85 (2002).
281. Chen, H., Cheng, H. & Bjerknes, M. One-step Coomassie brilliant blue R-250 staining of proteins in polyacrylamide gel. *Anal. Biochem.* **212,** 295–6 (1993).

APPENDIX

Bone 72 (2015) 53–64

Contents lists available at ScienceDirect

Bone

journal homepage: www.elsevier.com/locate/bone

Original Full Length Article

Lack of prolidase causes a bone phenotype both in human and in mouse

Roberta Besio [a,1], Silvia Maruelli [a,1], Roberta Gioia [a,1], Isabella Villa [b], Peter Grabowski [c], Orla Gallagher [c], Nicholas J. Bishop [c], Sarah Foster [c], Ersilia De Lorenzi [d], Raffaella Colombo [d], Josè Luis Dapena Diaz [e], Haether Moore-Barton [f], Charu Deshpande [f], Halil Ibrahim Aydin [g], Aysegul Tokatli [h], Bartlomiej Kwiek [i], Cigdem Seher Kasapkara [j], Esra Ozsoy Adisen [j], Mehmet Ali Gurer [j], Maja Di Rocco [k], James M. Phang [l], Teresa M. Gunn [m], Ruggero Tenni [a], Antonio Rossi [a], Antonella Forlino [a,*]

[a] Department of Molecular Medicine, University of Pavia, Pavia, Italy
[b] Bone Metabolic Unit, San Raffaele Scientific Institute, Milan, Italy
[c] University of Sheffield, Sheffield, UK
[d] Department of Drug Sciences, University of Pavia, Pavia, Italy
[e] Pediatric Hematology and Oncology, Hospital Universitario Vall d'Hebron, Barcelona, Spain
[f] Department of Clinical Genetics, Guy's and St Thomas' NHS Foundation Trust, London, UK
[g] Department of Pediatrics, Turgut Ozal University, Ankara, Turkey
[h] Department of Pediatrics, Hacettepe University, Ankara, Turkey
[i] Department of Dermatology, Medical University of Warsaw, Poland
[j] Gazi University Hospital, Pediatric Metabolic Unit, Ankara, Turkey
[k] Unit of Rare Diseases, Department of Pediatrics, Gaslini Institute, Genoa, Italy
[l] Basic Research Laboratory, Center for Cancer Research, NCI at Frederick, Frederick, MD, USA
[m] McLaughlin Research Institute, Great Falls, MT, USA

ARTICLE INFO

Article history:
Received 18 August 2014
Revised 29 October 2014
Accepted 14 November 2014
Available online 20 November 2014

Edited by: Robert Recker

Keywords:
Prolidase
Prolidase deficiency
Bone phenotype
Growth plate
Collagen

ABSTRACT

The degradation of the main fibrillar collagens, collagens I and II, is a crucial process for skeletal development. The most abundant dipeptides generated from the catabolism of collagens contain proline and hydroxyproline. In humans, prolidase is the only enzyme able to hydrolyze dipeptides containing these amino acids at their C-terminal end, thus being a key player in collagen synthesis and turnover. Mutations in the prolidase gene cause prolidase deficiency (PD), a rare recessive disorder. Here we describe 12 PD patients, 9 of whom were molecularly characterized in this study. Following a retrospective analysis of all of them a skeletal phenotype associated with short stature, hypertelorism, nose abnormalities, microcephaly, osteopenia and genu valgum, independent of both the type of mutation and the presence of the mutant protein was identified. In order to understand the molecular basis of the bone phenotype associated with PD, we analyzed a recently identified mouse model for the disease, the *dark-like* (*dal*) mutant. The *dal*/*dal* mice showed a short snout, they were smaller than controls, their femurs were significantly shorter and pQCT and μCT analyses of long bones revealed compromised bone properties at the cortical and at the trabecular level in both male and female animals. The differences were more pronounce at 1 month being the most parameters normalized by 2 months of age. A delay in the formation of the second ossification center was evident at postnatal day 10. Our work reveals that reduced bone growth was due to impaired chondrocyte proliferation and increased apoptosis rate in the proliferative zone associated with reduced hyperthrophic zone height. These data suggest that lack of prolidase, a cytosolic enzyme involved in the final stage of protein catabolism, is required for normal skeletogenesis especially at early age when the requirement for collagen synthesis and degradation is the highest.

Introduction

Prolidase is a cytosolic manganese-dependent peptidase and it is the only enzyme in vertebrates that is able to hydrolyze the tertiary amide bond present in imidodipeptides containing proline and hydroxyproline at their C-terminal end. Thus, prolidase is involved in the very last stage of protein catabolism, especially of proteins particularly rich in

* Corresponding author at: Department of Molecular Medicine, Biochemistry Unit, University of Pavia, Via Taramelli 3b, 27100 Pavia, Italy. Fax: +39 0382 423108.
E-mail address: aforlino@unipv.it (A. Forlino).
[1] These authors contributed equally to the work.

http://dx.doi.org/10.1016/j.bone.2014.11.009
8756-3282/

iminopeptides, such as fibrillar collagens [1,2]. Prolidase has an important role in proline recycling, both for protein synthesis and for cellular growth. In fact prolidase activity has been reported to affect both type I collagen synthesis and degradation and to be itself upregulated by stimulation of β1-integrin, the monomer of the integrin α1β1 specifically mediating type I collagen cell–matrix interaction [3–5]. Furthermore, its catalytic products, proline and hydroxyproline, stimulate hypoxia inducible factor α (HIF-1α), an important transcription factor having, among its target genes, vascular endothelial growth factor (VEGF) and glucose transporter-1 (GLUT1) [6]. Thus prolidase may also be indirectly involved in angiogenesis.

Given that type I collagen is the main component of the bone organic extracellular matrix and the importance of angiogenesis in bone development, a role for prolidase in skeletal development is to be expected. Indeed, a link between prolidase hyper-activity and hip dysplasia has been described and a reduction of prolidase activity was reported in a patient affected by osteogenesis imperfecta, a bone disease mainly characterized by the presence of abnormal type I collagen [7,8].

Lack of prolidase due to mutations in the *Peptidase D* (*PEPD*) gene is responsible in humans for prolidase deficiency (PD; OMIM 170100), a rare autosomal recessive disease characterized by defective wound healing, intractable skin ulcers, various degrees of mental retardation and recurrent infections with associated elevated plasma and urine imidodipetides [2,9,10]. Bone and joint abnormalities were occasionally described and included among the complication of the disease, but not investigated further in PD patients likely due to the more devastating effects of the other clinical problems [7,11,12]. A mouse carrying in homozygosis a spontaneous 4 bp deletion in exon 14 of *Pepd* gene has been recently described. The mutant mouse was initially named *dark-like* (*dal*) due to its characteristic darkly-pigmented fur. Homozygous *dal* mice also show small body size, reproductive degeneration, vacuolated cells at the cortical medullary junction of the adrenal gland, mild hydrocephalus, dense bone and dark urine [13]. They develop hypertrophic cardiomyopathy, but neither skin lesions nor recurrent infections were reported (in contrast to the reported human cases) [13,14]. Their strongly reduced prolidase activity makes *dal*/*dal* mice a potential model for investigating the role of prolidase in human metabolism.

To evaluate the function of prolidase in bone development and homeostasis, the bone phenotype was retrospectively analyzed in 12 PD patients, 9 of whom were molecularly characterized in this study, revealing 5 novel mutant alleles. All 12 patients showed a skeletal phenotype independently of gender, type of mutation or protein stability. The *dal*/*dal* mouse was analyzed to characterize the bone alterations caused by the lack of prolidase activity and to investigate the molecular basis of these defects.

Materials and methods

Patients

The clinical evaluation of the patients described in this study was provided from the referring Hospitals: P1 from Hospital Universitario Vall d'Hebron, Barcelona, Spain; P2 from Guy's Hospital, London, UK; P3, P4 and P9 from Gazi University Hospital, Ankara, Turkey; P5 and P8 from Hacettepe University Children's Hospital and Gulhane Military Medicine Academy, Ankara, Turkey; P6 and P7 from Medical University of Warsaw, Warsaw, Poland; P10 from U.O.C. Genetica Medica Policlinico Le Scotte, Siena, Italy; P11 from Copenhagen University Hospital, Copenhagen, Denmark and P12 from Gaslini Hospital, Genoa, Italy.

Molecular study

Genomic DNA and RNA were extracted from patient and control peripheral blood and cultured fibroblasts respectively by standard techniques. The 14 exons and exon boundaries of prolidase gene (*PEPD*) were sequenced as previously described [15]. Primer sequences will be available upon request. ENST00000244137 was used as cDNA reference sequence. The use of human samples was approved by the ethic committee of the University of Pavia, Italy (Prot 22/CE, Pavia).

Clinical evaluation of the skeletal outcome in PD patients

The evaluation of the skeletal feature was done retrospectively based on available medical reports.

Animals

The *dark-like* mice (*dal*/+), on a mixed CBA × C3H background, were provided by Dr. Gunn TM (Great Falls, MT) and C3H wild-type (WT) mice were purchased from Charles River. Both were maintained under standard experimental animal care protocol following the Italian Laws (Protocol N 1/2010) in the animal facility at the Dept. of Molecular Medicine of the University of Pavia (Italy).

Fibroblast and osteoblast primary cultures and protein lysates

Skin fibroblast and long bone osteoblast cultures were established from *dal*/*dal* and WT mice as described in Forlino et al. [16] and in Panaroni et al. [17], respectively. At confluence, cells were lysed in 50 mM Tris–HCl, pH 7.8, and protein concentration determined using the RC DC Protein Assay (Bio-Rad, Milan, Italy).

Bone and skin protein extraction

Femurs and tibias of WT and *dal*/*dal* mice (n = 3) were cleaned of soft tissue and bone marrow and decalcified in 14% EDTA pH 7.1, for 21 days. Skin from WT and *dal*/*dal* mice (n = 3) and decalcified bones were solubilized in RIPA Buffer (50 mM Tris–HCl pH 7.4, 150 mM NaCl, 1% Triton, 0.5% sodium deoxycholate, 0.1% SDS, 1 mM EDTA) in the presence of protease inhibitors (130 mM benzamidine, 2 mM N-ethylmalemide, 5 mM EDTA, 1 mM Phenylmethylsulfonyl fluoride) and proteins were quantified by RC DC Protein Assay (Bio-Rad, Milan, Italy).

Prolidase expression

Proteins from patients' fibroblast lysates (20–40 μg) and from skin and bone extracts (60–80 μg) of WT and *dal*/*dal* mice were separated on 10% SDS-PAGE under reducing conditions and electro-transferred to a PVDF membrane (Hybond-P, GE Healthcare Life Sciences, Euroclone Spa, Pero, Milan, Italy) at 100 V for 2 h. The membrane was incubated overnight at 4 °C with primary antibody against human prolidase (provided by Dr. J. M. Phang, NCI-Frederick MD, USA) diluted 1:1000 in TBS-T containing 5% milk. For normalization α-tubulin (Santa Cruz Biotechnologies, Santa Cruz, CA, USA) or β-actin antibodies (Sigma Aldrich, Milan, Italy) were used diluted 1:1000 in TBS-T. Secondary antibodies conjugated with horseradish peroxidase (ECL Mouse IgG, HRP-linked, GE Healthcare Life Sciences, Euroclone Spa, Pero, Milan, Italy; donkey anti-rabbit IgG-HRP, Santa Cruz Biotechnologies, Santa Cruz, CA, USA) and ECL Western Blotting Detection Reagent (GE Healthcare Life Sciences, Euroclone Spa, Pero, Milan, Italy) were used for signal detection. Films were digitalized using VersaDoc 3000 (BioRad, Milan, Italy), and band intensity evaluated by QuantityOne software (BioRad, Milan, Italy).

Prolidase activity assay

Prolidase activity was determined in blood and/or fibroblast lysates from patients and WT and *dal*/*dal* mice and in osteoblast lysates of WT and *dal*/*dal* mice as described in Besio et al. [18].

Determination of dipeptides in urine

Urine samples from 2 month old WT, *dal*/*dal* and *dal*/+ mice (n = 3) were collected on absorbent paper and eluted as described in Lupi et al. [19]. The samples were analyzed by capillary electrophoresis (CE) as described in Caselli et al. [15].

Mouse growth curve and femur length

Wild type, *dal*/+, *dal*/*dal*, male and female mice (n = 5) were weighed weekly from 1 week-old to 2 month-old. Femur length was measured from the femur head to the proximal epiphysis in WT and *dal*/*dal* mice, both male and female (n = 10), at postnatal days 30 and 60 (P30 and P60) by using a caliper accurate to 50 μm.

Skeletal staining

Alcian blue and alizarin red skeletal staining of *dal*/*dal* and WT mice at P10 and P30 (n = 3) was performed as described in Forlino et al. [16].

Histology and immunohistochemistry

For histological studies, left tibias from WT and *dal*/*dal* mice at P10, P21, P30 (n = 5 per group) were dissected and fixed in 4% PFA in PBS, decalcified in 14% EDTA pH 7.1 for 21 days and processed for light microscopy, according to standard procedures. Seven micrometer longitudinal tibia sections were cut using a RM2265 microtome (Leica Microsystems srl, Milan, Italy), mounted on Superfrost Plus slides (Menzel-Glaser, VWR, Milan, Italy) and stained with hematoxylin and eosin or toluidine blue. Pictures were acquired using a DFC480 digital camera (Leica Microsystems srl, Milan, Italy) connected to a light microscope (Dialux 20, Leica, Microsystems srl, Milan, Italy).

The resting, proliferative, and hypertrophic zones of the growth plate of P21 and P30 WT and *dal*/*dal* mice were delineated on toluidine blue stained sections on the basis of cell morphology, as reported elsewhere [20]. The height of the different zones of the growth plate, the number of columns per zone and the number of cells per column were measured on toluidine blue stained sections using the Leica Application Suite v 3.0 image analysis software (Leica Microsystems srl, Milan, Italy).

Picro-sirius red staining was also performed on tibia sections of WT and *dal*/*dal* mice at P21 and P30. A 0.1% solution of sirius red (Direct Red 80, Sigma-Aldrich, Milan, Italy) in saturated aqueous solution of picric acid was used. After staining, sections were rinsed in acidified water (87.5 mM acetic acid) and dehydrated in absolute alcohol, cleared and mounted in synthetic resin (DPX Mountant for histology, Sigma-Aldrich, Milan, Italy). To evaluate Sirius red birefringence, Sirius red stained sections were analyzed under polarized light, and images were taken by Leica DM2500 equipped with L ICT/P polarizer and a digital color camera LEICA DFC295 (Leica). The percentage of trabecular blood vessels was evaluated on hematoxylin and eosin-stained sections of P30 *dal*/*dal* and WT mice as described in Valdoorne et al. [21].

For immunohistochemical detection of proliferating cells in the growth plate, P30 *dal*/*dal* and WT mice (n = 4) were injected with 100 mg/kg of weight of bromodeoxyuridine (BrdU) 2 h before sacrifice. Tibias were dissected and processed as described above. Sections were treated with BrdU Staining Kit (Zymed Laboratories. Hysto-Line, Milan, Italy), according the manufacturer's suggestions; nuclear counterstaining was performed with hematoxylin. For the detection of apoptotic chondrocytes in tibia growth plate sections (n = 4), a TUNEL assay (DeadEnd Colorimetric TUNEL System, Promega, Milan, Italy) was performed, according to the manufacturer's instructions. Nuclei were counterstained with hematoxylin.

Bone structural properties evaluated by Peripheral Quantitative Computed Tomography

Tibias and femurs obtained from P30 and P60 WT and *dal*/*dal* mice (n = 10 per group) were analyzed by peripheral quantitative computed tomography (pQCT). pQCT measurements were performed using a Stratec Research SA + pQCT scanner (Stratec Medizintechnik GmbH, Pforzheim, Germany) with 70 μm voxel size as described in Panaroni et al. [17]. The scans were performed at the proximal metaphysis of tibiae, the distal metaphysis of femura, and the mid-diaphysis of both bones. For metaphyseal analysis, a distance from growth plate of 2.0 mm for tibia and 2.5 mm for femur was considered.

Evaluation of bone geometry by μCT

Whole femurs from WT and *dal*/*dal* mice at P30 (n = 6 per group) were scanned on a Skyscan μCT 1172 (Skyscan, Kontich, Belgium) at 50 kV and 180 mA using a 0.5 mm aluminum filter and a detection pixel size of 4.3 μm^3. Images were captured every 0.7° through 360° of rotation and analyzed using Skyscan software (CT.An). The ratio between bone volume to total volume (BV/TV, %), trabecular thickness (Tb.Th, μm) and number of trabeculae (Tb.N, mm^{-1}) were assessed in a 1 mm high region of trabecular bone 0.2 mm proximal to the distal growth plate. Bone volume (BV, mm^3), cortical thickness (Ct.Th, μm) and total porosity (Po, %) were assessed in a 1 mm high region of cortical bone at the midshaft. The voxel size was 4.3 μm^3, the thresholding was standardized across all bone samples using global thresholding in CTAn software (Skyscan). The mean grayscale for thresholded voxels in regions of interest was recorded and bone mineral density was calculated by linear extrapolation against mean grayscale values from regions of a 2 mm phantom rod pair containing 0.25 and 0.75 g/cm^{-3} CaHA (Skyscan).

Microindentation analysis of bone

Whole femurs were tested on the mid anterior surface using the Biodent Hfc Reference Point Indenter (RPI) device (Active Life Scientific, CA) with a testing protocol of 5 cycles at 2 N indentation force using a BP2 probe [22]. The measurements were performed within the middle one-third of the anterior surface of the femur, with the spacing between test sites being approximately 1 mm apart. Test values from four sites approximately 1 mm apart were averaged for each femur.

Analysis of collagen from bone and skin

Femurs and tibias of WT and *dal*/*dal* mice (n = 3 each genotype) were cleaned from soft tissues and bone marrow and decalcified in 14% EDTA pH 7.1 for 21 days. Skin and decalcified bone were hashed and collagen was obtained by pepsin digestion (0.1 mg/ml in 0.5 M acetic acid) followed by salt precipitation (0.9 M NaCl) [16]. The collagen samples were separated by 6% SDS-PAGE and the gel was stained with Comassie blue. Gel digitalization was performed by VersaDoc 3000 (BioRad, Milan, Italy).

Statistics

For the growth plate hystomorphometric analyses, at least 20 vertical measurements per zone per section were performed. An average of six sections per animal was analyzed and measurements were performed in the medial zone of the growth plate. For proliferation assays, all chondrocyte nuclei and BrdU positive chondrocyte-nuclei in the proliferative zone of the growth plate were counted to evaluate the percentage of replicating cells. Statistical differences between groups were evaluated by ANOVA and two tailed Student's *T*-test using Sigma Plot Statistic 11.0 software; a p-value < 0.05 was considered significant. All μCT data were analyzed by two-way analysis of variance with a Tukey

post-hoc analysis for effects of gender and genotype using GraphPad Prism Version 6.01 (GraphPad Software Inc, CA, USA). Statistical comparisons for pQCT and μCT were based on two-tailed Student's *T*-test with $p < 0.05$ considered statistically significant. All data are expressed as mean ± SD.

Results

Mutation identification

Mutation analysis was performed for 9 PD patients referred to us based on typical clinical features. The diagnosis was confirmed by prolidase activity evaluation (Table 1). All exons of the *PEPD* gene were sequenced and, when possible, heterozygosity was demonstrated in parents and/or relatives (Fig. 1 and Sup. Fig. 1). The identified mutant alleles are reported in Table 1 and Figs. 1A–F. In patient #1 a novel c.977G>A homozygous substitution responsible for p.Trp325* was detected (Fig. 1A). Patient #2 was compound heterozygous for the above described mutation c.977G>A and the more frequent transition c.1342G>A, the latter resulting in p.Gly448Arg substitution (Fig. 1B). The patients #3 and #4, siblings from a consanguineous marriage, were homozygous for the novel substitution c.202-2A>T (Fig. 1C) that results in skipping of exon 3 and activation of various alternative splice sites (Fig. 1G). In patients #5 and #9, a novel homozygous 4 base pair deletion was found in intron 3 c.329 + 4del (Fig. 1D). #6 and #7, siblings from non consanguineous parents, were compound heterozygous for the novel c.1354G>A causing p.Glu451Lys and the already described c.1342G>A (Fig. 1E). Patient #8 was homozygous for a novel nucleotide deletion c.874delT generating a premature stop codon at c.959 in exon 12 (Fig. 1F). The prolidase expression level in patient fibroblast lysates evaluated by western blotting was variable, depending on neither the type of mutation nor level of enzyme activity (Fig. 1H).

Bone phenotype in PD patients

The typical clinical features in human PD patients are severe skin ulcers, recurrent infections and varying degrees of mental retardation. Skeletal features are only occasionally reported and do not represent the most critical phenotype [1,23,24]. A more detailed phenotyping of our PD patients revealed the presence of bone abnormalities, independent of gender, type of mutation or presence of mutant protein. The skeletal findings were absent in heterozygous parents and other family members. We are aware of the limit of our observations due to the small number of patients, but the rarity of PD (1 < 1,000,000, http://www.orpha.net/) has to be considered. As detailed in Table 2 the majority of the patients showed short stature, hypertelorism, nose abnormalities, microcephaly, osteopenia and genu valgum (Figs. 1I–M).

Dal/dal mice

Recently, Jung et al. identified a spontaneous 4 bp deletion in exon 14 of *Pepd*, the gene encoding prolidase, in the *dark-like* (*dal*) mutant mouse. Homozygous *dal/dal* mice had undetectable levels of prolidase activity in blood, heart and liver [14]. Prolidase activity was measured in *dal/dal* fibroblasts and osteoblasts and it was found to be strongly reduced compared to WT (Fig. 2A), although the protein was present both in skin and bone lysates (Fig. 2B). An accumulation of undigested dipeptides in the urine of *dal/dal* mice was detected by capillary electrophoresis (Fig. 2C). The absence of prolidase activity and the iminodipeptiduria are the accepted criteria for the diagnosis of prolidase deficiency in human, thus, the *dal/dal* mice represent an useful model for the study of the bone phenotype in prolidase deficiency.

Bone phenotypic characterization of dal/dal mice

At birth, mutant *dal/dal* pups were indistinguishable from WT and heterozygous littermates, but by weaning age their size was smaller and the coat color darker. Their body weight was significantly reduced starting at P7 for females and P21 for males ($p < 0.05$) (Fig. 2D). Skeletal staining using alcian blue and alizarin red performed at P10 and P30 revealed no gross abnormalities (Sup. Fig. 2). The *dal/dal* mice femurs were significantly shorter in both genders at 1 (P30) and 2 (P60) months (Fig. 2E), but no rhizomelic phenotype was observed (Sup. Table 1). Heterozygous mice were indistinguishable from the WT

Table 1
PD patient cohort: prolidase activity, mutation information and main clinical phenotypes.

Case	Gender	Age (yr)	Activity blood (%)	Activity fibroblasts (%)	cDNA mutation	Protein mutation	Ulcers	Infections	Mental retardation	Bone phenotype
#1	F	2	9.1	5.6	c.977G>A; c.977G>A	p.Trp325*	Yes	No	Yes	Yes
#2	F	15		6.9	c.977G>A; c.1342G>A	p.Trp325*; p.Gly448Arg	Yes	Recurrent	Mild	Yes
#3	F	24	3.4		c.202-2A>T; c.202-2A>T	Alternative splicing	Yes	Recurrent	Yes	Yes
#4	F	20	4.3		c.202-2A>T; c.202-2A>T	Alternative splicing	Yes	Recurrent	Yes	Yes
#5	M	27	0.0		c.329 + 4del; c.329 + 4del		Yes	No	No	Yes
#6	M	10	7.7		c.1342G>A; c.1354G>A	p.Gly448Arg; p.Glu451Lys	Yes	Recurrent	Yes	Yes
#7	M	20	8.8		c.1342G>A; c.1354G>A	p.Gly448Arg; p.Glu451Lys	Yes	Recurrent	No	Yes
#8	M	23	0.9		c.874delT; c.874delT	Premature stop codon	Yes	Respiratory	No	Yes
#9	M	36	5.9		c.329 + 4del; c.329 + 4del		Yes	Recurrent	Yes	Yes
#10	F	Dead	4.3		c.1133_1135delACG; c.1301delT	Frameshift/ premature stop codon	Yes	Recurrent	Speech delay	Yes
#11	F	27		<10	c.611_623dupAGGCCCACCGTGA; c.611_623dupAGGCCCACCGTGA	Frameshift/ premature stop codon	Yes	Recurrent	Yes	Yes
#12	M	Dead at 11	36.0		c.1342G>A; c.1342G>A	p.Gly448Arg	Yes	Recurrent	Mild	Yes

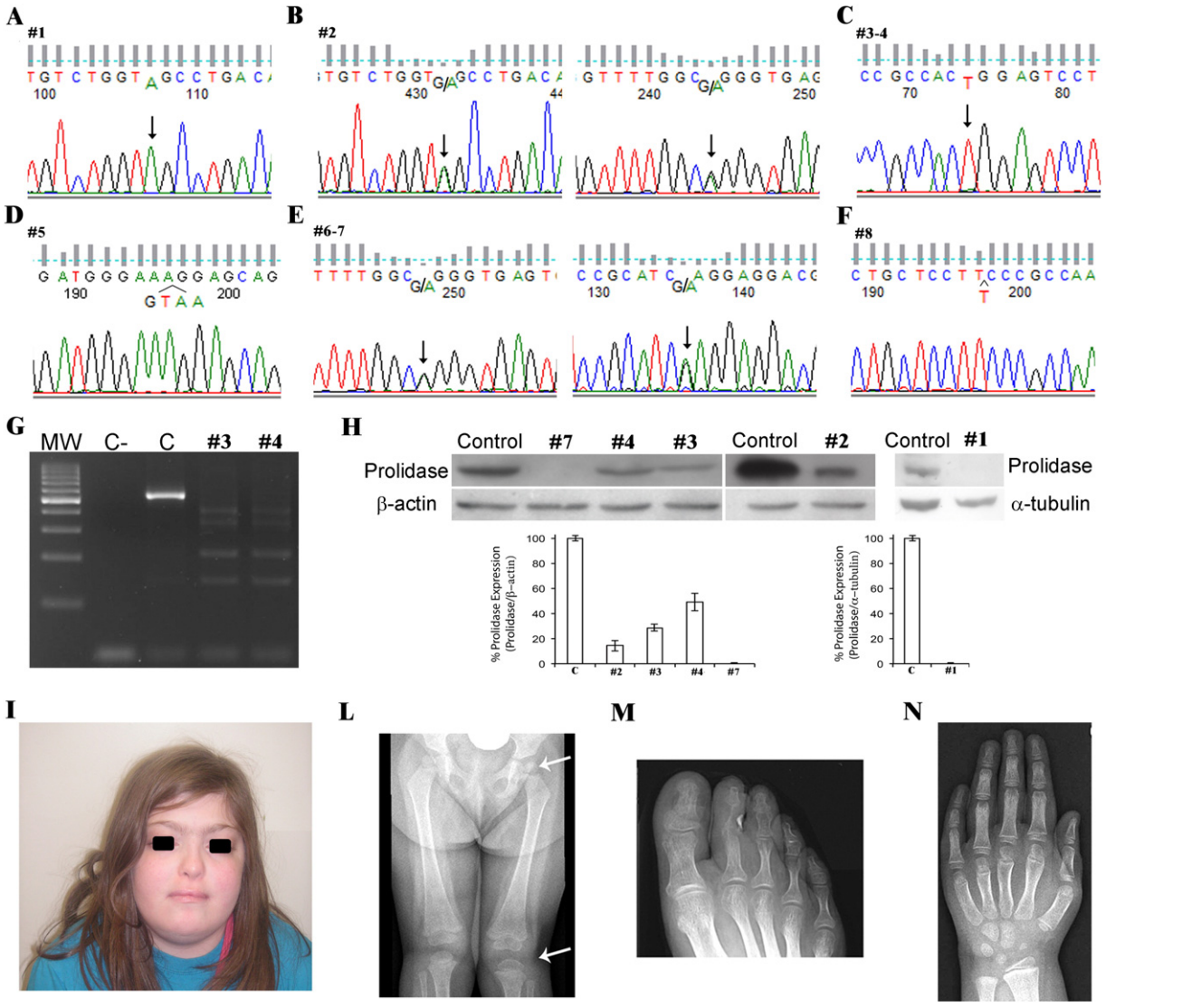

Fig. 1. PD patients' mutations detected by genomic DNA sequencing. Electropherograms showing: (A) c.977G>A in #1; (B) c.977G>A and c.1342G>A in #2; (C) c.202-2A>T in #3 and #4; (D) c.329 + 4del in #5; (E) c.1342G>A and c.1354G>A in #6 and #7; and (F) c.874delT in #8. (G) RT-PCR on RNA extracted from #3 and #4 revealed the skipping of exon 3 and the activation of various alternative splice sites. (H) Representative western blot performed on PD patients fibroblast lysates using the antibody against human prolidase. Densitometric quantification of prolidase expression is reported on the bottom. PD patient: (I) Patient #2 face showing hypertelorism and saddle nose; X-ray of PD patients: (L) #1 pelvis and lower limbs, where the arrows indicate coxa valga and knee valgum due to verticalization of the epiphysis of the distal femur; (M) #7 foot and (N) #12 hand revealing low bone mineral density/mass.

littermates in terms of weight, growth and external appearance (data not shown).

Geometrical and mechanical bone parameters in pubertal and post-pubertal dal/dal mice

Bone geometrical parameters of tibias and femurs at both metaphysis and diaphysis were evaluated in male and female P30 and P60 wild type and mutant mice by peripheral quantitative computed tomography (pQCT) (Table 3).

In both male and female *dal/dal* mice a generally reduced trabecular and cortical area at metaphyseal and diaphyseal regions was detected at both P30 and P60, even if at some time points and skeletal sites these differences did not reach statistical significance. A significant reduction in tibial metaphyseal trabecular area was seen in both female and male mice at P30. Cortical diaphyseal area and thickness were reduced in males at both sites and at each time point, but only in the tibia for females with the exception of thickness.

Cortical diaphyseal density was reduced only in males at P30, but in both genders at P60.

In female mutant mice at P30 periosteum circumference was reduced both in femur and tibia, but no difference was detectable at P60. Similar results were obtained for endosteum circumference at P30 whereas at P60 in tibia no difference was detectable and in femur was evident a significant increase. In male mutant mice a significant reduction was detected only for periosteum circumference in tibia at P30 and in tibia and femur at P60.

Calculated strength strain index (SSI) showed reduced strength at both skeletal sites at both ages for male mice, whereas for female SSI was reduced at the femur P30 and at the tibia at P60.

μCT analysis of femurs was performed in order to further investigate bone geometrical properties at 3D level and higher resolution. Both female and male were studied at P30, whereas only male bones were analyzed at P60 (Figs. 3A–B). In both gender trabecular bone volume and number were reduced in P30 mutant mice, as well as trabecular thickness. Interestingly all parameters were rescued at P60, at least in the analyzed male mice. No significant differences were detected in cortical

Table 2
Skeletal phenotype in PD patients.

Patient/country of origin	Short stature	Hypertelorim	Nose abnormalities (saddle nose)	Microcephaly	Osteopenia	Genu valgum
#1 Spain	No	Yes	No	No	Ne	Yes
#2 England	Yes [a]	Yes	Yes [b]	No	No [c]	Yes
#3 Turkey	Yes	Yes	Yes	Yes [d]	Yes [e]	Yes
#4 Turkey	Yes	Yes	Yes	Yes [d]	No	Yes
#5 Turkey	Yes [f]	No	Yes	Yes [f]	Ne	No
#6 Poland	No	Yes	No	No	Yes [e]	No
#7 Poland	No	Yes	No	No	Yes [g]	No
#8 Turkey	No	No	No	No	Yes [h]	No
#9 Turkey	No	Yes	Yes	Yes [d]	Yes [e]	No
#10 Italy	Yes	Ne	Ne	Yes	Ne	Ne
#11 Turkey	Yes	Ne	Ne	Ne	Ne	Ne
#12 Italy	Yes [i]	Yes	Yes	No	Yes [e]	Ne

ne: not evaluated.
[a] 9th percentile.
[b] Pinched nose; short columella.
[c] Femoral epiphyseal dysplasia.
[d] Clinical observation.
[e] X ray.
[f] <2SD.
[g] L1–L4: Z-score −1,9 to −2,5 average – 2,21 by DEXA.
[h] L1-L4: Z score < −1.33 by DEXA.
[i] <3rd percentile.

bone with the exception of a significant reduced bone volume in *dal*/*dal* male mice at P30; again rescue was detected in older animals. In WT male mice cortical porosity decreased from P30 (1.804% ± 0.377%) to P60 (0.851% ± 0.195%) whereas in mutant mice the value remained almost identical (0.815% ± 0.108% at P30; 0.949% ± 0.204% at P60).

Microindentation analyses were performed in *dal*/*dal* and WT mice in order to characterize the material bone properties that represent important contributors to whole bone strength [25,26]. The data obtained at P30 should be taken cautiously since the technology used was working at the limits of its capabilities mainly because the mean cortical bone thickness of all examined mice was below (about 150 μm) the recommended values for reliable data (about 200 μm). None of the evaluated parameters revealed significant differences between WT and mutant mice (Sup. Table 2). The higher incidence of damage to bones during preparation and during indentation at P30 is suggestive that *dal*/*dal* bones are weaker than those of the WT, though again this did not reach statistical significance ($p = 0.06$). No such observation was made in older mice.

Based on the geometrical parameters the bone structure of *dal*/*dal* mice appeared more fragile than those of WT, especially at younger ages when the growth/modeling requirement is higher. A partial rescue was detected in older animals.

Picro-sirius red staining of bone section and collagen analysis

In order to investigate the distribution and organization of collagen I in bone, picro-sirius red-stained tibia sections from P21 and P30 *dal*/*dal* and WT mice were analyzed by circular polarized light microscopy. In both genders, stronger red labeling of the mutant bone was evident, suggesting an increase in the amount of mature and homogeneously organized collagen fibrils (Fig. 4A). The amount of green birefringence, specific for newly deposited collagen, was reduced in mutant with respect to WT mice at both trabecular and cortical levels. Interestingly, the red staining was particularly strong at the growth plate level of mutant mice, but almost absent in wild type bones.

Electrophoretic analysis of collagen I extracted from skin and bone of *dal*/*dal* and WT littermates showed normal migration (Sup. Fig. 3).

Histological studies of epiphyseal cartilage

The physeal cartilage, responsible for the bone growth, was histologically analyzed (Fig.4B). Toluidine blue-stained sections of the proximal tibia revealed a normal growth plate architecture in P21 and P30 *dal*/*dal* mice (Fig. 4C). In both WT and mutant mice, the height of the growth plate decreased as expected with age due to the expansion of the secondary ossification center. Histomorphometric analysis of the mutant growth plates revealed a significantly shorter hypertrophic zone in both genders at all time points ($p < 0.05$), but no difference was detected at the proliferative zone (Fig. 4C, Table 4). At both ages the height of the hypertrophic cell columns and the number of cells for each column were also reduced in the *dal*/*dal* mouse growth plate (Table 4). A delay in the formation of the second ossification center was evident at P10 in mutant mice, suggesting a delay either in chondrocyte differentiation or vascularization, causing a consequent delay in the substitution of cartilaginous tissue with bone (Fig. 4D). Histomorphometric analysis of proximal tibia did not reveal any reduction of the trabecular blood sinusoid number in mutant mice with respect to WT littermates (Sup. Fig. 4).

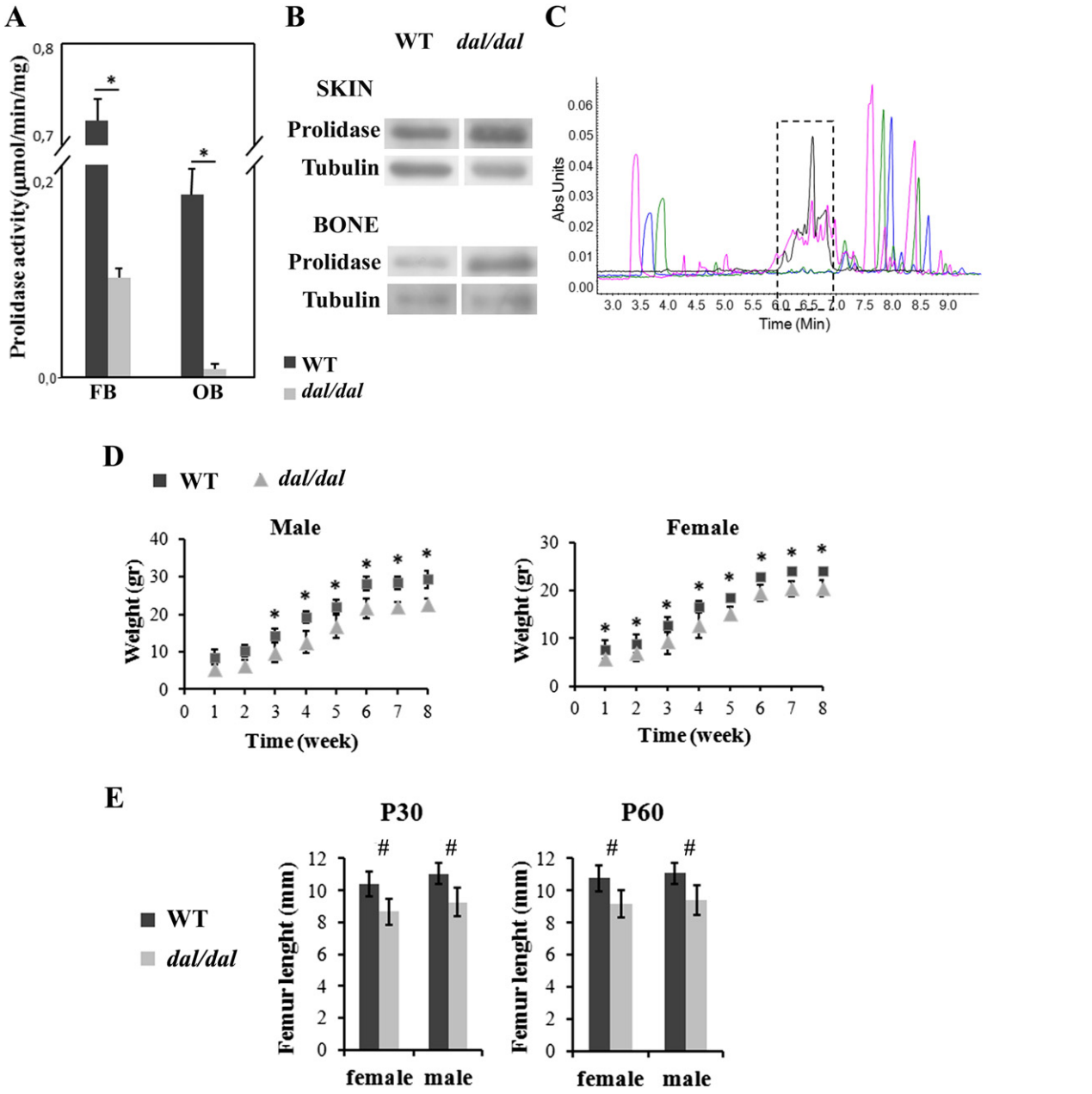

Fig. 2. The *dal*/*dal* mouse: a reliable model for prolidase deficiency. (A) Prolidase activity in wild type (WT) and *dal*/*dal* mice fibroblasts (FB) and osteoblasts (OB). (B) Representative western blot performed on WT and *dal*/*dal* mice skin and bone lysates using an antibody against prolidase. (C) Representative overlapped CE electropherograms of urine samples from *dal*/*dal* (pink trace), *dal*/+ (green trace) and WT (blue trace) mice. The dotted frame indicates the time window where dipeptides migrate as demonstrated by the use of appropriate dipeptides standard mixture (black trace). (D) Growth curve of WT and *dal*/*dal* mice (n = 5). (E) Femur length in P30 and P60 male and female WT and *dal*/*dal* mice (n = 10). Significant differences $p < 0.05$, denoted by an asterisk (*), $p < 0.005$ denoted by a pound symbol (#).

Compromised chondrocyte behavior in dal/dal growth plate

Given the reduced hypertrophic height in mutant growth plate, proliferation and apoptosis were evaluated. BrdU staining of proximal tibia sections revealed a significant reduction of the percentage of proliferating chondrocytes in the proliferative zone in P30 mutant mice (5.63% ± 1.90%) with respect WT littermate (8.98% ± 2.39%, $p < 0.001$) (Fig. 4E). TUNEL assay indicated an increase apoptosis in the proliferative zone in mutants (2.9% ± 0.8%) compared to controls (0.7% ± 0.5%, $p < 0.005$) (Fig. 4F). By contrast, in the hypertrophic zone, no statistically significant difference was detected (WT 4.5% ± 2.1%; *dal*/*dal* 5.6% ± 2.5%). These data suggest that lack of prolidase is particularly harmful to proliferating cells.

Discussion

In the present study we analyzed 12 patients for whom a diagnosis of prolidase deficiency (PD) was made based on clinical, biochemical and/or molecular criteria. Extremely low prolidase activity, the biochemical marker for the disease, was detected in blood and/or fibroblast lysates in all the patients (Table 1). Molecular characterization of 9 of the patients identified 5 novel causative mutant alleles (Fig. 1). No relationship could be found between the type of mutation and the typical PD clinical outcome (Table 1). All the patients studied showed skeletal features (Figs. 1I–N, Table 2).

The availability of the murine model *dark-like* (*dal*/*dal*), homozygous for a loss-of-function mutation in the gene encoding prolidase, allowed

Table 3
pQCT analysis of tibias and femurs of 1 and 2 month-old WT and *dal*/*dal* mice.

	P30				P60			
	Female		Male		Female		Male	
	WT	*dal*/*dal*	WT	*dal*/*dal*	WT	*dal*/*dal*	WT	*dal*/*dal*
Trabecular density (mg/mm^3)								
Metaphysis—tibia	96.80 ± 11.15	89.10 ± 12.95	113.47 ± 24.33	98.3 ± 16.96	214.08 ± 32.99	189.30 ± 47.52	237.74 ± 28.01	187.14 ± 63.46[a]
Metaphysis—femur	137.54 ± 41.89	86.37 ± 9.47[b]	172.69 ± 48.39	101.97 ± 16.94[b]	264.51 ± 21.47	195.94 ± 63.60[b]	235.03 ± 56.45	207.30 ± 34.24
Total area (mm^2)								
Metaphysis—tibia	1.96 ± 0.26	1.55 ± 0.31[b]	2.15 ± 0.39	1.66 ± 0.38[a]	3.58 ± 0.64	3.07 ± 0.77	4.24 ± 0.58	3.40 ± 0.90[a]
Metaphysis—femur	2.37 ± 0.42	1.79 ± 0.19[a]	2.48 ± 0.37	1.97 ± 0.23[b]	3.62 ± 0.49	2.94 ± 0.83[b]	4.02 ± 0.87	2.95 ± 0.49[b]
Diaphysis—tibia	0.76 ± 0.11	0.59 ± 0.7[b]	0.75 ± 0.12	0.64 ± 0.08[a]	1.04 ± 0.05	0.92 ± 0.14[b]	1.21 ± 0.13	1.02 ± 0.18[a]
Diaphysis—femur	1.27 ± 0.19	1.00 ± 0.06[b]	1.24 ± 0.13	1.11 ± 0.13	1.52 ± 0.16	1.54 ± 0.19	1.85 ± 0.17	1.68 ± 0.16[a]
Trabecular area (mm^2)								
Metaphysis—Tibia	0.96 ± 0.17	0.80 ± 0.13[b]	1.00 ± 0.13	0.86 ± 0.16[a]	0.97 ± 0.21	0.98 ± 0.18	1.20 ± 0.33	1.20 ± 0.27
Metaphysis—Femur	1.19 ± 0.17	0.97 ± 0.06[b]	1.04 ± 0.19	1.06 ± 0.11	0.74 ± 0.53	0.75 ± 0.31	0.80 ± 0.43	0.99 ± 0.19
Cortical density (mg/mm^3)								
Diaphysis—tibia	907.88 ± 38.76	905.64 ± 14.08	929.75 ± 41.90	888.07 ± 32.51[a]	1143.41 ± 15.39	1106.03 ± 27.45[a]	1150.43 ± 21.96	1124.31 ± 25.70[a]
Diaphysis—femur	854.28 ± 65.87	818.80 ± 68.44	870.14 ± 21.31	836.42 ± 21.2[a]	1163.23 ± 36.94	1096.95 ± 33.67[b]	1169.45 ± 18.14	1115.55 ± 58.61[a]
Cortical area (mm^2)								
Diaphysis—tibia	0.46 ± 0.06	0.39 ± 0.04[b]	0.48 ± 0.08	0.40 ± 0.05[a]	0.78 ± 0.04	0.68 ± 0.09[a]	0.91 ± 0.07	0.73 ± 0.11[a]
Diaphysis—femur	0.56 ± 0.13	0.49 ± 0.05	0.58 ± 0.05	0.49 ± 0.06[a]	1.00 ± 0.11	0.95 ± 0.15	1.21 ± 0.13	1.00 ± 0.15[b]
Cortical thickness (mm)								
Diaphysis—tibia	0.18 ± 0.01	0.18 ± 0.01	0.198 ± 0.03	0.178 ± 0.01[a]	0.29 ± 0.02	0.27 ± 0.02[a]	0.31 ± 0.01	0.27 ± 0.02[b]
Diaphysis—femur	0.16 ± 0.04	0.15 ± 0.05	0.17 ± 0.01	0.15 ± 0.01[a]	0.288 ± 0.02	0.266 ± 0.03	0.32 ± 0.02	0.27 ± 0.04[b]
Periosteum circumference (mm)								
Diaphysis—tibia	3.09 ± 0.23	2.72 ± 0.15[b]	3.05 ± 0.24	2.82 ± 0.19[a]	3.61 ± 0.09	3.38 ± 0.25	3.90 ± 0.21	3.56 ± 0.31[a]
Diaphysis—femur	3.99 ± 0.30	3.54 ± 0.11[b]	3.94 ± 0.20	3.73 ± 0.21	4.36 ± 0.22	4.39 ± 0.22	4.81 ± 0.22	4.59 ± 0.22[a]
Endosteum circumference (mm)								
Diaphysis—tibia	1.94 ± 0.21	1.59 ± 0.16[b]	1.81 ± 0.21	1.71 ± 0.15	1.81 ± 0.09	1.69 ± 0.25	1.95 ± 0.22	1.89 ± 0.23
Diaphysis—femur	2.97 ± 0.42	2.63 ± 0.36[a]	2.88 ± 0.21	2.79 ± 0.21	2.56 ± 0.17	2.72 ± 0.17[a]	2.83 ± 0.14	2.91 ± 0.18
Medullar canal (mm^2)								
Diaphysis—tibia	0.21 ± 0.05	0.14 ± 0.03[b]	0.187 ± 0.05	0.16 ± 0.05	0.18 ± 0.05	0.15 ± 0.05[b]	0.22 ± 0.04	0.19 ± 0.05
Diaphysis—femur	0.52 ± 0.12	0.39 ± 0.06[b]	0.51 ± 0.08	0.44 ± 0.08	0.40 ± 0.05	0.45 ± 0.06[b]	0.49 ± 0.07	0.55 ± 0.06[a]
SSI (mm^3)								
Diaphysis—tibia	0.10 ± 0.02	0.07 ± 0.001	0.11 ± 0.03	0.08 ± 0.02[b]	0.23 ± 0.01	0.172 ± 0.04[b]	0.28 ± 0.04	0.21 ± 0.05[b]
Diaphysis—femur	0.16 ± 0.04	0.12 ± 0.01[a]	0.18 ± 0.02	0.126 ± 0.02[b]	0.38 ± 0.06	0.34 ± 0.07	0.50 ± 0.07	0.4 ± 0.07[b]

[a] $p < 0.05$.
[b] $p < 0.005$.

us to shed new light on the molecular mechanism linking loss of enzymatic activity with skeletal development and homeostasis. Homozygous *dal*/*dal* mice reproduced the small size often observed in PD patients (Fig. 2D). The mutant mice had very low prolidase activity in fibroblast and osteoblast lysates and severe iminodipeptiduria, which represent the typical clinical signs for PD diagnosis (Figs. 2A, C). The mutant protein was stably translated in both skin and bone (Fig. 2B). This result is consistent with findings in human patients in whom, depending on how the mutation affects protein stability, some molecular defects destabilize the enzyme even at the transcript level, other mutations reduce protein translation, while in some cases the synthesis of prolidase is minimally or not at all affected.

Bone strength depends on both structure and material composition and is the dynamic result of adaptive modeling and remodeling processes. Different bones have different strengths based on the loads they have to tolerate and on their shape; thus, even among the long bones, tibia and femur properties can be differentially affected by diseases. Gender also modulates bone properties because of the effect of bone size and hormonal status during development and aging [27,28]. Thus, in order to deeply investigate the skeletal phenotype in PD mice, we used pQCT analysis to evaluate the geometrical parameters and structural properties of two different types of long bones, tibia and femur, in female and male *dal*/*dal* and control mice at pre- to peri-pubertal (P30) and pubertal age (P60). μCT was also carried out to further validate the data at microstructural level. Total trabecular and cortical areas were reduced in mutant mice of both genders and ages considered, demonstrating smaller bones than control littermates (Table 3). The femur length of *dal*/*dal* mice was also significantly reduced (Fig. 2E). Prolidase is known to affect both collagen synthesis and collagen degradation, two crucial processes in bone modeling/remodeling [3]. During long bone growth, periosteal apposition increases its diameter while concurrent endocortical resorption excavates the marrow cavity. A synchronized activity of the two events is necessary for normal radial bone growth. pQCT analysis of P30 female *dal*/*dal* long bones revealed that the absence of prolidase results in reduced periosteal and endosteal circumference suggesting a reduction in bone deposition and bone resorption respectively (Table 3). This resulted in unchanged cortical thickness. At P60, the periosteal bone circumference of the tibia was reduced causing significantly thinner bone, whereas in the femur a significant increase in endosteal circumference was detected, resulting in a trend toward reduced cortical thickness. In males, cortical thickness was reduced in both long bones at both ages, mainly due to reduced bone periosteal circumference (Table 3). We cannot anyway exclude an effect of body mass on the cortical bone parameters. Circular polarized light analysis of picro-sirius red-stained tibia sections revealed stronger red staining and reduced green fluorescence in mutant versus

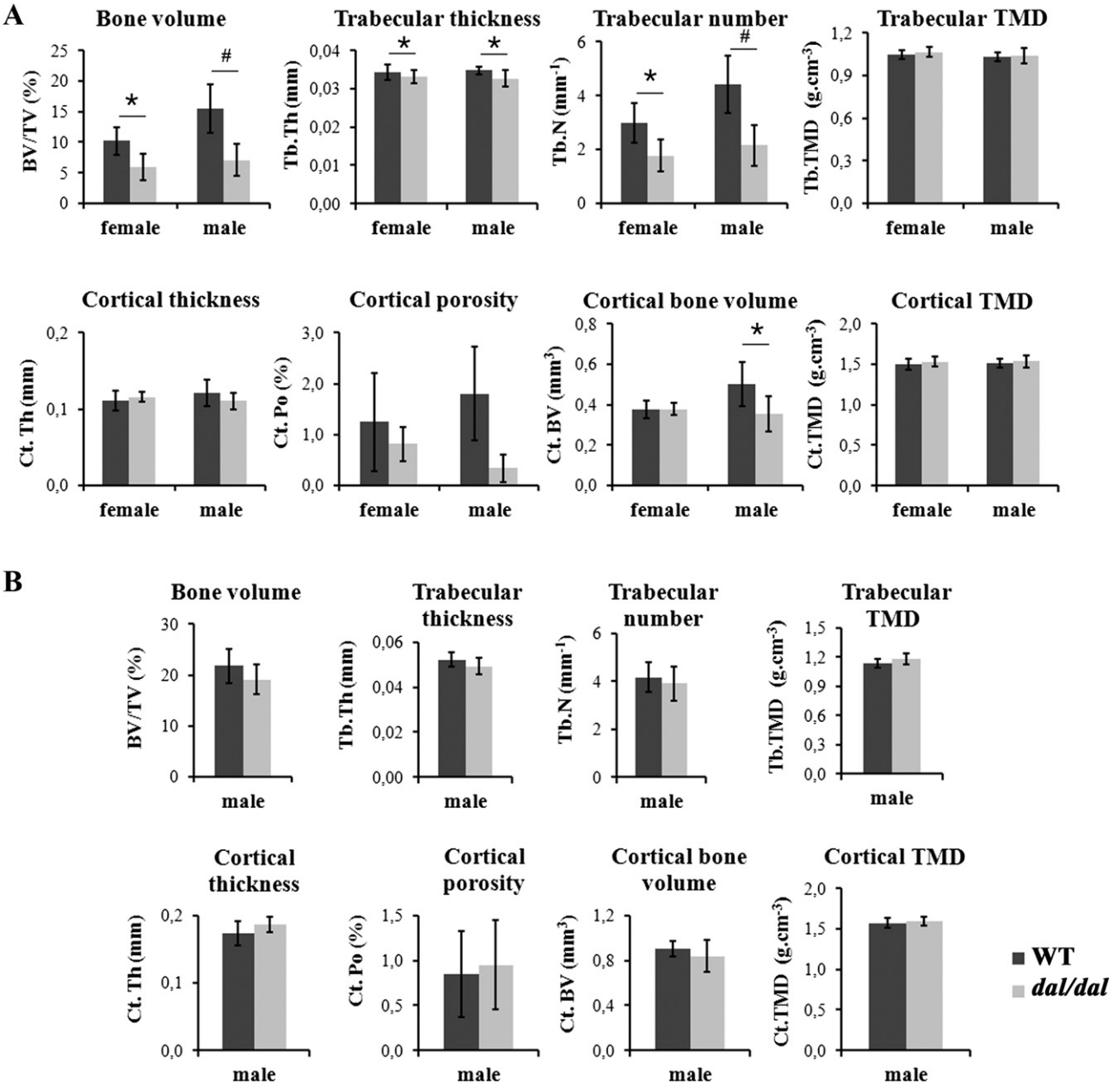

Fig. 3. μCT analyses. Femurs of 1-month-old (A) and 2-month-old (B) WT and *dal*/*dal* mice were analyzed. Significant differences $p < 0.01$, denoted by an asterisk (*), $p < 0.0001$ denoted by a pound symbol (#).

WT mice indicating an abnormal collagen fibers maturation at cortical and trabecular sites (Fig. 4A). The change in color from green to red of picro-sirius red-stained collagen fibers under circular polarized light due to fiber thickening is well recognized [29].

Another parameter often used to evaluate bone remodeling rate is cortical porosity. In P30 *dal*/*dal* mice of both genders, there was a trend to reduced cortical porosity, although without reaching significance, compared with WT littermates (Fig. 3A), supporting the presence of an altered bone structure at younger age normalizing in pubertal mice.

μCT analysis confirmed a significant reduction of bone size both at trabecular and cortical sites at P30. Interestingly a complete rescue was detected at P60 (Fig. 3B), suggesting that the more severe effect of lack of prolidase activity on long bones was limited to post-natal and pubertal ages, when bone remodeling during rapid growth is more active. Interestingly cortical BMD (bone mineral density) evaluated by pQCT was reduced both at P30 and P60 in mutant mice, but no difference was reported in TMD (tissue mineral density) measured by μCT analysis. This apparent discrepancy could be related to the different spatial resolution of the two methodologies. Due to the low voxel size (<5 μm^3), the mineral density measured by μCT is the expression of the properties of the bone tissue constituting the cortex, excluding vascular spaces (Haversian canal and Volkmann canals) that are included in density measured by pQCT [30]. Larger bone volume effect in pQCT-BMD due to the smaller bone size of the *dal*/*dal* mice [31] and different segmentation procedures might also contribute to this apparent descrepancy. Based on BMD results obtained by pQCT and TMD data from μCT we can hypothesize that the density differences between mutant and WT mice might be ascribed to the reduced bone mass/size of the *dal*/*dal* at the cortical and trabecular compartments rather than to a mineralization defect of its bone matrix.

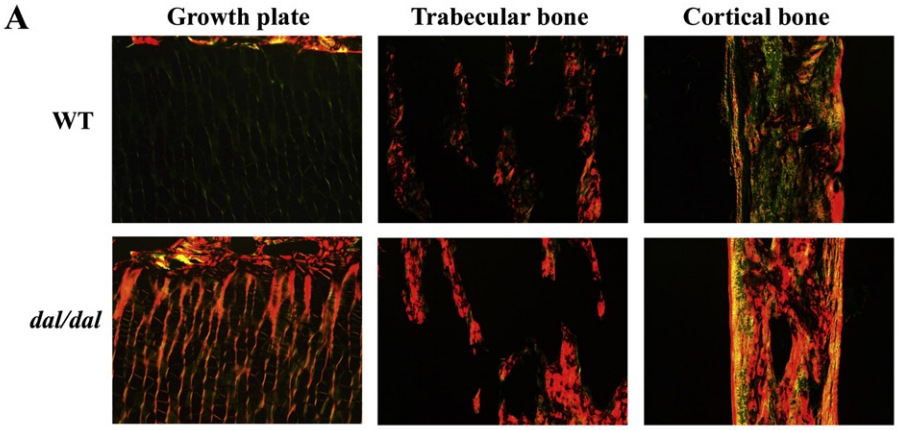
A
Growth plate
Trabecular bone
Cortical bone
WT
dal/dal

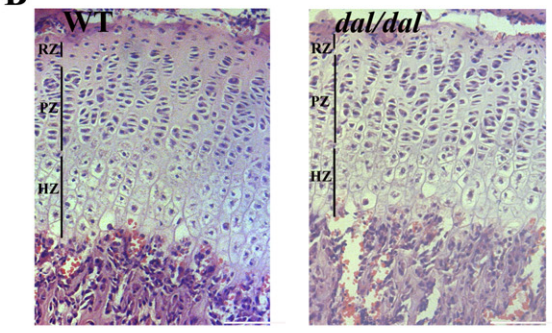
B
WT
dal/dal
RZ
PZ
HZ

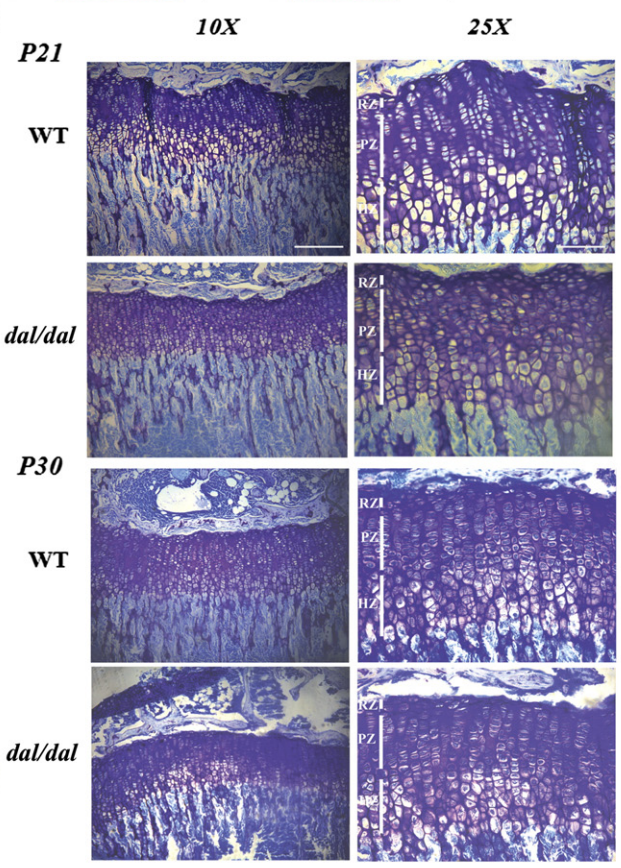
C
10X
25X
P21
WT
dal/dal
RZ
PZ
HZ

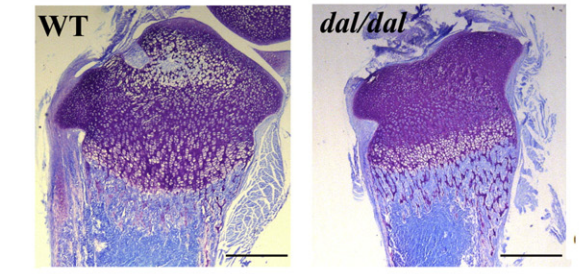
D
WT
dal/dal

P30
WT
dal/dal
RZ
PZ
HZ

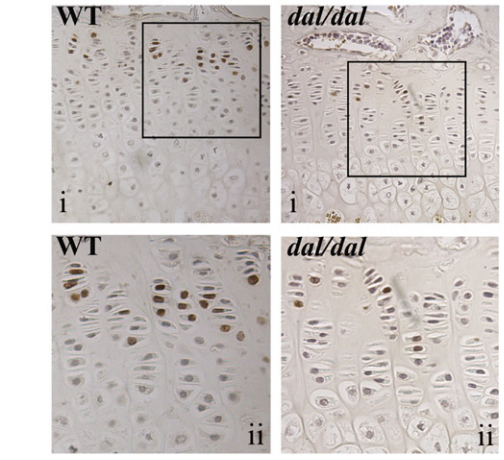
E
WT
dal/dal
i
ii

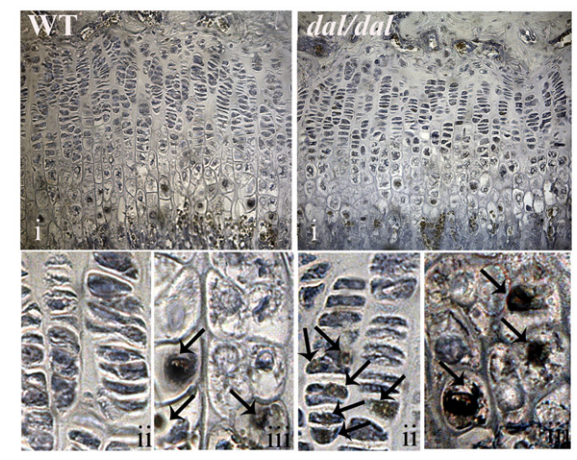
F
WT
dal/dal
i
ii
iii

Table 4
Histomorphometric parameters of the tibial growth plate in *dal/dal* mutants and WT littermates at P21 and at P30.

	P21				P30			
	Female		Male		Female		Male	
	WT	*dal/dal*	WT	*dal/dal*	WT	*dal/dal*	WT	*dal/dal*
Growth plate height (μm)	296 ± 24.7	258.9 ± 44.8	314 ± 52.2	286.2 ± 13.0	280.4 ± 16.8	251.9 ± 28.3	274.3 ± 16.9	257.2 ± 9.6
Proliferative zone height (PZ, μm)	134.2 ± 22.5	131.2 ± 24.5	135.5 ± 24.2	127.2 ± 15.7	119.2 ± 11.0	120.6 ± 18.0	130.5 ± 10.4	125.5 ± 2.2
Hypertrophic zone height (HZ, μm)	130.7 ± 19.8	99.8 ± 17.2[a]	158.9 ± 26.8	118.1 ± 15.9[a]	116.8 ± 9.3	101.4 ± 14.7[a]	129.0 ± 10.0	106.0 ± 9.4[a]
Resting zone height (μm)	26.5 ± 5.1	29.6 ± 11.6	23.6 ± 2.1	31.5 ± 18.4	31.9 ± 4.5	5.9 ± 0.7	24.6 ± 5.1	25.7 ± 4.7
Column height in the PZ (μm)	69.3 ± 20.1	59.6 ± 15.3	77.4 ± 18.4	60.2 ± 4.9	50.8 ± 7.0	63.5 ± 3.7	61.8 ± 9.8	66.1 ± 7.2
No. of cells for column in the PZ	9.5 ± 0.7	8.8 ± 1.8	9 ± 1.0	8.4 ± 0.3	6.1 ± 1.3	8.5 ± 0.4	8.5 ± 0.9	8.4 ± 2.5
Column height in the HZ (μm)	109.6 ± 21.8	67.4 ± 18.1[a]	139.1 ± 25.7	97.3 ± 2.3[a]	110.8 ± 5.8	83.1 ± 12.0[b]	115.9 ± 6.7	91.8 ± 13.1[a]
No. of cells for column in the HZ	5.8 ± 0.6	4.3 ± 0.4[b]	6.5 ± 0.5	5.2 ± 0.3[b]	5.9 ± 0.7	4.6 ± 0.7[a]	5.8 ± 0.3	4.8 ± 0.7[a]

[a] $p < 0.05$.
[b] $p < 0.005$.

Reduced long bone strength in *dal/dal* male mice was revealed by lower values of stress strain index compared to WT littermates (Table 3). Development and longitudinal growth of long bones depend on endochondral ossification, a strictly regulated process requiring proliferation and differentiation of chondrocytes in the growth plate as well as the synthesis of regionally specific extracellular matrix components. Alterations of these events are responsible for impaired skeletogenesis in various diseases [32]. Defects in metallo-proteases compromising ECM remodeling and thus impairing proper vascularization and recruitment of specialized cells such as chondroclast/osteoclast and osteoblast are known to cause severe skeletal defects as does lack of the bone angiogenic factor VEGF [33,34]. More recently it has been demonstrated that endoplasmic reticulum stress also contributes in modulating the outcome in bone diseases [35,36]. Prolidase is a cytosolic protease involved in catabolism and synthesis of fibrillar collagens and this is the first time that an alteration in an intracellular cytosolic protease has been shown to result in a bone phenotype in the PD murine model.

HIF-1α is known to be the major player allowing avascular cartilage to survive in hypoxic condition. HIF-1α regulates cartilage blood vessels invasion thanks to a stimulating effect on the transcription of VEGF isoforms. The catabolic products of prolidase, mainly hydroxyproline, are known to increase HIF-1α [6]. Although further experimental data will be required to demonstrate that, we can speculate that lack of prolidase may fail to properly enhance HIF-1α resulting in an impaired vascularization which in turn could be responsible for delay in osteoclast and osteoblast recruitment. It is also possible that decreased remodeling and accumulation of collagen in bone impairs the release and diffusion of VEGF, thus reducing its viability. Indeed, in PD patients' histological examination at ulcer sites demonstrated severe angiopathy and in one case magnetic resonance imaging revealed multiple microthrombosis in cerebral white matter [37]. No abnormal vascularization was detected in *dal/dal* mice metaphyses, but in mutant mice a delay in the formation of the second ossification center was evident at P10 (Fig. 4D). Indeed, impaired vascularization at the hypertrophic zone of cartilage growth plate should cause its enlargement as demonstrated in VEGF knock-out mice [38]. However, in homozygous *dal* mice there was a normal organization of the growth plate, but the height of hypertrophic zone was reduced probably due to increased apoptosis in the proliferative zone (Figs. 4C-F, Table 4). Other consequences may result from lack of prolidase activity at the metaphysis. Collagen is a major ligand of integrins and a significant reduction in the levels of several integrin transducers were detected in embryonic *dal/dal* mutant heart [14]. Previous data demonstrated that integrin α10β1 plays a specific role in growth plate morphogenesis and function. Mutant mice carrying a constitutive deletion of the α10 integrin gene, a collagen-binding integrin expressed on chondrocytes, developed long bone growth retardation and a reduced height of the hypertrophic zone together with an increased number of apoptotic chondrocytes [39]. Interestingly, in the *dal/dal* mutant mouse, a high number of apoptotic cells were detected in the proliferative zone, suggesting compromised cell viability. Previous in vitro studies have demonstrated that accumulation of undigested dipeptides was responsible for cellular death in long-term fibroblast cultures [40]. It is possible that a similar event occurs in proliferating chondrocytes explaining the reduced proliferating capability and the increase of apoptosis. Mutant chondrocytes may lose their ability to regulate collagen II turnover and indeed this could account for the brighter staining of cartilage growth plate by picro-sirius red under circular polarized light. Interestingly, an accumulation of collagen II was previously associated with delayed ossification at the chondro-osseous junction [41].

In conclusion, we have shown for the first time that prolidase is an important regulator of bone growth with a primary function during post-natal and pubertal ages, when the requirement for collagen synthesis and degradation is higher. Longitudinal bone growth was impaired, mainly due to chondrocytes inability to provide the microenvironment necessary to insure proper growth plate functions. Geometrical bone properties were also compromised in mice lacking prolidase activity and the reason for that remains still speculative. Either a secondary effect of the reduced overall body mass or an altered bone cellular activity could be hypothesized. Our data provide another piece to the puzzle of the complex mechanisms modulating bone development.

Supplementary data to this article can be found online at http://dx.doi.org/10.1016/j.bone.2014.11.009.

Competing interest statement

The authors declare no competing financial interest.

Acknowledgments

The authors wish to acknowledge Mr Angelo Gallanti, Department of Molecular Medicine, Biochemistry Unit, University of Pavia, Pavia, Italy,

Fig. 4. Histological studies of the growth plate. (A) Picro-sirius red staining of collagen type I in tibia sections (20×) from P30 *dal/dal* and WT mice. (B) Tibia sections from P30 WT and mutant mice stained by hematoxylin and eosin (10×, scale bar: 250 μm). (C) Toluidine blue stained sections of the proximal tibia epiphysis at P21 and at P30 at 10× (scale bar: 250 μm) and 25× (scale bar: 100 μm). RZ = resting zone; PZ = proliferative zone; HZ = hypertrophic zone. (D) Formation of the secondary ossification center of the proximal epiphysis of the tibia investigated at P10 by toluidine blue staining. (E) Proliferation in the proximal tibia of P30 WT and *dal/dal* mice, evaluated by BrdU staining (panels i, 25×). High magnification of proliferating chondrocytes in WT and *dal/dal* proliferative zone (panels ii). (F) Evaluation of apoptosis in the proximal tibia of P30 WT and *dal/dal* mice by TUNEL assay (panels i, 25×). High magnification of the apoptotic chondrocytes in WT and *dal/dal* proliferative zone (panels ii) and hypertrophic zone (panels iii). Arrows mark apoptotic chondrocytes.

for the tissue culture support and Dr Alessandro Rubinacci, MD, Head of the Bone Metabolic Unit, San Raffaele Scientific Institute, Milan, Italy, for the helpful discussion of the data. This work was supported by FONDAZIONE CARIPLO 2013-0612 to A.F., the European Community's Seventh Framework Programme under grant agreement n. 602300 (SYBIL) to A.R and A.F. and FONDAZIONE CARIPLO 2011-0270 to R.T.

References

[1] Royce PM, Steinmann B. Prolidase deficiency. Connective tissue and its heritable disorders. New-York: Wiley-Liss; 2002. p. 727–43.
[2] Lupi A, Tenni R, Rossi A, Cetta G, Forlino A. Human prolidase and prolidase deficiency: an overview on the characterization of the enzyme involved in proline recycling and on the effects of its mutations. Amino Acids 2008;35:739–52.
[3] Surazynski A, Miltyk W, Palka J, Phang JM. Prolidase-dependent regulation of collagen biosynthesis. Amino Acids 2008;35:731–8.
[4] Cechowska-Pasko M, Palka J, Wojtukiewicz MZ. Enhanced prolidase activity and decreased collagen content in breast cancer tissue. Int J Exp Pathol 2006;87:289–96.
[5] Palka JA, Phang JM. Prolidase activity in fibroblasts is regulated by interaction of extracellular matrix with cell surface integrin receptors. J Cell Biochem 1997;67:166–75.
[6] Surazynski A, Donald SP, Cooper SK, Whiteside MA, Salnikow K, Liu Y, Phang JM. Extracellular matrix and HIF-1 signaling: the role of prolidase. Int J Cancer 2008;122:1435–40.
[7] Soran N, Altindag O, Aksoy N, Cakir H, Taskin A, Soran M, Isikan E. The association of serum prolidase activity with developmental dysplasia of the hip. Rheumatol Int 2013;33:1939–42.
[8] Galicka A, Wolczynski S, Anchim T, Surazynski A, Lesniewicz R, Palka J. Defects of type I procollagen metabolism correlated with decrease of prolidase activity in a case of lethal osteogenesis imperfecta. Eur J Biochem 2001;268:2172–8.
[9] Endo F, Matsuda I. Molecular basis of prolidase (peptidase D) deficiency. Mol Biol Med 1991;8:117–27.
[10] Falik-Zaccai TC, Khayat M, Luder A, Frenkel P, Magen D, Brik R, Gershoni-Baruch R, Mandel H. A broad spectrum of developmental delay in a large cohort of prolidase deficiency patients demonstrates marked interfamilial and intrafamilial phenotypic variability. Am J Med Genet B Neuropsychiatr Genet 2009;153B:46–56.
[11] Marotte H, Gineyts E, Miossec P. Prolidase deficiency: a rare aetiology of arthritis. Joint Bone Spine 2010;77:88–9.
[12] Shrinath M, Walter JH, Haeney M, Couriel JM, Lewis MA, Herrick AL. Prolidase deficiency and systemic lupus erythematosus. Arch Dis Child 1997;76:441–4.
[13] Cota CD, Liu RR, Sumberac TM, Jung S, Vencato D, Millet YH, Gunn TM. Genetic and phenotypic studies of the dark-like mutant mouse. Genesis 2008;46:562–73.
[14] Jung S, Silvius D, Nolan KA, Borchert GL, Millet YH, Phang JM, Gunn TM. Developmental cardiac hypertrophy in a mouse model of prolidase deficiency. Birth Defects Res A Clin Mol Teratol 2008;91:204–17.
[15] Caselli D, Cimaz R, Besio R, Rossi A, De Lorenzi E, Colombo R, Cantarini L, Riva S, Spada M, Forlino A, Arico M. Partial rescue of biochemical parameters after hematopoietic stem cell transplantation in a patient with prolidase deficiency due to two novel PEPD mutations. JIMD Rep 2012;3:71–7.
[16] Forlino A, Porter FD, Lee EJ, Westphal H, Marini JC. Use of the Cre/lox recombination system to develop a non-lethal knock-in murine model for osteogenesis imperfecta with an alpha1(I) G349C substitution. Variability in phenotype in BrtlIV mice. J Biol Chem 1999;274:37923–31.
[17] Panaroni C, Gioia R, Lupi A, Besio R, Goldstein SA, Kreider J, Leikin S, Vera JC, Mertz EL, Perilli E, Baruffaldi F, Villa I, Farina A, Casasco M, Cetta G, Rossi A, Frattini A, Marini JC, Vezzoni P, Forlino A. In utero transplantation of adult bone marrow decreases perinatal lethality and rescues the bone phenotype in the knockin murine model for classical, dominant osteogenesis imperfecta. Blood 2009;114:459–68.
[18] Besio R, Monzani E, Gioia R, Nicolis S, Rossi A, Casella L, Forlino A. Improved prolidase activity assay allowed enzyme kinetic characterization and faster prolidase deficiency diagnosis. Clin Chim Acta 2011;412:1814–20.
[19] Lupi A, Rossi A, Vaghi P, Gallanti A, Cetta G, Forlino A. N-benzyloxycarbonyl-L-proline: an in vitro and in vivo inhibitor of prolidase. Biochim Biophys Acta 2005;1744:157–63.
[20] Vanky P, Brockstedt U, Hjerpe A, Wikstrom B. Kinetic studies on epiphyseal growth cartilage in the normal mouse. Bone 1998;22:331–9.
[21] Vandoorne K, Magland J, Plaks V, Sharir A, Zelzer E, Wehrli F, Hemmings BA, Harmelin A, Neeman M. Bone vascularization and trabecular bone formation are mediated by PKB alpha/Akt1 in a gene-dosage-dependent manner: in vivo and ex vivo MRI. Magn Reson Med 2010;64:54–64.
[22] Hengsberger S, Kulik A, Zysset P. Nanoindentation discriminates the elastic properties of individual human bone lamellae under dry and physiological conditions. Bone 2002;30:178–84.
[23] Bissonnette R, Friedmann D, Giroux J, Dolenga M, Hechtman P, Der Kaloustian V, Dubuc R. Prolidase deficiency: a multisystemic hereditary disorder. J Am Acad Dermatol 1993;29:818–21.
[24] Kurien BT, D' Sousa A, Bruner BF, Gross T, James JA, Targoff IN, Maier-Moore JS, Harley IT, Wang H, Scofield RH. Prolidase deficiency breaks tolerance to lupus-associated antigens. Int J Rheum Dis 2013;16:674–80.
[25] Guerri-Fernandez RC, Nogues X, Quesada Gomez JM, Torres Del Pliego E, Puig L, Garcia-Giralt N, Yoskovitz G, Mellibovsky L, Hansma PK, Diez-Perez A. Microindentation for in vivo measurement of bone tissue material properties in atypical femoral fracture patients and controls. J Bone Miner Res 2013;28:162–8.
[26] Gallant MA, Brown DM, Organ JM, Allen MR, Burr DB. Reference-point indentation correlates with bone toughness assessed using whole-bone traditional mechanical testing. Bone 2013;53:301–5.
[27] Mohan S, Hu Y, Edderkaoui B. Identification of gender-specific candidate genes that influence bone microarchitecture in chromosome 1. Calcif Tissue Int 2013;92:362–71.
[28] Orwoll ES, Belknap JK, Klein RF. Gender specificity in the genetic determinants of peak bone mass. J Bone Miner Res 2001;16:1962–71.
[29] Rich L, Whittacher P. Collagen and picrosirius red staining: a polarized light assessment of fibrillar hue and spatial distribution. Braz J Morphol Sci 2005;22:97–104.
[30] Bouxsein ML, Boyd SK, Christiansen BA, Guldberg RE, Jepsen KJ, Muller R. Guidelines for assessment of bone microstructure in rodents using micro-computed tomography. J Bone Miner Res 2010;25:1468–86.
[31] Brodt MD, Pelz GB, Taniguchi J, Silva MJ. Accuracy of peripheral quantitative computed tomography (pQCT) for assessing area and density of mouse cortical bone. Calcif Tissue Int 2003;73:411–8.
[32] Staines KA, Pollard AS, McGonnell IM, Farquharson C, Pitsillides AA. Cartilage to bone transitions in health and disease. J Endocrinol 2013;219:R1-12.
[33] Maes C, Carmeliet P, Moermans K, Stockmans I, Smets N, Collen D, Bouillon R, Carmeliet G. Impaired angiogenesis and endochondral bone formation in mice lacking the vascular endothelial growth factor isoforms VEGF164 and VEGF188. Mech Dev 2002;111:61–73.
[34] Page-McCaw A, Ewald AJ, Werb Z. Matrix metalloproteinases and the regulation of tissue remodelling. Nat Rev Mol Cell Biol 2007;8:221–33.
[35] Forlino A, Cabral WA, Barnes AM, Marini JC. New perspectives on osteogenesis imperfecta. Nat Rev Endocrinol 2011;7:540–57.
[36] Furuichi T, Nishimura G, Ikegawa S. Collagen abnormalities and endoplasmic reticulum stress in bone and cartilage. Clin Calcium 2013;23:1635–40.
[37] Arata J, Tada J, Yamada T, Oono T, Yasutomi H, Oka E. Angiopathic pathogenesis of clinical manifestations in prolidase deficiency. Arch Dermatol 1991;127:124–5.
[38] Maes C, Stockmans I, Moermans K, Van Looveren R, Smets N, Carmeliet P, Bouillon R, Carmeliet G. Soluble VEGF isoforms are essential for establishing epiphyseal vascularization and regulating chondrocyte development and survival. J Clin Invest 2004;113:188–99.
[39] Bengtsson T, Aszodi A, Nicolae C, Hunziker EB, Lundgren-Akerlund E, Fassler R. Loss of alpha10beta1 integrin expression leads to moderate dysfunction of growth plate chondrocytes. J Cell Sci 2005;118:929–36.
[40] Forlino A, Lupi A, Vaghi P, Icaro Cornaglia A, Calligaro A, Campari E, Cetta G. Mutation analysis of five new patients affected by prolidase deficiency: the lack of enzyme activity causes necrosis-like cell death in cultured fibroblasts. Hum Genet 2002;111:314–22.
[41] Ortega N, Wang K, Ferrara N, Werb Z, Vu TH. Complementary interplay between matrix metalloproteinase-9, vascular endothelial growth factor and osteoclast function drives endochondral bone formation. Dis Model Mech 2010;3:224–35.

OXFORD

Human Molecular Genetics, 2015, Vol. 24, No. 21 6118–6133

doi: 10.1093/hmg/ddv328
Advance Access Publication Date: 11 August 2015
Original Article

ORIGINAL ARTICLE

Altered cytoskeletal organization characterized lethal but not surviving Brtl$^{+/-}$ mice: insight on phenotypic variability in osteogenesis imperfecta

Laura Bianchi[1], Assunta Gagliardi[1], Silvia Maruelli[2], Roberta Besio[2], Claudia Landi[1], Roberta Gioia[2], Kenneth M. Kozloff[3], Basma M. Khoury[3], Paul J. Coucke[4], Sofie Symoens[4], Joan C. Marini[5], Antonio Rossi[2], Luca Bini[1] and Antonella Forlino[2,*]

[1]Functional Proteomics Laboratory, Department of Life Sciences, University of Siena, Siena, Italy, [2]Department of Molecular Medicine, Biochemistry Unit, University of Pavia, Pavia, Italy, [3]Orthopaedic Research Laboratories, Department of Orthopaedic Surgery, University of Michigan, Ann Arbor, MI, USA, [4]Center for Medical Genetics, Ghent University, Ghent, Belgium and [5]Bone and Extracellular Matrix Branch, NICHD, National Institute of Health, Bethesda, MD, USA

*To whom correspondence should be addressed at: Department of Molecular Medicine, Biochemistry Unit, University of Pavia, Via Taramelli 3/B, 27100 Pavia, Italy. Tel: +39 0382987235; Email: aforlino@unipv.it

Abstract

Osteogenesis imperfecta (OI) is a heritable bone disease with dominant and recessive transmission. It is characterized by a wide spectrum of clinical outcomes ranging from very mild to lethal in the perinatal period. The intra- and inter-familiar OI phenotypic variability in the presence of an identical molecular defect is still puzzling to the research field. We used the OI murine model Brtl$^{+/-}$ to investigate the molecular basis of OI phenotypic variability. Brtl$^{+/-}$ resembles classical dominant OI and shows either a moderately severe or a lethal outcome associated with the same Gly349Cys substitution in the α1 chain of type I collagen. A systems biology approach was used. We took advantage of proteomic pathway analysis to functionally link proteins differentially expressed in bone and skin of Brtl$^{+/-}$ mice with different outcomes to define possible phenotype modulators. The skin/bone and bone/skin hybrid networks highlighted three focal proteins: vimentin, stathmin and cofilin-1, belonging to or involved in cytoskeletal organization. Abnormal cytoskeleton was indeed demonstrated by immunohistochemistry to occur only in tissues from Brtl$^{+/-}$ lethal mice. The aberrant cytoskeleton affected osteoblast proliferation, collagen deposition, integrin and TGF-β signaling with impairment of bone structural properties. Finally, aberrant cytoskeletal assembly was detected in fibroblasts obtained from lethal, but not from non-lethal, OI patients carrying an identical glycine substitution. Our data demonstrated that compromised cytoskeletal assembly impaired both cell signaling and cellular trafficking in mutant lethal mice, altering bone properties. These results point to the cytoskeleton as a phenotypic modulator and potential novel target for OI treatment.

Received: April 13, 2015. **Revised and Accepted:** August 6, 2015

Introduction

Osteogenesis imperfecta (OI) is a hereditary skeletal dysplasia characterized by reduced bone mineral density (BMD), abnormal bone microarchitecture and frequent fractures in the absence of or in response to minor trauma (1). Extraskeletal manifestations are also reported affecting skin, ligament, heart and lung (2,3).

Osteogenesis imperfecta was traditionally considered a dominantly inherited disease affecting the genes encoding the α chains of type I collagen. More recently, recessive forms of OI have also been described, caused by mutations in a variety of genes mainly affecting type I collagen quantity, structure, synthesis, post-translational modification, secretion or extracellular processing (4,5).

The disorder covers a wide spectrum of clinical severity ranging from very mild osteoporosis to perinatal lethality, and the genotype/phenotype relationship is still poorly understood, both in dominant and in recessive forms (6,7). The phenotypic severity in the presence of type I collagen-mutated genes seems to be at least in part correlated to the gene involved. Correlating with type I collagen stoichiometry, *COL1A2* mutations generally result in a less severe phenotype than *COL1A1* mutations. Also, the position of mutations along the α-chains can modulate the outcome, with mutations at the N-terminus usually being less severe than substitutions in the middle or at the C-terminus of the chains. Specific regions in the triple helix were identified as important for the interaction between collagen and extracellular matrix proteins (Major Ligand Binding Regions), and mutations at these sites are particularly harmful (6). Furthermore, phenotypic variability associated with identical mutations, a common recurrent feature in hereditary diseases, has been described in dominant and recessive OI (8).

The dissection of the molecular basis of OI phenotypic variability is expected to significantly contribute to the understanding of the molecular mechanisms that characterize the disease, leading not only to the identification of novel biomarkers for diagnosis, therapy follow-up and drug design but also toward the delineation of new targetable pathways for novel therapeutic approaches.

The knock-in murine model Brtl$^{+/-}$ represents an important tool for understanding OI phenotypic variability in the presence of an identical defect (9). Brtl$^{+/-}$ mice carry a heterozygous point mutation in *Col1a1*, responsible for the Gly349Cys (p.Gly527Cys) substitution in one α1(I) chain, which was described to be causative in human dominant OI (10). Interestingly, these mutant mice can have either a moderately severe phenotype, resembling human OI type IV, or perinatal lethal OI, resembling OI type II (9).

In an attempt to understand the molecular basis of OI phenotypic variability, we previously performed deep analysis of collagen and tissue extracts from bone, skin and lung of Brtl$^{+/-}$ mice with lethal (ML) and non-lethal (MA) outcomes. Based on our results, we excluded that the variability of Brtl$^{+/-}$ outcome was attributable to differences in collagen structure, physical properties or interaction between mutant collagen helices (11,12). Instead we demonstrated that a difference in intracellular response to mutant collagen retention could be involved. We found, both in skin and in bone, differential expression of chaperones, proteasomal subunits, metabolic enzymes and proteins related to cellular fate in mice with different outcomes. Our data revealed that the intracellular machinery in lethal mice is less effective at coping with the intracellular retention of mutant collagen, favoring up-regulation of molecules involved in apoptosis and protein degradation, in contrast to the mice with a moderately severe outcome, in which chaperone up-regulation is predominant (13,14).

In the present report, using as a starting point our previously obtained transcriptomic and proteomic data from skin and bone tissues of newborn WT and Brtl$^{+/-}$ mice with moderately severe or lethal outcome, we took advantage of pathway analysis to functionally crosslink differentially expressed proteins to define possible phenotype modulators. Tissue 'hybrid nets' were generated by combining all the differentially expressed genes and proteins identified in mutant bone with several proteins detected with aberrant expression in mutant skin, and *vice versa*. These networks not only highlighted that OI similarly affected common pathways in both tissues but, in particular, they allowed a more comprehensive systems biology approach to accurately visualize functional cross-talk that exists between proteins detected with altered expression in mutants. This enabled a proper investigation of protein differences that were undervalued in our previous analyses and allowed further elucidation of the molecular basis of OI phenotypic variability. In particular, we focused on different expression patterns of three proteins that acquired central roles in hybrid nets and that belong to or are involved in cytoskeletal organization. Abnormal cytoskeleton was then experimentally detected in different tissues from Brtl$^{+/-}$ mice with lethal outcome, but not in surviving mutant mice. Calvarial and long-bone osteoblasts revealed an aberrant cytoskeleton affecting cell proliferation, collagen deposition, and integrin and TGF-β signaling with consequent impairment of bone structural properties. Lastly, abnormal cytoskeletal assembly was detected in fibroblasts obtained from lethal, but not from non-lethal, OI patients carrying a substitution at the same glycine.

Results

Hybrid networks of proteins differentially expressed in bone and skin reveal a role of the cytoskeleton in OI disease

Bone/skin and skin/bone hybrid networks were generated by processing together the differential expression data we previously obtained from transcriptomic and proteomic analyses separately performed on bone and skin samples from 1-day-old wild-type (WT) and Brtl$^{+/-}$ mice, with lethal (ML) or moderately severe (MA) OI phenotype (13,14). We performed MetaCore shortest path algorithm pathway analysis and obtained a first 'bone/skin hybrid network' (Fig. 1A) by co-processing genes and proteins differentially expressed in bone (Supplementary Material, Tables S1A and B) (13), and some proteins differentially expressed in skin, which were validated as differentially expressed also in bone by western blot (Supplementary Material, Table S2) (14). Among these latter proteins, only Oct3/4 was excluded from the analysis because of a 'form defect' of functional data processing. As known, this transcriptional factor is involved in several cellular mechanisms (15); thus, its inclusion in the list of proteins to be processed leads to the generation of pathways exclusively focused on it, obscuring other factors and processes that may be relevant in the pathogenic definition of the disease. All the proteins identified as differentially regulated in skin proteomic investigations not only entered into the hybrid net, but two of them, maspin and, in particular, vimentin became central hubs, as highlighted in Figure 1A, where proteins from skin analysis are encircled in red.

Based on the promising results obtained combining bone data with a subset of skin data, we also applied pathway hybridization in a skin functional study. All of the differentially expressed proteins identified in skin from newborn mutant mice (Supplementary Material, Table S3) (14) were processed by the MetaCore shortest

path algorithm in combination with all factors differentially expressed in calvarial samples, detected by proteomics and transcriptomics analyses (Supplementary Material, Table S1A and B) (13). Contrary to the bone/skin hybrid net, all of the bone deregulated factors were included among proteins to be processed by the software without experimentally proving their deregulation in skin

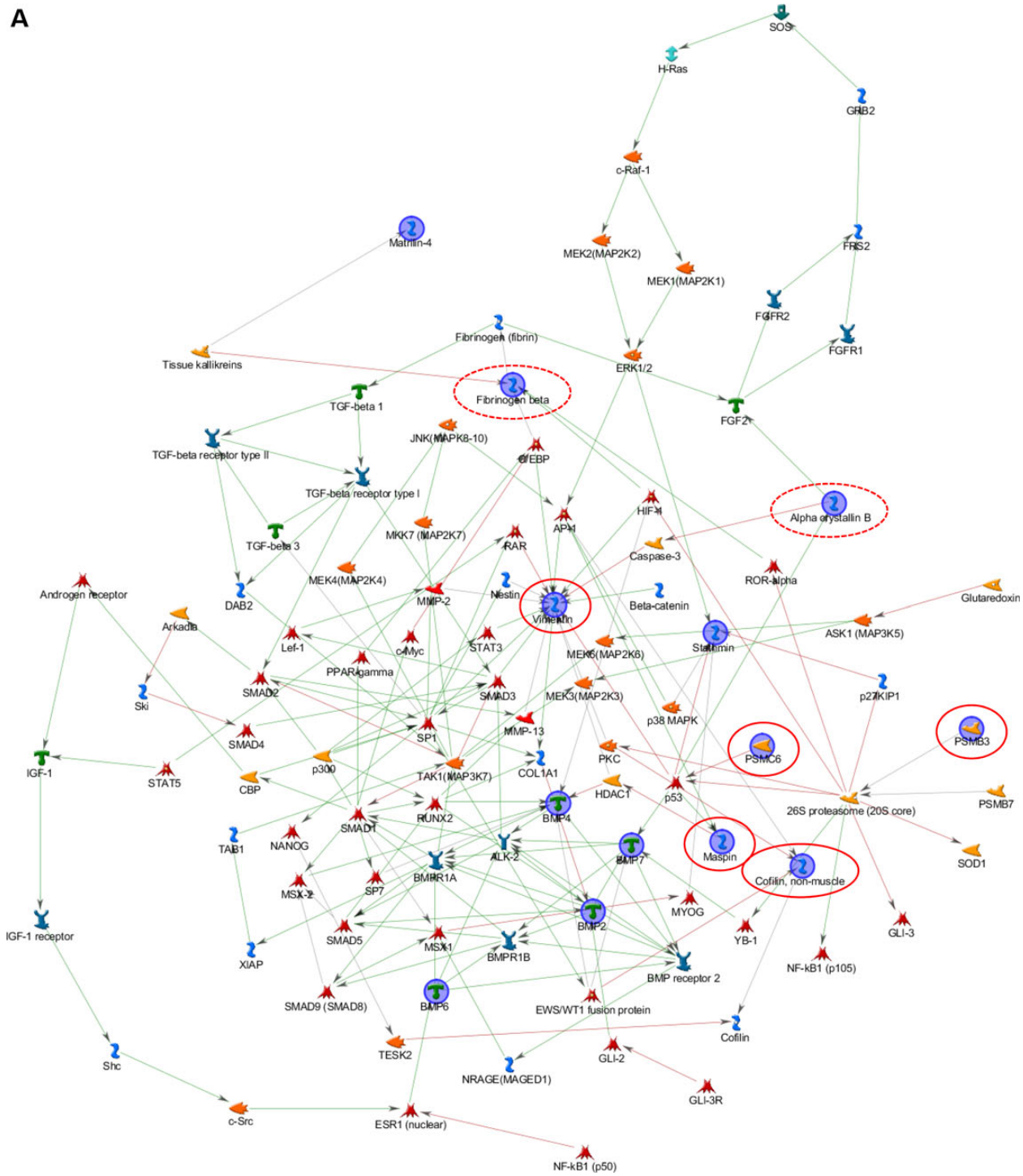

Figure 1. Hybrid networks generated by MetaCore analysis of proteins differentially expressed in bone and skin of lethal and surviving mutant mice and WT littermates. (**A**) Bone/skin hybrid network. Proteins detected as differentially expressed in skin, and experimentally proven to be deregulated also in bone by western blot assays, are highlighted by continuous red line. Proteins that were found differentially expressed both in skin and bone are circled in dashed red. (**B**) Skin/bone hybrid network. Proteins that were found differentially expressed in bone are surrounded by continuous green line, whereas proteins observed differentially expressed both in skin and bone are circled in dashed green. Network proteins are visualized by specific symbols, which define the functional nature of the protein (network caption). The edges indicate the relationships existing between individual proteins, and the arrowheads represent the direction of the interaction. The following line colors designate the nature of the interaction: red: negative effect; green: positive effect; gray: unspecified effect. PSMC6: 26S protease regulatory subunit S10B; PSMB3: proteasome subunit beta type-3; BMP: bone morphogenic protein.

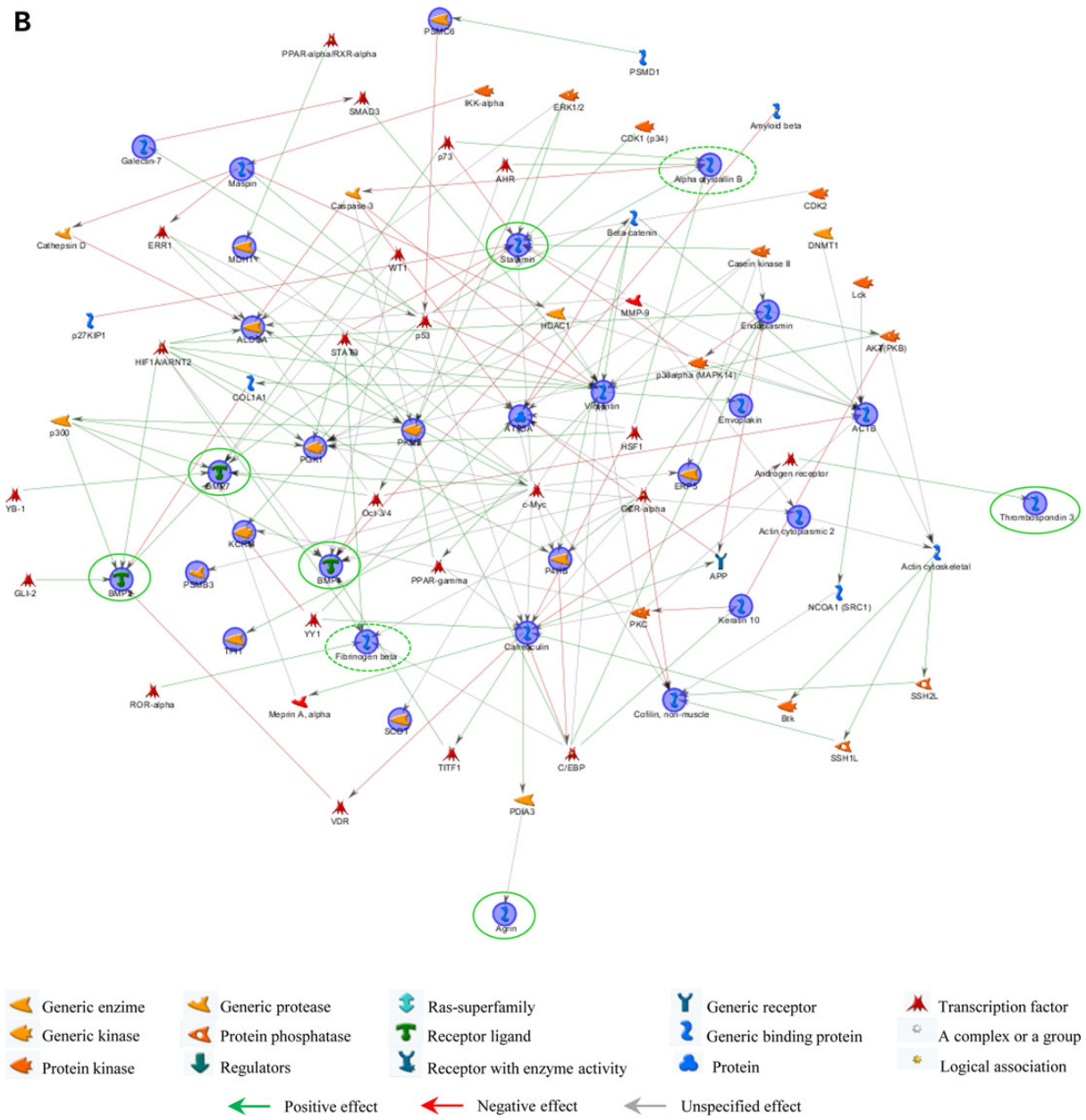

Figure 1. Continued

specimens. With the exception of gadd153, which was excluded from pathway analysis because it is not supported by the MetaCore in-house database, and of matrilin 4 and magp2, all factors with altered expression in mutant bone samples entered into the skin/bone hybrid net (Fig. 1B). Such proteins, shown by green circles in Figure 1B, were perfectly integrated into the net, and only agrin and thrombospondin 3 acquired marginal positions. In particular, stathmin became, with vimentin, one of the main central hubs of the network. Moreover, the integration of bone deregulated proteins did not cause substantial alteration of the original skin network obtained by processing proteins exclusively identified as differentially expressed in skin samples (14).

Clearly, skin and bone share altered cellular processes in which the same proteins are modulated. Hence, hybrid nets consistently support the hypothesis of the systemic nature of OI.

Vimentin and stathmin resulted in two principal central hubs in both hybrid analyses. They are likely to play some key roles in modulating and crosslinking OI-affected pathways. Vimentin is a class-III intermediate filament commonly expressed in various cell types, and its disassembly was described to be correlated to cytoskeleton collapse (16). We previously proved its down-regulation in skin and bone from Brtl$^{+/-}$ mice (14). Stathmin, which we found up-regulated at transcriptional level in bone from mutant lethal mice (13), is instead a microtubule filament-regulating factor that prevents tubulin dimer assembly and promotes disassembly of microtubules (17,18). Based on their functional relevance in both the hybrid nets and on their involvement in correlated cytoskeleton dynamics, we hypothesized the occurrence of an abnormal cytoskeleton organization in Brtl$^{+/-}$ animals.

In the original mutant skin proteomic analysis, we detected the deregulation of another protein with cytoskeleton remodeling activity that was also included into the skin net: cofilin-1 (14). This protein is known to regulate actin dynamics inducing F-actin depolymerization and inhibiting G-actin polymerization (19,20). Interestingly, cofilin-1 not only entered into the skin/bone hybrid net, but it was also included into the bone/skin net, when we added it to the list of skin proteins to be co-processed with all the bone-affected molecules (Fig. 1B).

According to our data, the three main cytoskeletal components, microtubules, microfilaments, and intermediate filaments, are apparently altered in OI. This disease was traditionally considered a disorder of bone extracellular matrix and only recently an intracellular effect on OI phenotype was demonstrated (13,14). Our hybrid pathway analysis further supports this latter concept pointing to cytoskeleton structures involved in OI outcome.

Different expression of stathmin and cofilin-1 in ML, MA and WT mice

In order to experimentally support the *in-silico* data, we analyzed stathmin and cofilin-1 expression levels in bone and skin samples from WT, ML and MA Brtl$^{+/-}$ mice by western blotting. As shown in Figure 2A for stathmin and in Figure 2B for cofilin-1, the expression profile was consistent in both tissues revealing an overexpression in ML mice with respect to both WT and MA animals. Cofilin-1 was also slightly up-regulated in MA versus WT. As ML Brtl$^{+/-}$ mice die when they were 1 day old owing to respiratory stress, the expression of stathmin and cofilin-1 was also evaluated in lung, where indeed the expression of both proteins was found to be up-regulated. However, while cofilin-1 was strongly over-expressed, a moderate increase of stathmin was detected in this tissue (Fig. 2A and B).

Cytoskeletal organization is altered in Brtl$^{+/-}$ lethal mice

The up-regulation of stathmin and cofilin-1 demonstrated in ML mice tissues together with the decrease of vimentin in ML skin and bone samples, as reported in Bianchi *et al.* (14), suggested a potential alteration of cytoskeletal organization in mice with different phenotypic outcome. Thus, in order to evaluate the cytoskeleton, immunohistochemistry was performed on calvaria and long bones, skin and lung tissues obtained from newborn WT and lethal and non-lethal mutant mice. Being a specific

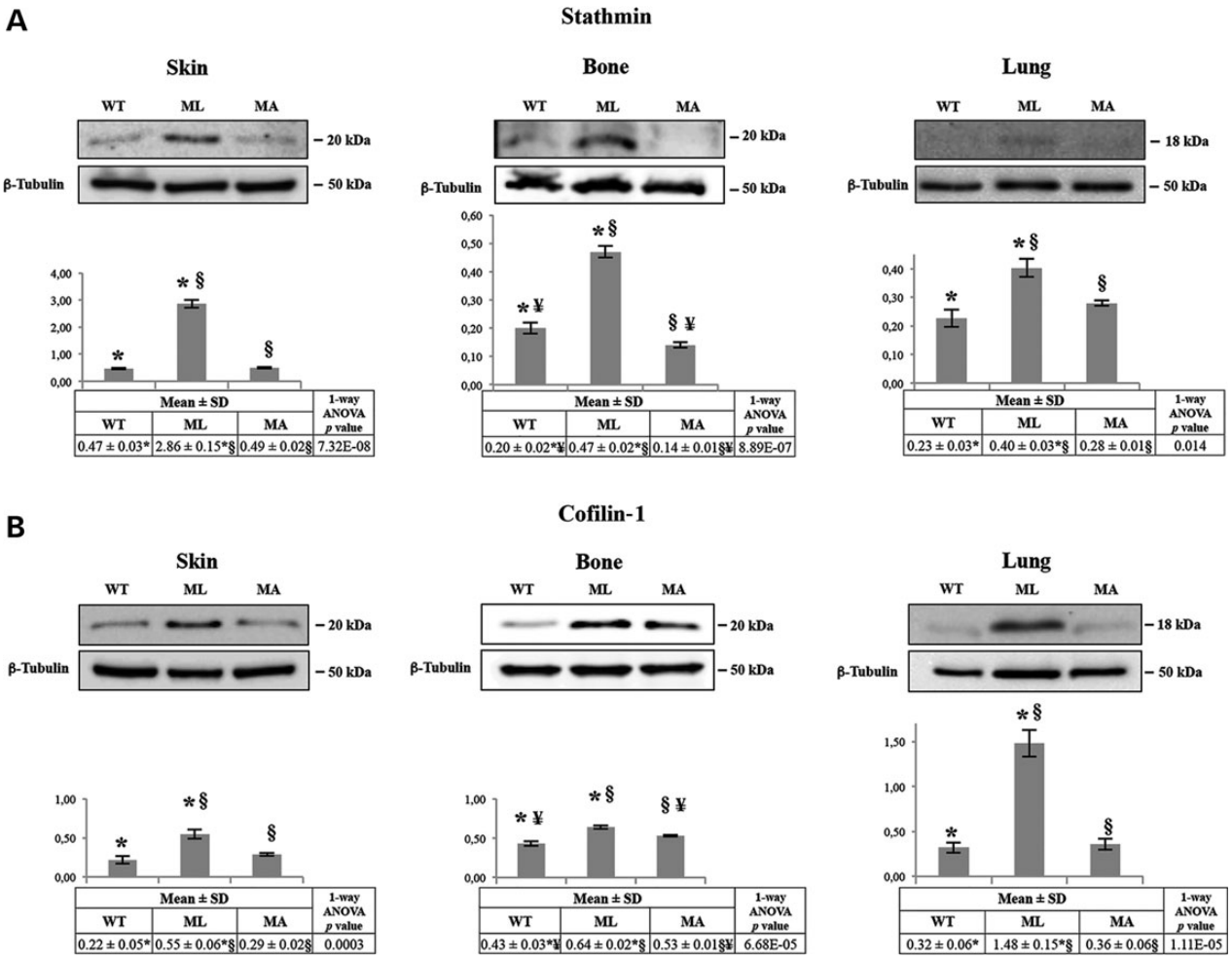

Figure 2. Expression analysis of some focal hubs from hybrid nets in skin, bone and lung tissues. (**A**) Representative western blots of stathmin and corresponding densitometric analysis are shown. In all the three analyzed tissues, stathmin is significantly up-regulated in Brtl$^{+/-}$ lethal (ML) mice with respect to surviving Brtl$^{+/-}$ mice (MA) and WT littermates. (**B**) Representative western blots of cofilin-1 and corresponding densitometric analysis are shown. In all the three analyzed tissues, cofilin-1 is significantly up-regulated in Brtl$^{+/-}$ ML mice. Histograms visualize normalized mean relative-integrated density ± SD values. *, ¥ and § symbols indicate the significance of expression changes occurring between WT and ML, WT and MA, and ML and MA mice, respectively.

marker for actin filaments, fluorescent phalloidin was applied for this purpose. In each analyzed sample, ML tissues revealed a strongly disorganized cytoskeleton that lost its typical framework when compared with MA and control mice (Fig. 3A). Actin fibers showed a punctuate organization rather than a well-organized reticular net.

Actin filaments and integrin-based focal adhesions (FAs) form an integrated system mediating cell–cell and cell–matrix interaction and influencing signal transduction. Thus, in order to evaluate whether cytoskeletal disorganization is associated with altered integrin-mediated signaling, immunohistochemistry on skin, long-bone and calvarial bone cryosections from ML, MA and WT mice using FA kinase antibody was performed (Fig. 3B).

In calvarial bone, a reduced number of FAs were present in mutant lethal mice with respect to MA and WT animals, whereas no difference was detected between mutant surviving mice and WT littermates (Fig. 3B, 1). Throughout the cortical bone, a high

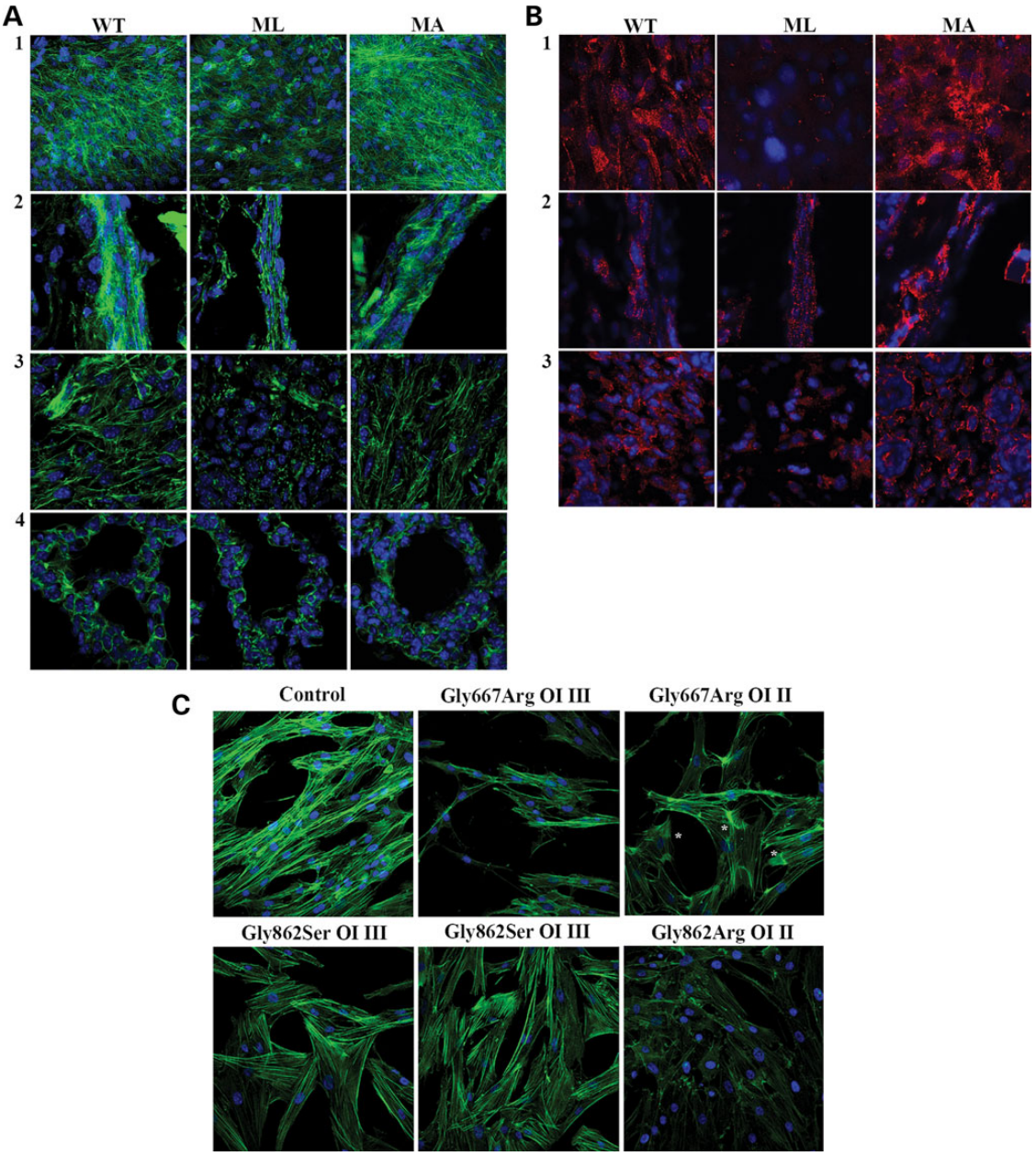

Figure 3. Analysis of the cytoskeletal organization in different tissues from WT, ML and MA mice and in human dermal fibroblasts from OI patients. (**A**) Fluorescently labeled phalloidin (green), specifically interacting with actin, was used to analyze the cytoskeletal organization of calvarial bone (1), long bone (2), skin (3) and lung (4) in WT, ML and MA animals. A disorganized network is evident in samples from mutant lethal mice. (**B**) The focal adhesions (FAs) were evaluated in calvarial bone (1), long bone (2) and skin (3) of WT, ML and MA animals using the FAKpY397 antibody (red). Altered distribution of FAs, indicating an abnormal integrin-mediated signal, is evident in lethal mice. (**C**) Fluorescently labeled phalloidin was used to analyze the cytoskeletal organization of fibroblasts obtained from control, two patients carrying the same α1(I) Gly667Arg substitution, but with different phenotype (severe OI type III and lethal OI type II, respectively), two patients carrying the same Gly862Ser substitution in α1(I) and affected by severe OI type III and in a patient with a Gly862Arg substitution in α1(I) and affected by lethal OI type II. Again a severely compromised cytoskeletal organization is evident only in the cells from the patients with lethal outcome. Asterisks indicate regions of dense fibers in the cytosol of cells from the lethal OI patient carrying Gly667Arg substitution. Counterstaining of the nuclei was performed using DAPI (blue).

number of small FAs were instead observed in long-bone osteoblasts from lethal mice (Fig. 3B, 2), whereas in MA and WT animals, FAs were mainly detectable on the endosteal surface. Interestingly, MA samples also showed a peculiar distribution of FAs, which often was concentrated in large spots (Fig. 3B, 2). In skin sections, the mutant lethal samples revealed a reduced number of FAs compared with MA and WT, and no difference was detectable between these last two groups (Fig. 3B, 3).

Cell proliferation is reduced in Brtl$^{+/-}$ lethal mice

Cytoskeleton disorganization is known to potentially affect cell proliferation. Thus, we isolated calvarial murine osteoblasts from WT, ML and MA mice to evaluate their proliferation. Osteoblasts from ML mice showed a proliferation impairment when compared with MA and WT littermates that reached significance at 5 days after plating ($P < 0.05$) (Fig. 4A).

TGF-β pathway is altered in Brtl$^{+/-}$ lethal mice

Alterations in the cytoskeleton may also compromise the activation of signal transduction pathways necessary to guarantee a proper cellular response to extracellular signals (21). One of the main growth factors involved in bone development is TGF-β. Following binding to its receptor, TGF-β activates a signal transduction pathway mediated by SMAD2/3 phosphorylation and nuclear translocation. Using specific antibodies, the expression levels of TGF-β, SMAD2/3 and activated p-SMAD2/3 were evaluated on calvarial bone lysates from ML, MA and WT mice by western blotting. A significant increase in TGF-β expression was detected in ML mice associated with a normal level of target phosphorylated SMAD2/3. Conversely, MA mice had a significant increase in p-SMAD2/3 signal, although increased expression of TGF-β compared with WT animals was not detected (Fig. 4B).

Expression of the early osteoblast transcription factor *Runx2* is decreased in Brtl$^{+/-}$ mice

Based on the TGF-β expression pattern described earlier, and as this factor is a key regulator of osteoblast differentiation, the expression of early (*Runx2* and *Osterix*) and late (*Bsp*) osteoblast markers was evaluated by qPCR on RNA extracted from calvarial bone of ML, MA and WT mice. Only *Runx2* was significantly reduced in both ML and MA Brtl$^{+/-}$ mice compared with WT littermates (ML: 0.46 ± 0.2, MA: 0.55 ± 0.13; WT: 0.90 ± 0.14; for ML, MA versus WT, $P < 0.05$, Supplementary Material, Fig. S1). *Col1a1* was not investigated because we already demonstrated no difference of its expression in a previous study (13).

Long-bone fractures are present and collagen content is decreased in mutant lethal mice

Staining with alizarin red and alcian blue was performed to evaluate skeletal configuration. A severely deformed rib cage

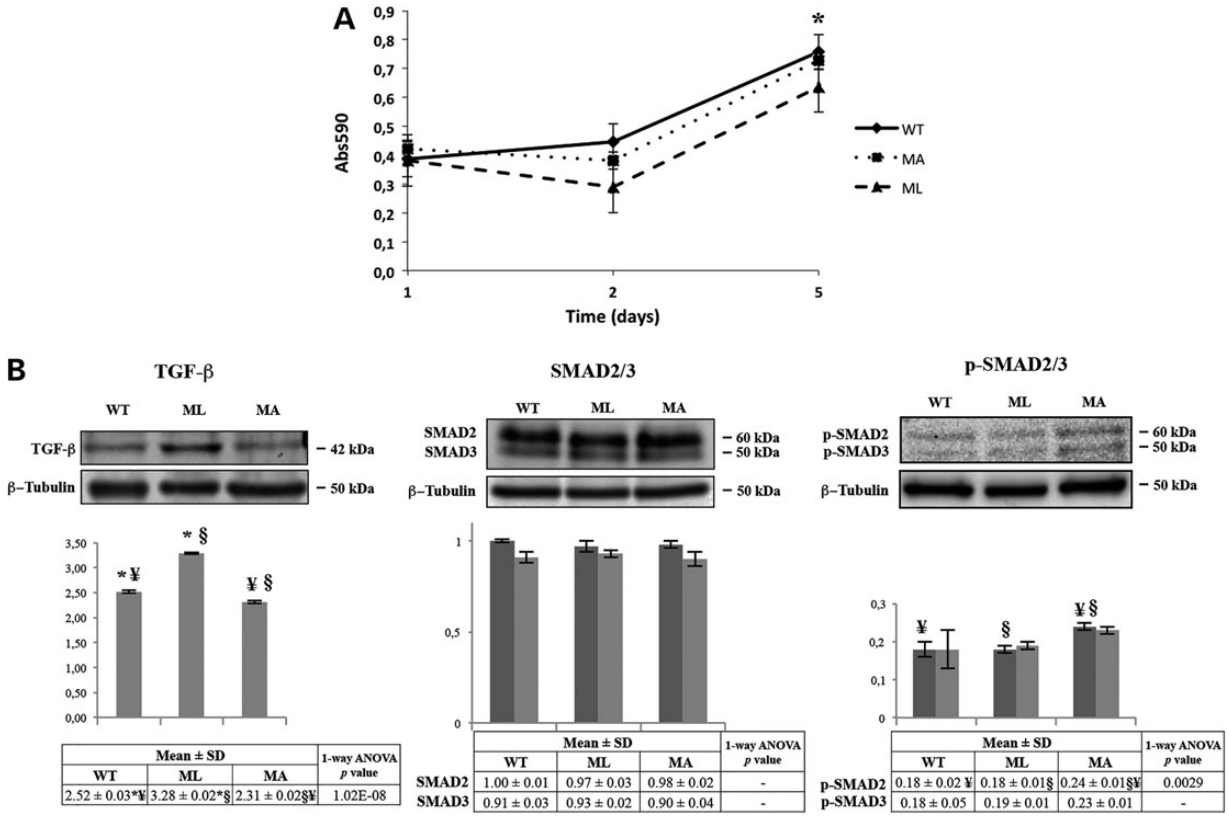

Figure 4. Osteoblast proliferation and expression analysis of TGF-β and its effector SMAD2/3 in bone from MA, ML and WT mice. (**A**) Proliferation in calvarial osteoblasts from ML mice is significantly impaired at d5 from plating (*$P < 0.05$). Each point was measured in triplicate, and each assay was repeated in three independent experiments. The mean values ± SD are reported. (**B**) Representative western blots using TGF-β antibody (left panel), SMAD2/3 antibody (center panel) and p-SMAD2/3 antibody (right panel). The densitometric analyses obtained by multiple replicative experiments are reported below western blotting images. TGF-β is up-regulated in ML mice whereas p-SMAD2/3 is up-regulated in MA animals. Histograms visualize normalized mean relative-integrated density ± SD values. *, ¥ and § symbols indicate the significance of expression changes occurring between WT and ML, WT and MA, and ML and MA mice, respectively. In SMAD2/3 histogram, dark gray bars represent SMAD2 and light gray bars represent SMAD3; in p-SMAD2/3 histogram, dark gray bars represent p-SMAD2 and light gray bars represent p-SMAD3.

with multiple rib fractures was evident in Brtl$^{+/-}$ mutants compared with WT. The rib fracture rate did not significantly differ between ML and MA animals (ML: 8.4 ± 1.1; MA: 7.6 ± 2.3), but both were higher in mutants as compared with WT samples, in which no fractures were present. Fractures were also detected in the ischium of ML (2.4 ± 0.6) and MA (2.6 ± 0.6) mice without significant differences between the two phenotypes, but again absent in WT littermate. Interestingly, fractures of the humerus were present only in ML mice (0.6 ± 0.54), suggesting that ML bones are more fragile (Fig. 5A). Picro-sirius red staining clearly showed a decrease in collagen in ML mice with respect to MA and WT animals in cortical and trabecular long bone (Fig. 5B). Picro-sirius red staining was also performed on lung sections mainly highlighting poorly inflated alveoli in ML mice (Supplementary Material, Fig. S2).

Trabecular bone volume and cortical thickness are reduced in mutant lethal mice

Histomorphometric analysis performed on toluidine-stained sections of femoral distal metaphyses from WT, ML and MA littermates allowed the evaluation of Bone Volume/Total Volume (BV/TV) and of cortical thickness. ML bones showed a significantly reduced BV/TV with respect to WT samples (ML: 44.914 ± 4.621%; WT: 52.040 ± 4.997%, $P < 0.05$). Similarly, cortical thickness was smaller in ML with respect to WT femurs (ML: 29.536 ± 2.072 µm; WT: 33.989 ± 2.650 µm, $P < 0.001$). No significant difference was detected for these two parameters between ML and MA (BV/TV, MA: 44.973 ± 5.401%, ML versus MA, $P = 0.986$; cortical thickness MA: 32.118 ± 3.288 µm, ML versus MA, $P = 0.145$), or MA and WT (BV/TV: MA versus WT, $P = 0.06$; cortical thickness MA versus WT, $P = 0.462$) (Fig. 5C).

NanoCT reveals less bone in mutant lethal mice

NanoCT analysis was performed on femurs of 1-day-old WT, ML and MA animals to better investigate their morphometric properties. Central diaphyseal BMD, tissue mineral density (TMD), bone volume fraction (BV/TV) and total area encompassed by the cross section were evaluated. BV/TV was significantly reduced in ML mutants when compared with WT (ML: 0.271 ± 0.008; WT: 0.315 ± 0.029, $P < 0.05$), but no difference was found between ML and MA or MA and WT mice. No difference in BMD, TMD and total area was detected among the three different groups of mice (Fig. 6). ML bones were shorter when measuring mineral-to-mineral surfaces between the proximal and distal secondary ossification centers compared with WT (ML: 2.013 ± 0.339 mm; WT: 2.433 ± 0.094 mm, $P < 0.05$). In contrast, no difference was detected between ML and MA or between MA and WT. Measurement of mineral-to-mineral length of alizarin red-stained femurs on independent samples confirmed the nanoCT data on length. Also humerus length, calculated by measuring the alizarin stained bone, was significantly shorter in ML than WT (ML: 2.67 ± 0.35 mm; WT: 3.06 ± 0.16 mm, $P < 0.05$).

Cytoskeletal analysis in fibroblast cell lines from OI patients

In order to extend our animal data to human samples, we investigated primary fibroblasts from two OI patients with the same α1

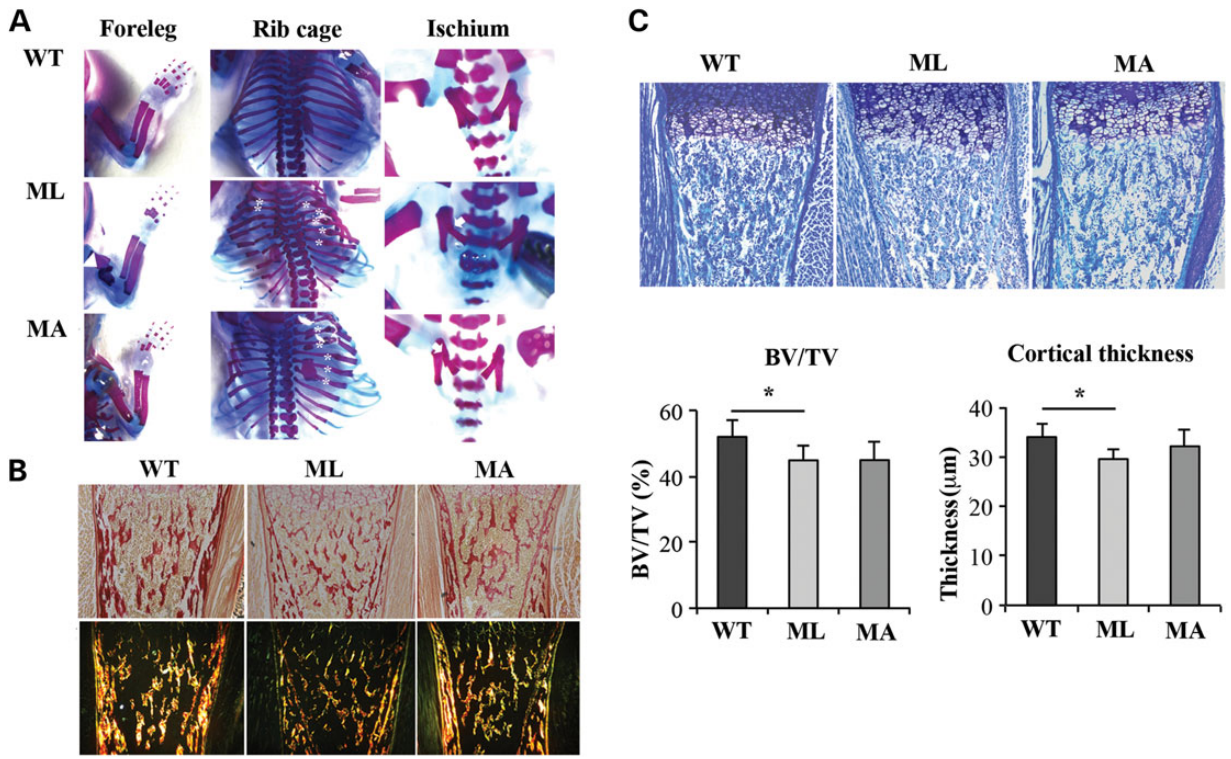

Figure 5. Comparison of skeletal features among ML, MA and WT mice. (**A**) Skeletal phenotype of Brtl$^{+/-}$ ML, MA and WT mice. Skeletal staining confirmed in mutant mice the characteristic severe OI phenotype including rib fractures (asterisk), flared ribcage and ischium fractures (arrow). Only in ML mice were long-bone fractures present (arrow head). For the skeletal staining, alizarin red, specific for bone, and alcian blue, specific for cartilage, were used. (**B**) Picro-sirius red staining of type I collagen in tibia sections from ML, MA and WT mice. ML samples revealed reduced collagen content in sections analyzed both under bright field (top panels) and under polarized light (bottom panels) (magnification 10×). (**C**) Histomorphometric analysis was performed on toluidine blue stained sections of the proximal tibia epiphysis of ML, MA and WT mice. BV/TV and cortical thickness were significantly reduced in ML mice compared with WT (BV/TV, $P < 0.05$; cortical thickness, $P < 0.001$) (magnification 10×).

(I)Gly667 to Arginine substitution (p.Gly845Arg) and, respectively, lethal (OI type II) or severe (OI type III) phenotype, as well as three OI patients heterozygous for substitutions to Serine (p.Gly1040Ser) or Arginine (p.Gly1040Arg) at α1(I) Gly862, with severe (OI type III) or lethal (OI type II) phenotype, respectively. Immunohistochemistry using labeled phalloidin revealed that cells from the lethal patients had a compromised cytoskeletal organization. Cells from the lethal proband carrying Gly667Arg revealed abnormal condensation of cytoskeletal fibers with irregular distribution in the cytoplasm, whereas Gly862Arg cells showed a completely altered cytoskeletal organization resembling the ML mice. In contrast, no difference from normal control was evident in fibroblasts with Gly667Arg and Gly862Ser substitutions and severe OI phenotype (Fig. 3C).

Discussion

In this study, we identified distinctive cytoskeletal alterations that distinguish different OI phenotypic outcomes. These changes affected cell proliferation and cellular signaling and compromised bone properties.

The molecular basis of lethal versus moderately severe outcomes in Brtl$^{+/-}$ mice has puzzled us since the generation of this murine model for classical OI. Phenotypic variability in the

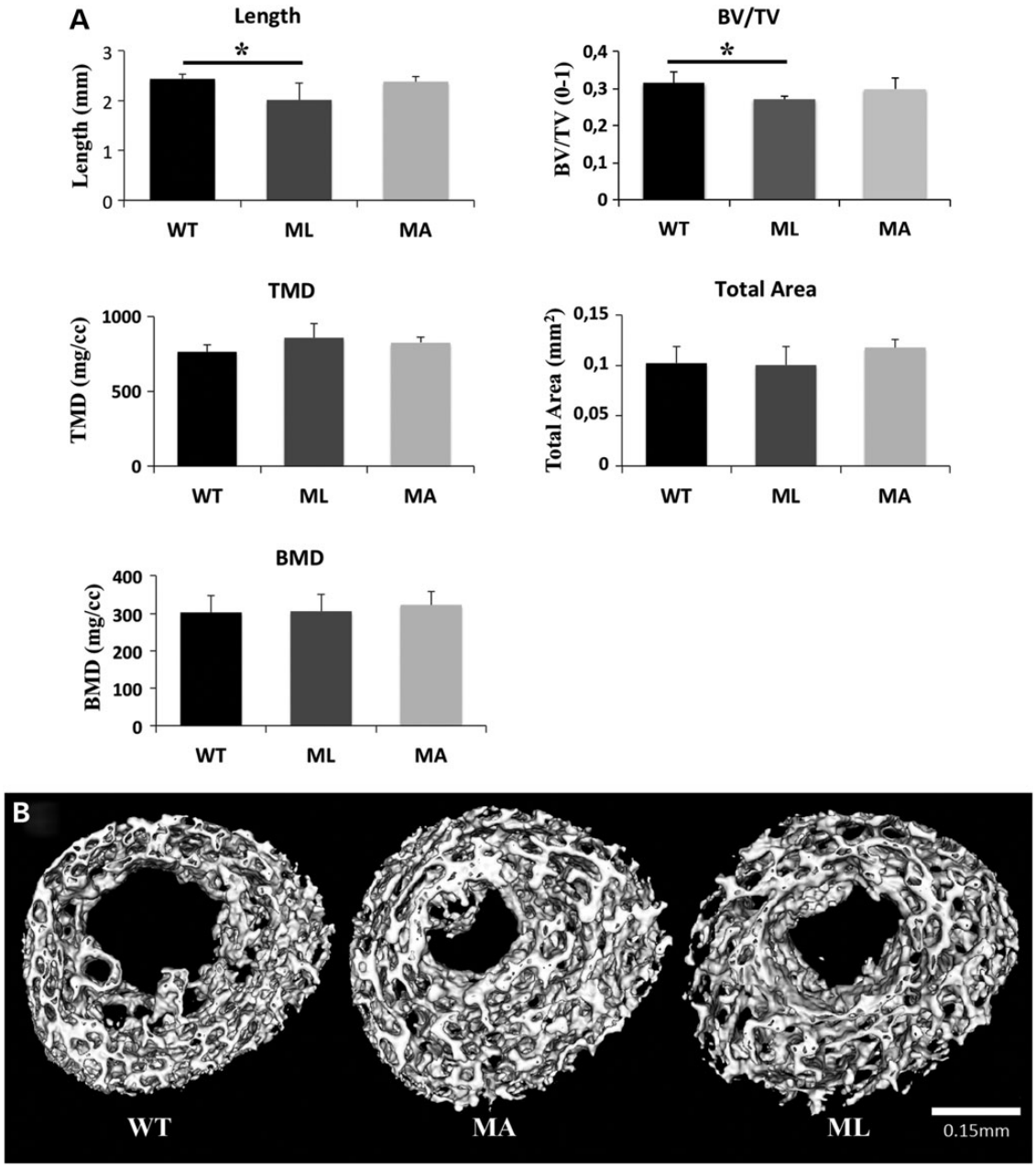

Figure 6. NanoCT was used to assess mineralized bone parameters in 1-day-old mouse femurs. (**A**) Lethal Brtl$^{+/-}$ mice showed a reduction in mineralized length between proximal and distal secondary ossification centers, and a reduced bone volume fraction of the trabeculated structure (BV/TV). TMD remained unchanged, and no significant differences in total cross sectional area and BMD were observed between genotypes. (**E**) Representative nanoCT images of femoral cross sections show a highly trabecular architecture.

presence of an identical mutation is described in human OI, and the elucidation of its cause is particularly relevant not only to better understand the disease pathophysiology but also to discover potential new targets for treatment. In the present study, we took advantage of powerful *in silico* tools for functional analysis, combining proteomic and transcriptomic data that were obtained from previous investigations on bone and skin samples from WT and Brtl$^{+/-}$ newborn mice with differing phenotypic outcomes (13,14). Pathway analysis integrates expression differences with known proteins acting in characterized cellular pathways, as properly supported by the scientific literature. The resulting functional analysis suggests the biochemical context in which the proteins of interest act and how their aberrant expression may alter cellular and/or tissue biology in physiological and pathological conditions. To our knowledge, this is the first time that hybrid networks have been generated in OI.

Hybrid networks point to different cytoskeletal organization in Brtl$^{+/-}$ mice with different outcomes

Hybrid networks, generated by MetaCore software, identified two cytoskeletal proteins as consistent central hubs: vimentin and stathmin. Vimentin, as a member of the family of intermediate filaments, is involved in maintaining cell integrity and in supporting and anchoring organelles in the cytosol (Fig. 7A). It has been reported to be involved in cell polarity, motility and signaling (22) and in wound healing (23). Stathmin, an ubiquitous small cytosolic phosphoprotein with cell proliferation regulating activity, is known to affect microtubule dynamics sequestering αβ-tubulin dimers and promoting microtubule disassembly by acting directly on microtubule ends (24,25). Although its exact role is not yet clear, stathmin plays a fundamental function in bone homeostasis by controlling the coupling of osteoblastic and osteoclastic activities. In fact, it promotes osteoblast differentiation and inhibits osteoclast formation (26).

Vimentin and stathmin are indirectly correlated as microtubule depolymerization leads to the collapse of vimentin and to a disordered distribution of its resulting short agglomerations (16) (Fig. 7A). The down-regulation of vimentin (14) and the up-regulation of stathmin in both skin and bone samples of lethal mice suggested compromised formation and organization of microtubule and intermediate filaments in these mutants Fig. 7B.

Cofilin-1 is a protein involved in cytoskeletal assembly that we previously described as deregulated in skin specimens from mutants. Here, cofilin-1 also proved dysregulated in Brtl$^{+/-}$ bone and lung. This factor modulates actin filaments by promoting F-actin depolymerization and by inhibiting G-actin polymerization (19) Fig. 7A. Cofilin-1 results well integrated into the two OI-hybrid nets thus suggesting its active involvement in OI-affected pathways and perhaps in the pathophysiology of the disorder. In this work, we demonstrated its overexpression in skin, bone and lung in ML mice when compared with MA and WT animals (Fig. 7B). Interestingly, microfilaments have been suggested to directly interact with vimentin filaments (27). Thus, as suggested for stathmin, a concomitantly altered presence of cofilin-1 and vimentin in ML mice may have combined detrimental effects on cytoskeleton properties (Fig. 7 B) (28).

According to our analysis, all three main components of the cytoskeleton, microtubules, microfilaments and intermediate filaments, are likely to be altered in mutants thus suggesting the occurrence of an aberrant cytoskeletal organization in lethal OI.

Cytoskeleton disorganization in Brtl$^{+/-}$ lethal mice affects cell proliferation, differentiation and bone properties

Immunohistochemistry data highlighted the occurrence of a systemic abnormal cytoskeletal network, characterized by punctuated actin fibrils. This was apparent in various Brtl$^{+/-}$ ML tissues expressing high levels of mutant type I collagen, such as skin, calvarial and long bone, and also lung. This latter finding is of particular interest because Brtl$^{+/-}$ lethal mice die a few hours after birth from respiratory failure and poorly inflated lungs, as showed by picro-sirius red staining (Supplementary Material, Fig. S2). However, we did not find any difference in rib cage structure or number of rib fractures between ML and MA mice. Thus, our observation supports a direct effect of the aberrant cytoskeleton on lung tissue, independent from skeletal abnormalities, as recently reported both in human patients and in a different murine model for OI (2).

The cytoskeleton is a dynamic protein network whose structure and reciprocal interactions are necessary for maintenance of cell mechanical properties, cell shape, cell proliferation and differentiation. The cytoskeleton regulates signaling pathways. Intracellular and extracellular stimuli utilize this network to maintain cell homeostasis (29,30). A distinct protein composition of the cytoskeleton has been reported for different cell types depending on specific cellular functions. In particular, the terminal differentiation of osteoblasts to osteocytes is characterized by a change in the distribution of actin binding proteins that are required to ensure the proper shape and mechanosensory functions of these cells (31,32). Perturbation of actin organization has been demonstrated to compromise osteoblast differentiation in C3H10T1/2 murine mesenchymal stem cells and to modulate the ability of murine osteoblastic cells to respond to fluid flow-induced signaling, which mimics mechanical signals *in vitro* (33,34).

Recently, mutations in plastin 3 (PLS3), a member of the plastin family that regulates the formation of F-actin bundles, have been reported as responsible for X-linked osteoporosis, hence underlining the relevance of cytoskeletal components in bone development (35).

In Brtl$^{+/-}$ lethal mice, the abnormal cytoskeleton affects osteoblast proliferation and is associated with compromised differentiation. qPCR data demonstrated decreased expression of *Runx2*, an early osteogenic marker, both in ML and MA mice compared with WT. We recently demonstrated a compromised ability to differentiate toward the osteoblast lineage in mesenchymal stem cells obtained from adult Brtl$^{+/-}$ mice (36). The altered cytoskeletal organization may exacerbate this effect by activating cellular apoptosis. As a consequence, the increase of pro-apoptotic factors was actually associated with the lethal outcome in our previous proteomic investigations on bone and skin tissues from Brtl$^{+/-}$ mice (13,14). A disorganized cytoskeleton can initiate or support cell death in various ways. For example, it may favor the release of the pro-apoptotic proteins BIM and BMF, which under normal conditions bind to cytoskeletal components, such as vimentin (37), and are inactivated by these interactions (Fig. 7A and B). Similarly, the detachment of the FAS death receptor from ezrin-mediated actin interaction can cause apoptosis (38).

Similarly to actin, the microtubule cytoskeleton is also known to control functional dynamics of various protein factors involved in gene transcription and cellular differentiation. Among these factors, microtubules regulate proteolytic degradation and processing of the hedgehog signaling mediators GLI2 and GLI3 (36), whose altered activity results in severe impairment of the skeleton (Fig. 7A and B) (39). While a physiological release of GLI2 by microtubule depolymerization results in the expression

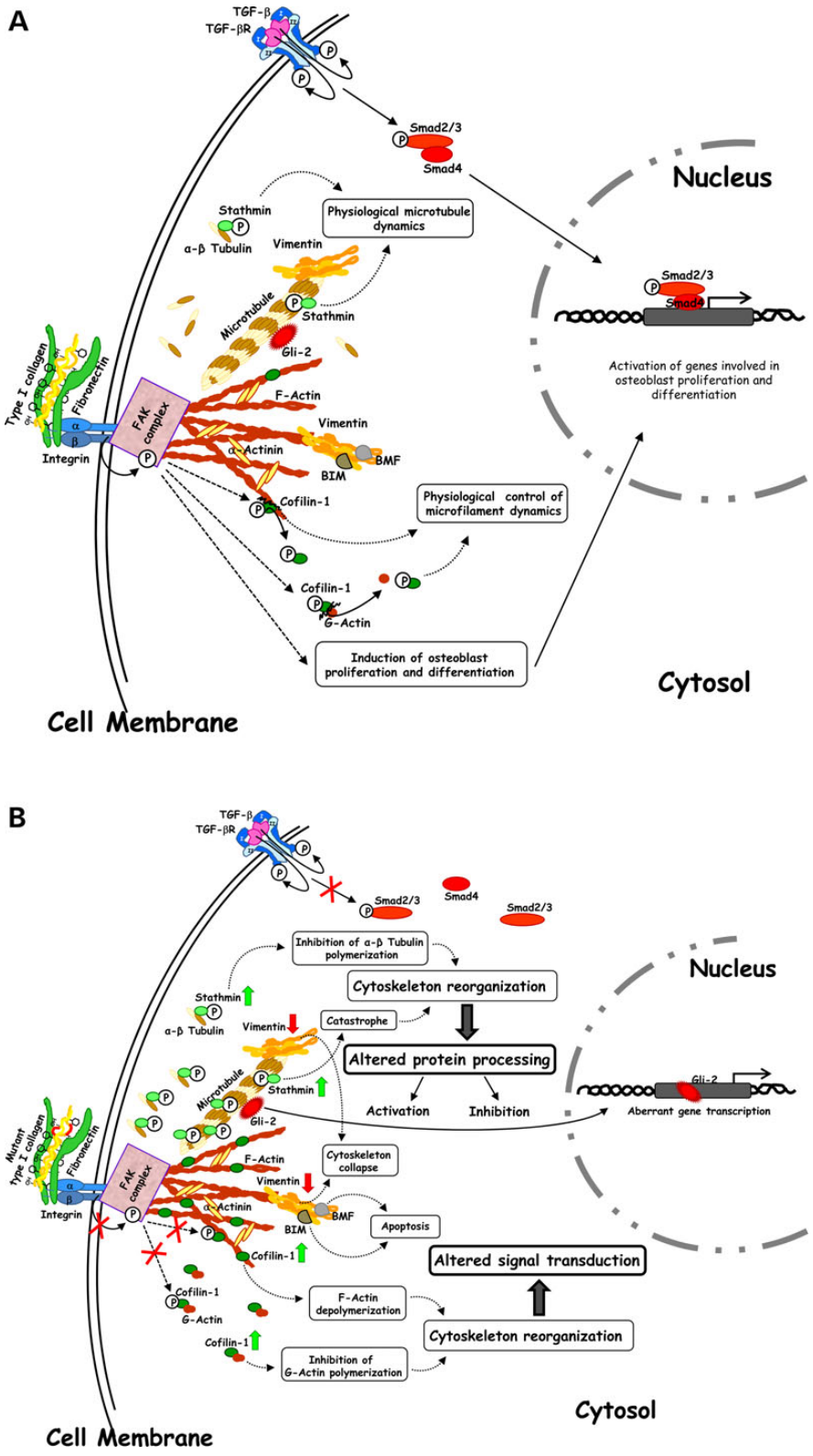

Figure 7. Schematic view of the physiological (**A**) and aberrant (**B**) cellular molecular dynamics regulated by cytoskeleton, which is functional in WT and MA Brtl$^{+/-}$ mice (A), and altered in ML Brtl$^{+/-}$ mice (B). (A) Stathmin, vimentin and cofilin-1 and focal adhesion kinase (FAK) complex contribute to control cytoskeleton structural plasticity thus influencing protein processing, signal transduction and gene expression. (B) Increase in the expression of stathmin and cofilin-1, decrease of vimentin and abnormal FAK complex contribute to abnormal cytoskeleton structural plasticity thus influencing protein processing, signal transduction and gene expression.

of genes involved in osteoblast differentiation and bone formation (Fig. 7A) (36), the occurrence of a constitutively activated expression of GLI2 suppresses bone formation in postnatal mice (40). This may be due to the GLI2-induced overexpression of BMP2 (41) (Fig. 7B), which we previously described in ML animals (13).

Reduced osteoblast proliferation and differentiation in Brtl$^{+/-}$ mice is associated with compromised bone properties: BV/TV and cortical thickness were reduced in developing femurs from lethal mice, and the length of mineralized femurs was shorter in ML compared with WT. Consequentially, long-bone fracture rate was increased in ML mice. Although no significant reduction was previously detected at the transcript level (13), less type I collagen was found to be deposited in the extracellular matrix of long bones from ML mice by picro-sirius red staining.

TGF-β and integrin-mediated signaling are altered in Brtl$^{+/-}$ lethal mice

In bone from Brtl$^{+/-}$ lethal mice, we found an increased presence of TGF-β that did not associate with an up-regulation, by phosphorylation, of the signal transduction pathway effector SMAD2/3. As the cytoskeleton is disorganized in ML mice, the TGF-β signaling might be disturbed. This may cause stimulation of TGF-β synthesis and the accumulation of its latent form in the extracellular matrix. In contrast, we found an up-regulation of phosphorylated SMAD2/3 in Brtl$^{+/-}$ alive mice. Interestingly, similar findings have been recently demonstrated for another dominant and a recessive murine model of OI, making the TGF-β pathway a broad target for development of novel OI therapy (42).

In addition, TGF-β signaling, as well as signal transduction by bone morphogenetic proteins (BMPs), is transduced in target cells only when the 'integrin system' is functionally active (43). The correct interaction between integrins and matrix proteins as well as integrins and cytoskeleton components has been widely demonstrated as a prerequisite for 'integrin system' activity (44–46). Integrins have also been implicated in control of TGF-β activation (47) according to specific functional interactions between integrins and the ECM and/or the cytoskeleton. Purified integrins are not able to activate the latent form of TGF-β (44,45). Therefore, it seems reasonable to assume that TGF-β signaling is negatively affected in mutant animals also by altered integrin activity, which in turn is caused by ECM and cytoskeleton structural and functional aberrances. Indeed, by immunohistochemistry, cells from mutant lethal mice revealed abnormal focal adhesion kinase distribution. Interestingly, fibronectin/integrin and type I collagen/integrin interactions are fundamental during early stages of osteoblast differentiation (48,49). In addition, the association between the cytoskeletal network and integrins may well serve as a reservoir for molecules involved in signal transduction (43).

Identical glycine substitutions altered fibroblast cytoskeleton only in lethal but not in severe OI patients

To investigate phenotypic variability in human OI is quite complicated owing to the difficulty in obtaining samples from families and patients with an identical mutation, but different outcomes. Based on the last review published by the Consortium for Osteogenesis Imperfecta mutations, 11 Gly substitutions in α1 (I) and 2 Gly substitutions in α2(I) are responsible for lethal or non-lethal outcomes when substituted by the same amino acid, and 32 Gly substitutions in α1(I) and 7 Gly substitutions in α2(I) cause lethal or non-lethal outcomes when substituted by a different amino acid (6).

We evaluated the cytoskeletal organization in primary fibroblast cell lines from patients carrying a substitution of the same glycine with either an identical (Gly667Arg) or a different (Gly862Ser and Gly862Arg) substituting amino acid with lethal or severe outcomes. Immunohistochemistry using phalloidin revealed a completely disorganized cytoskeleton in lethal cell lines that resembling the disorganized cytoskeleton identified in lethal Brtl$^{+/-}$ mice.

It is difficult to determine whether cytoskeletal organization is a primary or secondary modulator in OI. The presence of induced ER stress was reported to be responsible for cytoskeletal disorganization and apoptosis activation *in vitro* (50). A compromised ability to cope with mutant intracellular collagen retention causing intracellular stress was demonstrated in ML mice compared with MA (13,14). Thus, we can speculate that in cells producing higher amounts of collagen type I, the failure of chaperones to solve the cellular stress caused by mutant collagen retention may compromise cytoskeleton assembly, resulting in reduced differentiation and proliferation and finally causing increased apoptosis. On the contrary, the ability of the chaperones to properly address intracellular stress might allow cell survival by preserving normal cellular functions. Conversely, a predisposition to abnormal cytoskeletal organization in active secretory cells producing mutant collagen may result in intracellular stress causing altered cellular function.

Here, we demonstrated that a compromised cytoskeletal assembly impaired both cell signaling and cellular trafficking in mutant lethal mice. This results in altered bone properties thus pointing to the cytoskeleton as a novel target to develop new treatments for OI.

Materials and Methods

Animals

Brtl$^{+/-}$ heterozygous mice and WT littermates were maintained under standard experimental animal care protocol following the Italian Laws in the animal facility of the Department of Molecular Medicine of the University of Pavia (Italy). One-day-old mice were used for the present study. Genomic DNA was extracted from tail clip or skin pieces, and genotyping to distinguish heterozygous mutant animals from WT littermates was performed by PCR (51). Mutant mice were considered lethal when death occurred within 6 h from birth.

Protein network analyses

OI hybrid networks were generated using the MetaCore network building tool (Thomson Reuters, St. Joseph, MI, USA) and applying the shortest path algorithm. MetaCore includes a manually annotated and regularly updated database of protein interactions and metabolic reactions obtained by scientific literature. Gene names of differentially expressed proteins were imported into MetaCore and processed. Hypothetical networks were built combining experimental proteins/genes and additional not experimental proteins, included into the MetaCore protein database, which were judged by the program as essential to crosslink experimental data. According to the shortest path algorithm, only one additional element may enter into the net between two experimental proteins/genes. Hybrid nets thus include only experimental factors that are known to be tightly correlated. The relevant pathway maps were then prioritized according to their statistical significance ($P < 0.001$), and networks were graphically visualized as nodes (proteins/genes) and edges (the relationship between proteins).

Western blot

Skin, calvarial bone and lung protein extracts from 1-day-old ML and MA Brtl$^{+/-}$ mice, and WT littermates (at least $n = 3$ per group) were obtained by pestle-pounding minced specimens in the presence of the Laemmli buffer: 100 mM Tris–HCl pH 6.8, 2% (w/v) SDS, 20% (v/v) glycerol, 4% (v/v) β-mercaptoethanol. The sample solutions were then heated at 95°C for 5 min (52). For each sample, proteins (25 µg) were separated on 10% polyacrylamide gel and then transferred onto nitrocellulose (Hybond ECL, GE Healthcare) according to Towbin (53). Before immunodetection, gel sample loading was preliminary proved to be equivalent by Ponceau Red staining (0.2% w/v Ponceau S in 3% w/v trichloroacetic acid) of nitrocellulose. Immunodetection was achieved using the following antibodies: anti-β-Tubulin and anti-Stathmin antibodies from Santa Cruz Biotechnology (San Jose, CA, USA), both 1:1000 diluted; anti-Cofilin-1 from Abcam (Cambridge, UK), 1:1000 diluted; anti-TGF-β pan-specific antibody from R&D Systems (Minneapolis, MN, USA), 1:500 diluted; anti-SMAD2/3 and anti-phospho-SMAD2/3 both from Cell Signaling Technology (Danvers, MA, USA), respectively, 1:1000 and 1:500 diluted; and anti-Rabbit secondary antibody from Sigma–Aldrich (St. Louis, MO, USA), 1:7000 diluted. Hybridization with primary antibodies was performed overnight at room temperature. Incubation with specific HRP-conjugated secondary antibodies was then performed for 2 h at room temperature, and immunostained bands were visualized by chemiluminescence using ECL detection reagents (GE Healthcare, Uppsala, Sweden). Chemiluminescent signals were captured by ImageQuant LAS 4000 (GE Healthcare) digital imaging system. The obtained 1-D western blot images were then analyzed with the ImageQuant 3.0 software (Molecular Dynamics World Headquarters, Sunnyvale, CA, USA). β-tubulin immunoblotting ensured equal loading of samples.

Histology and immunohistochemistry

For histological studies, femurs from WT, ML and MA newborn mice ($n = 4$ per group) were dissected and fixed in 4% PFA in phosphate-buffered saline (PBS), decalcified in 14% EDTA pH 7.1 for 7 days and processed for light microscopy, according to standard procedures. Longitudinal femur sections of 7 µm were cut using an RM2265 microtome (Leica Microsystems Srl, Milan, Italy), mounted on Superfrost Plus slides (Menzel-Glaser, VWR, Milan, Italy) and stained with toluidine blue or picro-sirius red. Following toluidine blue staining, images were acquired using a DFC480 digital camera (Leica Microsystems Srl) connected to a light microscope (Dialux 20, Leica Microsystems Srl). The trabecular bone was evaluated on an area of 0.07 mm^2 manually delineated below the growth plate. The cortical thickness was measured five times for each section on a region of 200 µm, which was manually delineated from the end of the growth plate. All of the analyses were performed with the Leica Application Suite v 3.0 image analysis software (Leica Microsystems Srl) on three sections for each mouse.

For picro-sirius red staining, a 0.1% w/v solution of sirius red (Direct Red 80, Sigma–Aldrich, Milan, Italy) in saturated aqueous solution of picric acid was used. After staining, sections were rinsed in acidified water (87.5 mM acetic acid) and dehydrated in absolute ethanol, cleared and mounted in synthetic resin (DPX Mountant for histology, Sigma–Aldrich). Sirius red-stained sections were analyzed under polarized light, and images were acquired by Leica DM2500 equipped with L ICT/P polarizer and a digital color camera LEICA DFC295 (Leica).

For immunohistochemistry, skin, lung, limb and calvarial bones from ML, MA mutant and WT 1-day-old pups ($n = 3$) were dissected and, when necessary, cleaned from adherent connective tissue after sacrifice. Calvarial bones were cut into four pieces along the sutures, and parietal bones were used for the assay. Skin and bones were washed in PBS, fixed in 4% PFA for 24 h at 4°C and embedded in OCT. Following dissection and fixation in 4% PFA, lungs were successively incubated in 15 and 30% w/v sucrose in PBS o/n at 4°C, degassed under vacuum and embedded in OCT. Cryosections of 10 µm thickness were obtained using CM1850 UV cryostat (Leica) and mounted on Superfrost Plus slides (Menzel-Glaser, VWR). Sections were permeabilized in 0.2% v/v Triton X-100 in PBS for 90 min at RT, and blocking was performed by incubating the sections in 1% w/v BSA 0.01% v/v Triton X-100 in PBS for other 90 min at RT. Samples were then incubated overnight at 4°C in 0.01% Triton X-100-containing primary antibody Alexa 488-Phalloidin (Molecular Probes, Invitrogen) diluted 1:40 or in PBS, 1% BSA containing primary antibody FAKpY397 (Invitrogen) diluted 1:500. AlexaFluor 633 goat anti-rabbit IgG (Thermo Scientific) was used as secondary antibody diluted 1:500 in PBS, 1% BSA.

For human fibroblasts, 5×10^4 cells were plated on coverslip in 24-well plate in Dulbecco Modified Eagle's Medium (DMEM, Lonza, Milan, Italy) supplemented with 10% heat-inactivated Fetal Calf Serum (hiFCS, Euroclone, Pero, MI, Italy) and antibiotics. The day after the medium was removed, cells were washed in PBS and fixed in 3.7% PFA for 10 min at room temperature. Blocking was done by 30-min incubation in 1% BSA, 0.05% Triton X-100 in PBS. Alexa 488-Phalloidin staining was performed by 1-h incubation at RT in 1% BSA in PBS. The nuclei were counterstained by 4′,6-diamidino-2-phenylindole (DAPI; Sigma–Aldrich). Samples were examined by TCS SP2-Leica confocal microscope (Leica).

Expression analysis

Total RNA was extracted using TriReagent (Sigma–Aldrich) according to the manufacturer's protocol from calvarial bones of WT, ML and MA newborn mice ($n = 3$). DNase digestion was performed using the Turbo DNA Free Kit (Ambion, Applied Biosystems, Austin, TX, USA), and RNA integrity was verified using the Bioanalyzer 2100 (Agilent Technologies, Santa Clara, CA, USA). qPCR was performed on the Mx3000P Stratagene thermocycler using commercially available TaqMan primers and probes (Applied Biosystems) and TaqMan Universal PCR Master Mix (Applied Biosystems). All reactions were performed in triplicate. Expression levels for *Runx2* (Mm01269515_mH), *Osterix* (Mm00504574_m1) and *Bsp* (Mm00492555_m1) were evaluated. *Gapdh* (Mm99999915_g1) was used as normalizer. Relative expression levels were calculated using the ΔΔCt method.

Calvarial osteoblast culture

Murine osteoblasts were isolated from 1-day-old WT, ML and MA pups. At least five to six animals with the same genotype were pooled together to obtain a sufficient number of cells. After sacrifice, calvariae were removed, cleaned from fibrous tissues and sutures, washed two times with PBS at 37°C for 10 min in a shaker water bath and sequentially digested with 200 U/mL collagenase type II (GIBCO) at 37°C for 15–20 min. Cells obtained from the first two digestions were discharged, whereas cells from digestions 3, 4 and 5 were passed through a 70-µm polypropylene mesh filter and cultured in α-MEM (Lonza) added with 10% hiFCS, 25 µg/ml sodium ascorbate (Fluka) and antibiotics.

Osteoblast proliferation

Proliferation of osteoblasts from WT, ML and MA mice was evaluated at Passage 1 using the CellTiter 96 AQueous One Solution Cell Proliferation Assay (Promega, Madison, WI, USA) according to the manufacturer's protocol. Osteoblasts were plated in triplicate in 96-well plates at 2.5×10^3 cells per well in 100 µl of complete α-MEM medium. After 1, 2 and 5 days from plating, 20 µl of MTS solution was added to each well. After 4 h of incubation at 37°C, absorbance at 490 nm was measured using an ELISA plate reader.

Skeletal staining

Skin and internal organs were removed from WT, ML and MA mice ($n = 5$ for group) within a few hours after birth following sacrifice. The pups were fixed in 95% ethanol for 7 days and then stained with 0.3% w/v Alcian Blue 8GS and 0.1% w/v Alizarin Red S as described in Forlino *et al.* (1999) (9). Digitalized images were acquired using the digital camera DFC425C (Leica Microsystems Srl) connected to the stereomicroscope M165FC (Leica Microsystems Srl). Long-bone and rib fractures were considered based on the presence of callus to avoid including fractures owing to manual handling of the samples. The length of the mineralized part of the femur and humerus was calculated on the digitized images by measuring the alizarin stained distance between the width midpoint of the segment connecting both epiphyses.

NanoCT

Mouse hind limbs from ML, MA Brtl$^{+/-}$ and WT littermates ($n = 5$ per group) were scanned using a nano-computed tomography system (nanotom-s, phoenix|x-ray, GE Measurement & Control, Wunstorf, Germany) at 80 kV, 130 µA, 1000 ms integration time, four frame-averaging and a voxel size of 2.5 µm. The total scan time for each sample was 85 min. Images were calibrated to Hounsfield units for densitometry using a hydroxyapatite phantom scan. For all femora, a volume of interest (VOI) was selected by taking 10% of the mineralized length (region defined by onset of mineralization of primary trabeculae, from distal to proximal). The VOI was centered in the mid-diaphyseal region. A region of interest was then selected by using a spline function to manually contour a region encompassing the entire periosteal circumference of the bone. A highly trabecular structure with a thin cortico-trabecular shell was assessed together for total trabecular morphology and densitometry.

Human dermal fibroblasts

For two patients harboring the c.3118G>A mutation in *COL1A1* (Gly862Ser; p.Gly1040Ser, severe OI) and one patient carrying the c.3118G>C mutation in *COL1A1* (Gly862Arg; p.Gly1040Arg, lethal OI), a fibroblast cell culture was established from a skin biopsy taken from the probands' inner aspect of the upper arm, after informed consent. The fibroblasts from the two patients harboring the c.2533G>A mutation in *COL1A1* (Gly667Arg; p.Gly845Arg) associated with severe or lethal OI, respectively, were obtained from Dr Joan C Marini.

Statistics

Statistic differences between groups were evaluated by one-way ANOVA or by two-tailed Student's *T*-test using Sigma Plot Statistic 11.0 software. A $P < 0.05$ was considered significant. All data are expressed as mean ± standard deviation.

Supplementary Material

Supplementary Material is available at *HMG* online.

Acknowledgements

We thank Mr Angelo Gallanti, Department of Molecular Medicine, Biochemistry Unit, University of Pavia, Italy, for support on cell cultures, Dr Patrizia Vaghi, Centro Grandi Strumenti, University of Pavia, Italy, for technical assistance with confocal microscopy and Mrs Aileen M. Barnes, Bone and Extracellular Matrix Branch, NICHD, National Institute of Health, Bethesda, MD, USA, for technical assistance.

Conflict of Interest statement. None declared.

Funding

The work was supported by Fondazione Cariplo (grant No. 2013-0612), Telethon (grant No. GGP13098) and the European Community, FP7, 'Sybil' project (grant No. 602300).

References

1. Forlino, A., Cabral, W.A., Barnes, A.M. and Marini, J.C. (2011) New perspectives on osteogenesis imperfecta. *Nat. Rev. Endocrinol.*, **7**, 540–557.
2. Thiele, F., Cohrs, C.M., Flor, A., Lisse, T.S., Przemeck, G.K., Horsch, M., Schrewe, A., Gailus-Durner, V., Ivandic, B., Katus, H.A. *et al.* (2012) Cardiopulmonary dysfunction in the Osteogenesis imperfecta mouse model Aga2 and human patients are caused by bone-independent mechanisms. *Hum. Mol. Genet.*, **21**, 3535–3545.
3. Baldridge, D., Lennington, J., Weis, M., Homan, E.P., Jiang, M. M., Munivez, E., Keene, D.R., Hogue, W.R., Pyott, S., Byers, P. H. *et al.* (2010) Generalized connective tissue disease in Crtap-/- mouse. *PLoS One*, **5**, e10560.
4. Garbes, L., Kim, K., Riess, A., Hoyer-Kuhn, H., Beleggia, F., Bevot, A., Kim, M.J., Huh, Y.H., Kweon, H.S., Savarirayan, R. *et al.* (2015) Mutations in SEC24D, encoding a component of the COPII machinery, cause a syndromic form of osteogenesis imperfecta. *Am J Hum Genet*, **96**, 432–439.
5. Van Dijk, F.S. and Sillence, D.O. (2014) Osteogenesis imperfecta: clinical diagnosis, nomenclature and severity assessment. *Am. J. Med. Genet. A*, **164A**, 1470–1481.
6. Marini, J.C., Forlino, A., Cabral, W.A., Barnes, A.M., San Antonio, J.D., Milgrom, S., Hyland, J.C., Korkko, J., Prockop, D.J., De Paepe, A. *et al.* (2007) Consortium for osteogenesis imperfecta mutations in the helical domain of type I collagen: regions rich in lethal mutations align with collagen binding sites for integrins and proteoglycans. *Hum. Mutat.*, **28**, 209–221.
7. Rauch, F., Moffatt, P., Cheung, M., Roughley, P., Lalic, L., Lund, A.M., Ramirez, N., Fahiminiya, S., Majewski, J. and Glorieux, F. H. (2013) Osteogenesis imperfecta type V: marked phenotypic variability despite the presence of the IFITM5 c.-14C>T mutation in all patients. *J Med. Genet.*, **50**, 21–24.
8. Valadares, E.R., Carneiro, T.B., Santos, P.M., Oliveira, A.C. and Zabel, B. (2014) What is new in genetics and osteogenesis imperfecta classification? *J. Pediatr. (Rio J)*, **90**, 536–541.

9. Forlino, A., Porter, F.D., Lee, E.J., Westphal, H. and Marini, J.C. (1999) Use of the Cre/lox recombination system to develop a non-lethal knock-in murine model for osteogenesis imperfecta with an alpha1(I) G349C substitution. Variability in phenotype in BrtlIV mice. *J. Biol. Chem.*, **274**, 37923–37931.
10. Sarafova, A.P., Choi, H., Forlino, A., Gajko, A., Cabral, W.A., Tosi, L., Reing, C.M. and Marini, J.C. (1998) Three novel type I collagen mutations in osteogenesis imperfecta type IV probands are associated with discrepancies between electrophoretic migration of osteoblast and fibroblast collagen. *Hum. Mutat.*, **11**, 395–403.
11. Kuznetsova, N.V., Forlino, A., Cabral, W.A., Marini, J.C. and Leikin, S. (2004) Structure, stability and interactions of type I collagen with GLY349-CYS substitution in alpha 1(I) chain in a murine osteogenesis imperfecta model. *Matrix Biol.*, **23**, 101–112.
12. Forlino, A., Kuznetsova, N.V., Marini, J.C. and Leikin, S. (2007) Selective retention and degradation of molecules with a single mutant alpha1(I) chain in the Brtl IV mouse model of OI. *Matrix Biol.*, **26**, 604–614.
13. Forlino, A., Tani, C., Rossi, A., Lupi, A., Campari, E., Gualeni, B., Bianchi, L., Armini, A., Cetta, G., Bini, L. *et al.* (2007) Differential expression of both extracellular and intracellular proteins is involved in the lethal or nonlethal phenotypic variation of BrtlIV, a murine model for osteogenesis imperfecta. *Proteomics*, **7**, 1877–1891.
14. Bianchi, L., Gagliardi, A., Gioia, R., Besio, R., Tani, C., Landi, C., Cipriano, M., Gimigliano, A., Rossi, A., Marini, J.C. *et al.* (2012) Differential response to intracellular stress in the skin from osteogenesis imperfecta Brtl mice with lethal and non lethal phenotype: a proteomic approach. *J. Proteomics*, **75**, 4717–4733.
15. Zhao, F.Q. (2013) Octamer-binding transcription factors: genomics and functions. *Front. Biosci. (Landmark Ed)*, **18**, 1051–1071.
16. Goldman, R.D., Khuon, S., Chou, Y.H., Opal, P. and Steinert, P. M. (1996) The function of intermediate filaments in cell shape and cytoskeletal integrity. *J. Cell. Biol.*, **134**, 971–983.
17. Curmi, P.A., Gavet, O., Charbaut, E., Ozon, S., Lachkar-Colmerauer, S., Manceau, V., Siavoshian, S., Maucuer, A. and Sobel, A. (1999) Stathmin and its phosphoprotein family: general properties, biochemical and functional interaction with tubulin. *Cell. Struct. Funct.*, **24**, 345–357.
18. Cassimeris, L. (2002) The oncoprotein 18/stathmin family of microtubule destabilizers. *Curr. Opin. Cell. Biol.*, **14**, 18–24.
19. Bamburg, J.R. (1999) Proteins of the ADF/cofilin family: essential regulators of actin dynamics. *Annu. Rev. Cell. Dev. Biol.*, **15**, 185–230.
20. Bamburg, J.R., McGough, A. and Ono, S. (1999) Putting a new twist on actin: ADF/cofilins modulate actin dynamics. *Trends Cell. Biol.*, **9**, 364–370.
21. Pessoa-Pureur, R., Heimfarth, L. and Rocha, J.B. (2014) Signaling mechanisms and disrupted cytoskeleton in the diphenyl ditelluride neurotoxicity. *Oxid. Med. Cell Longev.*, **2014**, 1–21.
22. Ivaska, J., Pallari, H.M., Nevo, J. and Eriksson, J.E. (2007) Novel functions of vimentin in cell adhesion, migration, and signaling. *Exp. Cell. Res.*, **313**, 2050–2062.
23. Eckes, B., Colucci-Guyon, E., Smola, H., Nodder, S., Babinet, C., Krieg, T. and Martin, P. (2000) Impaired wound healing in embryonic and adult mice lacking vimentin. *J. Cell. Sci.*, **113** (Pt 13), 2455–2462.
24. Sobel, A., Boutterin, M.C., Beretta, L., Chneiweiss, H., Doye, V. and Peyro-Saint-Paul, H. (1989) Intracellular substrates for extracellular signaling. Characterization of a ubiquitous, neuron-enriched phosphoprotein (stathmin). *J. Biol. Chem.*, **264**, 3765–3772.
25. Charbaut, E., Curmi, P.A., Ozon, S., Lachkar, S., Redeker, V. and Sobel, A. (2001) Stathmin family proteins display specific molecular and tubulin binding properties. *J. Biol. Chem.*, **276**, 16146–16154.
26. Liu, H., Zhang, R., Ko, S.Y., Oyajobi, B.O., Papasian, C.J., Deng, H.W., Zhang, S. and Zhao, M. (2011) Microtubule assembly affects bone mass by regulating both osteoblast and osteoclast functions: stathmin deficiency produces an osteopenic phenotype in mice. *J. Bone Miner. Res.*, **26**, 2052–2067.
27. Esue, O., Carson, A.A., Tseng, Y. and Wirtz, D. (2006) A direct interaction between actin and vimentin filaments mediated by the tail domain of vimentin. *J. Biol. Chem.*, **281**, 30393–30399.
28. Chang, L. and Goldman, R.D. (2004) Intermediate filaments mediate cytoskeletal crosstalk. *Nat. Rev. Mol. Cell. Biol.*, **5**, 601–613.
29. Pollard, T.D. and Cooper, J.A. (2009) Actin, a central player in cell shape and movement. *Science*, **326**, 1208–1212.
30. Klymkowsky, M.W. (1999) Weaving a tangled web: the interconnected cytoskeleton. *Nat. Cell. Biol.*, **1**, E121–E123.
31. Tanaka-Kamioka, K., Kamioka, H., Ris, H. and Lim, S.S. (1998) Osteocyte shape is dependent on actin filaments and osteocyte processes are unique actin-rich projections. *J Bone Miner. Res.*, **13**, 1555–1568.
32. Kamioka, H., Sugawara, Y., Honjo, T., Yamashiro, T. and Takano-Yamamoto, T. (2004) Terminal differentiation of osteoblasts to osteocytes is accompanied by dramatic changes in the distribution of actin-binding proteins. *J. Bone Miner. Res.*, **19**, 471–478.
33. Arnsdorf, E.J., Tummala, P., Kwon, R.Y. and Jacobs, C.R. (2009) Mechanically induced osteogenic differentiation—the role of RhoA, ROCKII and cytoskeletal dynamics. *J. Cell. Sci.*, **122**, 546–553.
34. Malone, A.M., Batra, N.N., Shivaram, G., Kwon, R.Y., You, L., Kim, C.H., Rodriguez, J., Jair, K. and Jacobs, C.R. (2007) The role of actin cytoskeleton in oscillatory fluid flow-induced signaling in MC3T3-E1 osteoblasts. *Am. J. Physiol. Cell. Physiol.*, **292**, C1830–C1836.
35. van Dijk, F.S., Zillikens, M.C., Micha, D., Riessland, M., Marcelis, C.L., de Die-Smulders, C.E., Milbradt, J., Franken, A.A., Harsevoort, A.J., Lichtenbelt, K.D. *et al.* (2013) PLS3 mutations in X-linked osteoporosis with fractures. *N. Engl. J. Med.*, **369**, 1529–1536.
36. Gioia, R., Panaroni, C., Besio, R., Palladini, G., Merlini, G., Giansanti, V., Scovassi, I.A., Villani, S., Villa, I., Villa, A. *et al.* (2012) Impaired osteoblastogenesis in a murine model of dominant osteogenesis imperfecta: a new target for osteogenesis imperfecta pharmacological therapy. *Stem Cells*, **30**, 1465–1476.
37. Galluzzi, L., Bravo-San Pedro, J.M. and Kroemer, G. (2014) Organelle-specific initiation of cell death. *Nat. Cell Biol.*, **16**, 728–736.
38. Fais, S., De Milito, A. and Lozupone, F. (2005) The role of FAS to ezrin association in FAS-mediated apoptosis. *Apoptosis*, **10**, 941–947.
39. Mo, R., Freer, A.M., Zinyk, D.L., Crackower, M.A., Michaud, J., Heng, H.H., Chik, K.W., Shi, X.M., Tsui, L.C., Cheng, S.H. *et al.* (1997) Specific and redundant functions of Gli2 and Gli3 zinc finger genes in skeletal patterning and development. *Development*, **124**, 113–123.
40. Joeng, K.S. and Long, F. (2013) Constitutive activation of Gli2 impairs bone formation in postnatal growing mice. *PLoS One*, **8**, e55134.

41. Hyzy, S.L., Olivares-Navarrete, R., Schwartz, Z. and Boyan, B.D. (2012) BMP2 induces osteoblast apoptosis in a maturation state and noggin-dependent manner. *J. Cell. Biochem.*, **113**, 3236–3245.
42. Grafe, I., Yang, T., Alexander, S., Homan, E.P., Lietman, C., Jiang, M.M., Bertin, T., Munivez, E., Chen, Y., Dawson, B. *et al.* (2014) Excessive transforming growth factor-beta signaling is a common mechanism in osteogenesis imperfecta. *Nat. Med.*, **20**, 670–675.
43. Lai, C.F. and Cheng, S.L. (2005) Alphavbeta integrins play an essential role in BMP-2 induction of osteoblast differentiation. *J. Bone Miner. Res.*, **20**, 330–340.
44. Sheppard, D. (2005) Integrin-mediated activation of latent transforming growth factor beta. *Cancer Metastasis Rev.*, **24**, 395–402.
45. Munger, J.S., Huang, X., Kawakatsu, H., Griffiths, M.J., Dalton, S.L., Wu, J., Pittet, J.F., Kaminski, N., Garat, C., Matthay, M.A. *et al.* (1999) The integrin alpha v beta 6 binds and activates latent TGF beta 1: a mechanism for regulating pulmonary inflammation and fibrosis. *Cell*, **96**, 319–328.
46. Meredith, J.E. Jr., Winitz, S., Lewis, J.M., Hess, S., Ren, X.D., Renshaw, M.W. and Schwartz, M.A. (1996) The regulation of growth and intracellular signaling by integrins. *Endocr. Rev.*, **17**, 207–220.
47. Wipff, P.J. and Hinz, B. (2008) Integrins and the activation of latent transforming growth factor beta1 - an intimate relationship. *Eur. J. Cell Biol.*, **87**, 601–615.
48. Jikko, A., Harris, S.E., Chen, D., Mendrick, D.L. and Damsky, C.H. (1999) Collagen integrin receptors regulate early osteoblast differentiation induced by BMP-2. *J. Bone Miner. Res.*, **14**, 1075–1083.
49. Moursi, A.M., Globus, R.K. and Damsky, C.H. (1997) Interactions between integrin receptors and fibronectin are required for calvarial osteoblast differentiation in vitro. *J. Cell Sci.*, **110** (Pt 18), 2187–2196.
50. Seyb, K.I., Ansar, S., Bean, J. and Michaelis, M.L. (2006) beta-Amyloid and endoplasmic reticulum stress responses in primary neurons: effects of drugs that interact with the cytoskeleton. *J. Mol. Neurosci.*, **28**, 111–123.
51. Uveges, T.E., Collin-Osdoby, P., Cabral, W.A., Ledgard, F., Goldberg, L., Bergwitz, C., Forlino, A., Osdoby, P., Gronowicz, G.A. and Marini, J.C. (2008) Cellular mechanism of decreased bone in Brtl mouse model of OI: imbalance of decreased osteoblast function and increased osteoclasts and their precursors. *J. Bone Miner. Res.*, **23**, 1983–1994.
52. Laemmli, U.K. (1970) Cleavage of structural proteins during the assembly of the head of bacteriophage T4. *Nature*, **227**, 680–685.
53. Towbin, H., Staehelin, T. and Gordon, J. (1979) Electrophoretic transfer of proteins from polyacrylamide gels to nitrocellulose sheets: procedure and some applications. *Proc. Natl Acad. Sci. USA*, **76**, 4350–4354.

A third manuscript:

"**MCM5: a new actor in the link between pre-replication complex and Meier-Gorlin syndrome**"

by Annalisa Vetro, Salvatore Savasta, Annalisa Russo Raucci, Cristina Cerqua, Geppo Sartori, Ivan Limongelli, Antonella Forlino, Silvia Maruelli, Paola Perucca, Debora Vergani, Giuliano Mazzini, Andrea Mattevi, Lucia Anna Stivala, Leonardo Salviati, and Orsetta Zuffardi

of which I am coauthor has been accepted in January 2017 by the
European Journal of Human Genetics.